KU LEUVEN

ARENBERG DOCTORAL SCHOOL
FACULTY OF SCIENCE

Behavior of many ions in a Penning trap and results of the WITCH experiment

CERN-THESIS-2015-384
01/07/2015



Tomica Porobić

Supervisor:
Prof. dr. Nathal Severijns
dr. Paul Finlay, co-supervisor

Dissertation presented in partial fulfillment of the requirements for the degree of Doctor in Science

July 2015

Behavior of many ions in a Penning trap and results of the WITCH experiment

Tomica POROBIĆ

Examination committee:
Prof. dr. Mark Huyse, chair
Prof. dr. Nathal Severijns, supervisor
dr. Paul Finlay, co-supervisor
Prof. dr. Gerda Neyens
Prof. dr. Ricardo Raabe

dr. Marcus Beck
(Johannes Gutenberg-Universität Mainz)
Prof. dr. Etienne Liénard
(Université de Caen, France)

Dissertation presented in partial fulfillment of the requirements for the degree of Doctor in Science

July 2015

© 2015 KU Leuven – FACULTY OF SCIENCE
Uitgegeven in eigen beheer, Tomica Porobić, Celestijnenlaan 200D box 2418, B-3001 Leuven (Belgium)

Alle rechten voorbehouden. Niets uit deze uitgave mag worden vermenigvuldigd en/of openbaar gemaakt worden door middel van druk, fotokopie, microfilm, elektronisch of op welke andere wijze ook zonder voorafgaande schriftelijke toestemming van de uitgever.

All rights reserved. No part of the publication may be reproduced in any form by print, photoprint, microfilm, electronic or any other means without written permission from the publisher.

Acknowledgments

I would like to express my gratitude to all the people that supported this project through collaboration, fruitful discussion or in other ways. In the past four and a half years, their help was invaluable for its completion.

Foremost, I'm pleased to thank my supervisor, Prof. Nathal Severijns, for his support. Our discussions, and his input and guidance, were always very valuable and appreciated.

It's also a pleasure to thank the other present and former members of the WITCH collaboration, my co-supervisor Paul, Martin (whose expertise on Penning traps was essential), Michaël, Simon, Dalibor, Andreas, Elisabeth, Emil, Valentin. Of course, I would also like to thank the members of our wider collaboration, Claire, Gergelj, Philippe, Maciej, Peter... Special thanks goes to our collaborators from LPC Caen, who made it possible to perform a large part of the experiment at their laboratory: Xavier Fléchard, Etienne, Gilles, Xavier Fabian.

I am also grateful to the members of the examination committee: Prof. dr. Mark Huyse, Prof. dr. Gerda Neyens, Prof. dr. Ricardo Raabe, Prof. dr. Nathal Severijns, dr. Paul Finlay, dr. Marcus Beck and Prof. dr. Etienne Liénard.

I wish to thank all the other people who contributed to our experiment through their work at ISOLDE/CERN laboratory providing infrastructure and assistance. In particular, I would like to thank Fredrik, Emiliano, Magda...

Many thanks to the ICT staff at the IKS (Luc and Bert) for their assistance with my often unusual computer requests, as well as the technical staff at LPC Caen. I am indebted to the administrative staff (Isabelle, Fabienne, Danielle, Sally) for their quick and always efficient assistance.

Last but not least, thanks to all my friends and family for the support!

Tomica,
July 2015

Preface

The unification of all physical interactions, i.e. reduction of the multitude of observed phenomena to a small set of underlying common principles, has been a long-standing driving force in science. This idea extends from the pre-scientific world of Archimedes and Democritus, who introduced the concepts of axiomatic reduction of physical phenomena and the notion of the atom, respectively.

The Standard model stands as the pinnacle of this effort, unifying all known forces in nature with the exception of gravity into a single, self-consistent framework. It combines electromagnetism, the weak interaction, and the strong interaction, explaining how the 12 fermionic elementary particles – quarks and leptons – interact with the force-carrying gauge bosons – photons, gluons, weak bosons and Higgs bosons. However, the Standard model leaves open several important questions, e.g. the origin of phenomena such as P-and CP-violation, the hierarchy problem or the large number of *ad hoc* constants that do not follow from theoretical first principles. This strongly supports the idea that the Standard model is not – gravity notwithstanding – a complete theory of elementary particles and their interactions. In addition to previously mentioned shortcomings of the Standard model, the weak β-decay process provides another interesting opportunity for probing the physics beyond the Standard model. Exotic scalar and tensor couplings in the weak interaction, not yet experimentally excluded, present a conceivable extension to the Standard model, possibly indicating the existence of new force carrier particles.

This search also takes place at the high energy frontier, e.g. the Large Hadron Collider at CERN that is capable of producing new particles thereby discovering exotic forces. The low energy frontier then provides a complementary approach for uncovering these new physics phenomena, by precision measurements which aim to find small deviations from Standard model predictions.

WITCH (**W**eak **I**nteraction **T**rap for **CH**arged particles) is such an experiment, situated at the CERN/ISOLDE laboratory and combining two Penning traps

and a retardation spectrometer with the goal of a precise measurement of recoil ion energy spectra in β-decay that would lead to a determination of the $\beta - \nu$ angular correlation coefficient a and finding evidence of possible exotic interactions. The experimental proof-of-concept was performed in 2006 when the recoil energy spectrum of ^{124}In was measured. However, the $a_{\beta-\nu}$ was not extracted due to the complex decay scheme of the isotope. After that, the experimental focus was placed on ^{35}Ar. On line experiments in 2009 uncovered significant difficulties with background ions and unwanted Penning traps in the spectrometer, which were reduced after extensive modifications to the apparatus. The vacuum quality has been improved significantly, and a conductive wire was placed in the spectrometer to reduce the number of background electrons trapped in that section.

In 2011, a first data set that allowed the extraction of $a_{\beta-\nu}$ in ^{35}Ar decay was taken. However, low statistics precluded the determination of $a_{\beta-\nu}$ with precision. Before the November 2012 experiment an upgrade of the entire data acquisition system was performed, enabling us to uncover and characterize several previously unknown systematic effects. In addition, an extensive campaign that focused on the behavior of many ions in the Penning traps was undertaken. Focused on tests with stable ions, it characterized the collective effects that emerge in large ion clouds (with $10^5 - 10^6$ ions), including the shifts in resonant frequencies used for buffer gas cooling. Furthermore, the experimental results were successfully modeled and reproduced in realistic simulations with the Simbuca software package, validating its use for design and optimization of other high-capacity Penning traps.

The November 2012 data was analyzed and most systematic effects were taken into account. However, Monte Carlo simulations of the recoil spectrum uncovered an unexpected background component correlated with the number of radioactive ions in the decay trap. Unfortunately, this precluded a precise determination of $a_{\beta-\nu}$. In addition, a full characterization of this background component would require a large upgrade of the apparatus and a dedicated campaign with radioactive ions, which is presently not possible due to the high demand for beam time at the ISOLDE laboratory.

Abstract

Precision measurements of the $\beta - \nu$ angular correlation in nuclear β-decay provide a unique window into the physics beyond the Standard model. The WITCH (**W**eak **I**nteraction **T**rap for **CH**arged particles) experiment aims to measure this correlation, $a_{\beta-\nu}$, in order to impose a more stringent constraint on the exotic scalar current admixture in the β-decay Hamiltonian.

The apparatus is situated at CERN/ISOLDE laboratory and consists of a unique combination of a retardation spectrometer and two Penning traps, with one of them serving as a scattering-free source. This configuration is suited for a precise measurement of the energy spectrum of ^{35}Ar recoiled daughter ions. The shape of the spectrum then allows a determination of $a_{\beta-\nu}$ and consequently of the presence or absence of a scalar current.

Radioactive ^{35}Ar ions are created at ISOLDE by impinging 1.2 GeV protons on the target material. After being separated by a magnetic separator and bunched by REXTRAP, a high-capacity Penning trap, they are delivered to the WITCH beam line with an energy of 30 keV per ion. A pulsed drift tube then reduces this energy to $\sim$100 eV, enabling their capture in the cooler trap where they undergo buffer gas cooling and centering processes before being transferred to the decay trap. After decay, the energy spectrum of recoil ^{35}Cl daughter ions is probed in the retardation spectrometer before they are finally counted by an MCP detector.

Retardation spectra for various values of $a_{\beta-\nu}$ are simulated by SimWITCH, a Monte Carlo simulation software that tracks the recoil ions from a cloud in the decay trap through the spectrometer. The experimental spectrum is then fitted to simulated spectra and the value of $a_{\beta-\nu}$ can be extracted. The properties of the ion cloud from injection into the cooler trap to transfer into the decay trap are obtained with Simbuca, a simulation software package that exploits native GPU parallelism for fast *ab initio* simulation of ion cloud dynamics in a Penning trap, with realistic electric and magnetic field maps.

Furthermore, as the main focus of this work, systematic effects arising in large ion clouds (of $10^5 - 10^6$ ions) are studied experimentally with stable ^{39}K ions as well as computationally with Simbuca and comparatively analyzed and presented. Specifically, the influence of space-charge and buffer gas on cyclotron cooling resonances is investigated. Experimental ion cyclotron resonances are compared with *ab initio* Coulomb simulations and found to be in agreement, showing an increase of central values and FWHMs with increasing space-charge and buffer gas pressure. The ability to accurately simulate the behavior of large ion clouds in specific experimental conditions is of special interest for the design and optimization of high-capacity Penning traps and their operation as mass separators.

Another important systematic effect of the WITCH experiment, the magnetron eigenmotion of the ion cloud around the trap center, is experimentally studied under increasing space-charge conditions. In addition, the helium buffer gas pressure in the Penning trap is determined by comparing experimental cooling rates with simulations.

In June 2011, an experiment resulting in a first determination of $a_{\beta-\nu}$ with WITCH was performed, albeit with low statistics and with no systematic effects considered. The November 2012 experiment yielded a much larger data set. Combined with a significantly improved data-acquisition system, this enables us to uncover several important systematic effects and account for their influence. These include energy-dependent efficiency of the main MCP, two separate radioactive components stemming from the decay of overshot ^{35}Ar ions implanted into the main MCP detector and from the β-particles originating in the decay trap, and an effect of the magnetron motion of the entire ion cloud around the trap center. The data is then fitted with a function tailored to account for these systematic effects. However, another background component difficult to account for was found to significantly distort the low energy part of the recoil spectrum and hamper the extraction of $a_{\beta-\nu}$. Using Monte Carlo simulations of the spectrum, it is found that this component is most likely correlated with the amount of radioactive ions in the decay trap and is composed of low-energetic Gaussian-distributed rest gas or buffer gas ions. An overview of measures needed to characterize and reduce this background are given. Finally, constraints related to availability of radioactive beams at ISOLDE leading to the discontinuation of the project are discussed.

Beknopte samenvatting

Precisiemetingen van de $\beta - \nu$ angulaire correlatie in nucleair β-verval geven een unieke inkijk op fysica buiten het standaard model. Het WITCH (**W**eak **I**nteraction **T**rap for **CH**arged particles, oftewel de zwakke interactie val voor geladen deeltjes) experiment heeft als doel de correlatie coëfficiënt $a_{\beta-\nu}$ te meten en zo nauwere begrenzingen op te leggen op de inmenging van exotische scalaire stromen in de Hamiltoniaan van het β-verval.

De experimentele opstelling bevindt zich in het CERN/ISOLDE laboratorium en bestaat uit een unieke combinatie van een retardatie spectrometer en twee Penningvallen, waarbij een van de vallen dient als een verstrooiingsvrije bron van β-verval. Deze configuratie is geschikt voor een precieze meting van het energiespectrum van de terugkaatsende dochterkernen van ^{35}Ar. Uit het verloop van het spectrum kan de $a_{\beta-\nu}$ coëfficiënt bepaald worden en bijgevolg ook de aanwezigheid van een scalaire stroom in de Hamiltoniaan.

Radioactieve ^{35}Ar ionen worden aangemaakt in ISOLDE door 1,2 GeV protonen te schieten op een geschikt doelmateriaal. Na gescheiden en gebundeld te worden door een magnetische separator en REXTRAP (een Penning val met hoge ionencapaciteit), worden de ionen aangeleverd aan de WITCH beamline met een energie van 30 keV per ion. Vervolgens wordt de energie van de ionen verder verlaagt tot ongeveer 100 eV door een gepulste drift buis, wat hun vangst in de eerste Penningval mogelijk maakt. Hier worden de ionen gekoeld en gecenterd door een buffergas en vervolgens worden ze getransfereerd naar de tweede Penningval waar ze dienst doen als radioactieve bron. Na radioactief verval worden de ^{35}Cl dochterkernen op energie geselecteerd door de retardatiespectrometer en uiteindelijk geteld met een MCP-detector.

De retardatiespectra worden voor verschillende waarden van $a_{\beta-\nu}$ gesimuleerd met SimWITCH, een Monte Carlo software pakket dat de baan van de teruggestoten ionen volgt van de tweede Penningval tot de MCP-detector. Het experimentele spectrum wordt dan gefit aan de gesimuleerde spectra en

de waarde van $a_{\beta-\nu}$ kan aan de hand daarvan bepaald worden. De kenmerken van de ionenwolk, van injectie in de eerste Penning val tot transfer naar de tweede val, worden gekarakteriseerd met Simbuca, een simulatie softwarepakket dat gebruik maakt van de parallelliseerbaarheid van de GPU voor een snelle *ab initio* simulatie van ionenwolkdynamica in een Penningval met realistische elektrische en magnetische velden.

Het hoofdonderwerp van dit werk is een studie van systematische effecten die optreden in ionenwolken van $10^5 - 10^6$ ionen. Experimenteel wordt er gekeken naar het gedrag van een stabiele ^{39}K ionenwolk, wat daarna vergeleken wordt met computationele resultaten bekomen met Simbuca. Meer specifiek, de invloeden van ruimtelading en buffergas op cyclotronkoeling resonanties worden bestudeerd. Experimentele cyclotron resonanties worden vergeleken met *ab initio* Coulomb simulaties en de resultaten blijken overeen te stemmen: een toename van de centrale waarden en FWHMs met toenemende ruimtelading en buffergasdruk. Het vermogen om nauwkeurig het gedrag van grote ionenwolken te simuleren in specifieke experimentele condities is van speciaal belang voor ontwerp en optimalisering van hoge-capaciteit Penningvallen en hun operatie als massa separators.

Een tweede belangrijk systematisch effect dat bestudeerd wordt in dit werk is de magnetron eigenbeweging van de ionenwolk rond het centrum van de val bij toenemende ruimtelading. Ook wordt de helium buffergas druk in de Penningval bepaald door experimentele koelingssnelheden te vergelijken met simulaties.

In juni 2011 werd een eerste bepaling van $a_{\beta-\nu}$ met WITCH uitgevoerd, al zij het met lage statistieken en zonder enige systematische effecten in acht te nemen. In november 2012 werd het experiment herhaald met als resultaat een veel grotere dataset. Gecombineerd met een beter dataverwerkingssysteem, maakte dat ons mogelijk om enkele belangrijke systematische effecten bloot te leggen en er ook rekening mee te houden. Deze effecten omvatten een energie-afhankelijke efficiëncie van de MCP detector, twee verschillende radioactieve componenten komende van geïmplanteerde ^{35}Ar ionen in de detector en β-deeltjes uit de tweede Penningval, en de magnetron beweging van de volledige ionenwolk rond het centrum van de Penningval. Vervolgens is de data gefit met een speciale fitfunctie, welke de bovengenoemde systematische effecten in rekening brengt. Een bijkomende component van de achtergrond was echter moeilijk in rekening te brengen en blijkt de laag-energetische kant van het spectrum significant te vervormen, wat de extractie van $a_{\beta-\nu}$ zeer belemmerde. Door gebruik te maken van Monte Carlo simulaties van het spectrum hebben we gevonden dat deze component zeer waarschijnlijk gecorreleerd is aan de hoeveelheid radioactieve ionen in de tweede Penningval en dat hij bestaat uit laag-energetische, Gaussisch verdeelde restgas- of buffergas-ionen.

Ten slotte volgt een discussie van maatregelen die nodig zijn om deze achtergrondcomponent te karakteriseren en verminderen en ronden we dit werk af met een conclusie.

Contents

Abstract v

Contents xi

1 Introduction 1

1.1 Fermi's β-decay theory 1

1.2 From parity violation to electroweak unification 2

1.2.1 V–A theory and parity violation 2

1.2.2 Electroweak unification 4

1.3 β-decay in the Standard Model 5

1.3.1 General β-decay Hamiltonian 5

1.3.2 $\beta - \nu$ correlation 6

1.4 Ion recoil energy and a 8

1.4.1 Recoil spectrum 9

1.5 $\beta - \nu$ correlation experiments 11

1.5.1 Previous experiments 11

1.5.2 Current experiments 12

1.5.3 Experiments in preparation 13

1.5.4 Competition with LHC 13

2 The WITCH Experiment **15**

2.1 On-line radioactive isotope production at ISOLDE/CERN 15

2.1.1 REXTRAP 16

2.2 Beam line 17

2.2.1 Horizontal beam line 19

2.2.2 Vertical beam line 20

2.2.3 Diagnostics and beam optimization 20

2.3 Penning traps 22

2.4 Spectrometer 22

2.5 Main MCP detector and data-acquisition 24

2.5.1 MCP detector 24

2.5.2 Data acquisition 25

2.5.3 The Experimental Cycle 25

2.6 Choice of isotope 25

2.6.1 ^{35}Ar 29

3 Penning traps **31**

3.1 Penning trap principles 32

3.2 Single-particle Penning trap theory 33

3.2.1 Eigenmotions 33

3.3 Buffer-gas cooling 36

3.3.1 Ion excitations 37

3.4 Trap imperfections and deviations from single-particle theory . 40

3.4.1 Imperfections of the electric potential 40

3.4.2 Imperfections of the magnetic field 41

3.4.3 Many ions in the trap 42

3.5 WITCH Penning traps 42

3.5.1 Design 42
3.5.2 Electronics 45
3.5.3 Trapping procedure 46

4 Space-charge effects in Penning traps 49

4.1 Non-neutral plasma systematic effects 50
4.1.1 Introduction 50
4.1.2 Ion motion in a non-neutral plasma 51
4.1.3 Ion cloud energy 54
4.1.4 Quadrupolar excitation and buffer gas cooling 60
4.2 Space-charge effects in Penning ion traps 71
4.2.1 Abstract 71
4.2.2 Introduction 72
4.2.3 Nonneutral plasma in a Penning trap 73
4.2.4 Experimental setup 76
4.2.5 Experimental results 80
4.2.6 Simulations 85
4.2.7 Summary and outlook 94
4.2.8 Acknowledgments 96
4.3 Conclusion 97

5 Characterization of the MCP efficiency 99

5.1 Introduction 99
5.2 Experimental setup 100
5.2.1 Microchannel plates 100
5.2.2 The MCP detector 101
5.2.3 Signal processing 105
5.3 Efficiency of the microchannel plates 110

5.4 Efficiency measurement technique . . . 111
5.5 Motivation . . . 112
5.6 Experimental setup . . . 113
5.7 Experimental procedure . . . 114
5.8 Analysis . . . 118
5.8.1 Linearity of the charge normalization . . . 118
5.8.2 MCP detection efficiency . . . 122
5.9 Pulse height distribution . . . 128
5.10 Comparison between ion species . . . 130
5.11 Conclusion . . . 132

6 Data analysis of the November 2012 experiment 133

6.1 Introduction . . . 133
6.2 Data structure . . . 134
6.2.1 Events . . . 134
6.2.2 Cycles . . . 134
6.2.3 Runs . . . 137
6.3 Background reduction . . . 138
6.3.1 Sources of background . . . 140
6.3.2 Data filtering . . . 145
6.4 Data fitting . . . 148
6.4.1 Structure of the fit function . . . 149
6.5 Fit results . . . 151
6.5.1 Quality of the fit . . . 152
6.5.2 Amplitudes . . . 159
6.6 Monte Carlo background simulations . . . 161
6.7 Conclusion and outlook . . . 166

7 Conclusion **169**

Bibliography **173**

Chapter 1

Introduction

The WITCH experiment aims to measure the $\beta - \nu$ correlation coefficient $a_{\beta-\nu}$ with the purpose of determining the exact form of the weak interaction in β-decay. Presently, within the framework of the Standard model, it is known to be of V–A (vector – axial vector) form. However, exotic scalar (S) and tensor (T) couplings are not excluded with high precision, the former only to 6.5%. The goal of the WITCH experiment is to increase this precision, thereby imposing more stringent limits on the physics beyond the Standard Model in the electroweak sector. The theoretical background and motivation for this work are presented in this chapter.

1.1 Fermi's β-decay theory

The field of nuclear physics was born following the discovery of radioactivity by Henri Becquerel in 1897. Initially, radioactivity was viewed only as an anomaly in a world fully governed by laws of gravitation and electromagnetism, the only known fundamental forces at the time, contained within the framework of classical physics. The developments following the discovery of this deviation from the known framework eventually gave rise to a large part of modern physics. Soon after Becquerel's initial discovery, three distinct forms of the phenomenon were distinguished: α, β and γ radiation, differentiated by their behavior in a magnetic field. Only much later their true nature was discovered: α-rays consisted of ^{4}He nuclei, β-rays of electrons or positrons, and γ-rays of photons. Subsequently, it was found that β-decay differed in one important respect. It was caused by a new fundamental interaction – the weak interaction. In a

β-decay, a neutron undergoes conversion to a proton (or *vice versa*), emitting an electron (a positron) and an antineutrino (a neutrino) in the process.

There are three types of β-decay processes:

- β^- decay: $n \to p + e^- + \overline{\nu}_e$
- β^+ decay: $p \to n + e^+ + \nu_e$
- Electron capture: $p + e^- \to n + \nu_e$,

where n represents a neutron, p a proton, e^- an electron, $\overline{\nu}_e(\nu_e)$ an antineutrino (neutrino) and e^+ a positron.

In 1933, Fermi posited a theory of β-decay processes based on a four-fermion contact interaction. Its foundational hypotheses included the existence of Pauli's neutrino, β-decay products that consist of an electron and a neutrino, and proton-neutron model of nuclear structure. Furthermore, it was formulated analogous to the electromagnetic interaction, with the current in the Hamiltonian replaced by a proton-neutron current:

$$\mathcal{H}_F = g_F \overline{p} \gamma_\alpha n \overline{e} \gamma^\alpha \nu + h.c., \tag{1.1}$$

where g_F is the weak coupling strength, $\overline{p} = p^\dagger \gamma^0$, p being the proton field, γ_α the Dirac matrices, n the neutron field and $h.c.$ the Hermitian conjugate. The Fermi Hamiltonian takes into account only β-decay with spin, isospin and parity constant between the initial and final states (Fermi selection rule). The description of experimentally observed spin-changing β-decay processes (Gamow-Teller selection rule) required additional terms added to the original Fermi Hamiltonian.

1.2 From parity violation to electroweak unification

1.2.1 V–A theory and parity violation

While the original Fermi Hamiltonian is of the *vector* $\times$ *vector* form, the most general Lorentz-invariant form is a sum of scalar (S), vector (V), axial-vector (A), tensor (T) and pseudoscalar (P) terms:

$$\mathcal{H}_F = \sum_{i=S,V,A,T,P} G_i \overline{p} O_i n \overline{e} O_i \nu + h.c., \tag{1.2}$$

	Selection rules	Operators
Fermi	$\Delta I = 0$ $\Delta T = 0$ $\Delta \pi = 0$	S/V
Gamow-Teller	$\Delta I = 0, \pm 1$ $\Delta T = 0, \pm 1$ $\Delta \pi = 0$	T/A

Table 1.1: Selection rules for Fermi and Gamow-Teller transitions. T and π represent isospin and parity, respectively.

where G_i are the coupling constants and O_i the operators. This refinement, able to account for all β-decay data, was introduced by Gamow and Teller in 1936 [43]. The transitions can be classified with respect to their nuclear spin (I) change (see Table 1.1). All cases shown correspond to orbital angular momentum change $\Delta L = 0$, designated as *allowed* transitions, in contrast to *forbidden* transitions characterized by $\Delta L > 0$.

Both the Fermi and the Gamow-Teller Hamiltonians are parity-conserving. The next significant breakthroughs occurred in 1956 and 1957, when Lee and Yang proposed parity breaking in the weak interaction, and Wu et al. [116], in a classic experiment, discovered weak parity breaking in the β-decay of polarized ^{60}Co nuclei.

In 1957-1958, Feynman, Gell-Mann [36], Marshak and Sudarshan [101] incorporated the newly discovered large parity violation into the four-fermion contact interaction Hamiltonian, casting it in a current-current interaction form

$$\mathcal{H}_{V-A} = \frac{G_F}{\sqrt{2}} J_\mu^\dagger \cdot J_\mu \nu + h.c. \tag{1.3}$$

where $G_F/(\hbar c)^3 = 1.16639(1) \times 10^{-5} \mathrm{GeV}^{-2}$ is the Fermi coupling constant and the current J_μ is composed of a hadronic and a leptonic component

$$J_\mu = J_\mu^{had} + J_\mu^{lep} = \overline{u}\gamma^\mu(1-\gamma^5)d' + \overline{\nu}\gamma_\mu(1-\gamma^5)e, \tag{1.4}$$

where γ^5 is the fifth Dirac matrix and u and d up and down quarks, respectively. The form of the Hamiltonian is now vector (γ^μ) minus axial-vector ($\gamma^\mu\gamma^5$), manifestly breaking the conservation of parity. Other features of the theory

include lepton number conservation, maximal parity violation, conservation of the weak vector current, massless neutrinos and left-handedness of leptons.

Furthermore, in 1963 Cabibbo [26] introduced the θ_c mixing angle to account for the experimentally observed suppression of strangeness-changing processes:

$$d' = cos\theta_C \cdot d + sin\theta_C \cdot s = V_{ud}d + V_{us}s, \tag{1.5}$$

where d' is the weak, and d, s the mass quark eigenstates. This designation effectively "rotates" the weak eigenstates of quarks with respect to the mass eigenstates. In the case of β-decay, heavier quarks do not contribute in the first order

$$d' \simeq cos\theta_C \cdot d = V_{ud}d. \tag{1.6}$$

1.2.2 Electroweak unification

It is known today that the four-fermion contact interaction approximation provides us with the correct effective Hamiltonian of the low-energy β-decay processes. However, Fermi's theory suffers from severe limitations at high energies. In 1960, Lee and Yang proposed a heavy charged intermediate vector boson as a mediator of the weak interaction. This lead to a unification of weak and electromagnetic interactions within the $SU(2) \times U(1)$ gauge group and four massless gauge bosons as mediators [44, 111]. At lower energies, the theory explains the occurrence of the three massive vector bosons ($W^{\pm}$, Z^0) through spontaneous symmetry breaking and the Higgs mechanism. Today, the electroweak theory stands as a large part of the Standard Model of elementary particles, that consists of the three lepton generations

$$\begin{pmatrix}\nu_e \\ e\end{pmatrix}, \begin{pmatrix}\nu_\mu \\ \mu\end{pmatrix}, \begin{pmatrix}\nu_\tau \\ \tau\end{pmatrix}, \tag{1.7}$$

the three quark generations

$$\begin{pmatrix}u \\ d\end{pmatrix}, \begin{pmatrix}c \\ s\end{pmatrix}, \begin{pmatrix}t \\ b\end{pmatrix}, \tag{1.8}$$

the four gauge bosons as force mediators, and the Higgs boson. Generalizing Equation 1.5, the weak interaction mixes the mass eigenstates of the six quarks according to the Cabbibo-Kobayashi-Maskawa matrix [26, 62]

$$\begin{pmatrix} d' \\ s' \\ b' \end{pmatrix} = \begin{pmatrix} V_{ud} & V_{us} & V_{ub} \\ V_{cd} & V_{cs} & V_{cb} \\ V_{td} & V_{ts} & V_{tb} \end{pmatrix} \begin{pmatrix} d \\ s \\ b \end{pmatrix},$$

with primed letters designating the weak eigenstates. Unitarity of the CKM matrix is required for the normalization of the quark wave functions.

1.3 β-decay in the Standard Model

As a special case of the general weak interaction theory within the Standard model, a low energy four-fermion contact interaction approximation of nuclear β-decay can be constructed.

1.3.1 General β-decay Hamiltonian

The most general Hamiltonian density describing low-energy β-decay [67] is given by:

$$\begin{aligned} \mathcal{H}_\beta =& (\overline{p}n)(\overline{e}(C_S + C'_S\gamma_5)\nu) + (\overline{p}\gamma_\mu n)(\overline{e}\gamma_\mu(C_V + C'_V\gamma_5)\nu) \\ &+ \frac{1}{2}(\overline{p}\sigma_{\lambda\mu}n)(\overline{e}\sigma_{\lambda\mu}(C_T + C'_T\gamma_5)\nu) - (\overline{p}\gamma_\mu\gamma_5 n)(\overline{e}\gamma_\mu\gamma_5(C_A + C'_A\gamma_5)\nu) \ , \\ &+ (\overline{p}\gamma_5 n)(\overline{e}\gamma_5(C_P + C'_P\gamma_5)\nu) + h.c. \end{aligned} \tag{1.9}$$

where

$$\sigma_{\lambda\mu} = -\frac{1}{2}i(\gamma_\lambda\gamma_\mu - \gamma_\mu\gamma_\lambda). \tag{1.10}$$

The Hamiltonian includes all possible interaction types allowed by the Lorentz invariance and given by $\mathcal{O}_S = 1$, $\mathcal{O}_V = \gamma_\mu$, $\mathcal{O}_T = \frac{1}{\sqrt{2}}\sigma_{\lambda\mu}$, $\mathcal{O}_A = -i\gamma_\mu\gamma_5$ and $\mathcal{O}_P = \gamma_5$, with the letters S, V, T, A and P representing scalar, vector, tensor, axial-vector and pseudo-scalar interaction types, respectively. The C_i and C'_i constants are given by the relative strength of the couplings and their symmetry properties with respect to charge conjugation (C), parity (P) and time reversal (T). Parity conservation implies either $C_i = 0$ or $C'_i = 0$ and parity is violated if both $C_i \neq 0$ and $C'_i \neq 0$. Maximal parity violation implies $|C_i| = |C'_i|$.

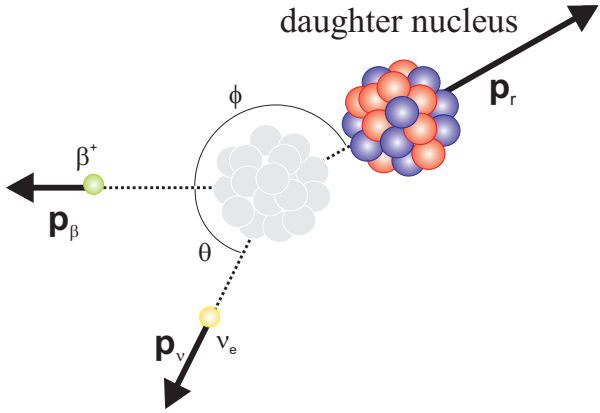


Figure 1.1: The kinematics of a β-decay event.

Charge-conjugation invariance results in $Re(C_i/C_i') = 0$ or $Re(C_i'/C_i) = 0$, i.e. when C_i are real, and C_i' purely imaginary. Time-reversal invariance results in all C_i and C_i' being real, up to an overall phase. Furthermore, the pseudoscalar term can be neglected to lowest order because the $\mathcal{O}_P = \gamma_5$ operator couples large and small components of the nuclear wave functions, resulting in a minute contribution.

1.3.2 $\beta - \nu$ correlation

The coupling constants C_i and C_i' cannot be deduced from the Standard Model theory and have to be determined empirically. Furthermore, they are not directly available as experimental observables (see Figure 1.1), but their dependence on β-decay observables can be derived from the general Hamiltonian (Equation 1.9). The most general expression for the decay rate distribution of the electron and neutrino direction and electron polarization from non-oriented nuclei for allowed decays is given by [55]

$$\omega(\boldsymbol{\sigma} \mid E_\beta, \Omega_\beta, \Omega_\nu) dE_\beta d\Omega_\beta d\Omega_\nu =$$

$$\frac{F(\pm Z, E_\beta)}{2\pi^5} p_\beta E_\beta (E_0 - E_\beta)^2 dE_\beta d\Omega_\beta d\Omega_\nu \frac{\xi}{2} \Bigg\{ 1 + a \frac{\boldsymbol{p}_\beta \cdot \boldsymbol{p}_\nu}{E_\beta E_\nu} + b \frac{m_\beta}{E_\beta} + \tag{1.11}$$

$$\boldsymbol{\sigma} \cdot \left[G \frac{\boldsymbol{p}_\beta}{E_\beta} + H \frac{\boldsymbol{p}_\nu}{E_\nu} + K \frac{\boldsymbol{p}_\beta}{E_\beta + m_\beta} \left(\frac{\boldsymbol{p}_\beta \cdot \boldsymbol{p}_\nu}{E_\beta E_\nu} \right) + L \frac{\boldsymbol{p}_\beta \times \boldsymbol{p}_\nu}{E_\beta E_\nu} \right] \Bigg\}$$

where $\boldsymbol{\sigma}$ is the spin vector of the β-particle and E_ν, $\boldsymbol{p}_\nu$ and Ω_ν are respectively the energy, momentum and angular coordinates of the neutrino, and E_0 the total available energy. Symbols with the β subscript represent analogous parameters of the β-particle. $F(\pm Z, E_\beta)$ represents the Fermi function, taking into account the Coulomb interaction of the decay products and the Z-charged (the upper sign corresponding to β^- decay, and the lower to β^+ decay) daughter nucleus. The normalization factor ξ is given by:

$$\begin{aligned} \xi = |M_F|^2 (|C_S|^2 + |C'_S|^2 + |C_V|^2 + |C'_V|^2) \\ + |M_{GT}|^2 (|C_A|^2 + |C'_A|^2 + |C_T|^2 + |C'_T|^2) \end{aligned} \tag{1.12}$$

where M_F and M_{GT} are the Fermi and Gamow-Teller nuclear matrix elements, respectively. The correlation coefficients a, b, G, H, K and L depend on both the nuclear matrix elements and coupling constants C_i and C'_i. The $\beta - \nu$ correlation coefficient is highly sensitive to possible scalar and tensor interaction type components in the β-decay, making it an interesting observable in the search for physics beyond the Standard Model. It is given by:

$$a\xi = |M_F|^2 \left[(|C_V|^2 + |C'_V|^2 - |C_S|^2 - |C'_S|^2 \mp \frac{\alpha Z m_e}{p_\beta} 2Im(C_S C_V^* + C'_S C'^*_V) \right]$$

$$+ \frac{|M_{GT}|^2}{3} \left[(|C_T|^2 + |C'_T|^2 - |C_A|^2 - |C'_A|^2 \pm \frac{\alpha Z m_e}{p_\beta} 2Im(C_T C_A^* + C'_T C'^*_A) \right], \tag{1.13}$$

including first order Coulomb corrections. This can be approximated in the case of a pure Fermi transition and with the time invariance intact to

$$a \approx 1 - \frac{|C_S|^2 + |C'_S|^2}{|C_V|^2}. \tag{1.14}$$

Interaction type	$a_{\beta-\nu}$
V	1
A	-1/3
T	1/3
S	-1

Table 1.2: The value of $\beta-\nu$ correlation coefficient $a_{\beta-\nu}$ for pure interactions.

The Fierz interference term, b, is given by:

$$b\xi = \pm 2\Gamma Re\left[|M_F|^2(C_S C_V^* + C_S' C_V'^*) + |M_{GT}|^2(C_T C_A^* + C_T' C_A'^*)\right], \quad (1.15)$$

with $\Gamma = \sqrt{1-\alpha^2 Z^2}$. It contributes to all other correlation coefficient measurements, in the case of a the measurable quantity being

$$\widetilde{a} = \frac{a}{1+\frac{m_e}{E_\beta}b}. \quad (1.16)$$

However, within the Standard model with only V and A couplings present, the Fierz interference term is zero, making the mixed terms in Equation 1.13 zero. Additionally, $b \equiv 0$ if the exotic couplings are purely right-handed ($C_i = -C_i'$). Since b depends linearly on the coupling constants, its measurement would provide a narrow inclusion band extending to infinity in the parameter plane, as constraint of the C_i vs. C_i' exotic couplings. The $\beta-\nu$ correlation coefficient $a_{\beta-\nu}$ depends on the coupling constant quadratically, increasing the experimental precision needed to constrain the coupling constants, but providing a finite inclusion region in the parameter plane. The values of $a_{\beta-\nu}$ for pure interactions are given in Table 1.2.

1.4 Ion recoil energy and *a*

Since measuring the correlation coefficient $a_{\beta-\nu}$ through p_β and p_ν directly is precluded by the extreme difficulty of detecting neutrinos, indirect methods are conventionally used. These include the measurements of β-recoil nucleus coincidence, secondary radiation or recoil ion energy spectrum. Kinematic properties of a β-decay event can be deduced in a coincidence measurement

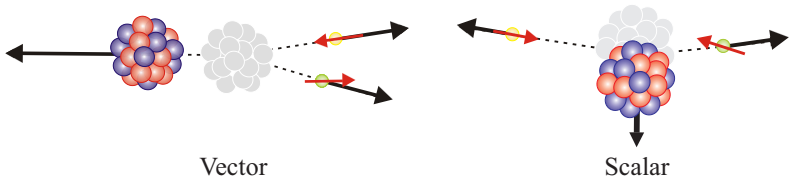


Figure 1.2: (**left**) The kinematics of a β-decay event for a vector current decay and (**right**) scalar current decay. In the latter case, the $\beta - \nu$ angle is predominantly high, resulting in lower recoil energies.

of the β-particle and the recoil ion. In this case, the Time-of-Flight (ToF) of the recoil ion is measured when a detection of a β-particle signals a decay has occurred. Energy and angle can then be calculated and $a_{\beta-\nu}$ obtained. This method is realized in the LPCTrap experiment [89]. In comparison, the WITCH experiment uniquely employs the integral recoil spectrum method, measuring only the spectrum of the total energy of the recoiled ions.

1.4.1 Recoil spectrum

It follows from theory that the vector type interaction in β-decay leads to a shape of the daughter ion energy spectrum significantly different with respect to the one governed by the scalar type interaction (see Figure 1.2). Therefore, a possible scalar admixture in the decay transition would present itself as a deviation of the experimentally observed recoil energy spectrum with respect to the one predicted by the V–A theory. $a_{\beta-\nu}$ determines the shape of the recoil spectra in accordance with the angular distribution relation:

$$W(\theta) = 1 + \frac{p_\beta \cdot p_\nu \cdot cos(\theta)}{E_\beta E_\nu} \widetilde{a}, \tag{1.17}$$

where θ is the angle between the β and ν particles. From Equation 1.17 it follows that for purely scalar interaction ($a_{\beta-\nu}$=-1) the decay angle θ will predominantly be large, approaching $\theta = \pi$, i.e. the β and ν particles will be emitted in opposite direction. This results in lower momentum and energy of the recoiled nucleus. Conversely, with increasing values of $a_{\beta-\nu}$, the θ decreases and the nuclei recoil with higher energies, modifying the spectrum with respect to low values of $a_{\beta-\nu}$ (see Figure 1.3).

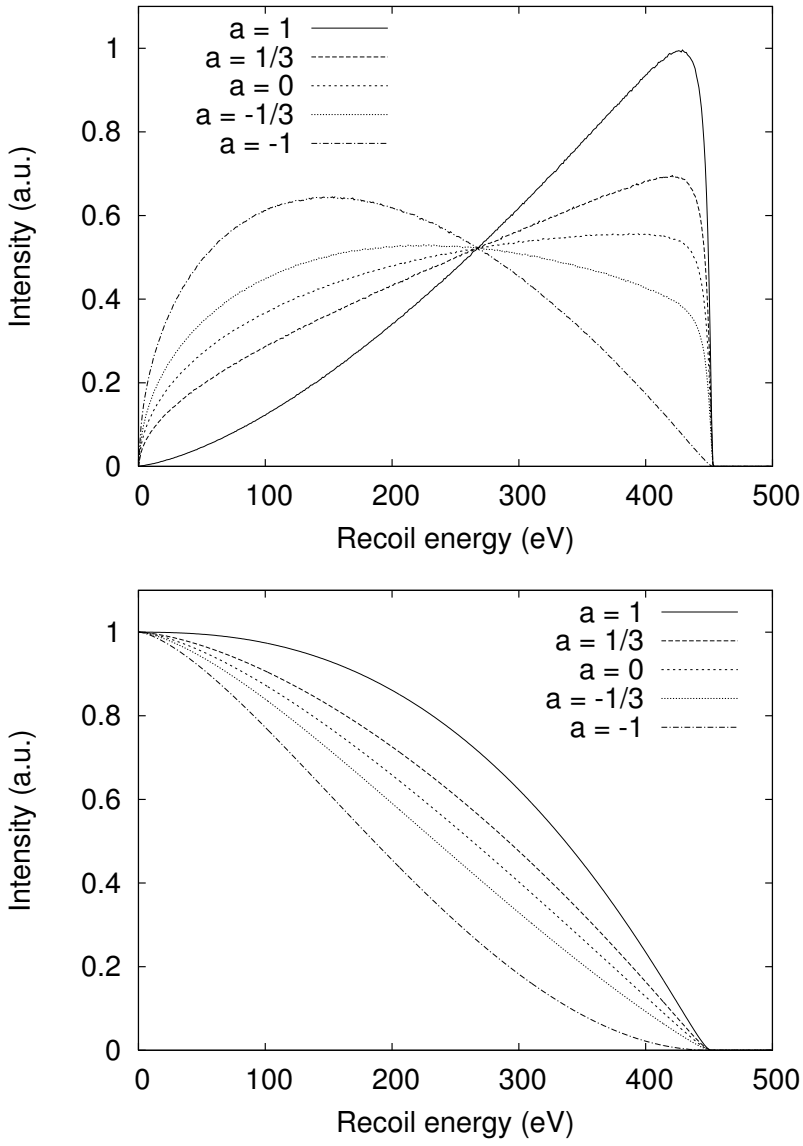


Figure 1.3: (**top**) Differential recoil ion energy plot for different values of $a_{\beta-\nu}$, i.e. different proportions of the scalar interaction admixtures in the case ^{35}Ar β-decay. (**bottom**) Integral spectra with matching values of $a_{\beta-\nu}$.

It is possible to calculate the end-point energy of the recoils from the Q-value of the decay:

$$E_{rec}^{max} = \frac{Q^2 \pm 2Qm_\beta c^2}{2(M_{at}(^A_Z X)c^2 + Q - m_\beta c^2)} \tag{1.18}$$

$$\approx \frac{Q^2 \pm 2Qm_\beta c^2}{2(M_{at}(^A_{Z\pm1} X)c^2)}, \tag{1.19}$$

where $M_{at}(^A_Z X)$ is the recoil ion mass, and the upper (lower) sign represents β^- (β^+) decay. In ^{35}Ar, the WITCH case of interest, this end-point recoil energy is equal to 452 eV.

Since the WITCH experiment uses a retardation spectrometer, it detects all the recoiled ions with energy above the retardation barrier, resulting in an integral spectrum which can then provide information and limits on the possible deviation from the standard V–A model. The goal of the WITCH experiment is to determine the limit for existence of this scalar admixture with as much accuracy and precision as possible.

1.5 $\beta - \nu$ correlation experiments

Several past and current experiments have focused on the $\beta - \nu$ correlation coefficient with the goal of determining the exact form of the weak interaction in β-decay. Recent advances in ion and atom traps have made them a popular choice in decay experiments. Today, measurements of the $\beta - \nu$ correlation coefficient use traps almost exclusively. Paul, Penning and electrostatic traps are used for ions, and magneto-optical (MOT) traps for the confinement of atoms. In contrast to solid sources which introduce back-scattering effects, traps provide a scattering-free environment, and are suitable for production and containment of isotopically pure and cooled samples.

1.5.1 Previous experiments

Historically, the 1963 ^{6}He experiment at Oak Ridge [57] is still known as the most precise determination of $a_{\beta-\nu}$ in a pure Gamow-Teller decay, yielding the constraint for the existence of tensor currents of $\frac{|C_T|^2+|C'_T|^2}{|C_A|^2+|C'_A|^2} \leq 0.4\%$.

In 1993, at ISOLDE/CERN, a determination of $a_{\beta-\nu}$ in a superallowed (pure Fermi) decay of ^{32}Ar was performed. The energy of the recoiled nuclei was calculated from the measured Doppler broadening of delayed protons after

β-decay, resulting in $a = 0.9989(65)$ [6]. This value was later revised to $a = 1.0050(52)$ due to improved precision of the ^{32}Ar Q-value [19].

The experiment with the TRINAT MOT (Magneto-Optical Trap) at TRIUMF [47] , using ^{38m}K, has yielded the most stringent limits on the existence scalar coupling to date, excluding them with a precision of 6.5% [51]. This experiment used the ToF spectrum of the recoiled nuclei in coincidence with the β-particle to reconstruct the decay event-by-event, resulting in $\widetilde{a} = 0.9981(30)^{32}_{37}$.

Another MOT based experiment was performed at Berkeley, determining $a_{\beta-\nu}$ in the case of ^{21}Na, a predominantly Fermi decay providing information on the exclusion limits for scalar currents. The result of $a_{\beta-\nu} = 0.5243(91)$ was published at first [94], in disagreement with the expectation under the Standard model of $a_{\beta-\nu} = 0.5587(27)$, i.e. by about 3σ [99]. This result was revised after a new measurement to $a_{\beta-\nu} = 0.5502(60)$ [109], in agreement with the Standard model. The reason for the initial discrepancy was identified as the creation of molecular Na, which in turn distorted the recoil energy spectrum.

1.5.2 Current experiments

The LPCtrap experiment at GANIL, Caen [89] employs a Paul ion trap of an open design, enabling the use of a much broader variety of elements in comparison to MOT traps. It also observes the ToF spectrum of recoiled nuclei in coincidence with the β-particle. In 2011, the experiment with ^{6}He [37], a pure Gamow-Teller β-decay, resulted in $a = 0.3335(73)$, within the Standard model limits. Subsequently, experiments involving ^{35}Ar were performed. The charge state distribution of ^{35}Ar decay product ^{35}Cl was measured [31], providing essential input for the analysis of the WITCH online data. Analysis with respect to $a_{\beta-\nu}$ in the ^{35}Ar decay is still underway. In late 2013, a ^{19}Ne campaign was started, yielding a preliminary dataset. ^{19}Ne is predominantly a mirror transition to ^{19}F ground state, providing an opportunity for the measurement of $a_{\beta-\nu}$ and constraining exotic currents C_S and C_T [12].

The aSPECT experiment [45] focuses on $\beta - \nu$ correlation measurements in the decay of free neutrons, with the advantage of avoiding nuclear structure related effects. However, the precision is still limited by the present knowledge of the neutron half-life. Situated at ILL Grenoble, it uses a neutron beam and a retardation spectrometer similar to the one used at WITCH. The first published result was $a = -0.1151(40)$ with the reported error purely statistical and systematic effects under investigation.

A linear radio frequency-quadrupole trap is employed at Argonne National Laboratory for β-decay precision measurements [95]. An experiment with

a predominantly Gamow-Teller β-decay in ^{8}Li, sensitive to tensor currents, has been performed recently [68]. It yielded $a_{\beta-\nu} = 0.3307(60)_{stat}(67)_{syst}$, a precision of about 3%.

A MOT experiment seeking to measure $a_{\beta-\nu}$ with a precision of about 0.1% in the decay of ^{6}He is currently underway at the University of Washington [61].

1.5.3 Experiments in preparation

Several trap-based experiments are currently planned or in commissioning phase. Two of those are situated at the Weizmann institute: one design is based on an electrostatic ion beam trap (EIBT) [32], capturing ^{6}He ions in an electrostatic mirror and observing recoiled ^{6}Li ions in coincidence with β-particles [11]. The other is based on a MOT used to trap neutron-deficient Ne isotopes with the decay measured in a coincidence measurement [98].

A double Penning trap system is under commissioning at the Texas A&M university, with the purpose to study $\beta - \nu$ correlation in T=2 superallowed beta-delayed proton emitters [71].

At the NSCL, a measurement of the double Doppler shift following the β-decay of ^{8}He is planned [98] with the intention to improve on a previous similar measurement on ^{18}Ne [34].

The Nab experiment, planned at the Spallation Neutron Source in Oak Ridge, seeks to measure both $a_{\beta-\nu}$ and Fierz interference term b in the β-decay of neutrons [85].

1.5.4 Competition with LHC

It has been shown that low energy searches for exotic scalar and tensor interactions remain competitive with the LHC after the recent upgrades in energy and intensity, if precision better than 10^{-3} is reached in the Fierz interference term in beta or neutron decays [96].

In the LHC experiments, possible new physics related to exotic scalar and tensor interactions is expected to be revealed in a channel with electrons and missing transverse energy (MET) $pp \rightarrow e + MET + X$, with underlying dynamics ($\overline{u}d \rightarrow e\overline{\nu}$) similar to β-decay. The most recent constraints from this search were produced by CMS [59] and are shown in Figure 1.4.

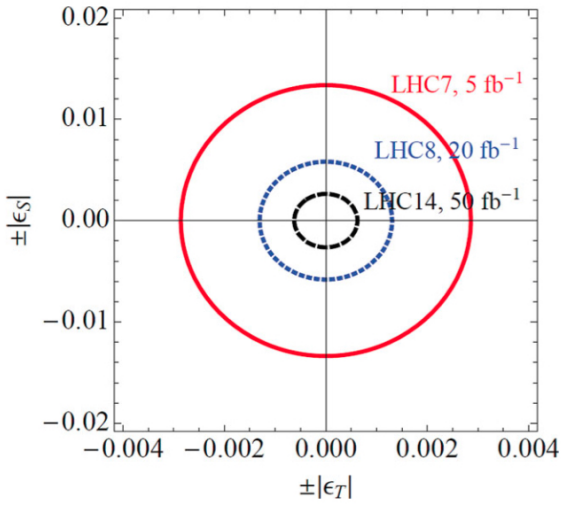


Figure 1.4: Solid red (dotted blue) line represents 90% C.L. on the exotic scalar and tensor interactions $|\epsilon_{S,T}|$ with 5 fb^{-1} (20 fb^{-1}) at $\sqrt{s} = 7$ TeV (8 TeV) taken by the CMS experiment in the $pp \to e + MET + X$ channel. Estimated future limit with higher energy and luminosity is represented by the black line. Figure from [76].

Chapter 2

The WITCH Experiment

In this chapter, an overview of the technical design of WITCH and its situation within the ISOLDE laboratory is presented.

2.1 On-line radioactive isotope production at ISOLDE/CERN

The WITCH experiment (see Figure 2.2) is situated at the ISOLDE (**IS**otope **S**eparation **O**n**L**ine **D**evice) facility [66], a laboratory for production and studies of a wide range of radioactive nuclei. ISOLDE is a part of CERN's accelerator complex, situated at the border of Switzerland and France, since 1967 (see Figure 2.1).

Various radioactive nuclei are produced by nuclear reactions occurring in a fixed target impinged on by high-energy (1.4 GeV) protons originating in the PS-Booster, the first in chain of accelerators with increasing energies. The protons arrive in bunches separated by 1.2 s, with a total current of about 2μA and impinge on the target, heated to $\sim$1000 °C to facilitate the diffusion of the radioactive ions. They are subsequently ionized in one of the ion sources (e.g. VADIS arc discharge [80] or RILIS resonant laser ionization [35]), accelerated to 30 – 60 keV and sent to one of the mass separators before being distributed to experiments. The General Purpose Separator (GPS) has a mass selectivity ($m/\delta m$) of about 500, while the High Resolution Separator (HRS) can achieve 5000. About 70 different elements can be produced by using different combinations of targets and ion sources, as well as about 700 different isotopes

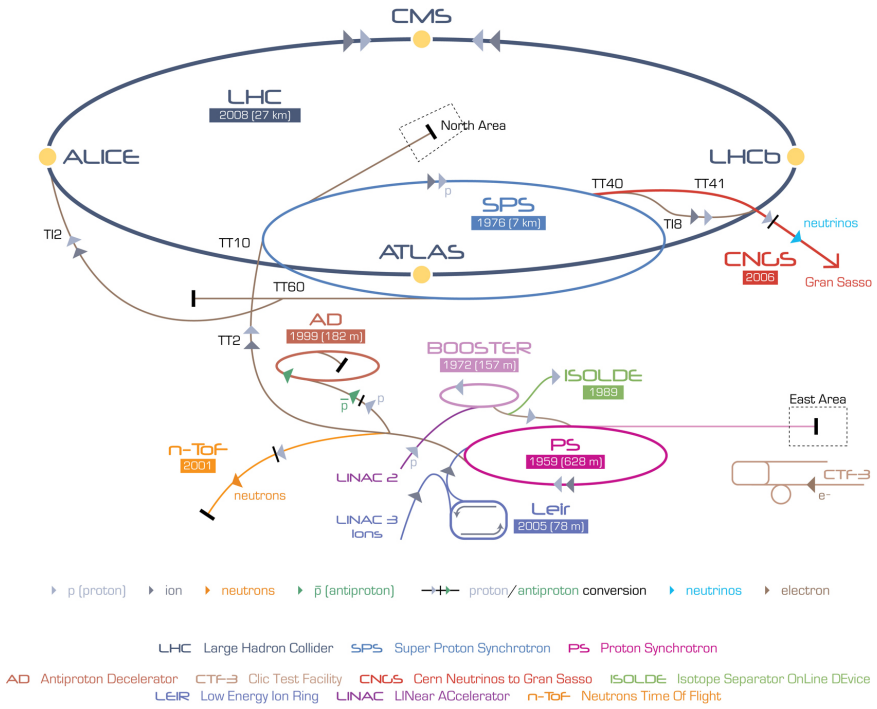


Figure 2.1: Overview of the CERN accelerator complex.

with intensities up to 10^{10} ions/s. The beams can be post-accelerated up to 3 MeV/nucleon, with an upgrade (HIE-ISOLDE) currently in progress allowing energies up to 10 MeV/nucleon.

2.1.1 REXTRAP

REXTRAP [7] is a high-capacity Penning trap used mainly for beam preparation for the current post-acceleration system REX-ISOLDE [49] and WITCH. A quasi-continuous beam delivered from the separator is cooled, bunched and additionally purified in REXTRAP, improving its transversal emittance and reducing the energy spread. The Penning trap is situated in a 3 T magnetic field and contains Ne or Ar buffer gas. The electric fields are relatively high, enabling the trapping of large ion clouds and arranged in a way that allows continuous filling of the trap with ions. The electrode structure consists of 30 electrodes with 4 cm diameter, with a central eight-fold segmented ring

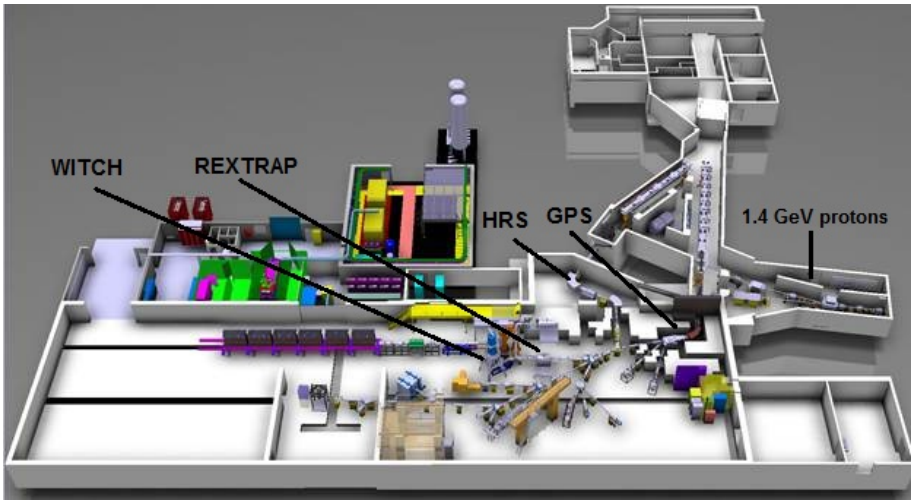


Figure 2.2: The ISOLDE facility overview.

electrode for performing excitations. The Penning trap is divided in two parts (see Figure 2.3), a high buffer gas pressure ($\sim 10^{-3}$ mbar) area for initial cooling of the energetic ions, and a low pressure ($\sim 3.2 \cdot 10^{-4}$ mbar) area where the *sideband* or *rotating wall* excitations are applied [7]. After preparation, ion bunches leave REXTRAP with energies in 30 – 60 keV range. The steepness of the ejection potential can be optimized in order for the bunch length to match the acceptance of WITCH's Pulsed Drift Tube (PDT).

An offline alkali surface ion source is available for testing and optimization purposes, capable of delivering ^{39}K, ^{41}K, ^{85}Rb, ^{87}Rb and ^{133}Cs.

2.2 Beam line

The WITCH beam line extends from REXTRAP to the entrance of the lower Penning trap and is composed out of a horizontal (HBL) and a vertical (VBL) part. Its primary purpose is to guide the ions towards the lower Penning trap, the cooler trap (CT), while reducing their energy from 30 keV to close to 0 eV. It is also used to connect auxiliary devices, e.g. the WITCH offline ion source [105].

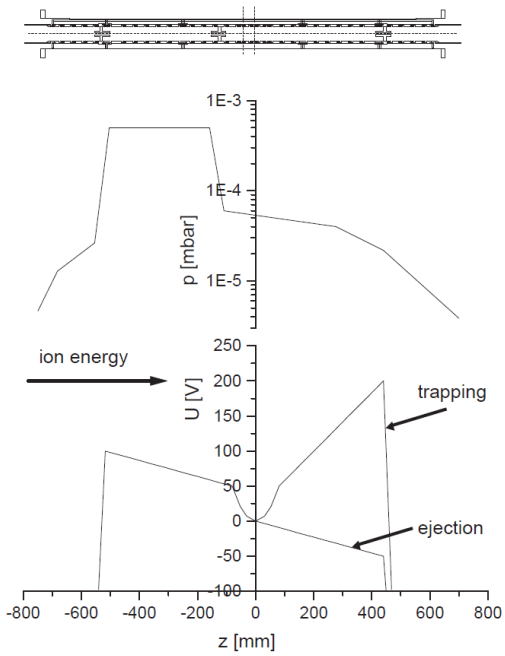


Figure 2.3: (**top**) Schematic of REXTRAP electrode system. (**middle**) Position dependence of buffer gas pressure. (**bottom**) Position dependence of the electric potential. Taken from [7].

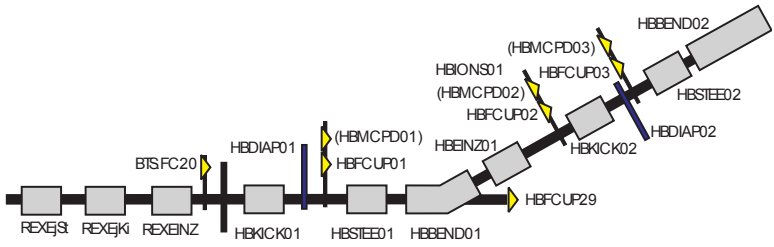


Figure 2.4: Overview of the horizontal beam line, with elements named according to Table 2.1. Elements shown leftmost are part of the REX beam line, named accordingly: REXEjSt is the REXTRAP ejection steerer electrode, REXEjKi the kicker electrode, REXEINZ the einzel lens, and BTS.FC20 a diagnostic Faraday cup.

Abbrev.	Beam line element
HB	Horizontal beam line
VB	Vertical beam line
KICK	Kicker
BEND	Bender
STEE	Steerer
EINZ	Einzel lens
RETA	Retardation electrode
PDT	Pulsed drift tube
DRIF	Drift electrode
FCUP	Faraday cup
MCPD	MCP detector
DIAP	Diaphragm
PIN	PIN diode
IONS	Cross-beam ion source

Table 2.1: Abbreviations used in Figure 2.4 and Figure 2.5.

2.2.1 Horizontal beam line

The horizontal beam line (Figure 2.4) guides the ions to a 90° bender which changes their trajectory vertically. Two sets of kickers, benders and steerers are used to accomplish this. The first kicker/bender pair (HBKICK01 and HBBEND01) deflects the ions trajectory by 29°, allowing additional diagnostic elements to be placed downstream, e.g. a Faraday cup or a tape station. The einzel lens (HBEINZ01) is a focal element in front of the second kicker/bender pair (HBKICK02 and HBBEND02) which guides the ions into the vertical beam line. Between both kicker/bender pairs, steerer elements (HBSTEE01 and HBSTEE02) are placed to fine-tune the ion trajectory in up/down and left/right axes, respectively. The bender electrodes consist of two spherical electrodes, while the kickers and the steerers are planar.

Diagnostic elements (MCP detectors and Faraday cups) are placed along the HBL for beam optimization and monitoring.

2.2.1.1 Offline ion source

The WITCH offline ion source with an RFQ [105] added the capability to perform systematic tests and optimize the WITCH system independently of REXTRAP. It is located above the central part of the HBL and connected to the HBL via a 90° bender electrode (ISBEND01). A surface alkali ion source emits stable ions which are subsequently cooled and bunched in a compact RFQ. The entire ion source and RFQ setup is in a Faraday cage at 30 kV potential.

2.2.2 Vertical beam line

The vertical beam line (see Figure 2.5) extends from the 90° bender HBBEND02 to the cooler trap, containing several pairs of steerer and drift electrodes for trajectory correction and a pulsed drift tube (PDT) [29] to reduce the ion energy from 30 keV to about zero. This method was preferred over elevating the entire trap system to 30 kV because of spatial limitations. The pulsed drift electrode switches from a high potential to a low one, typically 21 kV to -9 kV, while the ions are traversing through it, thereby eliminating most of their potential energy. This procedure takes about 1 μs and can be repeated at 5 Hz frequency, limited by the electronics. The ion bunch exits the PDT with 9 keV of kinetic energy and -9 keV of potential energy and is guided through an array of electrodes with potentials incrementally increased from -5 kV to 0 V. In this way, the ions arrive at the CT entrance with around 100 eV of kinetic energy.

Furthermore, the vertical beam line extends from a low magnetic field region of almost 0 T into the 3 – 9 T field present in the Penning traps. If the ion bunch has a significant transverse component of motion, it can be reflected by the high field (magnetic mirror effect). This reduces beam line transport efficiency and requires careful optimization.

A cross-beam offline ion source (VBIONS01) is also mounted close to the CT entrance. It provides stable ^{40}Ar ions for testing and optimization of the traps.

2.2.3 Diagnostics and beam optimization

Diagnostics

Real-time beam monitoring using MCP detectors and Faraday cups is the primary method of system diagnostics and efficiency optimization of the

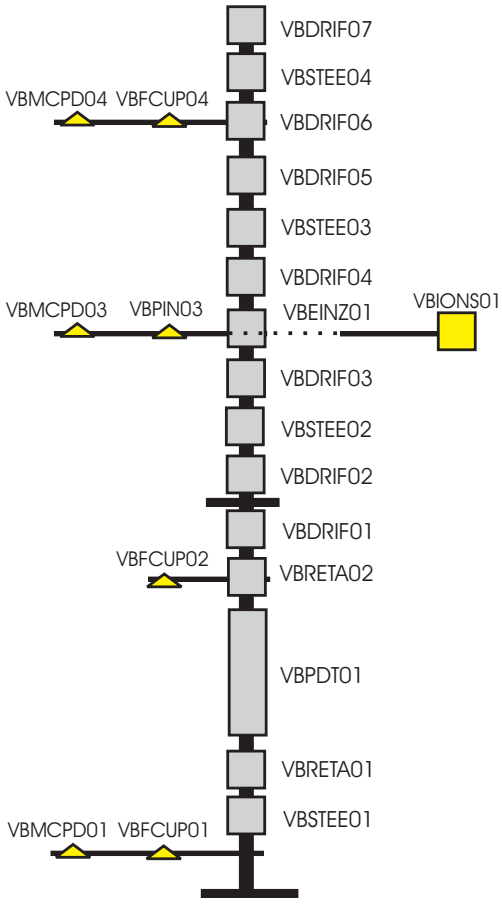


Figure 2.5: Overview of the vertical beam line, with elements named according to Table 2.1.

apparatus. As shown on Figure 2.4 and Figure 2.5, several Faraday cups and MCPs on movable feedthroughs are positioned along both beam lines.

Faraday cups measure the absolute amount of incident ions, i.e. the current or the total charge, depending on the mode of measurement. However, they are difficult to use with low ion numbers typically available at WITCH, e.g. $\sim 10^5$ ions corresponding roughly to $\sim$0.1 pA. Consequently, for beam transport optimization, MCP detectors are used in most cases. MCP detectors are

composed of a large number of micro-channels biased at a high potential difference, and each ion entering a channel creates an electron avalanche that is ultimately collected on the anode and recorded by an oscilloscope. A large ion bunch causes many channels of an MCP to fire simultaneously and the resulting sum of overlapping peaks cannot be reliably used to estimate the ion number. However, by using high-resistance termination and an oscilloscope, the individual ion signals can be integrated into a large peak representative of the total ion number in the bunch [28]. Integrated MCP pulses can be calibrated with a Faraday cup and the absolute number of ions impinging on the MCP can be extracted. This method is employed in Chapter 4 for ion numbers up to about $2 \cdot 10^5$. However, for very large ion bunches ($> 10^6$) the linearity of the MCP's response is no longer preserved.

A single diagnostic MCP is also present in the spectrometer and is used for optimizing the parameters of the Penning traps.

Additionally, holes (from 8 mm to 20 mm) and vertical and horizontal slits 1 mm in width exist for optimization of the beam profile.

Beam optimization

MCP detector read-outs and electrode voltage controls are integrated into a CS-framework based control system [104], allowing automated scanning of electrode voltages and beam intensity. The transmission efficiency of the whole beam line is optimized element-by-element, starting with the first one in HBL, and ending with the upper Penning trap (decay trap).

2.3 Penning traps

The central part of WITCH are two Penning traps, the cooler trap which initially captures the ion bunch, cooling and centering it in preparation for transfer to the decay trap (DT), which serves as a scattering-free source. Thorough understanding of ion cloud dynamics, including space-charge effects, energy and spatial distributions, is required for the analysis of online data. Chapter 3 presents an in-depth overview of the Penning traps.

2.4 Spectrometer

A retardation spectrometer (see Figure 2.6) of the MAC-E filter type is employed to measure the integral recoil spectrum of the recoiling daughter nuclei. The

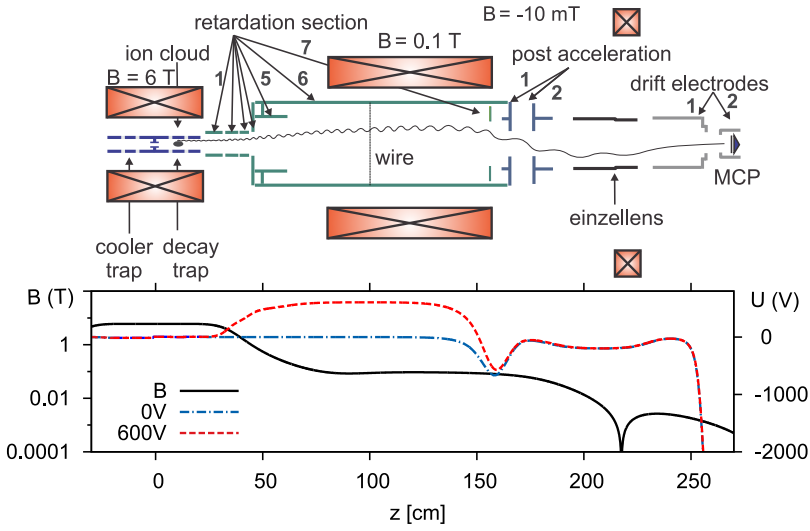


Figure 2.6: (**top**) Overview of the Penning traps with the spectrometer and the main MCP detector. The curved line represents the daughter ion trajectory from the DT to the main MCP. (**bottom**) Magnetic field strength (black) and electric potentials with the spectrometer at 600 V (red) and 0 V (blue) throughout this region are also shown. Taken from [91].

endpoint energy of the ^{35}Cl recoiled nucleus is only around 452 eV, and others do not typically exceed a few keV, excluding the use of other energy-sensitive detectors (e.g. solid-state, which have a threshold around 10 keV). The MAC-E filter employs a decreasing magnetic field to guide the daughter ions and convert their radial energy into axial via the so-called inverse magnetic mirror effect. In this way, the transverse momentum of the ions is adiabatically converted into longitudinal momentum. The ratio of the transverse energies in high-field and low field region will then be given by

$$\frac{KE_{1\perp}}{KE_{2\perp}} = \frac{B_1}{B_2}, \tag{2.1}$$

where $KE_{1\perp}$ and $KE_{2\perp}$ are the transverse kinetic energies in high and low field regions, while B_1 and B_2 are the field strengths, respectively. For typical fields of $B_1 = 6$ T and $B_2 = 0.1$ T, this results in 98.33% of radial kinetic energy being converted into axial. This energy conversion is necessary since the retardation

potential can probe only the axial energy component. Seven retardation electrodes (see Figure 2.6) provide the potential barrier that gradually increases from the DT to the analysis plane in the middle of main retardation electrode (nr. 6). Ions with kinetic energy sufficient to overcome the potential barrier (i.e. larger than qU_r, where U_r is the full retardation potential and q charge of the ion), will reach the post-acceleration section where they gain typically 4 – 8 kV of kinetic energy, in order to enhance the detection efficiency on the main MCP. After reacceleration, the ions are focused by an einzel lens and guided by 2 drift electrodes to the surface of the main MCP.

Although having superior energy resolution at very low energies, due to the presence of high electric and magnetic fields, retardation spectrometers can be susceptible to high levels of background ions. The combination of electric and magnetic field can form Penning-like traps in which ionized background atoms remain trapped, often gaining energy, causing further ionization and resulting in runaway discharges (see [103] for a detailed analysis). Spectrometers based on the same principle are also employed in aSPECT [46] and KATRIN [23] experiments.

2.5 Main MCP detector and data-acquisition

2.5.1 MCP detector

Reaccelerated recoil ions are counted by a large position-sensitive Roendtek DLD80 MCP detector with delay lines and an active diameter of 83 mm, capable of counting up to a rate of about 1 MHz, while also recording their spatial position. Although recording the number of counts is in principle sufficient to obtain a retardation spectrum, their position can provide useful information about the systematic effects, including the ion cloud size, its position in the decay trap, as well as the recoiled ions' trajectory through the spectrometer. Because of a possible energy dependence of their position on the detector plane, it is also crucial to verify that the entire beam profile is being captured by the MCP active area.

The detector efficiency is nominally 52.3(3)%, given by the ratio of the open area of the micro-channels and the total area. The efficiency is also influenced by the angle of incidence and velocity of the ions. The former is not of concern in the case of WITCH spectrometer, since reaccelerated ions have an angle of incidence below 0.05° [103]. The latter is in principle also not of concern since the ions impinge the surface of the MCP with 4 keV or more, well within the range of maximum efficiency. However, if the MCP surface active layer

is compromised, the threshold for efficiency saturation can be higher, i.e. it can still have significant energy dependence (see Chapter 5 for an in-depth description of the MCP and analysis of this effect).

2.5.2 Data acquisition

Until mid-2012, the acquisition consisted of two parts – a "fast" branch with the imperative of counting all the ions impinging on the MCP's surface, and a "slow" branch with much higher dead time, but capable of recording both the time (TDC) and the integrated charge (QDC) for all four delay line connections. During preparation for the 2012 online experiment, the data acquisition system was changed to a FASTER [2] based platform. FASTER is a modular, triggerless, fully digital DAQ system capable of handling up to a few hundred channels. The signals are fully digitized and time-stamped with a resolution of 7.8 ps, eliminating dead time limitations of the previous WITCH DAQ. A more detailed description is given in Chapter 5.

2.5.3 The Experimental Cycle

From the moment the ion bunch enters the WITCH beamline, the operation of a number of devices has to be coordinated in time on a scale spanning from microseconds to seconds. For this purpose, a National Instruments PCI-7811R FPGA card is used to produce an array of triggers after it receives the master trigger from REXTRAP (see Figure 2.7). A beam gate trigger is created first, allowing the ion bunch to enter by restoring a single electrode to its operating potential. Then the PDT discharges, slowing down the ions. Subsequently, the lower end cap electrode of the CT is lowered and then risen when the ion bunch enters, trapping them in a high box potential. With the ion cloud in the traps, excitation can be triggered for a specified duration, if needed. After preparation, the ion cloud is transferred to the decay trap, where it remains for 2 – 4 s to decay. During this time, scanning of the retardation voltages in the spectrometer is initiated.

2.6 Choice of isotope

The choice of isotope to be used for determining the limits on the possible scalar interaction admixture is constrained by the physical properties and also by several technical considerations:

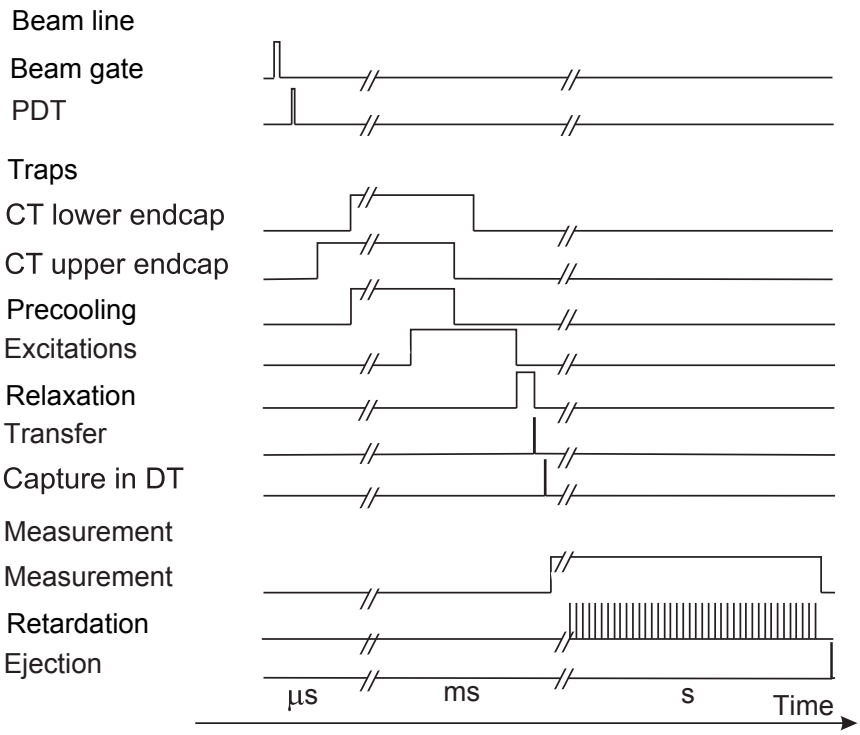


Figure 2.7: Schematic overview of the temporal structure of the WITCH experimental cycle.

• A **stable daughter isotope**. Short-lived daughter isotopes would decay in-flight or at the MCP in numbers significant enough to complicate data analysis. Although these effects could be taken into account by the SimWITCH tracking simulation, they would increase the simulation time and introduce new systematic effects. A long lived isotope would cause lingering background radioactivity.

• **Isobaric and isomeric purity.** If radioactive, an isobaric or isomeric contamination would introduce an unwanted component in the retardation spectrum. A stable impurity wouldn't have such severe consequences, but would still exasperate unwanted space-charge effects in the Penning traps. Although isobaric separation can be performed in REXTRAP or the cooler trap, this process incurs losses due to decay and has reduced efficiency for larger ion

mother	state	$t_{1/2}$ (s)	yield (ions/μC)	daughter	state	$t_{1/2}$ (s)	ΔE (MeV)	$T_{R,max}$ (eV)	P_{EC} %	BR %	a_{SM}
^{26}Al	isom	6.345	$6.8 \cdot 10^4$	^{26}Mg	gs	stable	4.23255(17)	280.7	0.082	> 99.997	1
	gs	7.4 10^5y	*		exc	476 fs	2.20	53.2		97.3	
^{34}Cl	gs	1.527	$1.3 \cdot 10^3$	^{34}S	gs	stable	5.49178(20)	387.9	0.080	> 99.988	1
	isom	1920	$2.2 \cdot 10^5$		exc	325 fs	3.511	138		28.5	
^{38}K	isom	0.924	$6.3 \cdot 10^6$	^{38}Ar	gs	stable	6.044440(11)	429.1	0.085	> 99.998	1
	gs	458	$7.9 \cdot 10^7$		exc	470 fs	3.7456	144.2		99.8	
					gs	stable	5.9131	408.9		<0.6	
^{42}Sc	gs	0.681	*	^{42}Ca	gs	stable	6.42563(38)	444.2	0.099	99.9941(14)	1
	excit	61.7	$1.5 \cdot 10^3$		exc	250 fs	3.8528	139.5		100	
^{46}V	gs	0.423	0	^{46}Ti	gs	stable	7.05071(89)	496.6	0.101	$99.9848^{+0.0013}_{-0.0042}$	1
^{50}Mn	gs	0.283	$7.6 \cdot 10^5$	^{50}Cr	gs	1.8 10^{17}y	7.63243(23)	542.3	0.107	99.9423(30)	1
	isom	105	*		exc	1.25 ps	4.6983	185.6		8.0	
^{33}Cl	gs	2.511	$1.4 \cdot 10^2$	^{33}S	gs	stable	5.5826(4)	414.5	0.074	98.45(14)	0.887(3)
					exc	1.17 ps	4.742	287.1		0.48	
^{35}Ar	gs	1.775	$2.0 \cdot 10^8$	^{35}Cl	gs	stable	5.9661(7)	452.6	0.072	98.36(7)	0.903(2)
					exc	150 fs	4.7458	271.3		1.23	

Figure 2.8: Isotopes of interest for the WITCH experiment, as listed in [27]. The isotopes include $0^+ \to 0^+$ superallowed transitions [51] and mirror nuclei transitions [99] that have a large β-decay Fermi component $|\rho^2| < 0.1$ and half-life between 0.2 s and 10 s.

clouds (see Chapter 4).

• A simple **decay scheme** is preferable. If the daughter isotope is not in ground state, it will de-excite by γ-emission or ejection of electrons. This results in additional components in the retardation spectrum, complicating the analysis.

• The **half-life** of around 2 s is optimal. Shorter half-lives result in large losses during the preparation phase which takes around 0.1 s in REXTRAP and 0.5 s in the cooler trap, while a long half-life would limit the achievable statistics of the experiment.

• **Sufficient yield** at the ISOLDE target. Since the capacity of the WITCH Penning traps is $\sim 10^6$ ions and the beam line transmission efficiency is typically $\sim$20%, the number of ions loaded into REXTRAP after each proton pulse should be $\sim 10^7$. High trap-loads can also be achieved by multiple loading of the cooler trap.

• **Low ionization potential** of the ions, reducing losses due to charge exchange with the buffer gas in REXTRAP or the cooler trap.

• **Decay mode** influences the achievable statistics significantly. In a β^- decay process, a 1^+ ion converts into a 2^+ ion, while in a β^+ process it becomes neutral. Neutral atoms are not contained by the Penning trap, and end up lost on the electrodes. However, the sudden change of the total charge causes single electron shake-off, resulting in 1^+ ion charge state with a probability of about 20%, and multiple electron shake-off resulting in 2^+ and higher charge states with probabilities of 5% and below in the case of the β^+ process. Therefore, β^+ decaying isotopes result in an order of magnitude less statistics, *ceteris paribus*.

When considering the physical potential of an isotope for testing the Standard model limits for the scalar current, a large and well quantified **Fermi component** in the decay is essential. Pure Fermi transitions, $0^+ \rightarrow 0^+$ superallowed decays are most suitable [51]. Decays of mirror nuclei[1] are also interesting, since a part of them have large Fermi-type component [99]. Isotopes satisfying these criteria are given in Table 2.8. In addition to these, isotopes decaying through electron capture (EC) are interesting due to the monoenergetic nature of this decay. It could be used to measure the energy resolution and the response function of the spectrometer. However, they are rare and typically have prohibitively long half-lives due to their low Q-values.

[1] Nuclei in which the number of protons in the mother nuclei equals the number of neutrons in the daughter, and the number of protons in the daughter nuclei equals the number of neutrons in the mother

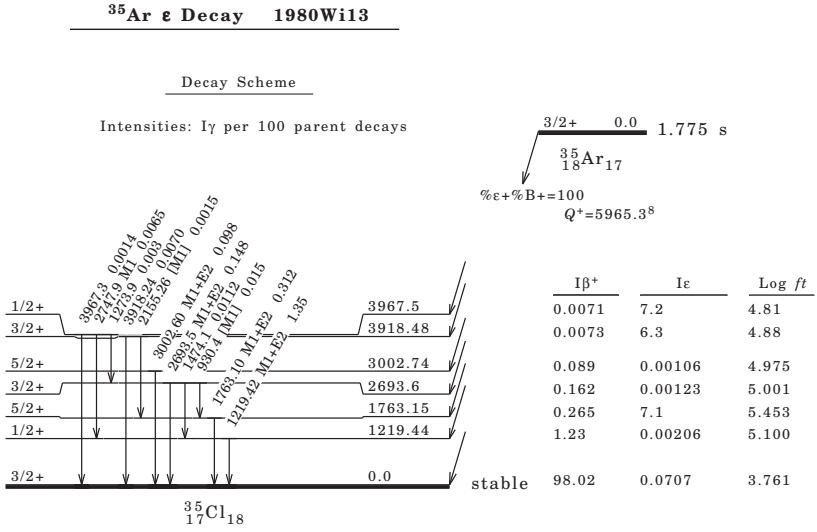


Figure 2.9: The decay scheme of ^{35}Ar [77].

2.6.1 ^{35}Ar

As shown in Table 2.8, ^{35}Ar nuclei undergo mirror decays with a dominant Fermi component, and with a half-life compatible with the experimental cycle of the WITCH apparatus. After significant efforts in improving the target technology by the ISOLDE target group [87], ^{35}Ar is routinely available in sufficient quantities, with target yields on the order of 10^8 ions/μC. Although it has the disadvantage of decaying in a β^+ process that results in large losses, the high production yield at ISOLDE makes it still advantageous in comparison with other candidates.

Decay scheme

If the β-decay does not proceed directly to ground state, the decayed ion recoils more than once (see Figure 2.9), resulting in a modified recoil spectrum. In the case of ^{35}Ar, the probability of a decay directly to ground state is about 98%, and for the 1.219 MeV level of ^{35}Cl about 1.2%. The deexcitation of this state then gives an additional 22.8 eV of energy to the ion, with the momentum distributed isotropically. This contribution introduces a minute effect that mimics a scalar current admixture [91] to the recoil spectrum, and has to be taken into account by the simulations used for interpretation of the data.

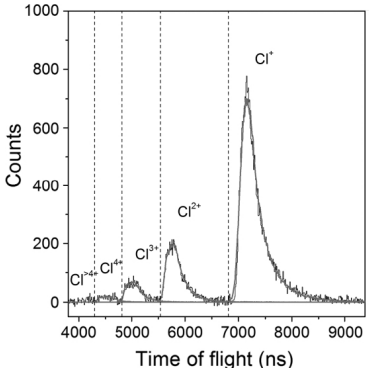


Figure 2.10: Time-of-Flight spectrum of ^{35}Cl daughter nuclei after β-decay of ^{35}Ar. Figure from [31].

Charge state	Proportion
1^+	74.6(1.0)%
2^+	17.3(4)%
3^+	5.7(2)%
4^+	1.7(2)%
5^+	< 1%

Table 2.2: $^{35}Ar^+$ β-decay product $^{35}Cl^{q+}$ distribution by charge state q [31].

Charge state distribution

Since retardation depends on the charge of the ions, higher charge states entering the spectrometer are retarded by proportionally lower voltages. Consequently, 2^+, 3^+ and higher charge states will be contained in the lower half of the retardation spectrum and to quantify their effects, it is essential to know the relative amounts of the produced charge states. The experiment quantifying this effect was realized by the LPCtrap group at GANIL in 2011 [31]. 72(10)% of the decayed ions remain neutral, while 28(10)% lose one or more electrons through shake-off. Time-of-Flight separation of different charge states used to determine the relative amounts is shown on Figure 2.10.

Chapter 3

Penning traps

In this chapter, an overview of Penning trap theory relevant for experimental results discussed in this work will be presented. This includes the single-particle theoretical framework as well as other effects arising from space-charge effects. The single-particle theory describes the motion of a single particle in a Penning trap with great accuracy and predictive power. However, when more than one ion is present, the single-particle theory provides only a qualitative description of the observed phenomena.

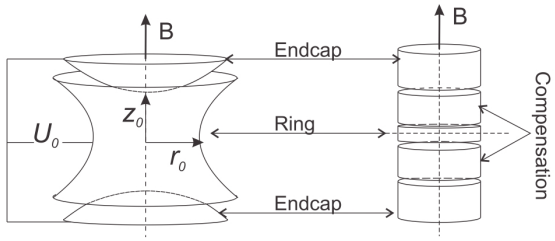


Figure 3.1: (**left**) Hyperbolic and (**right**) cylindrical Penning traps. Quadrupolar field in the cylindrical trap is achieved with additional compensation electrodes. Figure from [74].

3.1 Penning trap principles

Following the groundbreaking work of W. Paul and H.G. Dehmelt, charged particle traps have become widely used for mass filtering as well as for particle containment. Among other things, they provide the capability of trapping ions, electrons, positrons and other charged particles for prolonged observation or manipulation. In the ideal case, the particles can be suspended in vacuum indefinitely by a combination of electric and magnetic fields (Penning trap) or time-dependent electric fields (Paul trap).

The ideal Penning trap (Figure 3.1) employs static electric and magnetic fields to confine charged particles in a superposition of a static magnetic field $\mathbf{B} = B_0\hat{z}$ and a static electric field $\mathbf{E} = \nabla\phi$ given by

$$\phi = \frac{U_0}{2d^2}(2z^2 - x^2 - y^2) \tag{3.1}$$

where U_0 is the potential between the ring and the end cap eletrode and $d = \sqrt{(z_0^2 + r_0^2/2)/2}$ (see Figure 3.1). In this way, the magnetic field confines the particles radially, while the electric quadrupolar field provides axial confinement. A straightforward realization of this principle is the hyperbolic Penning trap (Figure 3.1, left), electrodes shaped as hyperboloids of revolution producing the field with the corresponding shape of equipotential surfaces. However, this design is cumbersome in practice and used only when superior precision is needed [42]. The cylindrical Penning trap (Figure 3.1, right) is an open variant of the hyperbolic trap, allowing significantly easier loading, ejection and particle manipulation within the trap. The quadrupolar electric field is in this case

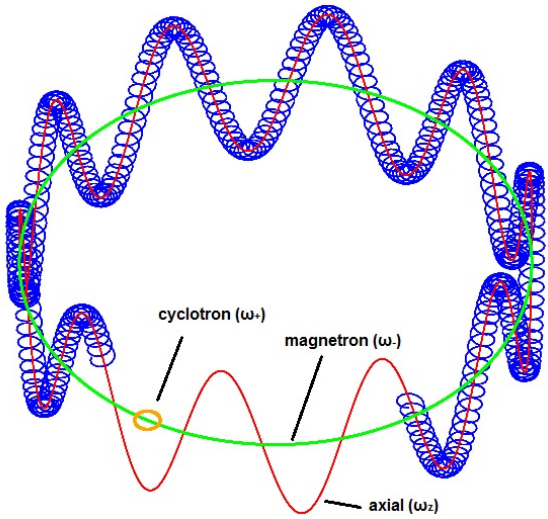


Figure 3.2: The reduced cyclotron ω_+, magnetron ω_- and axial ω_z eigenmotions of an ion in a Penning trap.

achieved by using additional correction electrodes situated on both side of the trap center.

3.2 Single-particle Penning trap theory

3.2.1 Eigenmotions

A massive charged particle moving through a magnetic field $\mathbf{B}$ and an electric field $\mathbf{E}$ experiences a force of the form:

$$\mathbf{F} = -q\mathbf{E} + q\mathbf{v} \times \mathbf{B}, \tag{3.2}$$

where q is the charge and v the velocity of the particle. The equation of motion can then be expressed as:

$$\ddot{\mathbf{r}} = \frac{q}{m}(\dot{\mathbf{r}} \times \mathbf{B} + \mathbf{E}), \tag{3.3}$$

which can be written in Cartesian coordinates as:

$$\ddot{x} - \omega_0 \dot{y} - \frac{1}{2}\omega_z^2 x = 0, \tag{3.4}$$

$$\ddot{y} + \omega_0 \dot{x} - \frac{1}{2}\omega_z^2 y = 0, \tag{3.5}$$

$$\ddot{z} + \omega_z^2 \dot{z} = 0, \tag{3.6}$$

where $\omega_0 = \frac{qB}{m}$ is equal to the free particle cyclotron frequency ω_c, and $\omega_z = \sqrt{\frac{2qU_0}{md^2}}$ the frequency of the axial harmonic oscillation. Since $\mathbf{B}$ is aligned axially, the axial oscillation is trivially decoupled. In order to decouple the motions in the x, y-plane, a coordinate transformation $u = x + iy$ to the complex plane is necessary, reducing Equation 3.4 and Equation 3.5 to

$$\ddot{u} - i\omega_0 \dot{u} - \frac{1}{2}\omega_z^2 u = 0. \tag{3.7}$$

Setting $u = e^{-i\omega t}$ leads to equation

$$\omega^2 - \omega_0 \omega + \frac{1}{2}\omega_z^2 = 0, \tag{3.8}$$

that has two solutions, i.e. the two eigenfrequencies, ω_+ and ω_-, with

$$\omega_+ = \frac{1}{2}(\omega_c + \sqrt{\omega_c^2 - 2\omega_z^2}), \tag{3.9}$$

$$\omega_- = \frac{1}{2}(\omega_c - \sqrt{\omega_c^2 - 2\omega_z^2}). \tag{3.10}$$

ω_- and ω_+ are conventionally designated as the magnetron and the modified cyclotron frequencies, respectively. The following identity also holds:

$$\omega_c = \omega_+ + \omega_- = \frac{qB}{m}. \tag{3.11}$$

Since a trapped ion has real eigenmotion frequencies, the condition for a stable orbit follows from Equation 3.9 and Equation 3.10

$$\omega_c^2 > 2\omega_z^2. \tag{3.12}$$

The minimal electric potential and magnetic field strength required to confine the ions can be expressed as

$$\frac{|q|B^2}{m} > \frac{4|U_0|}{d^2}, \qquad qU_0 > 0. \tag{3.13}$$

Finally, the parametric equations of three eigenmotions can be written as:

$$x(t) = R_+ sin(\omega_+ t + \phi_+) - R_- sin(\omega_- t + \phi_-), \tag{3.14}$$

$$y(t) = R_+ cos(\omega_+ t + \phi_+) - R_- cos(\omega_- t + \phi_-), \tag{3.15}$$

$$z(t) = A_z cos(\omega_z t + \phi_z), \tag{3.16}$$

with R_-, R_+ and A_z being the amplitudes, and ϕ_+, ϕ_- and ϕ_z arbitrary phases. It is now obvious that the motion of an ion in a Penning trap can be decomposed into two circular motions in the radial plane and an axial oscillation. One of the radial motions is a fast cyclotron rotation caused by the strong magnetic field, but with the frequency ω_+ reduced in comparison with the free-particle ω_c due to the presence of the electric field. The magnetron motion characterized by ω_- is a much slower rotation around the trap center, also caused by the combination of two fields **B** and **E**. Combined, they produce an epicycloidal motion, i.e. R_+ superimposed on R_- of the slow motion as shown on Figure 3.2.

The axial motion is a simple oscillation in the quadrupolar electric potential not influenced by **B**. Both the reduced cyclotron and axial motions are stable, in the sense that any energy outflow decreases the corresponding motional amplitude. However, the magnetron motion, having a potential maximum in the center of the trap, is unstable and energy loss (e.g. cooling by buffer gas present in the trap) causes an increase of the magnetron radius, leading to a loss of the particle on the electrode walls. This effect can be counteracted by external time-dependent fields (see Section 3.3.1.2). The hierarchy of the motional frequencies is given by the following inequalities:

$$\omega_c \approx \omega_+ >> \omega_z >> \omega_-. \tag{3.17}$$

Consequently, the reduced cyclotron and axial motions will lose energy in the presence of buffer gas much faster than the magnetron motion. Furthermore, in the first order approximation, the magnetron frequency does not depend on mass:

$$\omega_- \approx \frac{U_0}{2Bd^2}. \tag{3.18}$$

3.3 Buffer-gas cooling

Upon injection into the Penning trap, the ions can have up to a few hundreds eV of energy per ion. In order to cool them, *buffer gas* can be inserted into the trap. The ions then lose energy through random collisions with the buffer gas (see Figure 3.3). This process can be approximated by a continuous drag force acting on the ions:

$$\mathbf{F}_D = -\delta m \dot{\mathbf{r}}. \tag{3.19}$$

The intensity of the cooling is given by the coefficient $\delta = \frac{q}{m}\frac{1}{K_{mob}}\frac{p/p_N}{T/T_N}$, where K_{mob} is the ion mobility and pressure p and temperature T are given in normal pressure p_N=1.013·10^3 mbar and temperature T_N=273.15 K units, respectively. When this force is added to Eqs. 3.4, 3.5, and 3.6, the solutions become [29]:

$$x(t) = R_+ e^{\alpha_+ t} sin(\omega'_+ t + \phi_+) - R_- e^{\alpha_- t} sin(\omega'_- t + \phi_-), \tag{3.20}$$

$$y(t) = R_+ e^{\alpha_+ t} cos(\omega'_+ t + \phi_+) - R_- e^{\alpha_- t} cos(\omega'_- t + \phi_-), \tag{3.21}$$

$$z(t) = A_z e^{-(\delta/2)t} cos(\omega_z t + \phi_z), \tag{3.22}$$

where the frequencies modified by the presence of buffer gas are as follows:

$$\omega'_\pm = \omega_\pm \pm \delta\omega, \tag{3.23}$$

$$\delta\omega = \frac{\delta}{16} \cdot \frac{8\omega_z^2 + \delta^2}{(\omega_c^2 - 2\omega_z^2)^{3/2}}, \tag{3.24}$$

and the damping coefficients $\alpha_\pm$ are:

$$\alpha_\pm = -\frac{\delta}{2}\left(1 \pm \left(1 + \frac{\omega_z^2 + (\delta/4)^2}{\omega_c^2 - 2\omega_z^2}\right)\right). \tag{3.25}$$

From this equation it follows that in the first order $\alpha_+ = -\delta$ and $\alpha_- = (\delta/2)(\omega_z/\omega_c)^2$. Consequently, the magnetron motion expands in the presence of buffer gas ($\alpha_- > 0$), while the reduced cyclotron and axial motions contract ($\alpha_+ < 0$, $\delta > 0$). However, the absolute value of α_- is much lower than α_+ and $\delta/2$, resulting in much faster cooling of the cyclotron and axial motions and allowing for sufficient time to apply radio-frequency (rf) excitations in order to modify the ion motion.

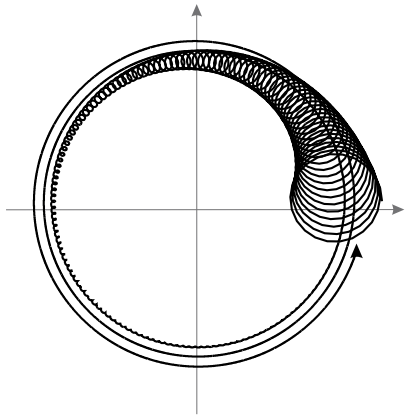


Figure 3.3: Buffer gas cooling. Illustration of the metastable state of an ion in a buffer gas-filled Penning trap. The radius of the fast cyclotron eigenmotion R_+ is seen to collapse quickly due to the presence of buffer gas, while the radius of the magnetron motion slowly increases. From [91].

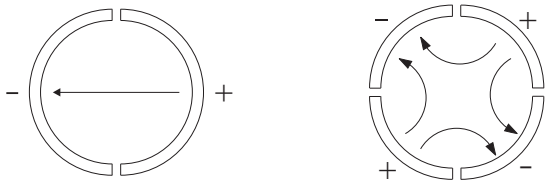


Figure 3.4: Cylindrical electrodes segmented to allow (**left**) dipolar and (**right**) quadrupolar excitations. Due to the shape of the electrodes, the field is dipolar (quadrupolar) in the first order only in the region around the center of the trap.

3.3.1 Ion excitations

A simple and readily available way of influencing the motion of ions in a Penning trap is by employing time-dependent multipolar electric fields. Depending on the purpose, radio-frequency dipoles, quadrupoles or octupoles can be employed to that effect. The time-dependent field is realized by a azimuthally segmented central electrode (see Figure 3.4).

3.3.1.1 Dipolar excitation

During dipolar excitations electric field is created in the central region of the Penning trap in the following form:

$$\mathbf{E}(t) = \frac{U_{rf}}{r_0} cos(\omega_{rf} t + \phi_{rf}) \mathbf{e}_x, \tag{3.26}$$

where U_{rf}, ω_{rf} and ϕ_{rf} are the voltage, frequency and phase of the excitation field, respectively, and r_0 the electrode radius. Inclusion of this force into the equations of motion results in a modification of Equation 3.4:

$$\ddot{x} - \omega_0 \dot{y} - \frac{1}{2}\omega_z^2 x - k_d cos(\omega_{rf} t + \phi_{rf}) = 0, \tag{3.27}$$

where $k_d = \frac{qU_{rf}}{mr_0}$. This equation can be solved analytically [27], yielding two resonant frequencies equal to ω_- and ω_+.

Dipolar excitation applied at one of the radial motional eigenfrequencies ω_- or ω_+ increases the magnetron radius of motion. However, the two cases differ in one significant respect:

- Excitation at ω_- increases the radius of all ions regardless of mass, since ω_- is mass independent. This type of excitation increases the magnetron radius of the ions approximately linearly and without limit.
- Excitation at ω_+ increases the radius of a single ion species, isotope or isobar, since ω_+ is highly mass-dependent. Furthermore, in the presence of buffer gas the radius is not increased without limit, but saturates. Unlike the excitation at ω_-, this process transfers significant energy to the ions, which is at a certain point equilibrated by collisions with the buffer gas.

3.3.1.2 Quadrupolar excitation

Quadrupolar excitations (see Figure 3.5, right) entail a transverse quadrupolar electric field of the form

$$\mathbf{E}_q = -2\frac{U_q}{r_0^2} cos(\omega_q t + \phi_q)(y\mathbf{e}_y - x\mathbf{e}_x) \tag{3.28}$$

in the center of the trap. It was found [25] that it has a dominant resonance frequency at ω_c. The most important feature of this type of excitation is the ability to couple the magnetron and cyclotron motions through inter-conversion

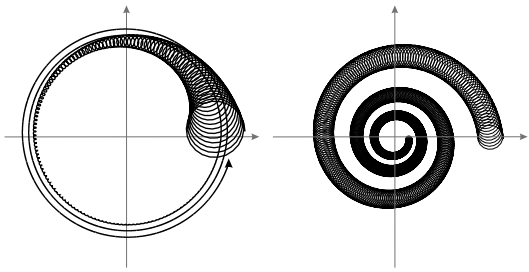


Figure 3.5: Comparison of buffer gas cooling (**left**) without excitation and (**right**) with quadrupolar excitation at ω_c. In the latter case, the magnetron motional amplitude is continuously converted into the cyclotron, which is undergoing buffer-gas cooling.

of the eigenmotion energies and amplitudes. In this way, the runaway expansion of the magnetron radius can be counteracted, resulting in centering of the ions. At $\omega_q = \omega_c$ the following relation holds [25]:

$$R_{\pm} = R_{\pm}(0)cos(\omega_{conv}t/2) \mp R_{\mp}(0)sin(\omega_{conv}t/2)cos(\phi_{rf} - \phi_{+} - \phi_{-}), \quad (3.29)$$

where $\omega_{conv} = k_q/2(\omega_{+} - \omega_{-})$ and $k_q = 2qU_q/mr_0^2$. The period of conversion from the pure magnetron motion to the pure cyclotron motion and *vice versa* is given by $T_{conv} = 2\pi/\omega_{conv}$.

Mass selective centering

As laid out in Section 3.3, the cyclotron motion will undergo a fast thermalization with the buffer gas in the trap due to its relatively high frequency, in contrast with the magnetron motion which remains in a metastable state due to its very weak coupling to the buffer gas thermal bath. This effect can be employed in combination with quadrupolar excitation at ω_c to decrease R_{-} while increasing R_{+}, with the latter being subsequently cooled off by the buffer gas. Effectively, the time-dependent electric field couples the magnetron and cyclotron eigenmotions and continuously interchanges their motional amplitudes. This technique, developed within the ISOLTRAP experiment [21, 92], is called buffer gas cooling or *sideband cooling* and is widely used for cooling charged particles in Penning traps. The magnetron can also be coupled to the axial eigenmotion [25], a technique used for cooling light ions and leptons.

3.4 Trap imperfections and deviations from single-particle theory

In real applications, numerous effects beyond the simple Penning trap theory can arise. These include effects caused by magnetic field misalignment with respect to the geometric trap axis, magnetic field inhomogeneity and decay, electric field departure from the perfect quadrupole case, space charge effects and image charges.

3.4.1 Imperfections of the electric potential

Electric field deviations from the perfect quadrupole are typically caused by imperfect electrodes or their mounting position, contact potentials or stray fields [53]. The electric field inside the trap can be written as

$$\Phi(\rho,\theta,\phi) = \sum_{l,m} a_{l,m}\rho^l P_l^m(cos\theta)cos(m\phi), \tag{3.30}$$

where P_l^m are associated Legendre polynomials and $0 \leq m \leq l$, and $a_m = \frac{U_0}{2z_0^m}C_m$, with U_0 being the potential difference between the endcap and ring electrodes, z_0 half of the axial trap length, and C_m a constant. The first term Φ_0 is an arbitrary constant, whereas the presence of the linear term $\Phi_1 = a_{1,0}z + a_{1,1}x$ implies the existence of a constant force that causes a shift of the trap center. The presence of this force does not affect the harmonicity of the trap potential, and therefore does not modify the eigenfrequencies. However, in combination with a low quadrupole trapping potential, it can result in a significant trap center shift, causing operational difficulties [53]. A similar effect has been observed at WITCH, where under low trapping potential the trap center was shifted enough for the diaphragm at the trap exit to partially block the transmission of the ion cloud (see Chapter 4).

The third term of the expansion 3.30 contains the quadrupole component, a term producing a quadrupolar potential tilted with respect to the z axis, and an elliptic term, respectively:

$$\Phi_2 = \frac{1}{2}a_{2,0}\left[2z^2 - x^2 - y^2\right] + 3a_{2,1}xz + 3a_{2,2}\left[x^2 - y^2\right]. \tag{3.31}$$

All the terms comprising Φ_2 preserve the harmonicity of the potential, but higher order terms of Φ are necessarily inharmonic. In the case of WITCH, the higher order terms amount to $C_4 = 0.0028$ and $C_6 = 0.00042$ [91]. The

eigenfrequency shifts caused by the octupole C_4 term will then be [21]:

$$\delta\omega_{\pm} = \pm\frac{3}{4}\frac{C_4}{z_0^2}\frac{\omega_z^2}{\omega_+ - \omega_-}(r_{\pm}^2 + 2r_{\mp}^2 - 2z^2), \tag{3.32}$$

$$\delta\omega_z = \frac{3}{4}\frac{C_4}{z_0^2}\omega_z^2(z^2 - 2r_+^2 + 2r_-^2), \tag{3.33}$$

$$\delta\omega_c = \frac{3}{4}\frac{C_4}{z_0^2}\frac{\omega_z^2}{\omega_+ - \omega_-}(r_+^2 - r_-^2). \tag{3.34}$$

Furthermore, the presence of ellipticity of the potential, caused by an inhomogenous contact potential or a deformity in the ring electrode [53], will modify the motional eigenfrequencies.

3.4.2 Imperfections of the magnetic field

Axis misalignment

A misalignment of the magnetic field axis with respect to the electric field axis in the spectrometer can have severe consequences for the measurement of the β-decay recoil spectrum, if not accounted for. This is because the retardation spectrometer probes only the ion energy component parallel with its electric field axis. In case of a misalignment between this axis and magnetic field axis that guides the ions, the recoil energy would be underestimated.

Furthermore, such a misalignment – if present in the traps – would modify the motional eigenfrequencies, being equivalent to the tilt of the electric quadrupole described in Sec. 3.4.1. However, the impact of this effect would be very small [91], negligible compared to other influences on the eigenfrequencies, e.g. space-charge.

Field precision homogeneity and decay

The relative homogeneity of the magnetic field inside the WITCH Penning traps is $\delta B < 10^{-5}$, corresponding to $\lesssim 100$ Hz uncertainty in ω_c. However, the total imprecision of B as reported in [103] from measurements of ^{133}Cs cyclotron frequency resonance is $\sim 1\%$ and can be caused by an imprecision of the magnet power supply or the disturbance of the magnetic field by ferromagnetic materials in the vicinity (the buffer gas tube for the cooler trap, the non evaporable getter (NEG) foil around the traps, etc.).

The magnetic field of superconducting magnets is also known to slightly decrease over time due to the flux creep phenomenon [9]. This effect was measured with high precision on a similar magnet at ISOLTRAP, and found to amount to

$-2.3 \times 10^{-8}/h$ [58] and is not significant for either online experiments or offline space-charge effect studies.

3.4.3 Many ions in the trap

When more than one ion is confined in a Penning trap, the quadrupolar electric potential will be distorted by the presence of additional charges, modifying the three single-particle eigenmotions and creating a fourth – rotation of the whole cloud around its center. Since the WITCH traps typically hold $\sim 10^5$ ions, this problem falls between the single-particle and plasma theoretical frameworks and requires the extensive use of simulations. Detailed experimental and computational investigation of this effect is presented in Chapter 4.

3.5 WITCH Penning traps

In this section the technical design parameters of WITCH Penning traps and auxiliary systems for buffer gas injection and electronic control are presented.

3.5.1 Design

The Penning trap system consists of two Penning traps, the cooler trap and the decay trap. The cooler trap is filled with Helium buffer gas and is used to cool and center the incoming ions. The decay trap serves as a scattering-free source and is under high vacuum ($\sim 10^{-8}$ mbar) in order to reduce disturbances to the cloud. The layout of the trap electrode stack is shown on Figure 3.6. Since the cooler trap typically contains buffer gas at $p_{CT} = 10^{-5} - 10^{-4}$ mbar, a pumping diaphragm 2 mm in radius and 5 cm in length is situated between them. Both the cooler trap and the decay trap technical design is based on ISOLTRAP's preparation trap [86]. Since the cylindrical design of the traps does not lend itself naturally to the creation of a quadrupolar potential, correction electrodes (CRE and DRE on Figure 3.6) are employed. Then the potential along the axis can be expanded as

$$\Psi(z) = \frac{U_0}{2d^2}\left(C_2 z^2 + \frac{C_4}{d^2} z^4 + \dots\right), \tag{3.35}$$

where C_n are the expansion coefficients, U_0 the potential between the end caps and the ring electrode, and d the characteristic dimension of the trap, equal to 1/30 for the cooler trap. By optimizing the higher order coefficients,

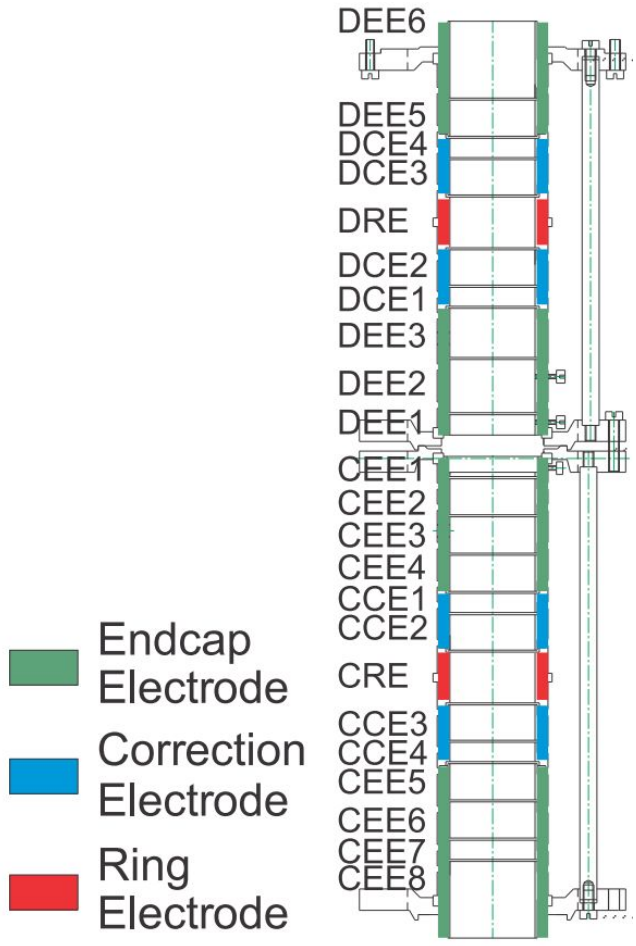


Figure 3.6: Layout of cooler and decay trap electrode stack (pumping diaphragm omitted). The buffer gas inlet is located on CEE2. The total height of the stack is 42.9 cm.

a quadrupolar potential in the vicinity of the trap center can be established. For this particular configuration of the electrodes, the necessary potentials are listed in Table 3.1. The ring electrode is eight-fold segmented to provide the capability of imposing dipolar, quadrupolar and octupolar excitation on the ion cloud (Figure 3.7). For typical parameters of the trap ($U_0 = 15$ V, B = 3 T)

Electrode	U_e/U_0
EEx	1
CE4	0.675
CE3	0.165
RE	0
CE2	0.165
CE1	0.675
EEx	1

Table 3.1: Ratio of the voltages on the trap electrodes U_e and the end cap electrode U_0 optimized to produce a quadrupolar potential. U_0 is typically in the 5 – 15 V range. EE denote the end cap electrodes, CE the correction electrodes and RE the ring electrode.

and ^{39}K ions, the eigenfrequencies are equal to:

- $\nu_c = 1.181267$ MHz,
- $\nu_+ = 1.181149$ MHz,
- $\nu_z = 16.684$ kHz,
- $\nu_- = 117.84$ Hz.

All trap electrodes are manufactured from high-conductivity oxygen-free copper and coated with 10-15 μm of nickel (to prevent diffusion of copper atoms to the surface) and a gold outer layer. Since nickel is ferromagnetic, it introduces unwanted modifications to the magnetic field. However, they are in the 10^{-8} – 10^{-10} level in ω_c and insignificant in comparison to the space-charge effects on ω_c. The electrodes are insulated with polyether ether ketone (PEEK), a durable material suitable for ultra-high vaccum environments and resistant to mechanical stress and heat exposure during baking. The whole structure is supported by titanium rods, which are non-magnetic and temperature resistant. In addition, a custom made NEG foil is wrapped around the Penning traps to enhance the vacuum.

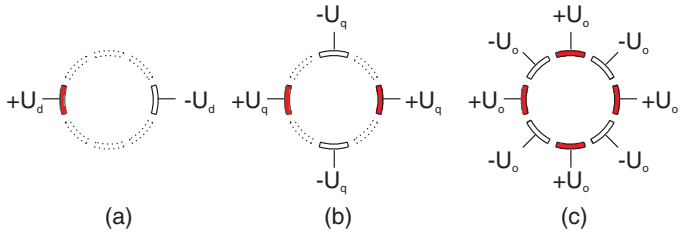


Figure 3.7: The segmented structure of the ring electrode. Segments with RF are emphasized for (a) dipolar, (b) quadrupolar and (c) octupolar excitation.

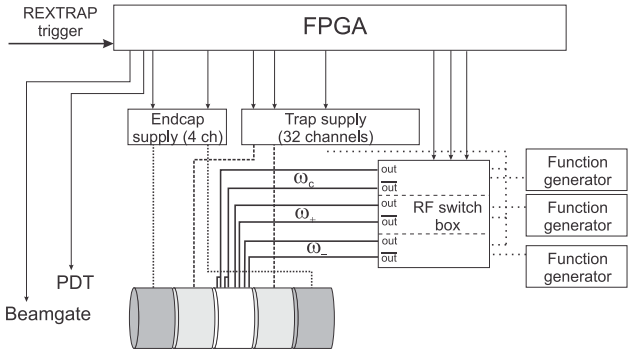


Figure 3.8: Schematic overview of the FPGA-generated triggers for trap operation.

3.5.2 Electronics

The electric fields used for the manipulation of the ion cloud are realized with 37 independent trap electrodes and electrode segments, all of them synchronized on micro- and millisecond timescales. This is accomplished by using a National Instruments PCI-7811R FPGA (Field Programmable Gate Array) card to produce an array of triggers that control the two power supplies for the traps (one providing high voltage up to 450 V for the end cap electrodes, and the other for the correction and ring electrodes) as well as three DS-345 Stanford Research Systems frequency generators for rf excitation. Their output is combined with the voltage power supply channel for the ring electrode by three in-house built *RF switch boxes* (see Figure 3.8).

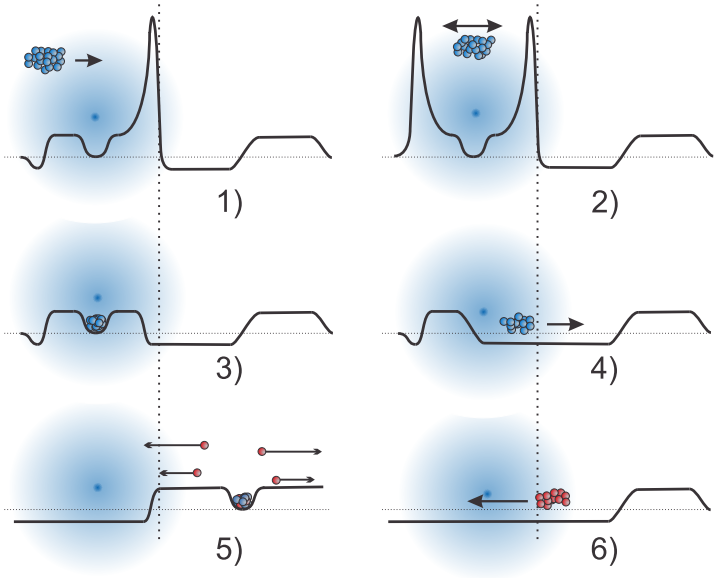


Figure 3.9: Six stages of the trapping cycle. The full line represents the potential, while the vertical dotted line separates the cooler trap (left) and the decay trap (right). The horizontal dotted line indicates the zero of the potential, and the blue sphere the buffer gas in the cooler trap.

3.5.3 Trapping procedure

After accumulation, cooling and bunching in REXTRAP or WITCH's autonomous ion source with an RFQ, the ions are pulsed down to a few hundred eV or less before arriving to the cooler trap. The entire process is pictured on Figure 3.9.

1. Pulsed-down ions enter the buffer gas-filled trap while the lower end cap electrode (CEE8) is set to a potential below 0 V. The upper end cap is set to a value sufficient to stop the bulk of the ions, typically around 100 V.

2. After the whole ion bunch is in the trap, the lower end cap is raised and the ions are left for a few hundred milliseconds to cool off the energy of the cyclotron and the axial motions.

3. As the ions are being cooled into the quadrupolar potential in the center of the trap, the potential on both end caps is lowered to 0 V. Meanwhile, the RF sinusoidal excitation potential with ω_c frequency is connected to the ring electrode segments in duration of 20 – 120 ms, typically. This results in cooling and centering of the magnetron motion, finalizing the preparation phase of the cycle. Optionally, a mass-selective purification scheme can be implemented in order to reduce the proportion of contaminants.

4. When the ion cloud is sufficiently cooled and centered, the quadrupolar trapping potential is transformed into a Wiley-McLaren potential [112] in both the cooler and decay trap with the purpose of transferring the ion cloud between the traps while avoiding to increase its size or the energy of the ions. Broadening of the energy distribution or the dimensions of the ion cloud significantly increases the systematic error [103]. The trapping potential form and its duration is crucial for optimal transfer, and requires careful selection.

5. After transfer, the potential in the decay trap is transformed to a quadrupole identical to the one previously present in the cooler trap, while the cooler trap potential is set to a flat negative one. This is the measurement stage of the cycle, in which the ions are left to decay while the energy of the recoils is probed in the spectrometer. It typically lasts for 2 – 5 seconds.

6. After the time prescribed for the β-decay measurement, the quadrupole barrier is lowered on one side of the decay trap, and the remaining radioactive ions released upstream into the beam line, in order to avoid any radioactive contamination of the spectrometer.

Chapter 4

Space-charge effects in Penning traps

In this chapter, the experimental and computational study of space-charge effects in WITCH Penning traps is presented.

Sections 4.1.1 and 4.1.2 provide a theoretical introduction to plasma physics in Penning traps relevant for this work. Section 4.1.3 focuses on the measurements and simulations of the ion cloud energy. In addition to Section 4.2, Section 4.1.4 presents further experimental and computational results on buffer gas cooling and excitation of the ion cloud.

Section 4.2 is dedicated to the paper ***Space-charge effects in Penning ion traps*** published in the journal *Nuclear Instruments and Methods in Physics Research Section A: Accelerators, Spectrometers, Detectors and Associated Equipment*, **785** (2015) 153–162. My contribution to the paper consisted of performing and interpreting all simulations, performing and analyzing experimental measurements, writing the entire manuscript and taking care of the submission process.

4.1 Non-neutral plasma systematic effects

Collective effects known in plasma physics start to arise in Penning traps containing large ensembles of ions. In this section, an overview of the intersections of ion trap physics and plasma physics relying on the nomenclature of e.g. [82] is presented.

4.1.1 Introduction

Unlike regular plasma, non-neutral plasma is a special case of the plasma state of matter in which the collection of particles is not neutral overall. E.g., in the case of WITCH Penning traps it contains only positively charged ions. In contrast to the single particle case (see Chapter 3) where the particle motion in the Penning trap can be fully described analytically, when more than one ion is present in the trap, i.e. in the case of non-neutral plasma and the intermediate region, the ion dynamics is altered due to arising collective effects. Such a collection of ions exhibits Debye shielding, an effect present in all types of plasma, where the charges rearrange themselves, neutralizing an outside electric field. However, unlike neutral plasmas, ion plasmas exert an electric field of their own.

Debye shielding (a process similar to electrostatic screening in electrolytes) occurs because the charges, although bound by the trapping potential, have enough freedom to rearrange their configuration within the ion cloud. In other words, the ions start to exhibit collective effects, and this process is used as one of the criteria for the emergence of plasma state of matter. Thus, when the size of the ion cloud is larger than the Debye length, λ_D, with

$$\lambda_D = \sqrt{\frac{k_B T \epsilon_0}{n q^2}}, \tag{4.1}$$

where k_B is the Boltzmann constant, T the temperature, ϵ_0 the vacuum dielectric constant, n the density of the ion cloud and q the charge of the particles it is said to be in the state of plasma. That is, the ion cloud is in the plasma state when the following criterion is satisfied:

$$\lambda_D < r_c, z_c, \tag{4.2}$$

where r_c and z_c are the cloud radius and axial half-length, respectively. The other criteria for the presence of plasma state is that many particles are present in the system:

$$n\lambda_D^3 >> 1. \tag{4.3}$$

From this condition it also follows that the kinetic energy of the particles exceeds the potential interaction of the nearest neighbors, causing the motion of the ions to be weakly correlated, i.e. the cloud to behave gas-like [82]. When this condition is not met, the short range forces can cause equilibrium states with highly correlated positions of the ions. In these cases, the ion cloud can resemble a fluid or even a solid [22]. The strength of the ion-ion forces can be gauged with the ratio of the potential and the kinetic energies of the nearest neighbors:

$$\Gamma = \frac{q^2}{4\pi\epsilon_0 a T}, \tag{4.4}$$

with the average particle separation defined via the density $n = 1/(4\pi a^3/3)$, where a is the lattice size. When $\Gamma \ll 1$, the interaction between the ions is small in comparison to their kinetic energy and the cloud behaves gas-like. In the $\Gamma \gtrsim 2$ range, weakly correlated behavior begins to appear, resulting in a liquid-like ion cloud. At $\Gamma \backsim 180$, a crystal lattice typically forms.

WITCH Penning traps typically contain $10^3 - 10^6$ ions. The criterion in Equation 4.2 is not necessarily satisfied at the lower end of this range, although, this does not invalidate most of the plasma physics results pertaining to ion traps [82]. However, in both cases it does significantly modify the single-particle equations of motion laid out in Chapter 3.

4.1.2 Ion motion in a non-neutral plasma

4.1.2.1 The effect of space-charge

The cumulative electric field created by the ion cloud causes a significant modification to the trapping potential. The axial oscillation frequency decreases due to the repulsive field of the cloud that individual ions encounter while moving along the magnetic field lines. Furthermore, the net potential can be inharmonic, making the analytical formulation of the problem difficult. In comparison with the single-particle magnetron, axial and cyclotron motions, the ions in the cloud also acquire a fourth eigenmotion, slow rotational drift $\mathbf{E} \times \mathbf{B}$ in the plane perpendicular to the magnetic field axis [82]. This motion can be expressed analytically when the shape of the cloud is known and the density constant. However, in a general case the problem is approachable only numerically. A non-neutral plasma ion cloud in a quadrupolar potential has a spheroidal shape with an outward space-charge induced electric field of the form:

$$E = a(\alpha)\frac{m\omega_p^2}{q}r, \tag{4.5}$$

where $\alpha = z_c/r_c$ is the aspect ratio of the cloud, a a coefficient describing the shape of the cloud and r is the distance from the cloud's center. Further, ω_p is the *plasma frequency*, defined as:

$$\omega_p = \sqrt{\rho q^2/\epsilon_0 m}, \tag{4.6}$$

with ρ the ion density in the cloud, typically approximated by a constant. In this case, the plasma frequency does not describe a real motion of the ions, but is useful as a combination of constants. The $a(\alpha)$ coefficient is given by:

$$a(\alpha) = \frac{1}{2}\left(1 - \frac{1}{\alpha^2 - 1} Q_1^0\left[\frac{\alpha}{\sqrt{\alpha^2 - 1}}\right]\right), \tag{4.7}$$

where Q_1^0 is the associated Legendre function of the second kind. The cumulative electric field of the ions given by Equation 4.5, causes the $\mathbf{E} \times \mathbf{B}$ drift, resulting in the cloud rotating rigidly with the frequency:

$$\omega_R = a(\alpha)\frac{\omega_p^2}{\omega_c}, \tag{4.8}$$

this relation being valid exactly only for $\omega_R \ll \omega_c$. Generally, the equations of motion of an ion at radius r from the center of the cloud can be obtained by adding the potential of the electric field E (Equation 4.5) to the quadrupolar trapping potential [113]. The modified axial oscillation eigenmotion frequency ω_z is then:

$$\omega_z'^2 = \omega_z^2 - \frac{\omega_p^2}{3}, \tag{4.9}$$

with the factor 3 denominator stemming from the spherical ion cloud shape and being smaller than 3 for prolate, while larger than 3 for oblate spheroids [56]. In the first approximation, the relative ω_z shift is equal to:

$$\frac{\Delta\omega_z}{\omega_z} \equiv \frac{\omega_z' - \omega_z}{\omega_z} \approx -\frac{\rho q R_0^2}{24\epsilon_0 U_0}, \tag{4.10}$$

where $R_0^2 = r_0^2 + z_0^2$ is a constant accounting for the trap geometry and U_0 the depth of the quadrupolar trapping potential. The frequencies of the two radial eigenmotions, the cyclotron and the magnetron motion, can be obtained analogously, yielding

$$\omega_\pm' = \frac{\omega_c}{2} \pm \sqrt{\left(\frac{\omega_c}{2}\right)^2 - \frac{1}{2}\omega_z^2 - \frac{\omega_p^2}{3}}. \tag{4.11}$$

Thus, the cyclotron eigenmotion frequency ω_+ is decreased by the presence of space-charge, while the magnetron frequency ω_- is increased. From Equation 4.11 it also follows that $\omega_c^2 \geq \omega_p^2$, giving a condition for stable

plasma confinement. It can be rewritten to express the maximum density of the confined plasma, i.e. the Brillouin limit [24]:

$$\rho = \frac{\epsilon_0 B^2}{2m}. \tag{4.12}$$

From this it follows that the maximum achievable density of the non-neutral plasma does not depend on Penning trap characteristics except the magnetic field B. The Brillouin limit in a Penning trap with $B = 3$ T and ^{39}K, the configuration used in most of the space-charge experiments presented in this work, is about $n = 0.61 \times 10^6/\text{mm}^3$

Furthermore, the space-charge also influences the resonance frequency of the field excitation used for sideband cooling ω_{cool}, causing it to broaden and shift to higher values (see Section 4.2 for details).

4.1.2.2 The effect of image charges

Ions in a Penning trap interact with the electrodes by causing a rearrangement of surface charges, in a way that is equivalent to a creation of *image charges* outside the trap [54]. This results in an attraction between the ion cloud and its image, which causes a slow drift around the center of the trap called the *diocotron motion*. It is of similar origin as the magnetron motion, both caused by electric fields originating at the electrodes. Its frequency ω_D is given by [82]:

$$\omega_D \approx \left(\frac{r_c}{r_w}\right)^2 \omega_R, \tag{4.13}$$

where r_w is the radius of the trap. When the diocotron motion is present, the cumulative slow drift frequency becomes:

$$\omega_S \approx \omega_- + \omega_D. \tag{4.14}$$

The fast eigenmotion is also modified by the presence of the image charge fields, and ω_+ becomes:

$$\omega'_+ \approx \omega_c - \omega_S. \tag{4.15}$$

However, the effect of the image charges becomes prominent only when the ion cloud is sufficiently de-centered. In the case of WITCH traps, this is not the case during normal operation or even with an eccentric magnetron motion with a radius of 1 – 2 mm, as detailed in Section 4.2.

4.1.3 Ion cloud energy

An ion cloud can be defined to be in thermal equilibrium when the energy of all its ions follows a single Maxwell-Boltzmann distribution and its motion is consistent with that of a rigid body, i.e. without shear or divergence. The ion cloud can then exhibit bulk motions, i.e. the cyclotron, magnetron and axial eigenmotions while remaining in thermal equilibrium [82]. However, any interaction of the cloud with external forces such as time-dependent fields caused by electrical noise, evaporative cooling or radioactive decay has an adverse influence on the equilibrium state.

In order to minimize the systematic effects attributable to the source [103], i.e. the ion cloud, it should be in an equilibrium state with its kinetic energy as close as possible to the temperature of the environment, i.e. the buffer gas. Thermalization with the buffer gas in the cooler trap results in the cooling of the ions to a mean kinetic energy of $E_K = k_B T \approx 25$ meV (293.15 K), with a Maxwell-Boltzmann distribution. However, the temperature can become significantly higher when the ion cloud reaches its final position in the decay trap, either due to incomplete thermalization after quadrupolar excitation or disturbance of the ion cloud during transfer.

The impact of the energy of the ions in the cloud when employed as a radioactive source is significant: The kinetic energy of the radioactive ions influences the recoil energy spectrum after decay through thermal Doppler broadening, increasing the systematic error of the $a_{\beta-\nu}$ [103]. The recoil energy of the radioactive ion will be shifted by the following amount:

$$E_r \longrightarrow E_r + E_K + 2\sqrt{E_r E_K}, \tag{4.16}$$

where E_r is the recoil energy and E_K the thermal energy. Therefore, it is essential to know the mean kinetic energy of the ions in the decay trap in order to minimize its systematic effect on $a_{\beta-\nu}$. To that effect, it is favorable to minimize the energy in the cooler trap, since the DT is under high vacuum ($\approx 10^{-8}$ mbar) and the ion cloud cannot undergo further cooling. Some of the experimental measurements and simulations of the energy distribution in the DT can be found in [91].

4.1.3.1 Measurements of the ion cloud energy

The total energy of an ion cloud in a Penning trap is composed of the kinetic energy, the potential energies of the field of confinement, the fields of the space-charge and the image charges, as well as gravitational energy. In the case

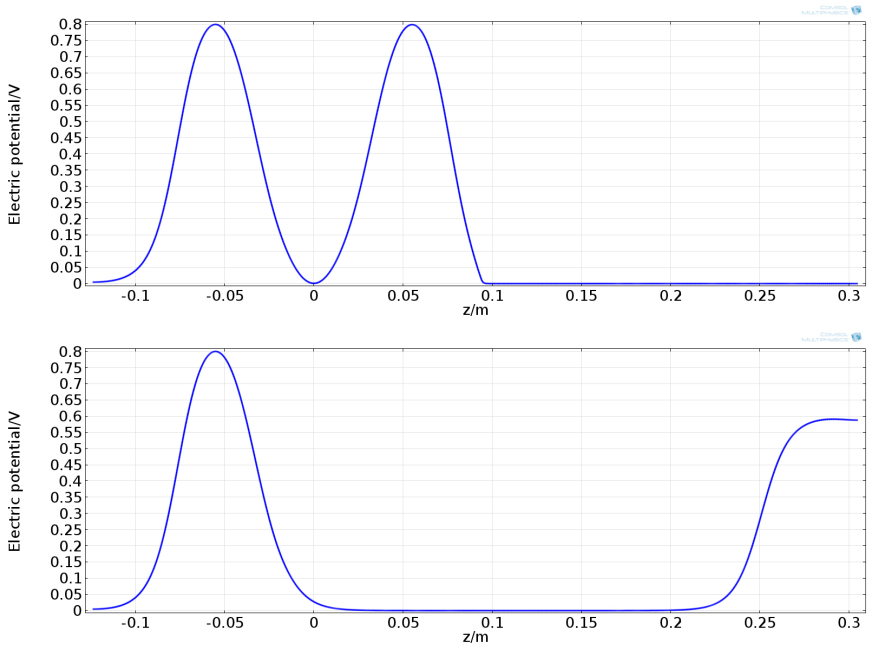


Figure 4.1: (**top**) Quadrupolar potential on the axis in the cooler trap before the ions are released. The center of the CT is at 0. (**bottom**) The potential in the traps with the CT top open and a retardation barrier at the end of the decay trap. The center of the DT is at 0.2 m.

of the WITCH traps, the only significant contributions are the quadrupolar confinement and space-charge potential energies, as well as the kinetic energy.

Unlike neutral plasma, non-neutral ion clouds have a tendency to be in thermal equilibrium [82]. Since in a state of equilibrium a single temperature for both the longitudinal and transversal axes exists, it is possible to estimate the total kinetic energy of the ion cloud by measuring only the longitudinal (axial) component.

At WITCH, the energy spread of clouds of $^{39}K^{+}$ ions from the offline ion source is measured by releasing the ions from the quadrupolar potential in the cooler trap. The energy was scanned by applying a variable blocking potential on the uppermost electrode of the decay trap (Figure 4.1). In this way, a cumulative axial energy spectrum of the ion cloud is obtained (Figure 4.2). Measurement of the total energy is also possible if the WITCH spectrometer is used to scan

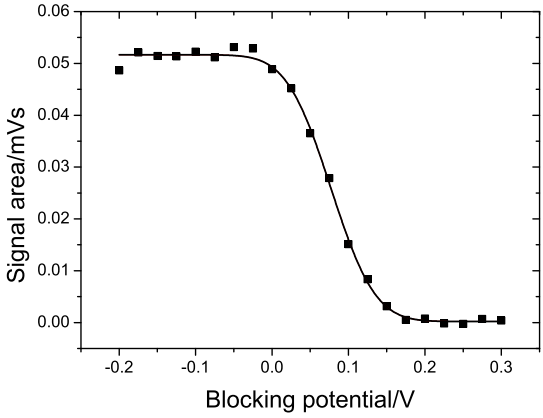


Figure 4.2: Transmission intensity vs. the blocking potential in the decay trap for $^{39}K^{+}$ ions. The intensity is given in mVs units, i.e. the area of the signal recorded by the oscilloscope connected to the MCP. The fitted curve is the integrated Maxwell-Boltzmann distribution.

the energy spectrum. However, due to its low ratio of length and radius, and symmetry breaking elements present (see [103]), there is a significant (~ 1 V) difference between the potential set on the electrode and the actual potential in the center. For that reason, a tracking simulation with a realistic 3D field map would have to be employed, which was not available at the time.

The mean energy and its spread are extracted by fitting the integral Maxwell-Boltzman distribution to the data. At the relatively high temperatures present here (~ 1000 K), the Maxwell-Boltzmann distribution can be approximated by the Gaussian. For each blocking potential a new trap load was used in order to preserve the thermal equilibrium. The fraction of the ions with kinetic energy higher than the blocking potential is transmitted and its intensity recorded by an oscilloscope connected to the diagnostic MCP in the spectrometer (see Chapter 2). Upon ejection, the upper side of the CT and the whole DT was set to 0 V, while the lower side of the CT remained in the quadrupolar configuration. The purpose of this was to preserve the ion cloud energy distribution as much as possible, since it would be shifted to higher energies if the cloud was kicked out. Nevertheless, the ion energy is still modified by switching one side of the quadrupole potential to zero, depending on the axial position of the ion cloud. Figure 4.2 shows the integral energy distribution of a small ion cloud ($\sim 3 \times 10^4$ ions) buffer-gas cooled for 300 ms without excitations and contained

in a 1 V quadrupolar potential. In order to reduce the influence of statistical fluctuations, each point represents an average of 10 measurements.

The process of scanning a potential barrier in order to obtain an integral ion energy spectrum can be fully simulated with the Simbuca package. Realistic field maps of the electric as well as magnetic fields were used. A specific field map for each blocking potential is generated by using a COMSOL model of the trap electrodes (see Figure 4.1), while the magnetic field map is calculated according to the specifications of the manufacturer (Oxford Instruments). Figure 4.3 shows comparisons of experimental integral energy spectra with simulation for matching parameters. The plots show energy spectra after 50, 75, 100 and 200 ms of buffer gas cooling without excitation. With the error bar purely statistical, it can be seen that there is a consistent discrepancy between experiment and simulation in most cases. The most probable causes are:

- A difference in the initial conditions, i.e. different initial energy and axial ion cloud size. The latter would cause the real and the simulated ion clouds to have different potential energies, and to gain a different amount of kinetic energy when one side of the quadrupolar trapping potential is switched off and the ions released.
- A difference in the transient potential that occurs when the trap is opened. In the simulation, the transition is immediate, while in reality it has a finite decay time as well as other possible idiosyncratic behavior of the power supply.

However, the experimental and the simulated energy spectra can be compared in another way. The energy in the simulation can be obtained without the final step of switching the potential and releasing the ions. Under the assumption that (in the experiment) the potential switch gives the ion cloud an energy kick of constant magnitude, the simulated spectrum can be fitted to the real spectrum with this potential offset as one of the free parameters. In this way, the buffer gas pressure can be estimated according to the formula (see Section 4.2 for details):

$$E_{TOT} = E_{Pot} + E_{kin}(0)e^{-2\delta t_{cool}/m} + E_{kin}(t_{cool} \longrightarrow \infty).$$

The other free parameter is then the exponential energy decay constant $-2\delta/m$, that is determined by the buffer gas pressure (and $E_{kin}(t_{cool} \longrightarrow \infty)$ is a common constant given by the background temperature of the buffer gas). This method was employed in Section 4.2.

Ion mobility and buffer gas pressure

The ion mobility is defined as the ratio of the drift velocity v_d of an ion in the buffer gas and the strength of the electric field E causing the drift:

$$K = \frac{v_d}{E}. \tag{4.17}$$

The cooling of an ion cloud in a buffer gas was first demonstrated in Penning traps in 1991 by Savard et al. [92]. It was found that energetic ions cool down exponentially in a buffer gas, in agreement with the results of the ion mobility theory [70] that determines the time dependence of ion velocity in a gas by the following formula:

$$v = v_0 e^{-\frac{q}{Km}t}, \tag{4.18}$$

where v_0 is the initial ion velocity, q the charge and m the ion mass. The conformity of the simulations and theory has been tested in this regard as well. Figure 4.4 shows the simulated buffer gas cooling curves for different initial Maxwell-Boltzmann distributions ranging from 100 eV to 25 eV per ion. The cooling time constant, determined by the gas pressure and molecular properties of Helium is constant in all cases, in agreement with the theoretical model.

Furthermore, since the average rate of momentum loss of an ion in a buffer gas is proportional to the collision rate with the gas molecules, the ion mobility K is inversely proportional to this rate. Consequently, a decrease in buffer gas pressure causes a decrease in the collision rate and an increase in K. Therefore, the cooling time constant increases (decreases) with a buffer gas decrease (increase). This behavior is reproduced with simulations (Figure 4.5). The sensitivity of the cooling time constant (Figure 4.6) on the buffer gas pressure variation enables the use of experimental time constants to determine the buffer gas pressure with relatively high precision. The buffer gas pressure inside a Penning trap cannot be measured directly, due to operational limitations of pressure gauges in high magnetic fields, as well as the potential interference of ionization from the gauge with trap operation.

Trap capacity

Figure 4.7 shows the dependence of the mean energy and its spread on the quadrupolar potential depth, again after 300 ms buffer gas cooling (at $\approx 2.5 \times 10^{-5}$ mbar) with quadrupolar excitations with amplitude V_{pp} =2 V. The mean energy, as well as its spread is seen to be rising proportionally with the amplitude of quadrupolar potential. This effect is due to increasing amount of ions, i.e. space-charge, present in the trap, with higher quadrupolar potentials confining larger amounts of ions. The Coulomb repulsion then causes the ions

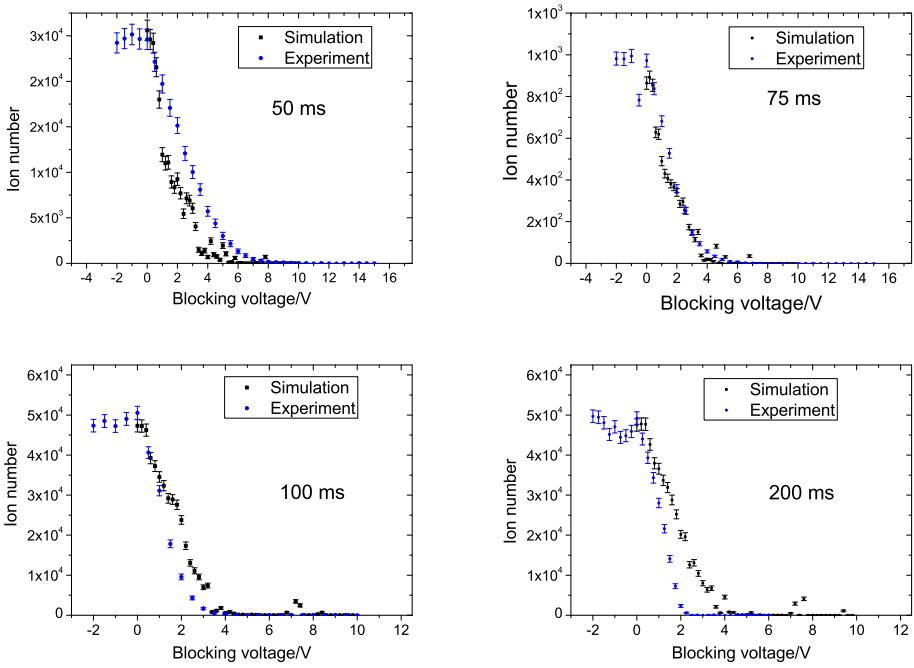


Figure 4.3: Energy scans of ions released from the cooler trap after 50 ms (**upper left**), 75 ms (**upper right**), 100 ms (**lower left**) and 200 ms (**lower right**) of cooling in buffer gas without excitation. Blue circles denote experimental and black squares simulated data.

to occupy higher potential energy states, which is converted to kinetic energy upon the release of the ion cloud or ejection of recoil ions due to radioactive decay. This component of the total ion energy cannot be cooled off, and it is therefore essential to accurately characterize its mean value and spread. Figure 4.16 shows the approximately linear relation between the maximum capacity of the trap and the quadrupolar trapping potential.

It can be seen from Figures 4.7 and 4.16 that a 10 V trap depth is required for the confinement of $\sim 2 \times 10^6$ ions, and that such a large amount of space-charge causes the mean energy per-ion to be ~ 1 eV. An energy shift of this magnitude in the decay trap corresponds to a shift of ~ 40 eV in the recoil energy of $^{35}Ar^+$ daughter ions in the spectrometer. This effect can produce a large systematic error in $a_{\beta-\nu}$ [103], making it necessary to take the space-charge energy effects

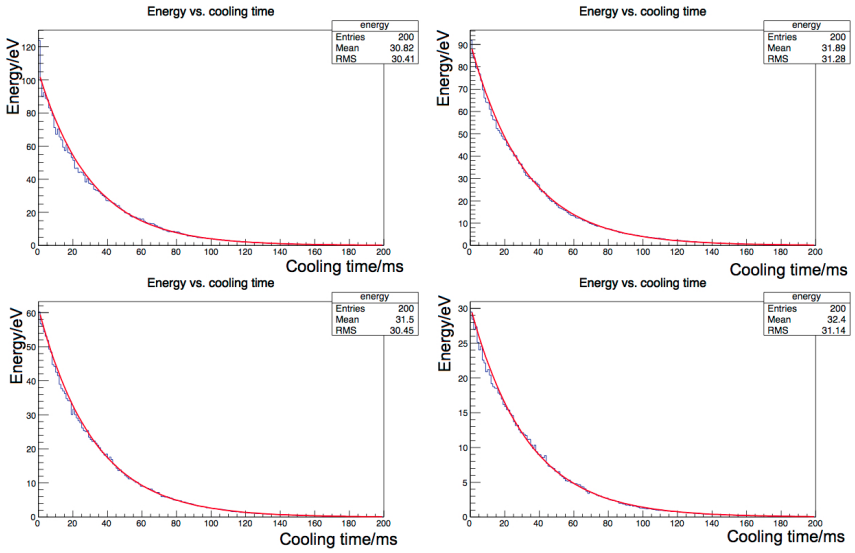


Figure 4.4: Average per-ion energy versus cooling time dependence of an ion cloud with different initial Maxwell-Boltzmann energy distributions: 100 eV (upper left), 75 eV (upper right), 50 eV /(lower left) and 25 eV (lower right). The buffer gas pressure is 2.5×10^{-5} mbar. The energy cooling constants $-2\delta/m$ obtained by fitting an exponential curve are (30.5 ± 1) ms, (31.8 ± 1) ms, (31.8 ± 1) ms and (32.0 ± 2) ms, respectively.

into account in both the Simbuca and SimWITCH ion tracking software.

4.1.4 Quadrupolar excitation and buffer gas cooling

The quadrupolar excitation of an ion at its cyclotron frequency ω_c centers its motion by "converting" the magnetron motional amplitude into the cyclotron one, which can subsequently be cooled off by the buffer gas due to its high frequency (see Section 3.3.1). When many ions are present, the Coulomb interaction significantly influences the ion dynamics, including its response to quadrupolar excitation at the cyclotron frequency ω_c. The collective space-charge of the ion cloud causes a shift and broadening of the single-particle cyclotron resonant frequency peak ω_c to higher values (generally denoted as ω_{cool}). More specifically, the space-charge introduces an electric field which results in the fourth eigenmotion of the cloud, the $\mathbf{E} \times \mathbf{B}$ drift [82]. Assuming a constant cloud density, i.e. $E \propto r$, this results in a rigid body motion of the

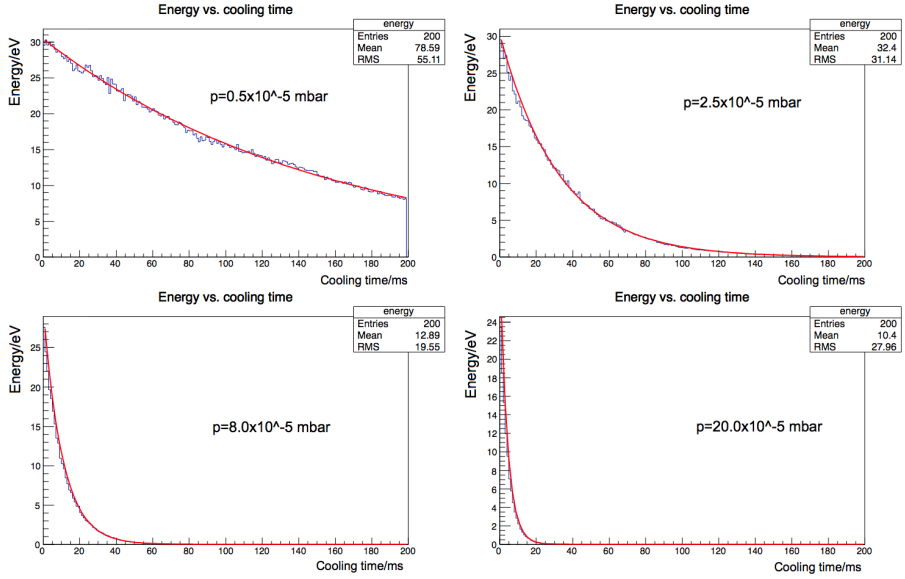


Figure 4.5: Average per-ion energy versus cooling time dependence of the ion cloud cooled in buffer gas with different pressures: 0.5×10^{-5} mbar (upper left), 2.5×10^{-5} mbar (upper right), 8.0×10^{-5} mbar (lower left) and 20.0×10^{-5} mbar (lower right). The initial energy distribution and dimensions of the ion cloud are the same in all cases. The energy cooling constants $-2\delta/m$ obtained by fitting an exponential curve are (153 ± 2) ms, (32 ± 1) ms, (11 ± 1) ms and (4.0 ± 0.5) ms, respectively.

entire ion cloud with the frequency ω_R (Equation 4.8). In the reference system rotating with the frequency ω_R together with the ion cloud, the frequency of the excitation field is now decreased. Therefore, in the laboratory system, the frequency of the cooling resonance ω_{cool} has increased.

Furthermore, the assumption of constant charge density of the ion cloud does not hold in a realistic ion cloud, i.e. the density is high in the center of the cloud and falls off towards the edges (see next section). This causes the cloud to possess a range of ω_{cool} frequencies resulting in a broad resonance with increasing width as more charge is added to the cloud. Variable charge density also causes its electric field to depart from $E \propto r$ proportionality, i.e. the potential is no longer quadratic and the ω_{cool} frequency cannot be calculated analytically, making the problem approachable only via numerical simulation.

These effects have been investigated in experimental [7, 48, 52], as well

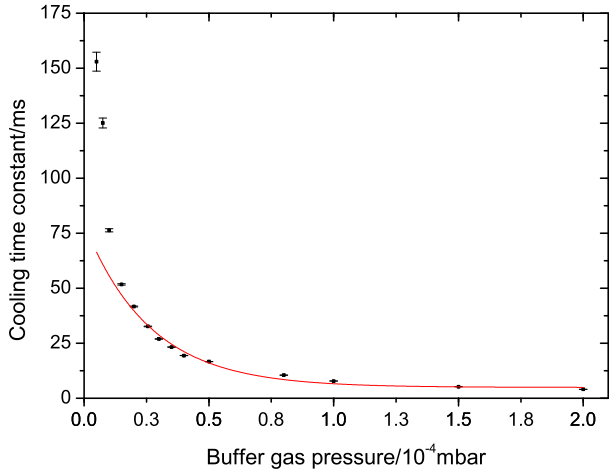


Figure 4.6: The dependence of the cooling time constant of the ion cloud on the Helium buffer gas pressure with a fitted exponential function (simulated data). In the pressure region from $0.2 \times 10^{-4} - 2.0 \times 10^{-4}$ mbar the dependence is roughly exponential, while at lower pressures the time constant exhibits an ever sharper rise.

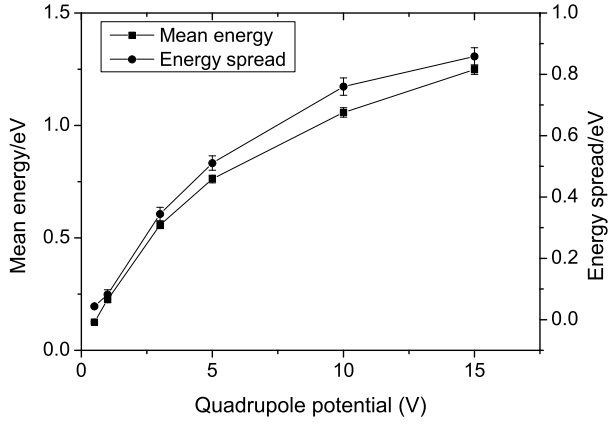


Figure 4.7: (**left axis**) Mean per-ion energy vs. the depth of the trapping potential . (**right axis**) Standard deviation of the energy distribution.

computational campaigns [15, 100]. An extensive analysis of experimental data and the corresponding Penning trap ion dynamics simulation with Simbuca is presented in Section 4.2. In addition, ion cloud dimensions, Coulomb scaling, coupling of the axial and radial modes and other phenomena relevant for sideband cooling were investigated computationally.

4.1.4.1 Spatial distribution

In addition to the energy distribution of the ion cloud, the knowledge of the spatial distribution is also required to fully characterize the phase space, and as an initial condition for the tracking simulation SimWITCH that is used in the search for deviations of the experimental recoil spectrum from the Standard Model expectation. If unaccounted for, the initial position of a decayed ion can cause a systematic error of up to 0.5% in $a_{\beta-\nu}$ [103]. The recoil energy is influenced by the total potential, i.e. the quadrupolar trapping potential at the point of decay combined with the ion cloud's self-field potential. The former depends on the trap depth and the axial size of the cloud, while the latter depends on the number of ions and can reach ~ 0.5 V for clouds of 10^6 ions. Systematic errors on the order of $\sim 0.5\%$ can occur if both effects are not taken into account by simulations.

The spatial distribution is constant when the ion cloud is in equilibrium. It is determined by:

- **External conditions**; The amplitude and steepness of the confinement potential determines the axial elongation of the cloud. E.g., an ion cloud will extend further axially in a shallow quadrupolar potential well in comparison with a deep one, given the same trap dimensions. The radial dimensions are influenced by the magnetic field B, that determines the cyclotron radius at a given energy, and the buffer gas temperature that determines the final energy of thermalization.
- **Internal properties of the cloud**; Primarily the number of ions in the cloud, determining the smallest radius that can be achieved by sideband cooling and centering.
- **History of the cloud**; The initial conditions and any subsequent manipulation of the cloud by excitation. Since the magnetron motion is not cooled off by the buffer gas and remains in a metastable state, the initial radius of the cloud is mostly preserved, and slowly expanding over long time periods (relative to the magnetron period). If quadrupolar excitation at ω_c is applied, the cloud contracts radially until equilibrium

with the space-charge force is reached. Conversely, the cloud expands without limit if dipolar excitation at ω_+ is applied.

Figure 4.8 shows the dependence of the average radial and axial displacements of the ions on the number of ions. The data refers to an equilibrium state of the cloud after 100 ms of buffer gas cooling (at 1×10^{-4} mbar) and 120 ms of sideband cooling (with 3 V excitation amplitude). The number of simulated ions is 2000, scaled with appropriate factors to achieve a cloud with the required space-charge. Both the radial and axial dimensions grow approximately logarithmically with ion number, due to the intra-cloud space-charge repulsion. For an ion cloud of 10^6 ions, the average axial ion displacement is close to 5 mm, while about 10% of the ions reach 10 mm or more. At this axial displacement, the quadrupolar potential is about 0.25 V (for a total trap depth of 5 V), corresponding to a shift of about 0.8% in $a_{\beta-\nu}$ (see Figure 4.9).

On Figure 4.10 simulated spatial distributions of two ion clouds (with 2×10^2 ions scaled to 2×10^3 and 2×10^5 ions) are shown. The ion clouds are cooled for 200 ms in buffer gas (at 2.5×10^{-5} mbar), followed by 80 ms of quadrupolar excitation at 3 V amplitude. It can be seen that the final radial size of the cloud is similar in both cases, while the cloud with 2×10^5 ions is axially about two times larger. More importantly, it can also be seen that the charge density in both ion clouds decreases rapidly from the dense core towards the outer sections. This inhomogeneity of the density causes the space-charge induced field to depart significantly from the quadrupolar form, causing a difference in motional eigenfrequencies at different radii, and therefore a broadening of the resonance peaks. It also significantly reduces the applicability of analytical models of the shift and broadening of the magnetron and cyclotron eigenfrequencies that rely on constant space-charge density (see [100], Sec. 4.2).

4.1.4.2 Coupling of radial and axial modes

Quadrupolar excitations applied by an azimuthally segmented ring electrode affect two radial (the magnetron and the cyclotron) eigenmotions, while not directly influencing the axial motion. However, when an ensemble of ions is trapped, the axial mode can still be influenced by quadrupolar excitations, via the Coulomb interaction between the ions and the radial compression of the cloud. In Figure 4.11, the time evolution of the average radii and axial dimensions of ion clouds with 10^3 ions and different total space-charge is shown. Before t=0, the ion cloud undergoes 100 ms of thermalization with the buffer gas ($p = 2 \times 10^{-4}$ mbar). At t=0, the cloud is in thermal equilibrium and starts being subjected to quadrupolar excitation (Vpp=3 V) for a total duration of 120 ms. It can be seen that the radial compression of the ion cloud, caused

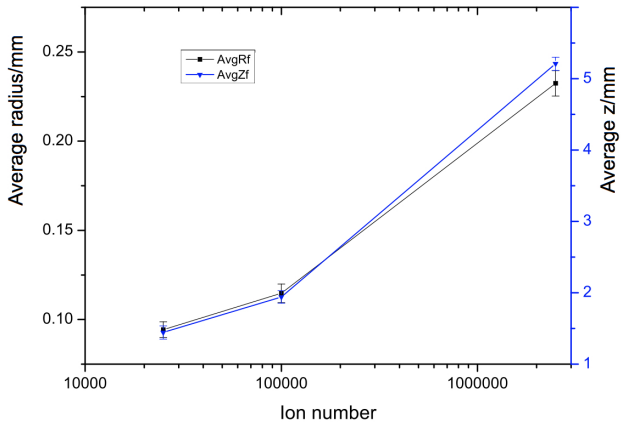


Figure 4.8: Dependence of the dimensions of the ion cloud on the ion number after the cooling and centering procedure. Average radial displacement (black) and axial displacement (blue) of ions in the cloud is shown.

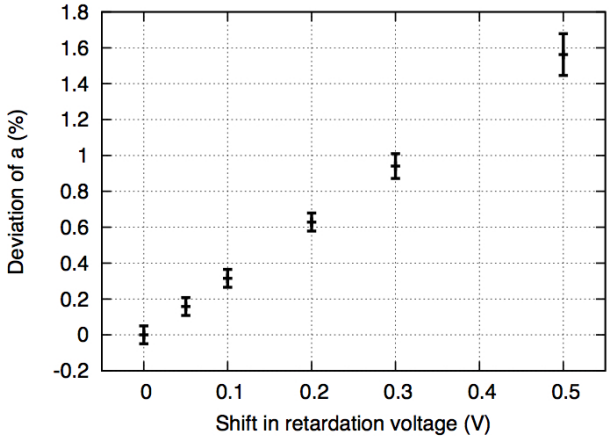


Figure 4.9: Dependence of the shift in the determination of a on the shift of the retardation potential, or equivalently, the potential of the initial position of the recoil ion. From [103].

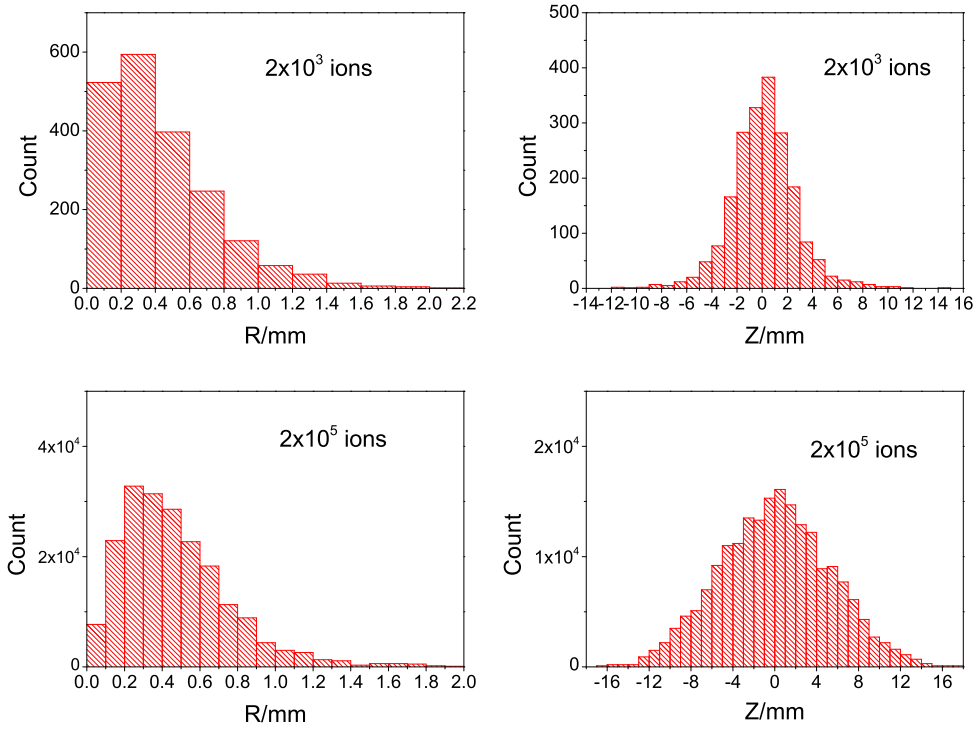


Figure 4.10: Histograms of the spatial distribution of two simulated ion clouds, with 2×10^3 (**top row**) and 2×10^5 (**bottom row**) ions. Both radial (**left**) and axial (**right**) distributions are shown. (See text for details.)

by the quadrupolar excitation, results in a sudden axial expansion as the ions are being pushed out by the radial compression and the modified space-charge field. Moreover, the axial expansion is much higher in high space-charge cases, implying that space-charge has a dominant influence on this effect. It is important to note that all simulations on Figure 4.11 have identical conditions except for the scaled space charge (the interaction with the buffer gas amounts to 10^3 ions in all cases shown). Subsequently, the new axial energy is slowly cooled off and the axial dimensions reduced, but the final axial size at t=120 ms remains larger than the starting size at t=0 in high space-charge cases.

Since this effect increases the axial size of the ion cloud (radioactive source), thereby increasing associated systematic effects (see Section 4.2.4.1), care needs to be taken to allow for sufficient axial motion relaxation time during the

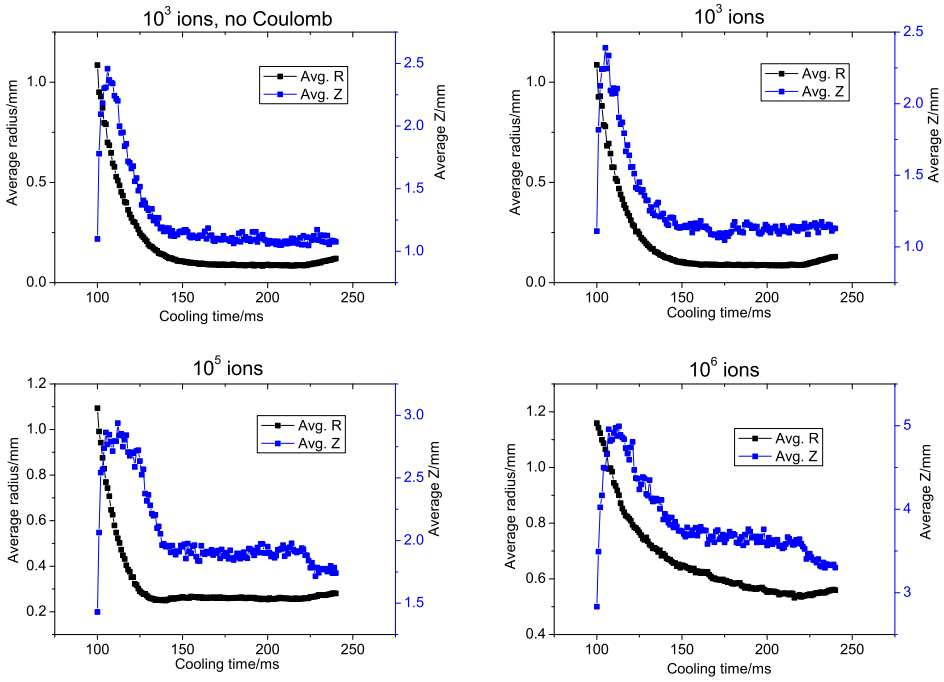


Figure 4.11: The evolution of the average ion radius and axial displacement in a cloud of 10^3 ions scaled to represent a space-charge of 0, 10^3, 10^5 and 10^6 ions, respectively. The excitations are applied at t=0 on a previously thermalized ion cloud (see text for details).

preparation phase in the cooler trap.

4.1.4.3 Coulomb scaling

Due to the limitations of current GPU technology, in cases where more than about 2500 ions are required, the charge of each ion is scaled up in order to simulate much higher space-charge conditions. The Coulomb scaling has been tested by comparing the average radii and energies at the end of a full preparation cycle, for ion clouds with different ion numbers, but scaled to the same total space-charge (see Section 4.2 for more details). It was found that the scaling gives consistent results up to about a factor of 100. In addition to the final state comparison of the ion cloud (Section 4.2), it is useful to verify

the consistency throughout the full cycle. In Figure 4.12, the evolution of the average ion radius as a function of time in the cycle is therefore shown. The ions are created at t=0, spatially randomized according to a Gaussian distribution, and are given a random energy according to a Maxwell-Boltzmann distribution with a maximum at 10 eV. During the first 200 ms, the ions cool off most of the kinetic energy in the buffer gas, which severely reduces the cyclotron radius, while the magnetron radius slightly increases. The decrease of the cyclotron radius is visible in the beginning of the 200 ms period, while the slight increase of the magnetron radius becomes noticeable towards the end. At t=200 ms, quadrupolar excitation is applied for 120 ms and with 3 V amplitude, resulting in a rapid decrease of the average magnetron (and therefore total) radius. The radial compression of the ion cloud encounters a space-charge limit close to t=300 ms in the two cases on Figure 4.12 (bottom) with high total space-charge. Furthermore, for the two low space-charge cases (with scaling factors 25, 50 and 100) the values for the two ion clouds are consistently within error bars, while for the two high space-charge cases (scaling factors 200, 400 and 800), there is a discernible mismatch. The average radius of the ion cloud with 500 simulated ions and the higher scaling factor falls consistently below the values for the one with 1000 ions scaled with a lower factor in the second part of the cycle when the excitation is applied (Figure 4.12, bottom right). In addition, it can be seen that in the first 20 ms of the cycle, there is significantly more scatter of the averages in the cases with low space-charge. This is probably due to clustering effects caused by the space-charge (see [117] for a discussion of other clustering effects observed in WITCH Penning traps).

Figure 4.13 shows the average per-ion energy in the respective simulations. The agreement between the two curves in each graph is good in the first 200 ms of buffer gas cooling, while a discrepancy appears during the excitation phase in both high space-charge ion clouds (bottom graphs). The sudden rise in average per-ion energy at t=200 ms is due to the energy that is pumped into the cloud by the quadrupolar excitation field and which converts the magnetron motional amplitude into the cyclotron one, which carries about 5 orders of magnitude more energy. The scatter in the low space-charge case is also present, however, in this case it is more pronounced at t=200 ms when a large amount of energy is injected into the system, disrupting the thermal equilibrium.

Finally, it can be concluded that the full cycle data supports the validity of the Coulomb scaling up to a factor of about 100.

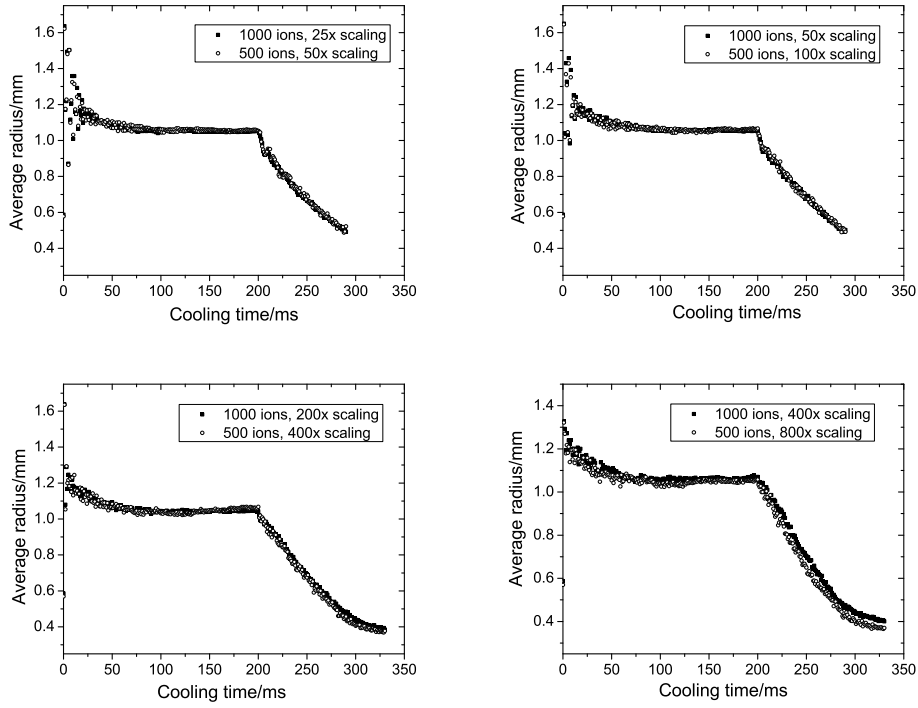


Figure 4.12: Comparison of the time evolution of the average ion trajectory radius when different numbers of ions are scaled to represent the same space charge. For both curves on each graph the product of the number of ions and the scale factor is the same. The ions are created at t=0, cooled in a He buffer gas until t=200 ms, when quadrupolar excitations begin (see text for more details). A discrepancy in the scaling starts to appear for factors (200, 400) and increases for (400, 800).

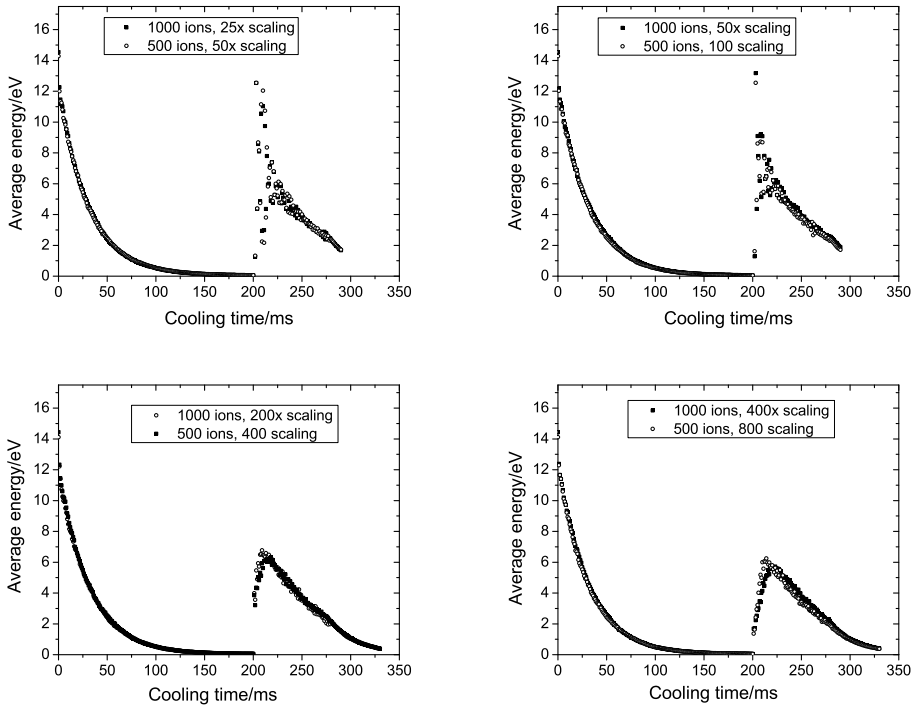


Figure 4.13: Comparison of the average per-ion energy in cases described in Figure 4.12 and text. The discrepancy between the two scaling factors again appears for high space-charge cases (100, 200) and (400, 800). See text for details.

4.2 Space-charge effects in Penning ion traps

T. Porobić[1], M. Beck[2], M. Breitenfeldt[1], C. Couratin[1], P. Finlay[1], A. Knecht[3], X. Fabian[4], P. Friedag[2], X. Fléchard[4], E. Liénard[4], G. Ban[4], D. Zákoucký[5], G. Soti[1], S. Van Gorp[1], Ch. Weinheimer[2], E. Wursten[1], N. Severijns[1]

[1] *KU Leuven, Instituut voor Kern- en Stralingsfysica, Celestijnenlaan 200D, 3001 Leuven, Belgium*

[2] *Universität Münster, Institut für Kernphysik, Wilhelm-Klemm-Strasse 9, D-48149 Münster, Germany*

[3] *PH Department, CERN, CH-1211 Geneva 23, Switzerland*

[4] *LPC Caen, ENSICAEN, Université de Caen, CNRS/IN2P3, F-14070 Caen, France*

[5] *Nuclear Physics Institute, ASCR, 250 68 Rež, Czech Republic*

4.2.1 Abstract

The influence of space-charge on ion cyclotron resonances and magnetron eigenfrequency in a gas-filled Penning ion trap has been investigated. Off-line measurements with $^{39}K^{+}$ using the cooling trap of the WITCH retardation spectrometer-based setup at ISOLDE/CERN were performed. Experimental

ion cyclotron resonances were compared with *ab initio* Coulomb simulations and found to be in agreement. As an important systematic effect of the WITCH experiment, the magnetron eigenfrequency of the ion cloud was studied under increasing space-charge conditions. Finally, the helium buffer gas pressure in the Penning trap was determined by comparing experimental cooling rates with simulations.

4.2.2 Introduction

In recent years, Penning ion traps have become established as versatile tools for trapping charged particles in plasma physics, atomic physics, as well as nuclear and particle physics. Specific applications include e.g. beam preparation [7], mass spectrometry [18], nuclear decay studies [63], antimatter studies [8], strongly coupled plasmas [102] and low energy precision measurements of fundamental interactions [108].

The Weak Interaction Trap for CHarged particles (WITCH) [16, 64], the focus of this work, is a double Penning trap system situated at ISOLDE/CERN and aiming at determining the β-ν angular correlation coefficient a in the mirror β-decay of ^{35}Ar to a precision better than 0.5%. In the Standard model, nuclear β-decay is modelled as a purely V (vector) - A (axial-vector) interaction. However, Lorentz invariance also allows scalar, tensor and pseudo scalar interaction components. At present, the existence of scalar and tensor currents is experimentally ruled out to a precision of only about 10% [97]. The β-ν angular correlation coefficient's sensitivity to the exotic scalar current in the case of ^{35}Ar in principle allows providing stringent experimental constraints on physics beyond the Standard Model [17, 64, 72, 108].

The WITCH Penning traps act as a scattering-free source of radioactive ^{35}Ar, typically containing large ion clouds (with 10^4 – 10^6 ions) to enhance statistics. However, if more than one ion is present in a Penning trap, the trapping potential deviates from the quadrupolar shape and causes shifting of motional eigenfrequencies, as well as shifting and widening of the ion cyclotron resonance frequency required for sideband cooling [7, 48]. Moreover, centering becomes more difficult due to Coulomb repulsion. Consequently, this hampers efficient ion cloud cooling, centering and purification. Space-charge thus significantly contributes to systematic effects caused by source properties, i.e. ion cloud dimensions and temperature. Ion clouds of this size and density are still not fully in the plasma régime, and are therefore beyond reach of both single particle and collective motion analytical frameworks. Numerical simulation presently remains the only feasible way of modelling such phenomena. For this purpose,

the Simbuca [107] simulation package was employed in this work on Graphical Processor Units (GPUs), taking advantage of their intrinsic parallelism.

Many other Penning trap experiments experience limitations caused by space charge-related effects. ISOLTRAP's precision mass spectrometry depends on precise determination of the ions' fast eigenmotion frequency and efficient isobar purification at the MR-ToF device [115], both being affected by frequency shifts and other space-charge phenomena [52]. REXTRAP [110], a high-capacity preparation trap at ISOLDE, aims for mass-selective operation, as well as efficient cooling of large (10^8) ion clouds. PIPERADE [10] (currently under construction) is a high-capacity isobar separator for the SPIRAL2/DESIR facility, the operation of it being limited by a space-charge induced frequency broadening and shift of the sideband cooling frequency.

In the case of WITCH, understanding of such phenomena is essential not only for efficient tuning and operation of the traps, but also for an accurate characterization of the systematic effects observed in on-line experiments. Furthermore, successful numerical simulation is important for gaining a deeper understanding of space-charge effects in current Penning trap experiments, as well as for the design of future ones. In this work, a systematic experimental and computational study of space-charge effects on ion motional modes and buffer-gas cooling efficiency is presented, thereby extending earlier work that was reported in [7, 15, 29, 107].

4.2.3 Nonneutral plasma in a Penning trap

4.2.3.1 Penning trap principles

Charged particles are radially confined in a Penning trap by a strong axial magnetic field $\mathbf{B} = B\hat{\mathbf{e}}_z$ and axially by an electrostatic quadrupolar potential of the form

$$U = \frac{U_0}{2d^2}(z^2 - r^2/2), \tag{4.19}$$

where U_0 is the potential between the end cap and ring electrodes, and d a parameter given by the trap geometry, characterizing the depth of the potential well.

The motion of a single particle is then a superposition of three eigenmotions with corresponding eigenfrequencies: the magnetron (ω_-), the axial harmonic (ω_z), and the modified cyclotron (ω_+) motion. The radial frequencies satisfy equation

$$\omega_{\pm} = \frac{\omega_c}{2} \pm \sqrt{\frac{\omega_c^2}{2} - \frac{\omega_z^2}{2}}, \tag{4.20}$$

while the axial frequency is given by

$$\omega_z = \sqrt{\frac{qU_0}{md^2}}, \tag{4.21}$$

where q and m are the charge and mass of the ion. The sum of the two radial frequencies is the true cyclotron frequency (ω_c), given by

$$\omega_c = \omega_+ + \omega_- = \frac{q}{m}B. \tag{4.22}$$

For high magnetic fields the three eigenfrequencies satisfy the following inequality: $\omega_- \ll \omega_z \ll \omega_+$. After entering the trap, ions start losing their kinetic energy via collisions with the buffer gas. This interaction can be modelled phenomenologically by a continuous drag force acting in the direction opposite to the ions' motion:

$$\mathbf{F} = -\delta m \mathbf{v}, \tag{4.23}$$

where δ is the damping constant, given by:

$$\delta = \frac{q}{m}\frac{1}{K_{mob}}\frac{p/p_N}{T/T_N}, \tag{4.24}$$

with K_{mob} the reduced ion mobility, and p/p_N and T/T_N the gas pressure and temperature relative to normal pressure and temperature, respectively. In this model, the axial harmonic oscillation and reduced cyclotron radial motion amplitude (R_+) are damped, while the magnetron motion is unstable, and its amplitude (R_-) increases as:

$$R(t) = R_{\pm}(0)e^{(\mp\delta(\omega_{\pm}/(\omega_- + \omega_+))t)}. \tag{4.25}$$

This effect can be mitigated by coupling the magnetron motion to either the axial or the reduced cyclotron motions via radio-frequency (RF) excitations at the sum of frequencies of both motions. The latter coupling is usually used with ions, with the RF frequency $\omega_{rf} = \omega_c = \omega_+ + \omega_- = \omega_{cool}$ in the case of a single ion, where ω_{cool} represents the *optimal* centering and cooling frequency of the RF excitation, i.e. the frequency for which the highest number of ions is centered.

In this way, the radius of the magnetron motion can be decreased, resulting in centering and cooling of the trapped ions. This method, known as buffer gas (or sideband) cooling [92], is used by many Penning trap systems for ion cooling and centering, e.g. REXTRAP, ISOLTRAP [75] and SHIPTRAP [20]. Because of its mass selectivity, it is also used for ion species purification when magnetic beam separator resolution is not sufficient.

With only one ion in the trap, the equations of motion can be solved analytically, with both the buffer gas and the excitation field taken into account, resulting in damped oscillatory interconversion of the fast and slow radial motions:

$$R(t) = R_{\pm}(0)e^{(-\delta/2t)}. \tag{4.26}$$

This cooling and centering continues until thermal equilibrium with the buffer gas is reached, limiting the final amplitudes.

4.2.3.2 Many ions in a Penning trap

When more than one ion are present in a Penning trap, the increased space-charge modifies the net potential influencing the ions, and the observed effects start to diverge from the single-particle theory outlined in the previous subsection, making the problem difficult to approach analytically. The space charge produced by $\sim 10^5 - 10^7$ ions typically present in a high-capacity trap like WITCH causes significant deviations from the single-particle picture, but still does not always satisfy the criterion for a true plasma, i.e. the Debye length $\lambda_D = \sqrt{kT/4\pi\rho^2}$, where T and ρ are respectively the temperature and density, can still exceed the cloud's dimensions. Consequently, numerical simulation is the only feasible approach for ion cloud dynamics modelling in these cases. Nevertheless, many plasma physics results remain valid in this intermediate region [82].

An ion cloud of a prolate spheroidal form and constant density in the center of a Penning trap will produce a radially outward electric field proportional to r, the radius. This field causes the $\mathbf{E} \times \mathbf{B}$ drift, resulting in a rigid rotation of the cloud around its main axis, i.e. the fourth eigenmotion at the frequency

$$\omega_r = \frac{a(\alpha)\rho q}{\epsilon_0 B}, \tag{4.27}$$

where a is a coefficient determined by the spheroid aspect ratio α, ρ the ion cloud density and ϵ_0 the dielectric constant. Since the frequency ω_{cool} is given in the reference frame of the ion cloud, the rotation causes an increase of the

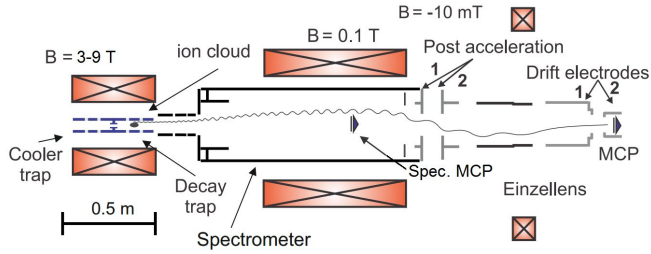


Figure 4.14: Schematic overview of the WITCH Penning traps with the retardation spectrometer, spectrometer MCP, re-acceleration section and position-sensitive MCP.

sideband cooling frequency in the laboratory frame, ω'_{cool}. This shift amounts to $2\omega_r$ in the ideal case [7], but if the density of the cloud is not constant, making its potential no longer quadratic, the problem becomes approachable only via numerical simulation. Through modifying the effective potential in the trap, the space-charge also changes the motional eigenfrequencies [113]:

$$\omega'_{\pm} = \frac{\omega_c}{2} \pm \sqrt{\left(\frac{\omega_c}{2}\right)^2 - \frac{1}{2}\omega_z^2 - \frac{\omega_p^2}{3}}, \tag{4.28}$$

where $\omega_p^2 = \rho q / m\epsilon_0$ is the plasma frequency. This results in a decrease of the modified cyclotron frequency ω_+ and an increase of the magnetron frequency ω_- with increasing space-charge. Equation 4.28 is valid for spherical ion clouds with constant density. The denominator of the plasma frequency term stems from the cloud shape, and for prolate ellipsoids becomes smaller than 3 [56].

4.2.4 Experimental setup

In a radioactive beam experiment with the WITCH setup (see Fig. 4.14), cooled bunches of ^{35}Ar are prepared in REXTRAP and then sent into the WITCH beam line at 30 keV kinetic energy before being pulsed down to about 9 keV by a pulsed drift cavity [29]. They are further decelerated electrostatically to ∼100 eV before entering the cooler trap (CT), where they are captured in a nested potential (a low quadrupolar potential around the trap center with high box-like potential on the end caps) and thermalized with the helium buffer gas (to ∼0.025 eV), with a total efficiency of ∼20%. The cooled and centered

ions are transferred to the second Penning trap (decay trap, DT) that serves as a scattering-free source. ^{35}Cl daughter ions recoil from the decay trap into a retardation spectrometer (MAC-E filter [83]), where their integral energy spectrum is probed by a variable retardation barrier. Since the DT is situated in a high magnetic field region (typically 3 – 9 T) and the analysis plane of the retardation spectrometer is in a low field region (0.1 T), up to 98.33% of the ions' radial energy is converted to axial energy. The ions that pass the retarding potential are re-accelerated by a 3 kV potential and focused on a position sensitive Micro-Channel Plate (MCP) detector [28, 69].

All experiments presented in this work have been performed using stable $^{39}K^{+}$ ions originating from REXTRAP's offline ion source and subsequently cooled and bunched by REXTRAP, or from WITCH's dedicated off-line surface ionization ion source with an RFQ for cooling and bunching [105].

4.2.4.1 WITCH Penning traps

The WITCH ion trapping system [16, 65] consists of two cylindrical Penning traps (electrode layout shown in Fig 4.15). the first (CT) is used for preparation of the ion cloud using buffer gas and excitations, while the second (DT) serves as storage for the ion cloud and acts as a scattering-free radioactive source. To achieve sufficient vacuum conditions for the radioactive source and spectrometer, the DT is separated from the CT, which contains He buffer gas at $10^{-5} - 10^{-4}$ mbar, by a differential pumping diaphragm of 2 mm diameter. They are both situated within a superconducting magnet with field homogeneity of $\delta B \leqslant 10^{-5}$.

The trap electrodes have a 4 cm diameter and are made of oxygen-free copper double-coated with Ni and Au. The CT is 25 cm, while the DT is 20 cm long. Each trap has an eight-fold segmented central electrode for creating the RF excitation potential. Their maximum ion capacity is estimated to $\sim 10^7$ ions, while the instantaneous capacity depends mainly on the space-charge of the ion cloud and the depth of the quadrupolar potential well in the trap, with typical operating values being in the range 0.5 – 15 V (see Fig. 4.16). The voltages on the electrodes between the end cap and the central electrode are scaled so as to produce a quadrupolar potential well in the region of a few centimeters around the trap center.

The detection system used for these measurements consisted of two MCP detectors (the first in front of the CT and the second one behind the DT, in the spectrometer), a Faraday cup (FC) situated in front of the traps on the same feedthrough as the first MCP, and a full range pressure gauge close to the buffer gas valve. Since this gauge is located outside the trap, it was used only for indirect estimation of the buffer gas pressure in the CT.

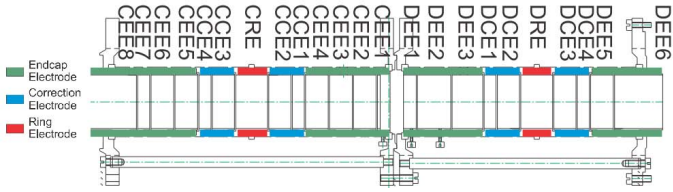


Figure 4.15: Schematic overview of the WITCH Penning traps with their electrodes marked (C stands for cooler trap, and D for decay trap). The pumping diaphragm between the traps is not shown. High voltage is applied on the end cap electrodes while ions still have high energy. A quadrupolar trapping potential around the trap center (CRE and DRE electrodes) is achieved with correction (CCE and DCE) and central ring electrodes. Ions are excited by a time dependent potential on the eight-fold segmented central ring electrodes. Figure taken from [91].

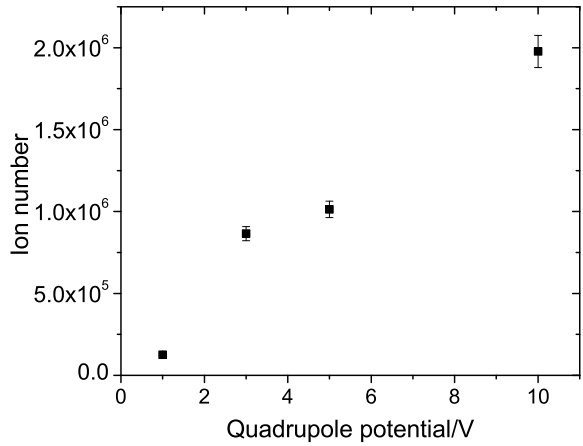


Figure 4.16: The dependence of the trap capacity on the depth of the quadrupolar potential well after 300 ms of buffer gas cooling with quadrupolar excitations at 3 V amplitude.

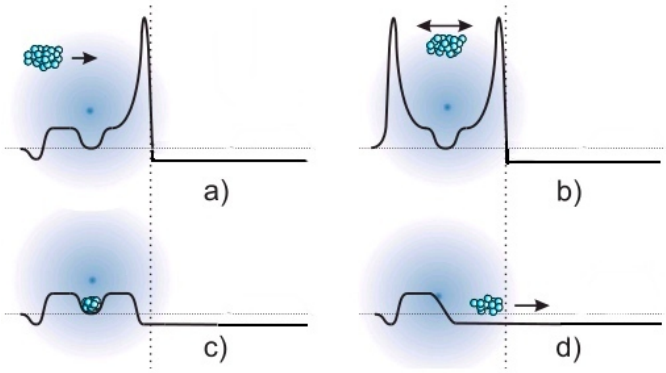


Figure 4.17: Operation of the cooler Penning trap. a) Ions entering the trap. b) High ($\sim$ 100 eV) energy ions trapped by the end caps. c) Ions cooled into a quadrupolar potential in the trap center, end caps potential lowered, excitations applied. d) Cloud ejected from the CT towards the diagnostic MCP behind the traps.

4.2.4.2 Measurement procedure

The number of ions entering the trap was controlled via beam line electrodes with a switch (beam gate) before the ions were pulsed down to low kinetic energies. As the pulsed-down ions approached the CT, its lower end cap electrode (CEE8 on Fig. 4.15) was set below 0 V, while the upper end cap (CEE1) was at a potential sufficient to block the ions (50 – 200 V, depending on the tuning, Fig. 4.17a). When the bunch was fully within the trap, CEE8 was raised to the same potential as CEE1 (Fig. 4.17b). This loading procedure was repeated several times if large ion clouds were needed.

When the ions had lost enough kinetic energy through buffer gas collisions, the end cap potentials were lowered and the ions were fully confined by the quadrupolar potential of the inner electrodes (Fig. 4.17c). Typically, this process takes up to 200 ms, depending on the buffer gas pressure. If needed, at this point a quadrupolar RF field could be applied to center and compress the ion cloud. For that purpose, the RF was applied at ω_{cool} and 3 V amplitude, for 20 –120 ms.

Since radial compression via excitations can expand the cloud axially, a short cooling period without excitation to reduce axial amplitudes followed if needed. Finally, the ions were ejected through the pumping diaphragm and DT, both at 0 V (Fig 4.17d), and were detected with the diagnostic MCP in the spectrometer. Cooling and centering efficiency for the particular measurement are given by the number of ions passing through the diaphragm and being detected on the MCP.

4.2.5 Experimental results

4.2.5.1 MCP Calibration

For estimating the absolute number of ions in the Penning trap, a calibrated, chevron-stacked, 4 cm diameter MCP detector manufactured by Photonis was used. It was operated in integral mode, adding all the charge impinging on its surface into a single pulse. It was shown previously that the area of such a pulse can accurately represent the amount of charge impinging on the detector plates [28], provided special care is taken to avoid saturation effects. WITCH and REXTRAP's offline ion sources provided ^{39}K cooled ion bunches used for this calibration. The ion number per bunch was varied using an electrode synchronized with the measurement cycle as a beam gate. The MCP plates were biased to -2 kV and the signal height and area were read out by an oscilloscope connected to a PC running a Labview based control and data acquisition system [104]. The MCP was calibrated *in situ*, without breaking the vacuum between the calibration and subsequent measurements. The calibration was performed using a Keithley 6514 electrometer connected to a movable Faraday cup situated at the same axial position in the beam line as the MCP. Care was taken that both measuring devices capture the entire beam profile. Faraday cup current readings for each beam gate setting were averaged and recorded, together with MCP pulse heights and areas. The pulse heights were found to follow a linear dependence with the pulse areas and the charge measured by the Faraday cup, as shown in Fig. 4.18. This allowed using both the pulse areas and heights of the calibrated MCP to estimate the true number of ions in the Penning trap.

4.2.5.2 Effects of space-charge on cooling and centering

Like some other existing or planned Penning traps [7, 10], WITCH operates under high space-charge conditions, leading to unwanted phenomena such as a shift and peak broadening of the cyclotron cooling resonance. Earlier

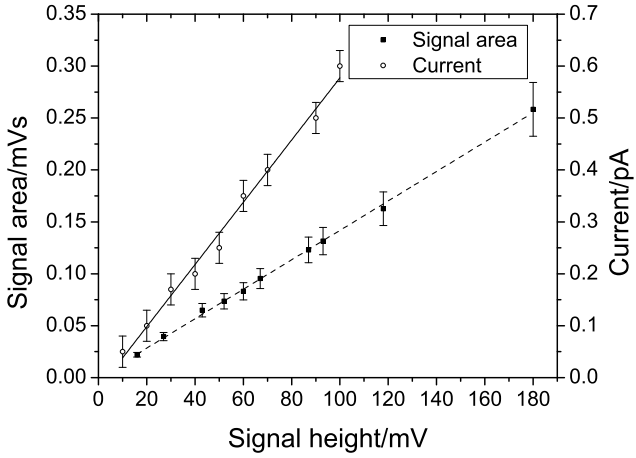


Figure 4.18: (right axis) Averaged ion beam current, measured with an electrometer connected to a Faraday cup, showing a linear dependence with the height of the signal on the MCP, validating the MCP calibration for ion bunches resulting in averaged currents below 0.6 pA. (left axis) Area of the MCP signal, showing a linear dependence with the height of the signal on the MCP. Each data point represents an average of 10 measurements.

investigations have already identified the relevance of these limiting factors for effective Penning trap operation [7, 15, 48, 52]. In the case of a single ion species, it was found that both increased space-charge and increased buffer gas pressure lead to higher optimal cyclotron cooling and centering frequencies ω_{cool}, i.e. the frequencies corresponding to the peak of the RF excitation resonance.

In this section, systematic effects of space-charge and buffer gas pressure on the sideband cooling frequency ω_{cool} were studied. Ion clouds were prepared as described in Sec. 4.2.4.2 and ejected through the 2 mm diaphragm, with optimal cooling and centering resulting in greater intensities recorded on the diagnostic MCP.

Figure 4.19 shows two series of measurements at different buffer gas pressures. The cyclotron resonance peak position and FWHM were measured for each, in dependence with the ion number. The preparation scheme consisted of 200 ms buffer gas cooling without excitations followed by 80 ms of quadrupolar RF cooling with 3 V amplitude. The buffer gas pressure, as measured with the gauge outside the traps, differed by a factor of four between the different

measurements ($p_{gauge,low} = 0.8 \times 10^{-2}$ mbar, $p_{gauge,high} = 3.2 \times 10^{-2}$ mbar). In comparison with the estimation from Section 4.2.6.3, the pressures used here were lower and higher, respectively, than the calibration point. However, the exact pressure in the cooler trap p_{CT} is difficult to estimate accurately, since its dependence on p_{gauge} is not known. With other experimental conditions unchanged, increased buffer gas pressure causes the resonance peak position to shift and FWHM to increase by a few hundred Hz in the high buffer gas case. Thus, while improving the cooling speed via collisions, too high buffer gas pressure hampers efficient centering and possible mass selective operation of the trap through resonance broadening. Peak positions and FWHMs are found to shift to higher values linearly with the number of ions, having roughly the same respective slopes for both buffer gas pressures.

Results shown here are only a subset of all results obtained in this experimental campaign. In others, different cooling and excitation schemes were used. The buffer gas cooling time was varied between 100 ms and 200 ms, and the excitation time in the 20 to 120 ms range, while p_{gauge} was typically varied in the range given above. For all experimental conditions, the resonances were qualitatively similar to Fig. 4.19, i.e. there was a single Gaussian shaped resonance peak with properties consistently following the same trends with variable number of ions and buffer gas pressure. This consistency and reproducibility allowed us to compare the ion cloud behavior shown here to simulations, with the goal of optimizing operational trap parameters, benchmarking the Simbuca simulation software and providing insight into experimentally unavailable ion cloud properties (see Sec. 4.2.6).

4.2.5.3 Effects of space-charge on the magnetron motion

In a perfectly cylindrical Penning trap with a quadrupolar electrostatic potential, a centrally injected ion cloud (or one recentered by excitation) remains centered while the ions in it perform a magnetron motion around the trap's geometrical center. However, if the electrostatic field contains asymmetrical components, or if the geometric and magnetic field axes are not aligned, the center of the ion cloud will rotate around a point off the trap center at the magnetron frequency. This behavior was observed in the WITCH traps only for very low trap depths ($\sim$1 V).

In this case, an eccentric motion of the ion cloud in a shallow trap typically has a larger radius than the diaphragm situated between the CT and DT. Depending on the phase of the motion, this can result in the diaphragm blocking the ions upon ejection. This then causes a periodic dependence of ion intensity on trapping time, as shown in Fig. 4.20, with the difference between the peak

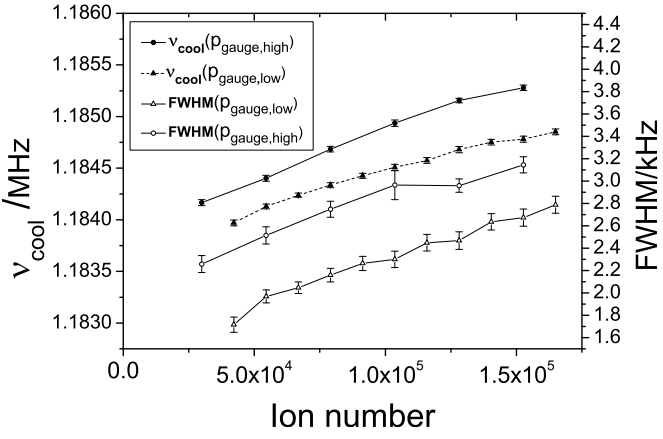


Figure 4.19: Cyclotron frequency $\nu_{cool} = \omega_{cool}/2\pi$ and FWHM dependence on the number of ions and buffer gas conditions. Results are shown for two buffer gas pressures, i.e. $p_{gauge,low} = 0.8 \times 10^{-2}$ mbar and $p_{gauge,high} = 3.2 \times 10^{-2}$ mbar, measured outside the traps. The measurement sequence consisted of 200 ms cooling w/o excitations, 80 ms cooling and centering with quadrupolar excitation at 3 V, and ejection. The buffer gas pressure (p_{gauge}) was kept constant for each of the two measurements.

central values corresponding to the magnetron motion period. This effect was further confirmed by ejecting the ion cloud from the traps onto a position sensitive MCP at different phases of the magnetron motion. From the radius of the motion projected on the detector, using the ion tracking simulation software SimWITCH [40], it was found that the radius of the ion cloud motion around the trap center ranges from 1-4 mm. This is still too far from the trap walls (electrodes have a diameter of 40 mm) to induce image charges large enough to significantly modify the magnetron frequency [113]. In the first approximation, the magnetron frequency of a single ion in the trap is given by Eq. (4.20). However, in high space-charge conditions, the additional radial electric field will shift this frequency to higher values, given by Eq. (4.28).

The effect of the eccentric motion of the ion cloud is found to be more pronounced for lower trapping potentials and disappears for higher ones (∼15 V), since in the latter case the ion cloud is much more compact, resulting in larger numbers of ions successfully passing the diaphragm. Depending on the orientation of the crystal lattice at the surface, electrodes can have different contact potentials, i.e. a gold plated ring electrode, such as installed in both the CT and DT,

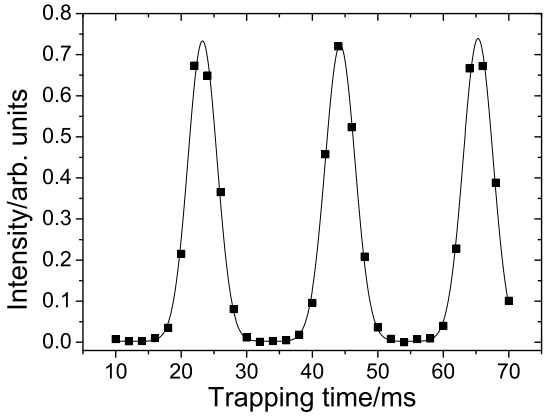


Figure 4.20: Ion intensity measured after ejection of the ion cloud through the diaphragm. Because of the eccentricity of the magnetron motion, only certain phases result in full transmission through the diaphragm. A Gaussian function is fitted to each peak.

can produce a potential difference of up to ∼0.4 V [106] between its segments, causing a shift of the electrostatic trap center with respect to its geometric center. Together with a misalignment of the magnetic and electric fields, this effect was identified as a possible cause for the observed motion. A confirmation in the form of a direct measurement of the contact potential or the field misalignment is not available at this time. However, since the intensity of the radioactive source (ion cloud) is effectively modulated at the magnetron frequency as shown on Fig. 4.20, the characterization of ω_- and its space-charge dependence is essential for the analysis of the WITCH experiment online data.

Since the WITCH experiment, unlike other high space-charge traps, benefits from a low trapping potential to reduce other systematic effects [103], the eccentricity of the magnetron motion presents a significant systematic effect [117], introducing an oscillatory effect superposed on the retardation spectrum data. Furthermore, since each radioactive ion trap load varies due to target conditions and in-trap decay, any dependence of the magnetron frequency on the number of ions has to be characterized and taken into account during data analysis. This effect was experimentally studied for different values of the trapping potential ranging from 0.5 V to 2 V and different amounts of charge in the trap (Fig. 4.21). It was found that the magnetron frequency increases linearly with the number of ions in the trap. Equation 4.28 implies $\omega_- \propto \rho$ to first order, supposing

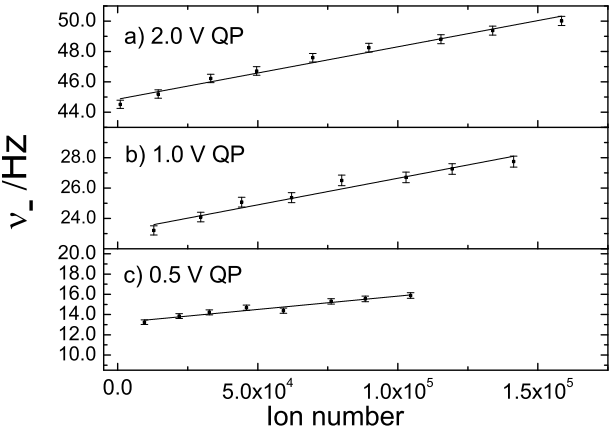


Figure 4.21: Dependence of the experimental magnetron frequency, ν_-, on the number of ions for different quadrupolar trapping potential: a) 2.0 V, b) 1.0 V, c) 0.5 V.

that ρ is uniform. Since ρ is not experimentally available, it was simulated for the relevant space-charge range and other trap parameters matching the ω_- measurement. It was found that ρ varies significantly within the cloud, being highest in the center and very low at outer radii. An average ρ value was therefore calculated using the volume containing 95% of the ions. Its dependence on ion number was found to be approximately linear with a very small quadratic component, in the $10^4 - 10^5$ range (Fig. 4.22). Although the simulation confirms ρ is not uniform as is assumed in the theoretical calculation of the ω_- shift, the observed ω_- shift is still linear with ion number, suggesting that the exact shape of $\rho(r)$ does not have a large influence on the ω_- space-charge shift.

4.2.6 Simulations

Generally, the number of numerical operations needed for a Coulomb interaction simulation scales with $\mathcal{O}(N^2)$, where N is the number of particles, but approximative methods such as the Barnes-Hut tree [13] and fast multipole method [90] reduce this to $\mathcal{O}(NlogN)$ and $\mathcal{O}(N)$, respectively. Recently, a novel *ab initio* method for N-body gravitational interaction simulations using GPUs was developed [50] and implemented in Simbuca [107], a software package for simulation of trapped ion cloud dynamics. Simbuca implements the K_0

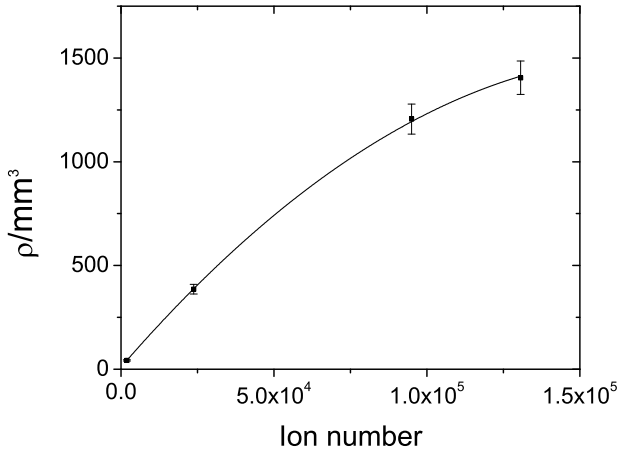


Figure 4.22: Simulated average density of the ion cloud for different space-charge conditions. The density dependence is almost linear for ion numbers in the selected $10^4 - 10^5$ range. The volume of the cloud is defined as the volume containing 95% of all ions.

realistic buffer gas collision model [81] and dipolar, quadrupolar, octupolar and rotating wall excitations, together with customized electro- and magnetostatic field maps. The fifth-order Dormand-Prince [33] method with adaptive time step was used as integrator. In the following, Simbuca simulations of the effect of space-charge on the cyclotron resonance frequency and FWHM will be presented and compared with experimental data.

4.2.6.1 Setup of the simulations

The effect of space-charge on the cyclotron resonance frequency, i.e. the frequency ν_{cool} at which the magnetron-cyclotron motion interconversion via quadrupolar excitation achieves maximal effectiveness, was investigated using the Simbuca simulation software by scanning the excitation frequency around ν_c. Simulation parameters were selected to reproduce the experimental conditions described in Sec. 4.2.5.2. The magnetic field map was obtained from the manufacturer (Oxford Instruments), and the electrostatic field of the cylindrical electrode stack calculated using a COMSOL [1] model matching the trap geometry laid out in Section 4.2.4.1. The asymmetry of the CT potential

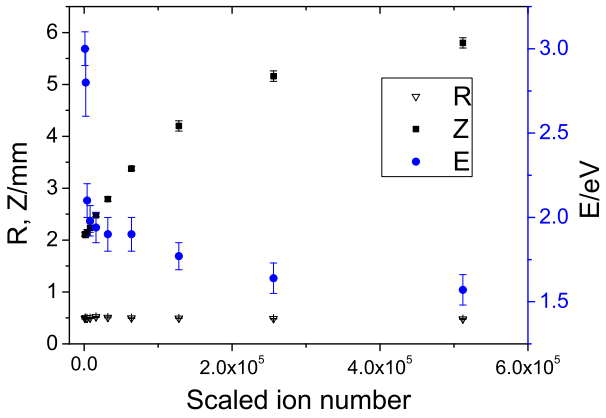


Figure 4.23: Dependence of the average radius R, average axial displacement Z (left axis) and average energy per ion E (right axis) on the scaled number of ions (given by Ions$\times SF$ in Table 4.1) for clouds of 1000 ions.

described in Sec. 4.2.5.3 is not accounted for by the simulations, but does not play a role in the ν_{cool} scans presented here, as it does not cause a measurable effect for the high end cap potentials of ~ 15 V used in these measurements. Ion clouds of 500-2000 ions with their charge scaled to simulate space-charge conditions corresponding to clouds of $10^3 - 2 \times 10^5$ ions were simulated (the consistency of this approach is shown in Sec. 4.2.6.2).

The ions are created in the center of the trap within a prolate spheroid with a radius of 1 – 2 mm and major axis of 10 – 20 mm and are given an initial kinetic energy (KE), Gaussian distributed and centered around 50 eV. Furthermore, it was found that the initial KE has no influence on the cooling rate of the ion cloud, i.e. the average KE decays exponentially with a time constant determined only by the intrinsic buffer gas parameter δ, in agreement with buffer gas cooling theory (Eq. (4.26)).

4.2.6.2 Consistency of the Coulomb scaling

Implementation on a GPU allows for a large degree of parallelization in N-body interaction calculations and results in simulation times reduced by orders of magnitude compared to a modern CPU. While this provides a large improvement in computational speed, simulating ion clouds with N larger than a few thousand

is still impractical with modern GPUs, and a scaled Coulomb method is therefore employed here. The linearity and consistency of this approximation was verified to hold up to a scaling factor (SF) of about 100.

The Coulomb scaling was tested by direct comparison of ion clouds scaled up to a factor of 6 to reference clouds of 1^+ ions, e.g. a cloud of 500 6^+ ions was compared to a a cloud of 3000 1^+ ions. However, since it is not feasible to test the scaling factors directly for ion clouds larger than a few thousand ions due to computation time constraints, the simulations were set up so as to cross-check increasing scaling factors from 1 to 1024, for pairs of ion clouds scaled to the same total charge and ranging from 10^3 to 5×10^5 ions. Clouds of 1000 ions scaled by a factor of n and a cloud of 500 ions scaled by a factor of $2n$ were compared (see Table 4.1), with n ranging from 1 to 512.

The ion clouds were subjected to cooling and centering schemes matching the ones used in other simulations presented here, i.e. consisting of 200 ms cooling from a high (10 – 50 eV) kinetic energy, 80 ms of centering with quadrupolar excitations and 10 ms of relaxation. The time evolution of macroscopic parameters sensitive to space-charge effects, such as the average ion radius R, the average axial displacement Z, and the per-ion energy E, was compared for complementary pairs of ion clouds (Table 4.1). Furthermore, the dependence of these parameters on the scaling factor, for clouds of 1000 ions, is shown on Fig. 4.23. As can be seen in Table 4.1, the average radial position of the ions in the cloud is typically different by a few percent only (i.e. well within error bars) for ion cloud pairs up to scaling factors (64,128), but diverging significantly for (128,256) and higher SFs. It is notable that the final R of all ion clouds of 10^3 – 1.28×10^5 ions is approximately equal, indicating that the centering efficiency is still not significantly hampered by the space-charge in this range. However, the axial displacement Z increases significantly for higher factors, due to more ions being "pushed out" axially when the cloud is "squeezed" radially by the excitation field forces. The average per-ion energy E at t=290 ms also agrees well for ion clouds scaled below factor 128.

Ions	SF	R/mm	Z/mm	E/eV
1000	1	0.490±0.013	2.11±0.04	3.08±0.14
500	2	0.500±0.009	2.12±0.05	3.25±0.16
2000	1	0.491±0.011	2.05±0.03	2.58±0.15
500	4	0.503±0.008	2.16±0.08	2.81±0.12
3000	1	0.494±0.010	2.06±0.05	2.26±0.11
500	6	0.500±0.009	2.11±0.09	2.27±0.09
1000	2	0.503±0.014	2.10±0.03	2.84±0.19
500	4	0.503±0.008	2.16±0.08	2.81±0.12
1000	4	0.494±0.017	2.15±0.05	2.15±0.12
500	8	0.507±0.009	2.07±0.08	2.29±0.11
1000	8	0.498±0.008	2.24±0.09	1.98±0.09
500	16	0.501±0.008	2.22±0.03	1.94±0.10
1000	16	0.516±0.012	2.48±0.03	1.94±0.09
500	32	0.501±0.008	2.22±0.03	1.94±0.10
1000	32	0.511±0.008	2.79±0.04	1.92±0.10
500	64	0.500±0.006	3.07±0.08	1.94±0.08
1000	64	0.497±0.005	3.38±0.04	1.86±0.09
500	128	0.498±0.013	3.67±0.08	1.84±0.09
1000	128	0.494±0.005	4.25±0.05	1.77±0.08
500	256	0.473±0.007	4.74±0.11	1.56±0.09
1000	256	0.485±0.005	5.16±0.08	1.64±0.09
500	512	0.433±0.007	5.19±0.23	1.43±0.09
1000	512	0.479±0.012	5.81±0.10	1.57±0.09
500	1024	0.424±0.006	5.76±0.23	1.35±0.06

Table 4.1: Number of simulated ions and their Coulomb scaling factor (SF), average radius (R), average axial displacement (Z) and average energy per ion (E) at t=290 ms. The error bars are the standard deviations of several values of R, Z and E around t=290 ms, the end of the cycle. Top 6 rows show a direct comparison of scaled ion clouds to a reference cloud with 1^+ ions, while the rest show a comparison of clouds of 500 ions scaled by $2n$ to clouds of 1000 ions scaled by n, with n increasing from 2 to 512. The dependence of the parameters on the scaled number of ions in the case of 1000 simulated ions is shown in Fig. 4.23.

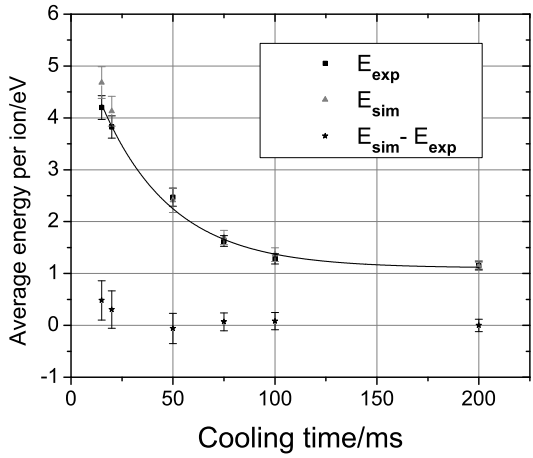


Figure 4.24: Dependence of the mean axial energy per ion after ejection on the cooling time. Experimental data points E_{exp} (squares) are shown together with results from simulations E_{sim} (triangles). The line represents an exponential decay function fitted to the experimental data. The difference $E_{sim} - E_{exp}$ is also shown (stars).

However, there is a trend of decreasing E with increasing total space-charge (see Fig. 4.23). The largest component of E stems from the residual energy of the quadrupolar excitations, indicating that ion clouds with lower total space-charge absorb more energy from the exciting field. This is most probably due to stronger shielding of the field by outer ions in cases of higher Coulomb scaling.

4.2.6.3 Buffer gas pressure estimation

The effect of buffer gas atoms on trapped ions with significantly higher energy than the buffer gas itself can be adequately modelled by viscous damping (Eq. (4.23)). This force will cause an exponential time-dependence of the ion velocity:

$$v(t) = v(0)e^{-\delta t/m}, \tag{4.29}$$

where δ is given by Eq. (4.24). The time dependence of the total ion energy can then be written as:

$$E_{TOT} = E_{Pot} + E_{kin}(0)e^{-2\delta t_{cool}/m} + E_{kin}(t_{cool} \longrightarrow \infty), \tag{4.30}$$

where $E_{kin}(0)$ represents the initial kinetic energy of the ions, $E_{kin}(t_{cool} \longrightarrow \infty)$ the lower energy limit of the buffer gas cooling, i.e. thermalization with the buffer gas, and E_{Pot} the potential energy.

For different cooling times ranging from 20 to 200 ms the ion energy was measured by releasing the cloud from the CT into the DT, where a retardation barrier was varied from 0 to 10 V while other parameters were kept constant. In this way, the axial energy of the ion cloud was obtained as a function of the cooling time. This exponentially decaying cooling curve is shown in Fig. 4.24. It should be noted that this curve does not reach thermal equilibrium at a kinetic energy of about 0.025 eV. This is because a constant offset is produced when the quadrupolar trapping potential is switched to release the ions (see Fig. 4.17 d), resulting in a total energy upon ejection of about 1.45 eV. The simulation was then fitted to the experimental cooling curves with buffer gas as the free parameter, resulting in a p_{CT} estimate. The small discrepancies between experimental and simulated data in Fig. 4.24. seen for the earliest cooling times are due to small differences in the not precisely known initial conditions for the real and simulated ion clouds. The buffer gas pressure was found to be $p_{CT} = 2.5(9) \times 10^{-5}$ mbar when the pressure at the gauge position was $p_{gauge} = 2 \times 10^{-2}$ mbar.

4.2.6.4 Simulation of sideband cooling resonances

The ion cloud was subjected to the same manipulations as in the corresponding experimental study: energetic ions were contained by a high end cap potential ($\sim$ 150 V), then cooled into a nested central quadrupolar potential well ($\sim$ 15 V) for up to 200 ms without excitations, and finally subjected to quadrupolar excitations for 80 ms at 3 V amplitude. The frequency was scanned over a few kHz from -2 kHz to 3.5 kHz around ν_c to determine the optimal cooling and centering frequency ν_{cool}, i.e. the central value and FWHM of the resonance curve. Figure 4.25 (top) shows such a scan of ν_{cool} for 2000 ions scaled with a factor of 100, corresponding to a cloud of 2×10^5 ions in a buffer gas with $p_{CT} = 2.5 \times 10^{-5}$ mbar (see Sec. 4.2.6.2). A period of 100 ms of buffer gas cooling without excitations is followed by 120 ms of cooling and centering via quadrupolar excitations with 3 V amplitude. The ions were considered to be

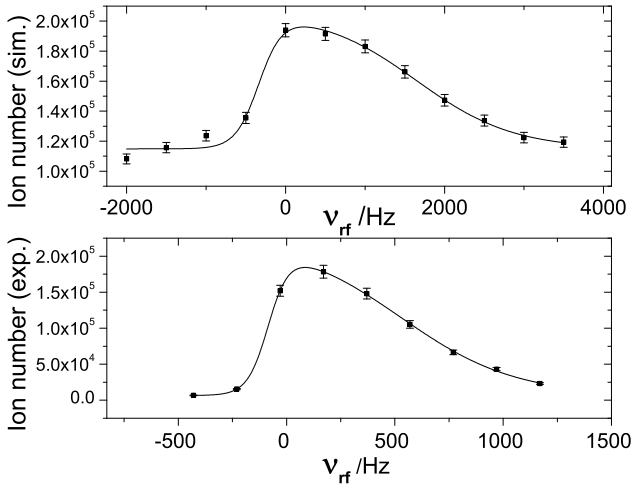


Figure 4.25: Experimental scan of the cooling frequency ν_{cool} shift (bottom) and a simulated scan with matching parameters (top). Zero of the horizontal axis corresponds to ν_c. The empirical fitted function is an asymmetric double sigmoid.

centered if the radius of their motion was smaller than the diaphragm radius. Figure 4.25 (bottom) shows an experimental scan with matching parameters. Both resonances are asymmetric in shape, with the number of ions rising sharply at the lower end of ν_{rf} and decreasing more gradually at the high-frequency side. This behavior is in agreement with results of the mean-field model of the space-charge frequency shifts from [100]. The optimal cooling frequency, ν_{cool}, is accurately reproduced by simulations. However, the FWHMs of the experimental resonance peaks are reproduced less well and there is an offset of the baseline due to incomplete knowledge of the initial position of the ion cloud in the trap.

Figure 4.26 compares measured and simulated relative shifts of the optimal cooling frequency ν_{cool} for experimental data and simulated ion clouds in identical conditions as described previously. The offset corresponding to zero ions was extrapolated and used as reference for experimental and simulation data. The simulation is in good agreement with experimental data, especially in view of the uncertainties in the estimation of p_{CT} and in our understanding of the initial conditions of the ion cloud.

Figure 4.27 shows a simulation of the difference in frequency shifts $\Delta\nu_{cool}$

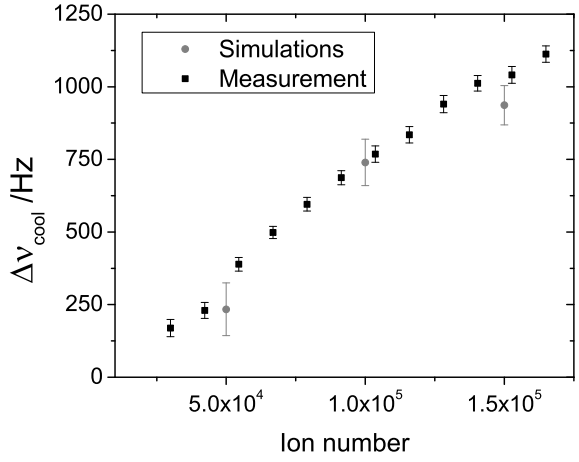


Figure 4.26: Comparison of measured and simulated relative shifts of the cooling frequency ν_{cool}.

between $p_{CT} = 2.5 \times 10^{-5}$ mbar and $p_{CT} = 1.0 \times 10^{-4}$ mbar, with all other simulation parameters kept constant. The ν_{cool} resonance frequency of the ion cloud increases for higher values of p_{CT}, being in qualitative agreement with experimental data shown on Fig. 4.19. It should be noted though that quantitative comparison of data on Fig. 4.19 and Fig 4.27 is not possible, since the estimation (see Sec. 4.2.6.3) for p_{CT} is not available in these cases.

Figures 4.28 and 4.29 show the simulated dependence of the ν_{cool} peak FWHM on p_{CT} and on space-charge, i.e. the number of ions, respectively. The FWHM is increasing with p_{CT}, in qualitative agreement with experimental data. However, an accurate quantitative comparison of the effect of the space-charge and p_{CT} on the FWHM is limited by the precision and availability of the experimental value for p_{CT}. Furthermore, while Coulomb scaling can consistently reproduce the space-charge conditions of a large ion cloud ($\sim 2 \times 10^5$ ions), the cumulative interaction with the Helium buffer gas in the case presented here amounts only to a cloud of 2×10^3 ions. This mismatch of simulated and experimental conditions is identified as a possible reason for the discrepancy between the simulated and experimental FWHM that can be seen in Fig. 4.29. The simulation is seen to significantly underestimate the FWHM for the experimentally estimated $p_{CT} = 2.5 \times 10^{-5}$ mbar. For the higher simulated pressure of 1×10^{-4} mbar the FWHM behavior is similar to the case of lower space charge values, although sharply rising at about 2×10^5 ions. Since the simulation of $\sim 10^5$ ions without Coulomb

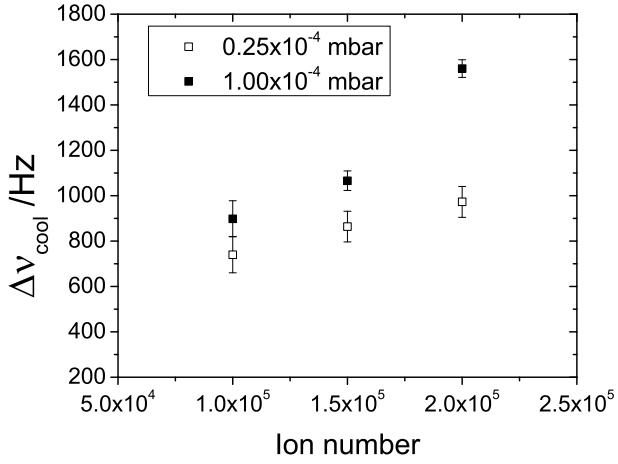


Figure 4.27: Comparison of simulated ν_{cool} shifts for different buffer gas pressures in the CT.

scaling with current GPU technology is not feasible because of computation time limitations, these effects will require improvements in simulation speed for accurate predictions under the given experimental conditions.

4.2.7 Summary and outlook

Systematic effects related to space-charge present challenges for successful operation of the WITCH system as well as other existing or planned Penning traps. They have been investigated both experimentally and numerically in this work.

The buffer gas pressure inside the cooler trap was estimated through measurement of the ion cloud cooling rate and comparison with simulations. Since pressure gauges cannot be operated in the close vicinity of a Penning trap, this approach provides a useful, albeit less accurate alternative.

Off-center magnetron motion of the entire ion cloud was observed experimentally in the WITCH Penning traps. It was found to be of significant importance as a systematic effect in the WITCH on-line experimental data. Its eigenfrequency ν_- was studied under different space-charge conditions. It was found that it rises proportionally with the number of ions, as is expected from theory. This

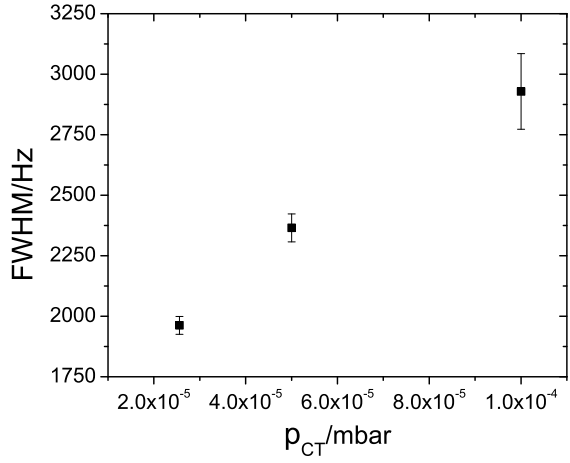


Figure 4.28: Dependence of the FWHM of the simulated ν_{cool} on p_{CT} for a cloud of 10^5 ions.

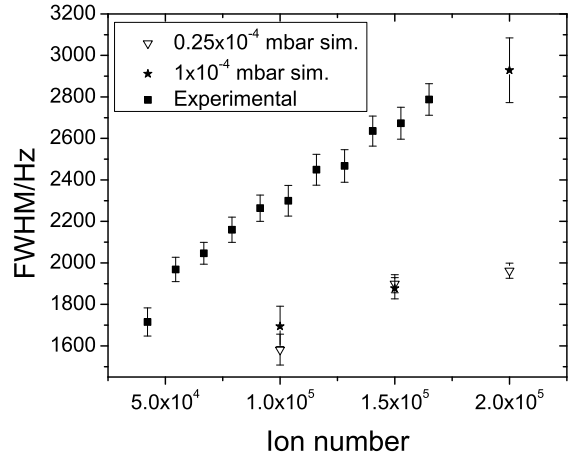


Figure 4.29: Comparison of simulated ν_{cool} FWHM dependence on the amount of ions for different buffer gas pressures with experimental data.

result provides an essential correction to the on-line retardation spectrum data of WITCH [84].

The influence of space-charge on the eigenfrequency ν_{cool} has been investigated. $^{39}K^{+}$ ions were subjected to the buffer gas cooling technique and its effectiveness in different space-charge and buffer gas conditions was measured. It was found that space-charge and buffer gas both independently cause the increase of center frequencies and FWHM's of the cooling resonances. The results are in agreement with experimental investigations of these effects conducted in another high-capacity gas-filled Penning trap (REXTRAP) [7,48]. The properties of the ν_{cool} peaks i.e. their center frequency and FWHM in specific experimental conditions are of special interest for improving the understanding of high-capacity Penning traps and their operation as mass separators.

The Simbuca software for *ab initio* simulation of ion cloud dynamics in particle traps was benchmarked against experimental results, successfully simulating complex dynamics of a large ion cloud in a buffer-gas filled Penning trap modelled using realistic field maps. Shifts of ν_{cool} peaks under increasing space-charge were accurately reproduced for different experimental conditions, while other effects such as the influence of space-charge and of the buffer gas pressure in the trap on the FWHM were reproduced qualitatively. With the help of a novel simulation method on GPU's that allows significantly higher simulated number of ions, these results expand on earlier computational studies of space-charge and buffer gas effects on cooling resonances in Penning traps [15,30].

These results establish Simbuca as a promising tool for Penning trap optimization and design. The study presented here, i.e. the investigation of the effect of space-charge on ion dynamics, further contributes toward the effort to understand fundamental properties of Penning traps and to increase their application domain.

4.2.8 Acknowledgments

We are indebted to A. Herlert for critically reading and commenting the manuscript.

This work is supported by the European Union Sixth Framework program through RII3-EURONS (contract no. 506065), the Flemish Fund for Scientific Research FWO, project GOA 2010/10 of the KU Leuven, the German BMBF under Grant No. 06MS270 and by the Grants No. LA08015 and No. LG13031 of the Ministry of Education of the Czech Republic.

Effect (units)	$S = 1\%$	$S = 0.5\%$	$S \leq 0.2\%$
	$\delta a = 1\%$	$\delta a = 0.5\%$	$\delta a \leq 0.2\%$
Space-charge potential	$\pm 6 \times 10^5$	$\pm 3 \times 10^5$	$\pm 1 \times 10^5$
(number of ions)	$\pm 4 \times 10^6$	$\pm 2 \times 10^6$	$\pm 5 \times 10^5$
Inaccurate ion cloud	0.43	0.17	0.07
energy (eV)	0.13	0.06	0.035
Shift in ret. pot. (V)	0.35	0.2	0.1
	N/A	N/A	N/A

Table 4.2: Quantitative impact of systematic effects discussed in this chapter on $a_{\beta-\nu}$. Magnitudes of the shift (S) and uncertainty (δa) of $a_{\beta-\nu}$ are shown in the first two rows when the number of ions, energy of the ion cloud or the retardation potential deviates from the assumptions used in simulations by an amount given in the lower rows. E.g., the number of ions wrong by 3×10^5 ions causes a shift of $a_{\beta-\nu}$ by 0.5%. The dimension of the ion cloud is not determined experimentally. However, it depends directly on the energy of the cloud. See [103] for more details.

4.3 Conclusion

In this chapter the paper *Space-charge effects in WITCH Penning traps* and additional results on non-neutral plasma systematic effects in WITCH Penning traps were presented.

In Section 4.1 an overview of relevant non-neutral plasma theory was presented. The energy of the ions and its dependence on the number of ions in the cloud was measured and compared with simulation. Capacity of the cooler trap was determined for different potential depths. Spatial distribution of simulated ion clouds in dependence on their space-charge was studied and its impact on a systematics discussed. The coupling of axial and radial motional modes in a Penning trap via space-charge was studied computationally. Finally, the validity of Coulomb scaling used in the simulations was investigated in more detail and its validity up to a factor of 100 confirmed.

The impact of space-charge related effects on the determination of $a_{\beta-\nu}$ is summarized in Table 4.2.

In Section 4.2 the effect of space charge on the frequency of the cyclotron and magnetron eigenmotions was studied both experimentally and computationally. It was found that the cyclotron cooling resonances both shift to higher

frequencies and widen under the influence of space-charge. The former effect was accurately simulated with Simbuca software package, while the latter was reproduced only qualitatively. The increase of the magnetron motional eigenfrequency under space-charge conditions was quantified experimentally. Buffer gas pressure in the cooler trap was estimated by comparing experimental and simulated cooling rates.

Chapter 5

Characterization of the MCP efficiency

In this chapter, a characterization of the main WITCH MCP detector efficiency with various stable ion species is presented.

5.1 Introduction

Microchannel plates are an indispensable tool in nuclear physics, frequently used for ion beam monitoring and nuclear reaction or decay product detection, providing single-hit counting with high time resolution and position information.

The WITCH experiment employs a large, position sensitive MCP detector as its principal data acquisition tool. It is located at the top of the setup (see Figure 2.6) and used to count the recoil daughter ions that have enough energy to cross the retardation barrier in the spectrometer. The operational requirements for such a detector include high efficiency in the range of a few keV at high frequencies, for ions up to ~ 150 atomic mass units and charge states up to 5^+. Position sensitivity is also desirable for monitoring the beam spot and verifying that it is fully contained on the active surface of the detector, as losses due to defocusing lead to systematic errors in $a_{\beta-\nu}$.

Depending on the nucleus, recoiled ions typically have very low kinetic energy up to ~ 1 keV, requiring the usage of MCP detectrors. In order to enhance their detection efficiency, they are re-accelerated to $3.2 \cdot q$ keV, where q is the

ionic charge state. Unlike semiconductor and scintillator detectors which are not sensitive at the required energies or do not provide position information, respectively, micro-channel plate (MCP) detectors with delay lines provide good efficiency for ions above 3 keV and a spatial resolution of ~ 0.1 mm [69]. However, they can be affected by variations of the efficiency across the surface, as well as gradual deterioration of the MCP properties caused by impinging energetic particles and resulting in decreased efficiency. The former effect is explored in-depth in [41], while the characterization of the latter in the case of the WITCH MCP detector is the topic of this chapter.

5.2 Experimental setup

In this section, the configuration of the MCP detector, auxiliary electronics and the data acquisition system is described.

5.2.1 Microchannel plates

Microchannel plates are an assembly of $10^5 - 10^6$ individual electron multipliers embedded in a highly resistive glass substrate. Primary particles (electrons, ions or photons) impinging on the semiconductive coating of the channels create secondary electrons. A high difference of the potential between the entrance and the exit of each channel enhances this process, creating an electron avalanche in a process analogous to a conventional photomultiplier tube (see Figure 5.1). The channels have a small angle bias with respect to the axis of the plate in order to increase the probability of the impinging particles hitting the walls.

The plates used in the WITCH experiment are fabricated by Photonis (LongLife$^{\text{TM}}$ series). The active surface of the channels consists of a 200 nm layer of conductive NiCr, followed by a 20 nm layer of SiO_2 and finally a 1 nm layer of doped SiO_2 which emits secondary electrons after an impact [41]. The geometric properties of the microchannels and the plates are listed in Table 5.1. The two MCPs that comprise the WITCH detector are mounted in a chevron stack, in which the microchannels of the two plates are joined under an angle smaller than 180° (see Figure 5.2). This assembly is favorable for avoiding feedback, since the electron avalanche can create positive ions close to the exit of the channels, which are then reabsorbed. A chevron assembly of MCPs can provide gain factors up to 10^7 with high time resolution (<100 ps) and spatial resolution limited by the center-to-center spacing of the channels. The WITCH detector, produced by RoentDek Handels GmbH, can typically perform at a

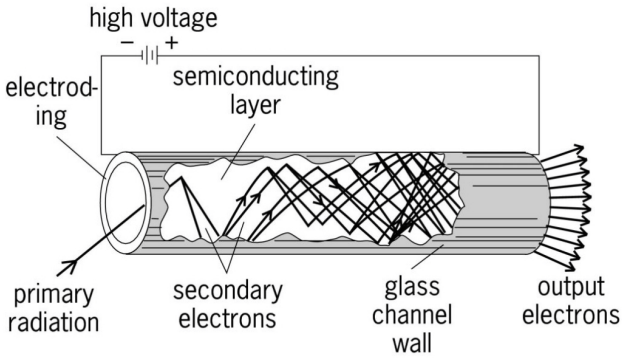


Figure 5.1: An illustration of the MCP working principle. A primary particle impinges on the inner surface of the microchannel and creates an electron shower enhanced by a potential difference across its length. From [114].

Outer diameter	86.6 mm
Active diameter	83 mm
Thickness	1.5 mm
Pore size (diam.)	25 μm
Center-to-center spacing	32 μm
Aspect ratio (channel length/dia.)	60
Bias angle	$8° \pm 1°$
Open area ratio	$(50 \pm 5)\%$
Channels in active area	$(5.5 \pm 0.6) \cdot 10^6$

Table 5.1: Geometric characteristics of the Photonis MCP used in the WITCH experiment [4].

position resolution of <0.1 mm, up to 1 MHz rates and 10 – 20 ns multi-hit dead time [4].

5.2.2 The MCP detector

The WITCH MCP detector is situated on top of the system, facing upstream in order to record the number of ions passing over the retardation barrier in the spectrometer. In addition to the two microchannel plates, it consists of the

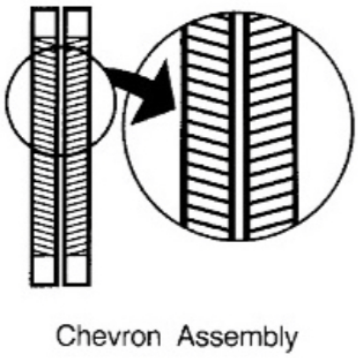


Figure 5.2: Two MCP plates stacked in a chevron configuration, reducing the feedback of the amplified signal. From [14].

delay line anodes that provide the position information and the electronics that process the raw signal before it is transmitted to the data acquisition system (FASTER, see Section 5.2.3.1).

The layout of the complete MCP detector setup is shown in Figure 5.3. The two MCPs are joined by two ceramic (Marcor) rings partially coated with copper so that an acceleration grid can be mounted in front, if necessary. Behind the plates, two delay line anodes collect the charge leaving them. An aluminum plate is placed behind the delay lines for protection. The whole structure is fixed on a insulating Peek ring, which rests on a CF-200 flange (see Figure 5.3). Furthermore, the entire structure is enclosed within a cyllindrical electrode (not shown on Figure 5.3) with a hole over the MCP active area, which is usually kept at the same potential as the front plate of the MCP detector (see [41] for more details).

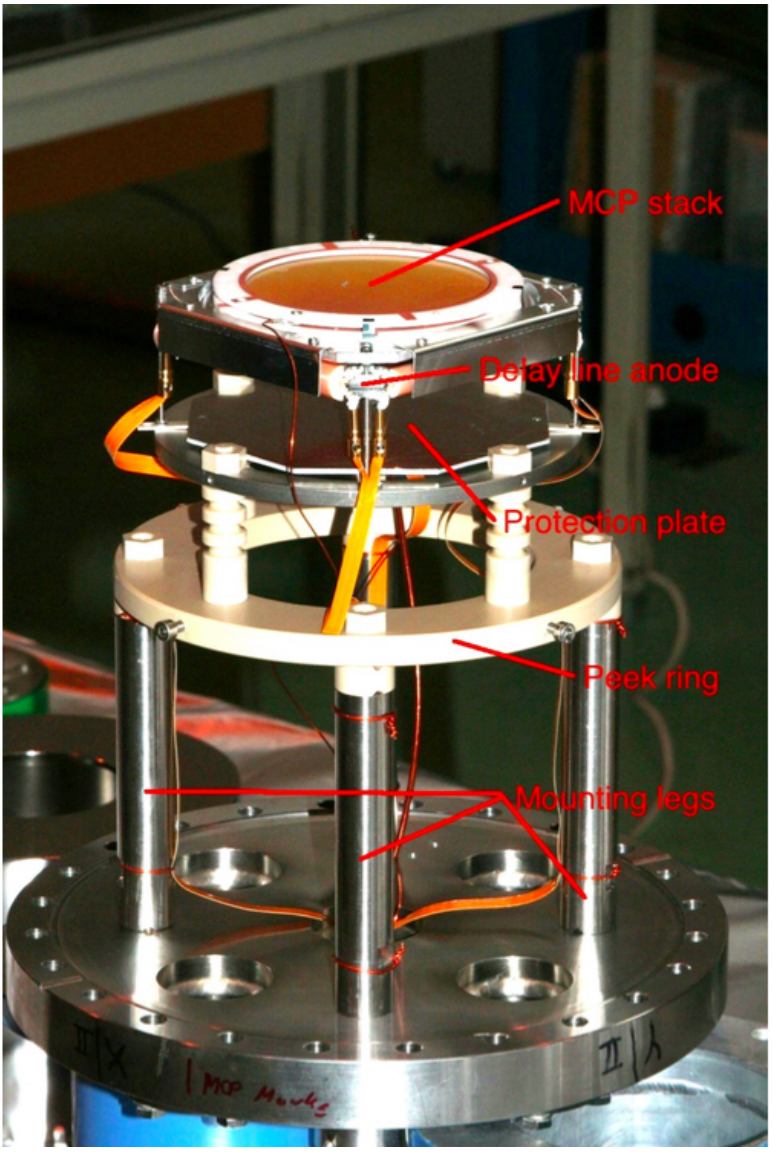


Figure 5.3: The layout of the complete MCP detector setup (without the cylindrical electrode SPDRIF02 enclosing it). From [41].

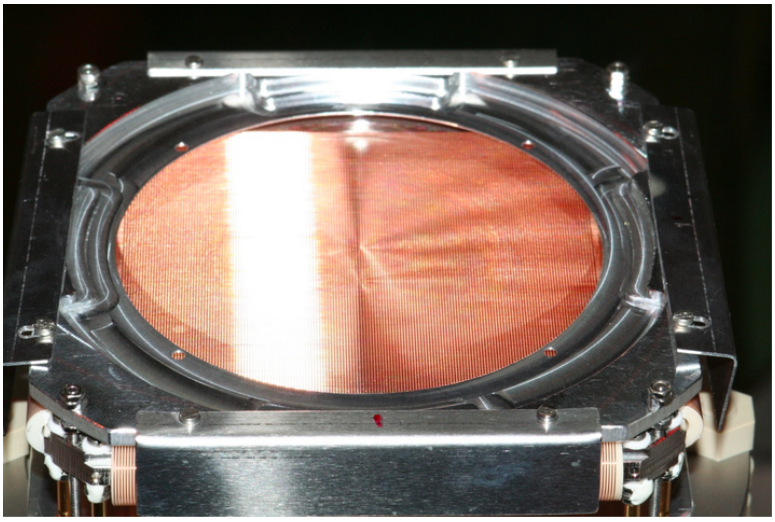


Figure 5.4: The copper delay lines with the mounting plate for the MCPs. From [41].

The delay line anode

Two coils wound around a plastic holder with a metal core comprise the delay line anode (see Figure 5.4). One of the coils provides the X direction position of the microchannel that ignited, while the other provides the Y direction position information. Furthermore, each coil has two wires pitched at 0.5 mm, the *Signal* and the *Reference*. The *Signal* is at a slightly higher potential than *Reference* (+37.5 V), attracting more electrons created by an event, while the *Reference* wire picks up the common noise that is later subtracted from the *Signal*. The electron avalanche that hits the wires creates signals which are recorded at all 4 ends of the delay line wires (X1, X2, Y1, Y2). Since the total travel time for each line is known (see Table 5.2), the position of the hit can be reconstructed from the time differences X2 – X1 and Y2 – Y1 (see Figure 5.6).

The delay line system is very prone to shortcuts between the X and Y or *Signal* and *Reference* wires due to conductive impurities, and very careful handling is essential.

Biasing voltage

The high voltage for the MCP detector is supplied by a CAEN 570N unit connected to a voltage divider (Figure 5.5) that creates the different potentials

Axis	Position	R/Ω	Delay/ns
X	Inner delay line	13.0	90
Y	Outer delay line	13.3	90

Table 5.2: Position, full resistance across the wires and the time necessary for a signal to traverse the wires of the delay lines system.

needed for the biasing of the MCP plates and signal readout. As marked on Figure 5.5, they consist of the *MCP front* and *MCP back* (the potential difference that biases the plates), *Holder* (the potential of the delay line holder), *Reference* (the potential of the delay line reference wires) and *Signal* (the potential of the delay line signal wires). All voltages are supplied through the Roentdek FT12TP box which contains a 10 kΩ protective resistor for *Front*, and 1 MΩ resistors for the other connections. The voltage divider is in a separate box, made in-house, and the resistances can be adjusted as necessary. For instance, the whole detector can be elevated to a higher potential by replacing the 1.2 MΩ resistor (see Figure 5.5) with a higher resistance. The constant potential difference between the *Signal* and *Reference* is created by a Roentdek BAT3 battery pack.

Typically, the detector operates within the following potential differences:

- -2100 V to -2600 V between *Front* and *Back*,
- -500 V to -300 V between *Back* and *Reference*,
- 0 V to -250 V between *Back* and *Holder*,
- -20 V to -50 V between *Reference* and *Signal*.

5.2.3 Signal processing

Raw signals from the MCP plates and the delay lines are first decoupled from the high bias voltage, amplified and sent to the data acquisition system (FASTER).

5.2.3.1 FASTER data-acquisition system

FASTER (Fast Acquisition System for nuclEar Research) [38] is a modular data acquisition system designed to fully replace NIM and CAMAC modules typically

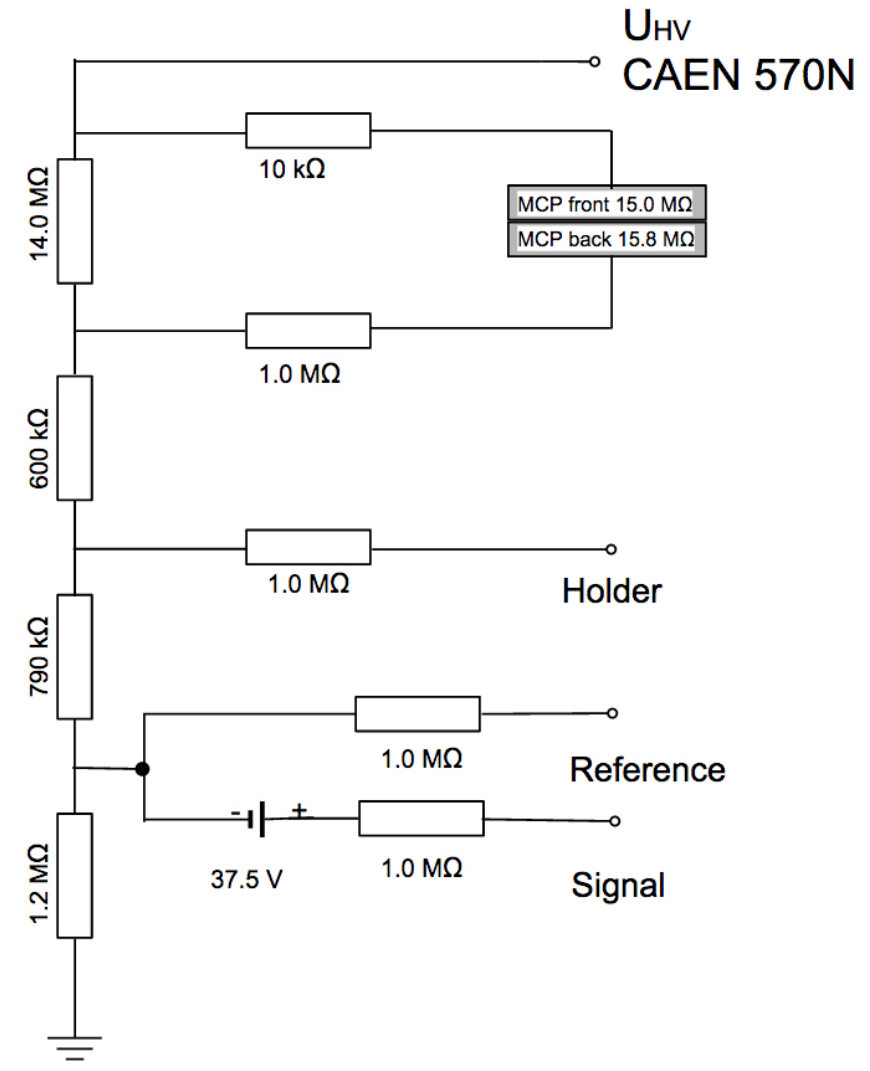


Figure 5.5: The schematics of the voltage divider and the FT12TP box for the MCP detector. The 1 MΩ (except *Front* that has 10 kΩ) protective resistances are contained in the FT12TP, while the voltage divider is in a separate box with exchangeable resistors, suited for e.g. placing the whole detector on a higher voltage by replacing the 1.2 MΩ resistor connected to the ground with a higher one.

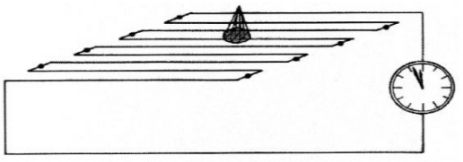


Figure 5.6: The working principle of the delay lines. From the time difference of the signal arrival on each end of a delay line, the position of the ion hit is reconstructed. From [4].

used for data acquisition in nuclear physics (e.g., discriminators, TDCs, QDCs and logic modules). The system is user-customizable and can operate with up to ~ 100 channels on modular logic boards.

Furthermore, it can operate without a trigger input, with all the data in the stream digitized and time-stamped. Raw data can be grouped into events on-the-fly with user-defined time windows or coincidence criteria.

TDC/QDC module

Time and charge measurements (TDC/QDC) are executed on modular CARAS daughter cards which digitize the signal and process it fully on-board [38]. After digitization, the signal is timestamped, discriminated and the charge integrated, yielding time and charge information. The digitization is performed on a 12-bit 500 MHz analog-to-digital converter, with a time-stamp accuracy of 2 ns. However, in ToF measurements the resolution of the time difference between two signals can be down to 7.8 ps, depending on the signal height. The TDC/QDC module (see Figure 5.7) integrates several components that replace standard NIM/CAMAC modules:

- event counter,
- charge integrator,
- trigger module with threshold and constant fraction discriminators,
- oscilloscope,
- baseline restoring,
- dynamic range tuning,
- polarity tuning.

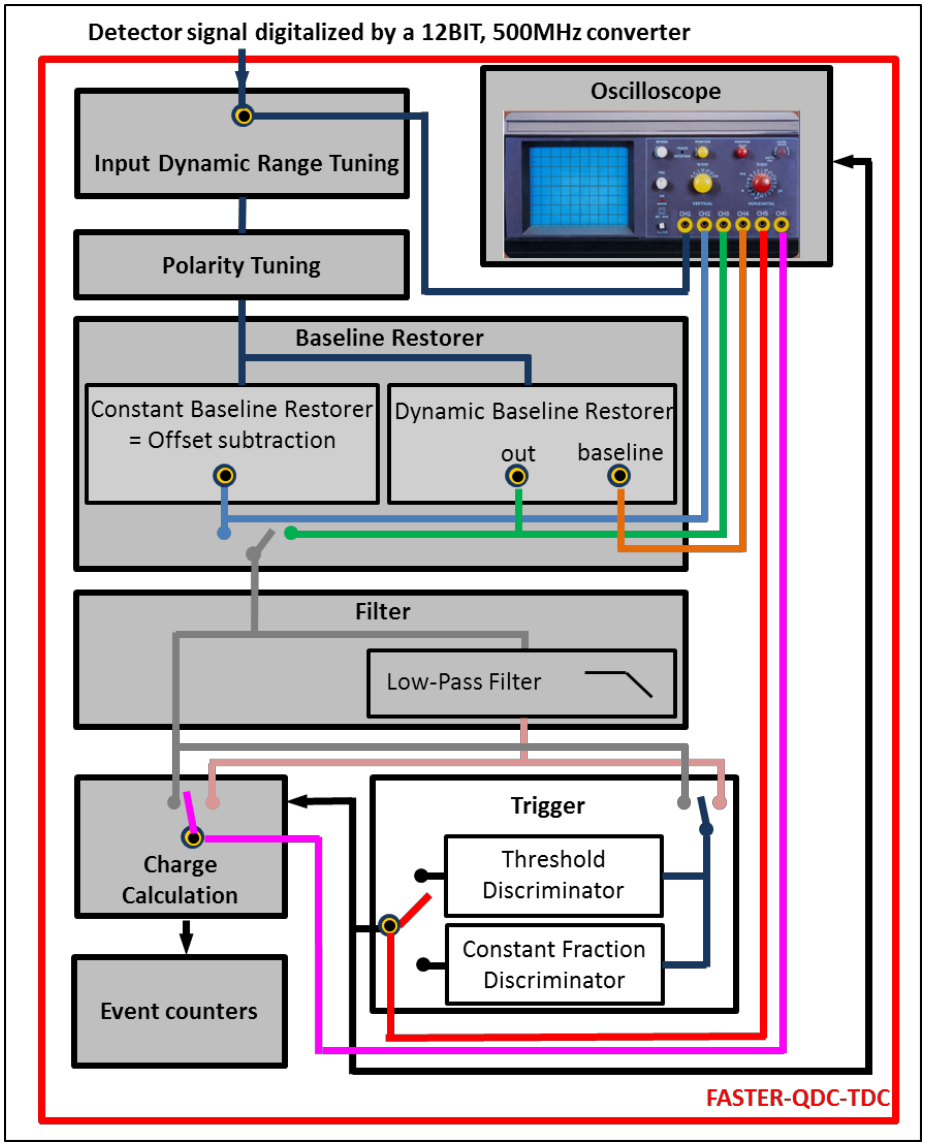


Figure 5.7: Diagram of the on-board processing of a detector signal in the FASTER TDC/QDC module. From [38].

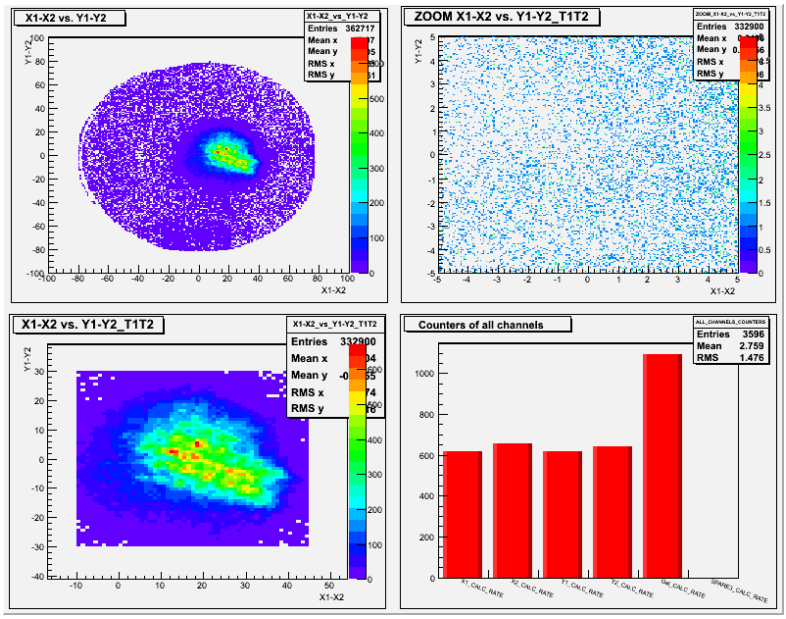


Figure 5.8: ROOT Histogram Builder window showing the histograms of events from the entire MCP surface (upper left), two surface cuts (upper right and lower left) and counters for individual delay lines. It can be used for online data monitoring and analysis with the FASTER data acquisition system.

ROOT Histogram Builder

ROOT Histogram Builder (RHB) [5] is an application compatible with CERN's ROOT framework. It can be used in combination with the FASTER data acquisition system for online visualization and histogramming of the data stream (see Figure 5.8).

5.2.3.2 Main signal

The voltage pulse created by the charge collected after the amplification process in the microchannels can be read out either at the front of the MCP or the back. After decoupling the main MCP signal from the biasing high voltage with a 1 nF capacitor [4], it is processed by Roentdek proprietary electronics. The details of the processing and the electronic schematics are witheld by the

Radiation type	Energy range/keV	Max. detection efficiency/%
Ions	0.5 – 2	47
(H^+, He^+, Ar^+)	2 – 50	47
	50 – 200	33
electrons	0.2 – 2	47
	2 – 50	33

Table 5.3: Maximum nominal detection efficiency for ions and electrons in different energy ranges for the WITCH MCP detector [41].

manufacturer. Subsequently, the signal is amplified by the Roentdek FAMP1+ preamplifier with a gain of 60 and sent to the FASTER data acquisition system.

5.2.3.3 Delay line signals

The 8 signal and reference delay lines are decoupled from the biasing high voltage by an array of four 1 nF capacitors and 1.2 MΩ resistors. The noise is reduced by subtracting the reference from the signal by a pulse transformer (see [41] for technical details). This is accomplished in a RoendTek proprietary electronic box FT12TP situated close to the detector, but outside the vacuum chamber. The processed signals are amplified by a factor of 100 in a LeCroy 612 A 12 channel amplifier and then fed into the data acquisition system.

5.3 Efficiency of the microchannel plates

The efficiency of MCP detectors depends on the properties of the impinging radiation and of the microchannel plates. The former is given by the type, energy and the angle of incidence of the particle (see Table 5.3), while the latter is given by the geometrical open area, the biasing potential and the quality of the MCPs [39]. The MCPs are typically capable of producing a constant amount of charge during their lifetime [4], with the efficiency decreasing towards the end of their lifetime. However, it is well known that the detection efficiency of the MCPs saturates and becomes independent on the ion mass, energy or charge above a few keV if the electronic threshold is set to a sufficiently low value [69].

5.4 Efficiency measurement technique

Several measurement techniques have been implemented in the past with the goal of measuring the MCP detection efficiency for ions. These include the photoelectron-photoion coincidence [78], the discontinuous Faraday cup calibration and the continuous calibration [69]. They can be employed for either absolute or relative efficiency measurements. The first method allows the measurement of absolute MCP efficiency by photo-ionization of atoms and their detection in coincidence with the corresponding electrons, without requiring the knowledge of absolute beam intensity incident on the MCP. The other two methods quantify the absolute ion current arriving at the MCP, either by switching the beam between the MCP detector and a Faraday cup or by using a transparent grid and a continuous beam.

In the latter case (presented in [69]), a collimated ion source is directed towards a MCP. As shown on Figure 5.9, transparent metallic grid is placed between them in order to monitor the absolute ion current arriving at the MCP. Alkali ion sources ($^6Li^+$ and $^{23}Na^+$) were used to produce 1^+ ions with variable energy in the range 500 – 3500 eV. The beam is collimated by an opening (C) with a 4 mm diameter. A monitoring grid (MG) with 10% transparency is placed between two 90% transmission grids in order to insulate the MG from the surroundings. Further downstream, two 10% transmission grids (A) are placed, attenuating the current in order to avoid saturation effects and damage to the MCP. Another 90% transmission grid is placed in front of the MCP to create a uniform post-acceleration field that enhances the transport of ions, especially below 1 keV. The incident energy of the ions was scanned between 500 eV and 3500 eV by adjusting the potential on the front plate of the MCP detector. Simultaneously, the current on the grid was monitored in order to obtain the current required for normalization of MCP counts, i.e. to compare relative efficiencies for different ion energies. However, since the ions hitting the grid cause secondary electron emission, this procedure still does not result in absolute efficiency dependence on ion energy. For that purpose, after each scan of the potential, the relation between the current on the grid and the Faraday cup is measured, providing an estimate of the real ion beam current in dependence on the grid current. The absolute efficiency was found to saturate at $\sim$ 2500 – 3000 eV for $^6Li^+$ and $\sim$ 3000 – 3500 eV for $^{23}Na^+$, at $\epsilon_{abs} = (52.3 \pm 0.3)\%$ (see [69] for more details).

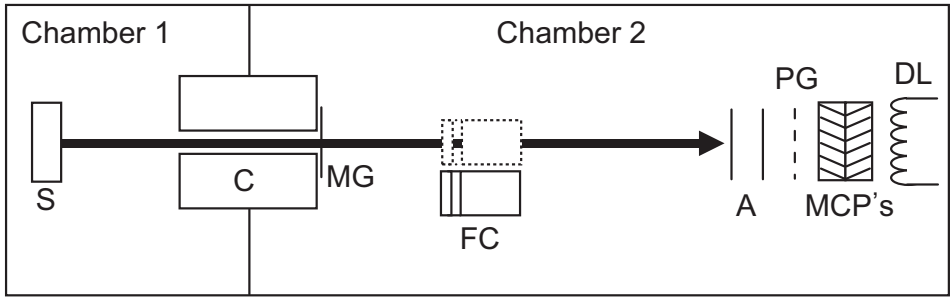


Figure 5.9: The schematic overview of the LPC Caen setup for MCP detector calibration. Source (S), collimator (C), monitoring grid (MG), movable Faraday cup (FC), attenuators (A), post-acceleration grid, and the MCP with delay lines (DL) are shown. Figure from [69].

5.5 Motivation

The measurements of the MCP efficiency dependence on the ion energy presented in this work were performed at the LPC Caen in November 2013 and February 2014, following the principle laid out in the previous section, albeit with a slightly modified setup. The motivation for a precise characterization of the efficiency arose when it was realized the MCP detector wasn't performing as expected during the online experiment in November 2012. Specifically, the pulse height distribution (PHD) of the ion events had a skewed Gaussian appearance, while for a properly working MCP a Gaussian distribution is expected. Similar pulse height distributions were found in [69] in combination with reduced detection efficiency for ions of energies below about 3 keV, while at higher energies, the efficiency reached a plateau and the PHD distribution became Gaussian [69]. Furthermore, the retardation spectrum of ^{35}Ar was consistent with a reduced efficiency at low energies, i.e. for the 1^+ charge state (see Chapter 6). While the energy of WITCH ions is around 3 keV for the 1^+ and around 6 keV for the 2^+ charge state of the ^{35}Cl daughter ions, it is probable that any damage (e.g. caused by a previous calibration with an alpha source, reported in [41]) could shift the efficiency plateau of the MCP detector towards higher energies. A 40 kBq ^{241}Am source was used, with α-particle energy of about 5.5 MeV. A total of $\sim 7.5 \times 10^7$ particles from this source were recorded during the calibration measurements in 2012 [41]. A mask was used in front of the MCP in these measurements. The mask pattern can clearly be seen in all later measurements (Figure 5.11), which is explained as further evidence of the extensive radiation damage caused by the α-particles.

That would cause a greatly reduced efficiency for 1^+ ^{35}Ar daughter ions in comparison with 2^+ and higher charge states, which would then lead to a distorted β-decay retardation spectrum. With the purpose of investigating the magnitude of this effect, relative efficiency of the WITCH MCP detector was measured for different energies of the impinging ions.

5.6 Experimental setup

The setup consisted of a cross-shaped vacuum chamber with the WITCH MCP and an ion source (IS) on opposite sides. The chamber was evacuated by a turbomolecular pump connected to a prevacuum scroll pump. A full range vacuum gauge was installed to monitor the vacuum conditions (with the typical pressure suitable for operation of $\sim 10^{-7}$mbar). However, the gauge was turned off during measurement, since it creates large amounts of background ionization.

The ion source stack (Figure 5.10) consists of an exchangeable heat activated pellet that produces positive alkali (^{6}Li, ^{23}Na and ^{85}Rb) ions and electrostatic elements for beam manipulation. The IS is put on a high positive voltage (1.7 – 2.7 kV) to accelerate the ions, with three steering electrodes available for moving the beam spot across the MCP surface and one lens electrode for focusing. The ion source stack is also fitted with an attenuating grid (of a factor of 10^4) to reduce the beam intensity from a few pA to around a few kHz of event frequency before it reaches the MCP, in order to avoid saturation and damage to the MCP. The grid (also used to measure the beam current or the total charge collected) is enclosed by a transparent Faraday cup-like device that captures most of the secondary electrons. The device resembles a true Faraday cup, with the exception of a central opening on the top to allow beam passage. However, this opening can also let some of the secondary electrons released by the grid escape, causing a systematic error in current readings. For this reason, only relative efficiencies can be extracted from the data with sufficient accuracy.

The total charge collected on the monitoring grid is measured by a Keithley System Electrometer in Coulomb measurement mode. A five-channel FASTER system is used for reading out the main MCP signal (acquired from the back plate) and the four delay lines which provide position information. The MCP voltage divider (see Figure 5.5) was modified to allow independent setting of the front and back plate voltages while keeping voltage over the plates constant at 3150 V. This allowed changing the ion energy while keeping the ion source acceleration voltage constant. Since the secondary emission properties depend on the ion source energy, it is advantageous to keep the ion source on a constant voltage of 2.7 kV while adjusting the ion energy via the MCP front plate. This

reduces the variation of secondary electron emission intensity and results in a more reliable normalization. The ion source potential is kept constant for most of the measurements, with the exception of some additional measurements with the source at 1.7 kV to access the low energy efficiency behavior of the MCP.

Although the absolute charge and therefore the absolute efficiency cannot be measured with sufficient accuracy because of systematic effects caused by the systematic error in the charge measurement, for constant source properties this introduces merely a constant offset, and is therefore a suitable approach for calculating relative efficiencies.

5.7 Experimental procedure

The measurements were performed in pairs for each ion energy, a principal measurement with the beam spot located consistently as in the online experiment (see Figure 5.11), and a measurement of the background, with the ion beam steered onto the edge of the MCP, well separated from the original beam spot position, since any overlap would make background subtraction difficult. The beam spot was focused within a radius of about 1 cm and the count rate kept at ~ 1 kHz in order to avoid saturation. The current on the grid, at this count rate, was typically ~ 1 pA and was controlled solely by the heating power of the ion source filament.

The front plate was varied in the range from 0 to -4 kV, while the IS acceleration was fixed at 2.7 kV or 1.7 kV, resulting in total ion energies ranging from 1.7 keV to 6.7 keV. The measurements were performed in series, with energies scanned from 3.1 keV to 6.7 keV in steps of 300 eV for each ion species and with the IS at 2.7 kV. Additional measurements were performed in 1.8 – 3.4 keV range with the IS at 1.7 kV. The purpose of these was to determine the efficiency curve at very low energies and verify its conformity with the high energy efficiency curve. Each of the measurement series was repeated twice to verify reproducibility. In addition to efficiency measurements, linearity of the charge collected at the grid with the number of counts recorded by the FASTER DAQ was tested. For this purpose, the ion source intensity was varied while all other parameters remained constant.

Ion species used in these measurements consist of $^{6}Li^{+}$, $^{23}Na^{+}$ and $^{85}Rb^{+}$. $^{39}K^{+}$, the most suitable replacement for ^{35}Ar, was not available at the time.

Data acquisition

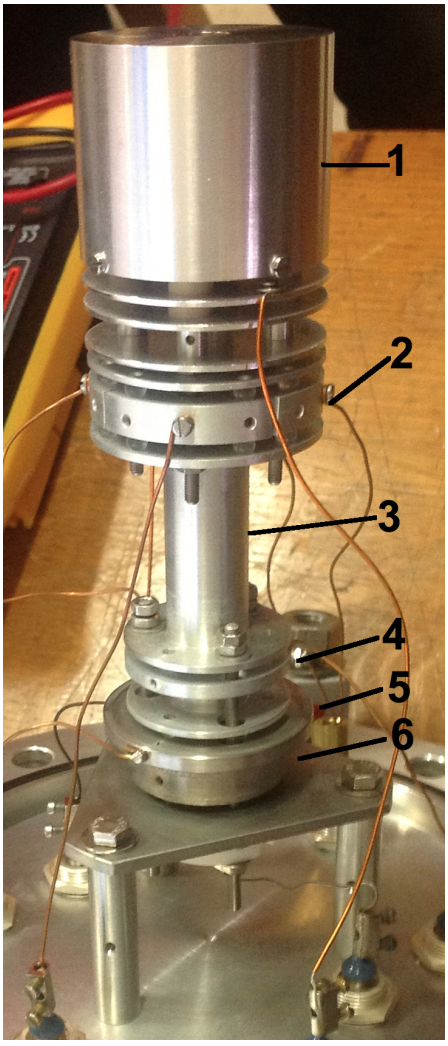


Figure 5.10: The ion source stack. Faraday cup with an opening on top (1), beam steering electrodes (2), drift electrode (3), electrostatic lens (4), extraction electrode (5) and ion source heater (6) are shown. The attenuating grid (see text for details) is situated inside the Faraday cup.

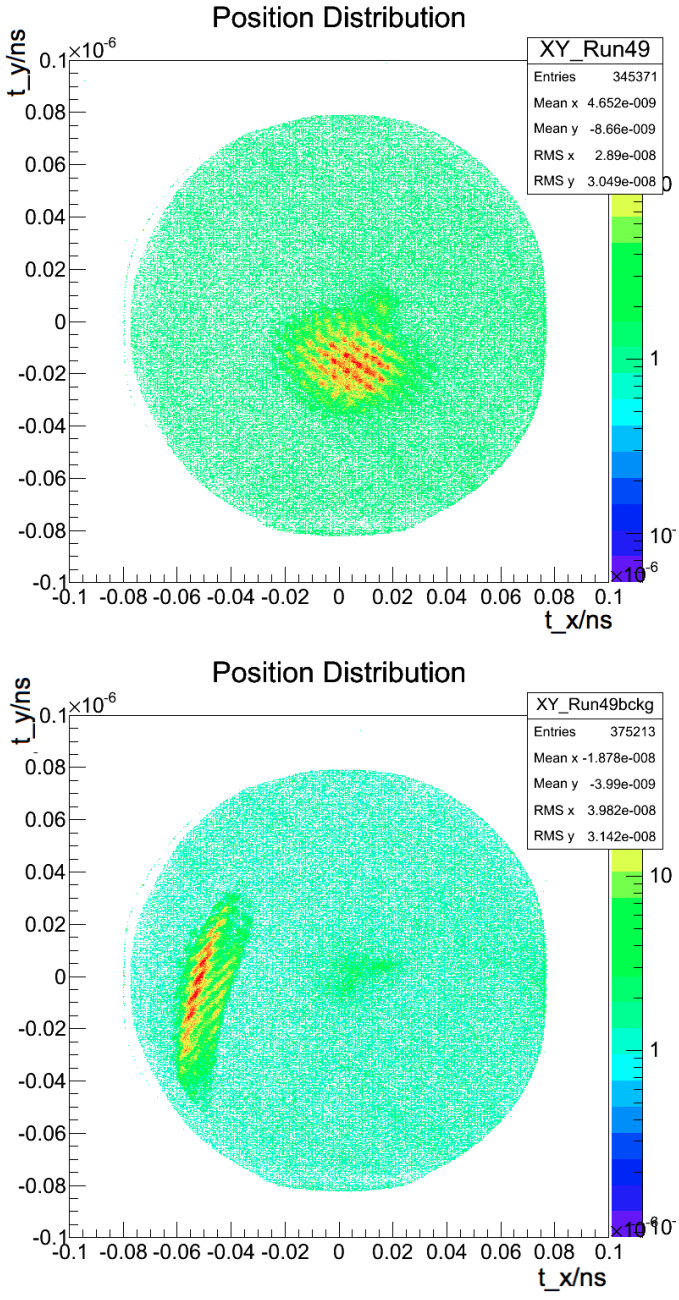


Figure 5.11: (**top**) The 2D histogram of a measurement with the beam spot at the standard position (see text for details). (**bottom**) Histogram of a background measurement with the beam spot at the edge of the MCP. The axes show the time difference from the delay lines.

Runs	Energy range/eV	Scan step/eV	IS pot./V	MCP Front	Ion spec.
3 – 12	3000→6500	500	2500	-500→-4000	^{23}Na
17 – 23	3500→6500	500	2500	-1000→-4000	^{23}Na
24 – 32	3900→4300	50	2500	-1400→-1800	^{23}Na
41 – 53	3100→6700	300	2700	-400→-4000	^{23}Na
54 – 58	1800→3400	300,500	1700	-100→-1700	^{23}Na
59 – 63	1800→3400	300,500	1700	-100→-1700	^{23}Na
64 – 76	3100→6700	300	2700	-400→-4000	^{23}Na
86 – 98	3100→6700	300	2700	-400→-4000	^{85}Rb
99 – 103	2000→3400	300	1700	-600→-1700	^{85}Rb
104 – 108	2000→3400	300	1700	-600→-1700	^{85}Rb
109 – 121	3100→6700	300	2700	-400→-4000	^{85}Rb
109 – 121	3100→6700	300	2700	-400→-4000	^{85}Rb
142 – 154	3100→6700	300	2700	-400→-4000	^{6}Li
155 – 159	1800→3400	500	1700	-100→-1700	^{6}Li
160 – 172	3100→6700	300	2700	-400→-4000	^{6}Li
173 – 177	1800→3400	500	1700	-100→-1700	^{6}Li

Table 5.4: List of all energy scans and their parameters. Run numbers, energy range and step size of the scan, the acceleration potential of the ion source, the voltage range of the MCP's front side and the ion species are listed, respectively.

The data was acquired by the FASTER system (see Section 5.2.3.1 for configuration details) and consisted of:

- the timing data of the main MCP signal and the 2 delay lines, with 4 delay line signals (t_{x1}, t_{x2}, t_{y1}, t_{y2}) that provide the position data ($t_{x1} - t_{x2}$, $t_{y1} - t_{y2}$),
- the pulse height data for the main signal and 4 delay line signals.

The electronic threshold was set at the same very low value as in the online experiment (5mV). The data stream was subsequently grouped into events and formatted as a ROOT tree, for easier analysis and visualization.

5.8 Analysis

In this section first the linearity between the total integrated charge on the monitoring grid and the number of counts on the MCP detector will be checked, for all ion species used and for the different settings of the ion source and the detector voltages. Thereafter, the measurements of the energy-dependent MCP detection efficiency for the different ion species and settings will be presented.

5.8.1 Linearity of the charge normalization

Runs	Charge/nC	Current/pA	IS Accel./V	MCP pot./V	Ion species
33 – 40	0.14→5.3	0.2→4.2	2700	-4000	^{23}Na
77 – 78	3.1→4.1	5.2→6.8	2700	-4000	^{23}Na
79 – 85	0.35→3.6	0.5→5.7	1700	-4000	^{23}Na
122 – 129	0.11→3.3	0.4→10.0	2700	-4000	^{85}Rb
130 – 134	0.28→3.1	1.0→10.0	1700	-4000	^{85}Rb
135 – 141	0.14→3.7	0.4→10.0	2700	0	^{85}Rb
178 – 182	0.21→3.4	0.7→10.0	1700	-4000	^{6}Li
183 – 189	0.08→3.0	0.2→9.8	2700	-4000	^{6}Li
190 – 195	0.26→3.0	0.8→10.1	2700	-3000	^{6}Li
196 – 199	0.29→1.6	1.0→5.3	2700	0	^{6}Li

Table 5.5: List of the measurements of total collected charge on the grid/FC vs. the corresponding MCP counts, i.e. the tests of charge normalization data.

Both the beam spot ion counts and the corresponding background ion counts on the MCP are normalized by the total integrated charge on the monitoring grid. Therefore, it is essential to verify that in both cases the charge and the number of counts have a linear relationship, since a departure from linearity can be caused by MCP dead time effects or other mechanisms of ion loss between the grid and the MCP and impair the accuracy of the normalization. The linearity of the total charge with the total number of counts on the MCP was measured along with each series of efficiency measurements. The charge is integrated over a period of 5 minutes in each case, i.e. a large total charge corresponds to a high current on the grid and high MCP count rates. This procedure was repeated for a very broad range of ion source currents, typically from below 0.5 pA to around 10 pA and for both ion source acceleration voltages, 1.7 kV and

2.7 kV. A full list of measurements is in Table 5.5. Results will be discussed below for each of the ion species used. The error on the measured values was estimated from the precision of the electrometer and the expected statistical fluctuation of the MCP counts. In some cases, the deviation of the points from the linear fit exceeds the expected error; this is most likely due to transient background of ions or neutral particles that is difficult to quantify.

The variation of the total charge collected on the grid during the measurements is shown on Figure 5.12. Although in some cases the charge changes significantly from run to run, fluctuations between beam spot and corresponding background measurements are around 0.1 nC, i.e. well within the linear regime. However, the variation between measurements that are not consecutive is up to 1 nC, indicating that the emission of the ion source fluctuates significantly even with constant heating power.

^{23}Na

Figure 5.13 shows the linearity measurements for ^{23}Na ions with the ion source at 1.7 kV and 2.7 kV acceleration potential, respectively. In the latter case, the dependence conforms well with expectations. The curve is linear for low charges and deviating slightly for very high charges. In the region used in the efficiency measurements ($\sim$ 1 nC), the dependence is linear. For the 1.7 kV at the IS case, normalization seems less reliable. The curve is shifted by about -0.7 nC on the vertical axis, and seems to be more parabolic. This shift could be caused by an excess of neutrals, or by ionization created between the grid/FC and the MCP. In both cases, the reduced χ^2 value of the fit (~ 5) shows that the error bars, estimated from the accuracy of the electrometer and MCP count statistics, are much too small. Enlarging the error bars by a factor of 5–10 results in a good fit ($\chi^2/\nu \sim 1$), while still providing precision sufficient to ensure linearity.

A significant source of uncertainty can be a variable background including a significant number of neutral particles. Furthermore, it is notable that the linear dependence is less steep for 2.7 kV acceleration potential (i.e. $\sim 5 \cdot 10^{-6}$ vs. $\sim 9 \cdot 10^{-6}$ slope). This is most probably caused by a difference in the amount of secondary electrons that are emitted from the grid and escape through the opening on the Faraday cup at 2.7 kV compared to the 1.7 kV case.

Even with these small inconsistencies, it can be concluded that the dependence is sufficiently linear within short intervals, enabling the use of integrated charge for normalization of the MCP counts.

^{85}Rb

The charge normalization linearity test was performed in the same way as

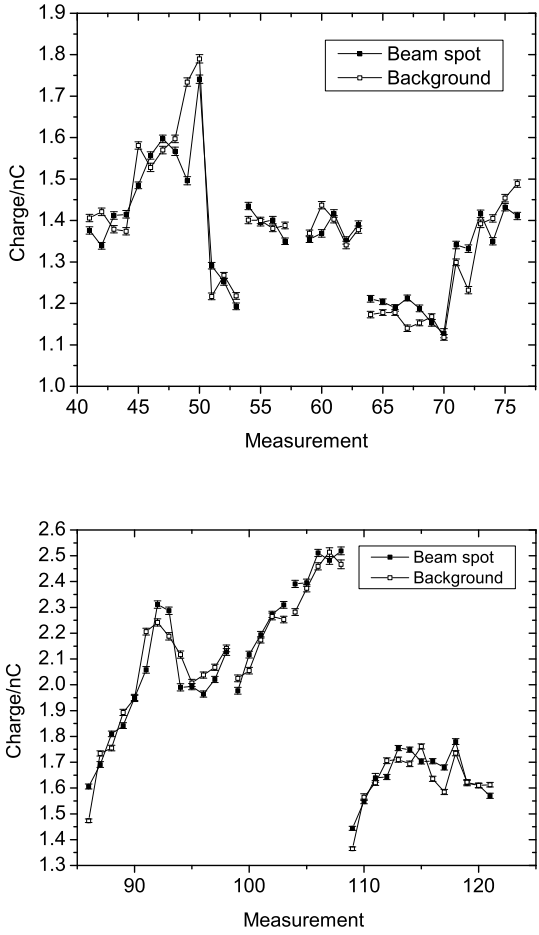


Figure 5.12: Total charge collected on the grid for each beam spot measurement (solid squares) and background measurement (open squares) with measurement numbers from Table 5.4 and 5.5. The top plot shows the charge for ^{23}Na, the bottom plot for ^{85}Rb ions. The variation between the beam spot and the respective background measurements is typically less than 0.1 nC. See Table 5.4 and Table 5.5 for the parameters of each measurement.

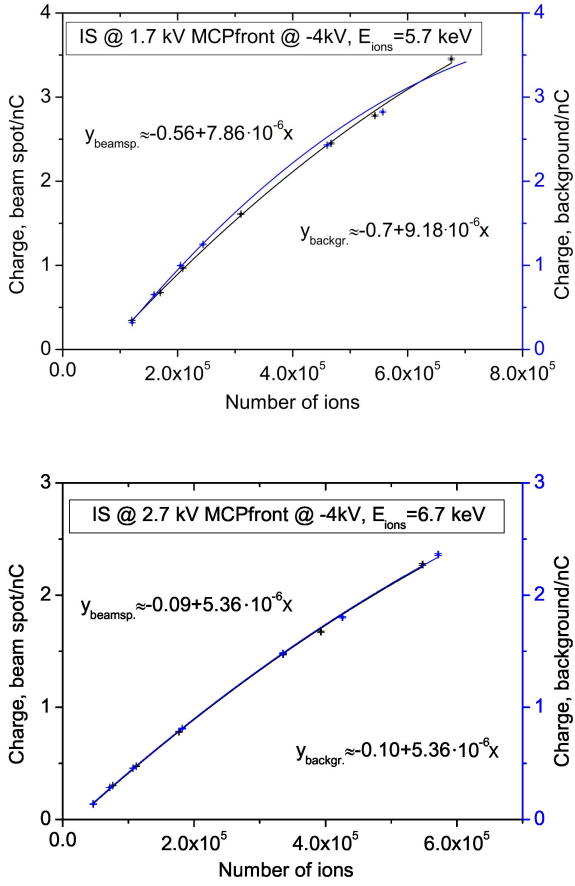


Figure 5.13: The dependence of the number of ^{23}Na ions counted by the MCP detector and the total charge collected on the grid/Faraday cup (see text for details). (**top**) Ion source at 1.7 kV, with the total ion energy equal to 5.7 keV. (**bottom**) IS at 2.7 kV, with the total ion energy equal to 6.7 keV

in the ^{23}Na case. In addition to measurements with the ion source at 1.7 kV and 2.7 kV, in both cases with the front plate of the MCP at 4 kV, a measurement with the front plate of the MCP at 0 V potential was performed. With the IS set to 1.7 kV acceleration potential and the MCP front to -4 kV (Figure 5.14, top panel), the slope in the background measurement is slightly steeper than the beam spot slope (9.09×10^{-6} vs. 8.16×10^{-6}). Very similar behavior is

observed for the ^{23}Na case and is probably caused by the loss of ions occurring when the beam is steered close to the MCP's rim for background measurements. With the IS set to 2.7 kV and the MCP front to -4 kV (Figure 5.14, bottom panel), this difference is smaller (as is in the corresponding ^{23}Na measurement), probably due to different focusing for the two different IS acceleration voltages.

In the third case, with the IS at 2.7 kV and front plate at 0 V (Figure 5.15), significantly more scatter of the points around the fitted line is present, but the dependence remains linear. Both beam spot and background plots are less steep than in previous cases, i.e. for the same amount of charge on the normalization device, a lot more counts are recorded on the MCP.

This may be caused by an excess of electrons coming from the grid/FC, which are normally repelled when the MCP front plate is set to -4 kV, but are unhindered when the potential is 0 V. This effect indicates that the normalization is not accurate in the absolute sense, but can nevertheless be used for relative normalization of consecutive beam spot and background measurements.

^{6}Li

The charge normalization linearity for the ^{6}Li ion source was tested using the same method as in the cases of ^{23}Na and ^{85}Rb. Both 1.7 kV and 2.7 kV ion source acceleration potentials exhibit linear dependence within error bars. With the ion source at 1.7 kV (Figure 5.16, bottom), the slope is slightly different for beam spot and background measurements, which is again probably due to ion losses off the MCP's rim.

It can be concluded that for all 3 ion species (^{6}Li, ^{23}Na and ^{85}Rb) the relation of the collected charge and the number of ions is sufficiently linear to allow normalization of consecutive beam spot and background measurements. However, there are small discrepancies caused by the charge collection grid, most likely due to secondary electron emission.

5.8.2 MCP detection efficiency

In this section, the data pertinent to the energy dependence of the MCP detector efficiency is discussed. The energy of ^{6}Li, ^{23}Na and ^{85}Rb ions was scanned in two phases. The first phase included the energy range of 1.8 – 3.4 keV with the ion source at 1.7 kV, while the second was in the 3.1 – 6.7 keV range with the source at 2.7 kV. The full range of scans was then immediately repeated to verify reproducibility. The 2D histograms for the beam spot and the background measurements containing position data were constructed and normalized with respect to the total charge collected on the grid. A cut was made on the

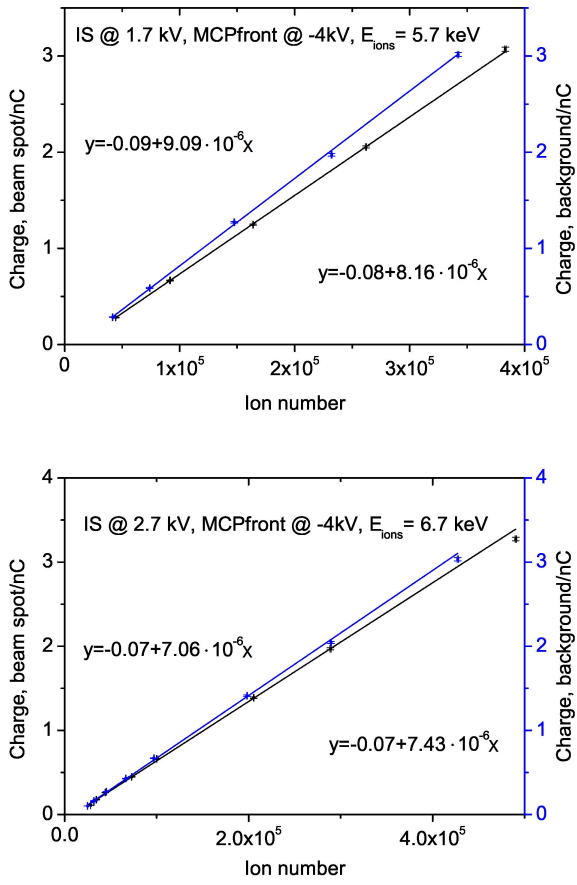


Figure 5.14: Dependence between the number of ^{85}Rb ions counted by the MCP detector and the total charge collected on the grid/Faraday cup (see text for details). (**top**) Ion source at 1.7 kV, with the total ion energy equal to 5.7 keV. (**bottom**) IS at 2.7 kV, with the total ion energy equal to 6.7 keV

beam spot position and the respective cut of the background was subtracted from the measurement with the ions focused on the beam spot position (see Figure 5.17). The background (Figure 5.17, bottom left) contains ions as well as neutral particles originating from the ion source that are not affected by the electrostatic steering elements.

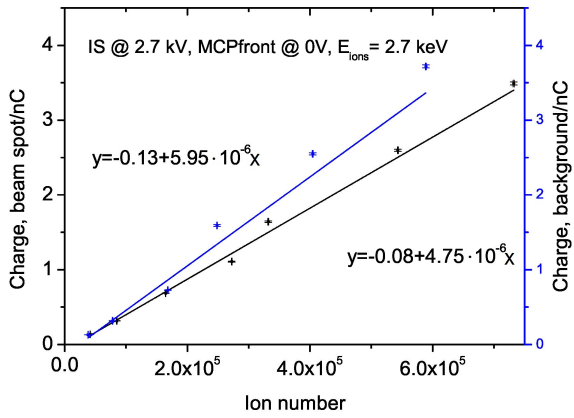


Figure 5.15: Dependence between the number of ^{85}Rb ions counted by the MCP detector and the total charge collected on the grid/Faraday cup with the IS acceleration potential set to 2.7 kV and the front plate of the MCP to 0 V (see text for details).

^{23}Na

Figure 5.18 shows normalized, background subtracted ion intensities in the designated beam spot, which is used to directly compare the MCP detector efficiency at different ion energies. The two phases of measurement (1.7 kV and 2.7 kV at the ion source) are shown. The error bars are propagated from the statistical fluctuation of MCP counts and the precision of the electrometer. The scatter of the higher energy points, where efficiency saturation is reached, slightly exceeds the error bars, indicating that other sources of error are present, most likely transient background not accounted for by subtraction. In the region significant for the 1^+ charge state (3 – 3.5 kV), three overlapping series of measurements (two with IS at 1.7 kV and one with IS at 2.7 kV) are in good agreement. However, the fourth (with the source at 2.7 kV potential) is systematically below. This points to systematically different levels of background ionization in the region behind the grid/Faraday cup or a difference in the neutral background. The cause is likely to be the instability of the ion source. From the two energy scans with data above 4 keV, it can be concluded that the efficiency reaches a plateau at ~ 4.25 keV, a significantly higher value than ~ 3 kV found in [69]. The series of 2.7 kV measurements that is consistent with both 1.7 kV series was selected for calculating the relative efficiency.

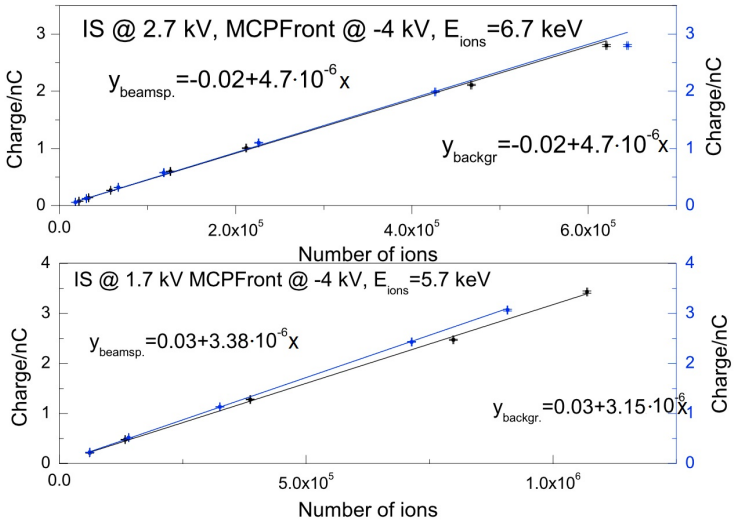


Figure 5.16: The dependence between the number of ^{6}Li ions counted by the MCP detector and the total charge collected on the grid/Faraday cup with the IS acceleration potential set to 2.7 kV and the front plate of the MCP to -4 kV V (see text for details).

We want to add here that the data in the 5.5 – 6.7 keV range is excluded from the analysis and the efficiency estimation because it exhibited a large degree of fluctuation around the saturation plateau. This behavior was also observed for ^{85}Rb and ^{6}Li at high ion energies and is most likely due to background ionization ignited by the ion source high voltage. For this reason, to estimate the relative efficiency it is probably better to use the average of the four points in the stable plateau interval from 4.25 to 5.5 keV. It can be then concluded that an about 10% efficiency decrease is seen for ^{23}Na in the 1^{+} charge state energy range (i.e. the energy region from 3.1 keV to 3.6 keV), with the efficiency plateau reached in the 2^{+} range (energy region from 6.2 keV to 6.7 keV).

^{85}Rb

As for ^{23}Na, the efficiency versus ion energy was scanned in two phases, first for 1.8 – 3.4 keV with the ion source at 1.7 kV, then for 3.1 – 6.7 keV with the source at 2.7 kV. All the scans were repeated to verify reproducibility. Again, one of the scans is consistently higher in intensity (Figure 5.19). It is likely that this is also caused by ionized background created between the grid/FC and the

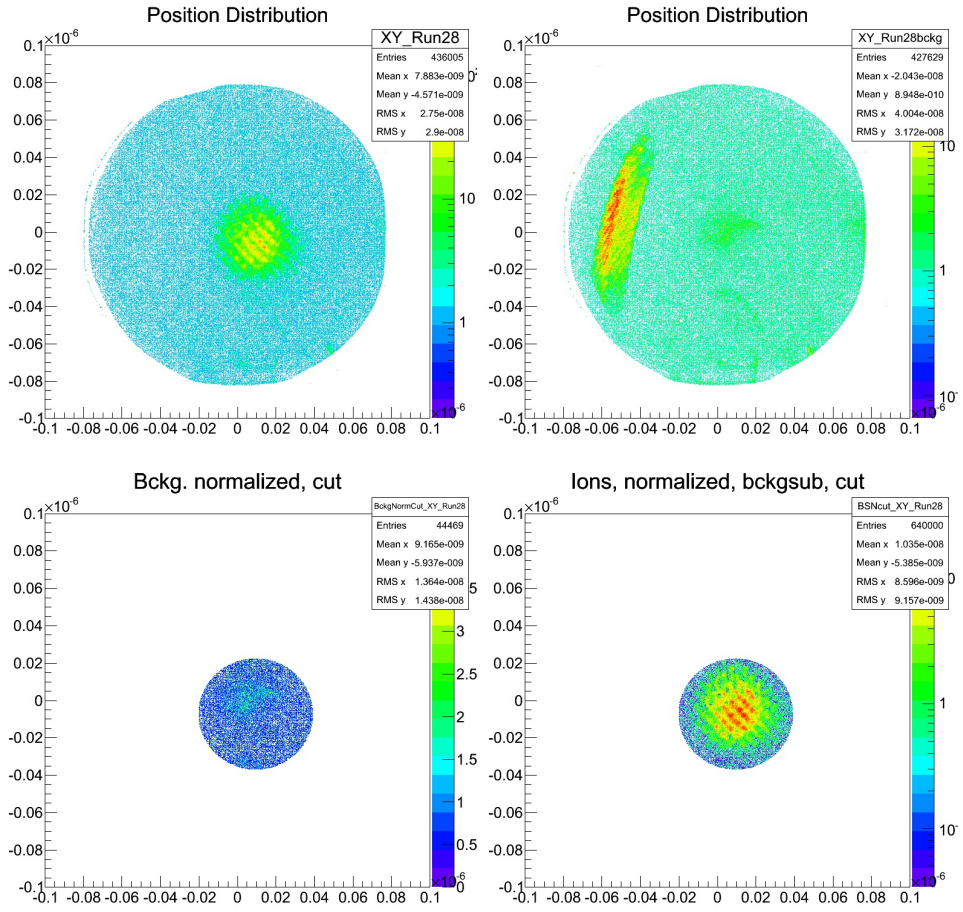


Figure 5.17: Overview of the background subtraction procedure. (**top left**) Measurement at the position of the beam spot in the online experiment. (**top right**) Measurement of the background. The ions are deflected to the MCP rim. (**bottom left**) A cut showing the background at the original beam spot position. A small peak of neutral atoms not affected by deflection is visible. (**bottom right**) The final histogram of the normalized beam spot with the background subtracted.

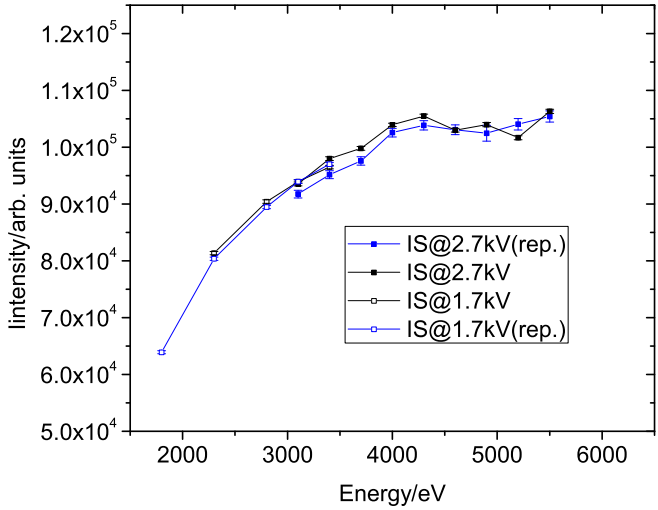


Figure 5.18: Normalized, background subtracted intensities in dependence with the ion energy for ^{23}Na. Two series of scans for each source potential are shown.

MCP or neutral atoms that do not contribute to the collected charge, but are detected by the MCP. The highest energy measurements again show significant fluctuations around the plateau and are excluded from analysis. However the points in the 4.5 keV – 5.5 keV interval exhibit a stable plateau. The average normalized background subtracted ion intensity of these points was therefore taken as reference for the relative efficiency calculation. The series of runs consistent with both 1.7 kV series is again selected for the relative efficiency estimation itself. In this case, the efficiency in the energy interval of the 1^+ charge state (i.e. the energy region from 3.1 keV to 3.6 keV) is 10 – 15% below the plateau, which is reached around 4.6 keV.

^{6}Li

The ion energy scans with ^{6}Li were conducted as for ^{23}Na and ^{85}Rb. Figure 5.20 shows the normalized, background subtracted intensities for all 4 energy scans. There seems to be a lot of fluctuation in the high-energy region this time, and the measurements with 1.7 kV ion source acceleration do, moreover, not transition smoothly to the 2.7 kV region, likely due to excessive background

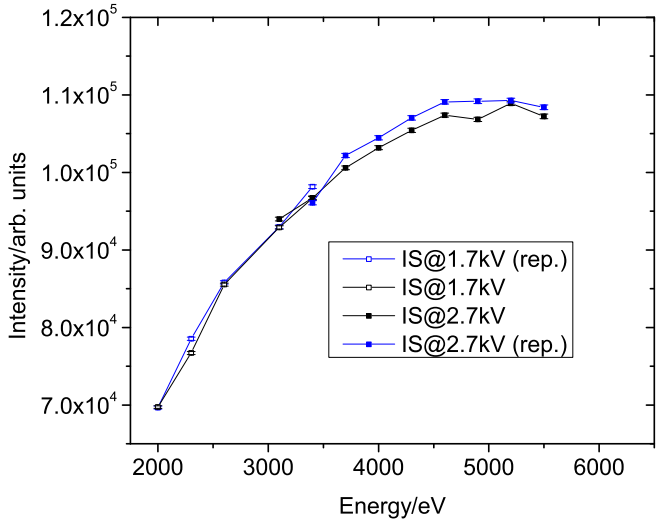


Figure 5.19: Normalized, background subtracted intensities in dependence with the ion energy for ^{85}Rb. Two series of scans for each source potential are shown.

ionization causing inaccurate charge normalization values. Furthermore, the difference between the two measurements is greater than for the other two ion species, which is attributed to the higher instability of the ion source. The efficiency plateau is difficult to determine due to fluctuations and inconsistency of the two measurements.

5.9 Pulse height distribution

MCPs detect impinging particles by multiplying the charge initially created on impact, via secondary electron production in the micro-channels. This secondary electron emission is the result of two processes: emission caused by the electric potential of the impinging particle and kinetic emission, a consequence of direct kinetic energy transfer. For velocities higher than 10^5 m/s (corresponding to $\sim$ 100 eV for ion masses considered here), kinetic emission is the dominant effect. Consequently, the secondary electron yield, and therefore the efficiency, increase with ion velocity. Their dependence is given by the Parilis-Kishinevskii

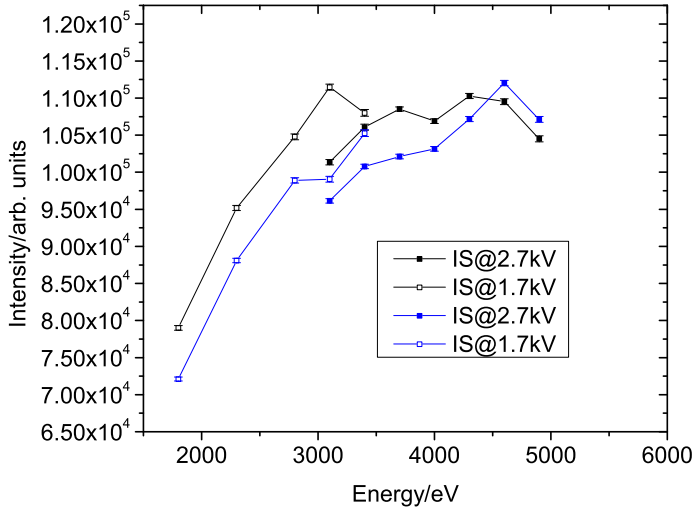


Figure 5.20: Normalized, background subtracted intensities versus the ion energy for ^{6}Li. Two series of scans for each source potential are shown.

relation [79]:

$$Y = a \times v \times tan^{-1}[b(v - v_0)], \tag{5.1}$$

where Y is the yield, a and b species-dependent coefficients, v the ion velocity and v_0 a threshold velocity. For $v \gg v_0$, the proportionality relation $Y \propto v$ is valid.

Assuming that mean QDC values (Figure 5.21) are directly proportional to the secondary electron yield, it is useful to observe their mean height in dependence with ion energy (Figure 5.22). It can be seen that the mean height of the QDC starts to rise linearly only beyond 5 keV for all ion species. However, the Equation 5.1 it is expected to be linear across the whole range because of relatively high velocities involved ($v \gg v_0$). Furthermore, at a given energy, the yield is expected to be higher for lower masses, which is not the case for ^{85}Rb. This unusual behavior can be a result of the damage caused to the micro channels by earlier tests with high-energy α-particles. Figure 5.21 is showing a skewed Gaussian shape of the pulse height distribution (PHD) of the main signal. Undamaged MCPs biased with the nominal bias voltage exhibit Gaussian PHD shapes in the case of ions. However, a skewed PHD shape is found to be present in all of the data discussed here, as well as the online data. The skewing on the

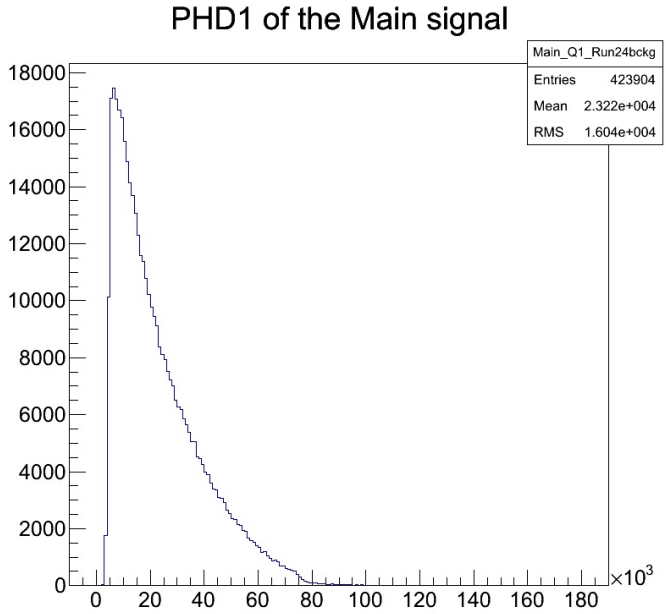


Figure 5.21: The main MCP signal QDC spectrum of a typical measurement.

low energy side of the curve is characteristic of an electronic threshold set too high or of the ion energy being below the MCP's efficiency plateau [69]. Since the threshold was set to a very low value (5 mV) in comparison with the average signal height, and the energy range was up to 6.7 kV, well above the efficiency plateau of a fully working MCP detector, this behavior is thus attributed to damaged microchannel plates. This hypothesis is supported by the mesh pattern of reduced efficiency within the beam spot seen on Figure 5.17 (bottom right), which corresponds to the metal mesh placed between an α-source and the MCP in a previous surface efficiency calibration [41].

5.10 Comparison between ion species

From Equation 5.1 it follows the MCP efficiency scales with ion velocity, i.e. the ratio of efficiencies for two ion species should be proportional to $\sqrt{\frac{M_2}{M_1}}$, where M_1 and M_2 are the masses of the species. The comparability of the absolute

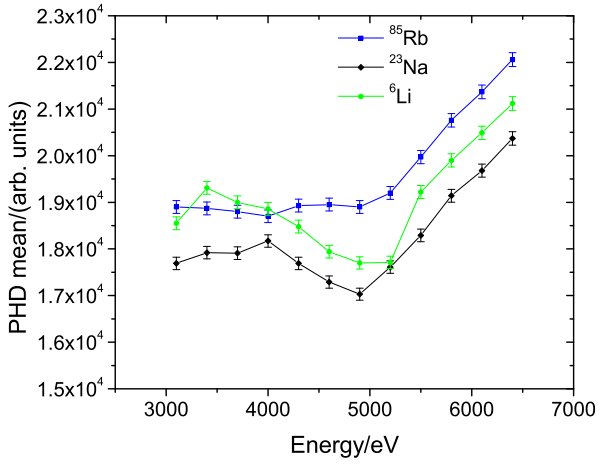


Figure 5.22: Mean pulse height distributions versus ion energy for all three ion species.

efficiency dependence shown on Figure 5.18 to Figure 5.19 is limited because of the difference of the neutral background levels in these cases. This is most likely due to intrinsic differences between the source pellets for ^{6}Li, ^{23}Na and ^{85}Rb ions, that can have different rates of emission of neutral particles that are not accounted for by the normalization procedure. In order to minimize this effect, relative values were used to compare the efficiencies for ^{6}Li, ^{23}Na and ^{85}Rb (see Figure 5.23). The data points for each ion species were therefore divided by the respective averaged plateau, with the high energy part being excluded due to increased fluctuation in that region. As can be seen, those relative efficiencies conform to the expected ion species mass trend, with lower masses achieving higher efficiencies at the same energy. The ^{23}Na curve is placed centrally between ^{6}Li and ^{85}Rb curves roughly in line with the scaling. Fully quantitative comparison is complicated by the fact the efficiency is a convolution of the velocity with other parameters (e.g., electronic threshold) and therefore not expected to scale exactly with $\sqrt{\frac{M_2}{M_1}}$. However, the experimental precision of these data is of adequate quality to provide a correction of the data from online experiments with ^{35}Ar.

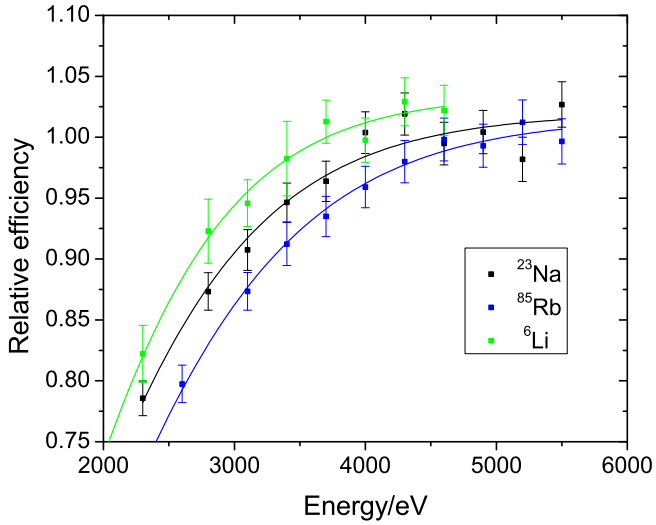


Figure 5.23: Relative efficiencies versus energy for ^{6}Li, ^{23}Na and ^{85}Rb ion species.

5.11 Conclusion

In this Chapter, the characteristics and the configuration of the main MCP detector and the data acquisition system was presented. The measurements were performed at LPC Caen. Furthermore, the MCP relative efficiency dependence on ionic energy was characterized in a series of measurements with an offline ion source. The efficiency was found to reach a plateau at higher values than expected for an undamaged MCP detector. The efficiency curves were measured for ^{6}Li, ^{23}Na and ^{85}Rb ion species with the purpose of correcting the data taken in an online experiment with ^{35}Ar. Furthermore, it was found that the efficiency of the 1^{+} and the 2^{+} charge state differs by about 10-15%, insufficient to account for the distortion in the online recoil ion spectrum.

Chapter 6

Data analysis of the November 2012 experiment

In this chapter, the analysis of the online data from the November 2012 experiment is presented. A brief introductory overview of the previous ^{35}Ar experiments is presented in Section 6.1. The structure of the data is described in Section 6.2. The most important sources of background and methods of background reduction are identified and described in Section 6.3. Section 6.4 deals with data fitting with the purpose of extracting the $a_{\beta-\nu}$ parameter with results being presented in Section 6.5. Finally, Section 6.6 describes the Monte Carlo simulations of the experimental spectrum performed with the goal of characterizing the background processes which ultimately prohibit the extraction of a value for $a_{\beta-\nu}$ from this data set.

6.1 Introduction

The experiment of November 2012 was the third online experiment with the WITCH spectrometer featuring ^{35}Ar. All three employed CaO targets at the ISOLDE's General Purpose Separator (GPS) system (see Chapter 2 for more details). However, previous experiments with ^{35}Ar, in June 2011 [108] and October/November 2011 [41] yielded limited results due in the former case to very poor target performance and in the latter case to problems with the dead time of the CAMAC DAQ system, both resulting in reduced statistics. The experiment of 2012 employed a new nanostructured target technology [88] featuring improved yield and durability of the target material, as well as very

low isobaric ^{35}Cl contamination. This improvement resulted in the acquisition of a sufficient number of events to extract the $a_{\beta-\nu}$ parameter with the required statistical precision of $\lesssim 0.5\%$.

6.2 Data structure

During preparation for the 2012 experiment, the CAMAC data acquisition system used in all previous experiments was replaced by a FASTER-based DAQ with more flexibility and virtually no dead time (see Chapter 5 for a more detailed description). The raw signals read out from the MCP were grouped into *events*. The events were grouped into *cycles*, according to their time of occurrence with respect to the moment when the proton pulse impinges on the target. The cycles were grouped into *runs*, still larger collections of data defined by the retardation potential of the spectrometer and the presence or absence of radioactive ions in the system. Only events in which all 5 signals (main MCP signal and 4 delay line signals) were present were accepted in the offline analysis.

6.2.1 Events

The FASTER DAQ was configured to record both the time and the pulse height (charge) information from the main signal of the MCP and the 4 delay lines that provide the position information for each event. Furthermore, the DAQ also recorded the main trigger coming from REXTRAP and the retardation potential of the spectrometer. The main signal and the delay line signals were grouped into an event if the delay line signals arrived within the 120 ns time window following a main signal. This was considered as an indication that all 5 signals originated from the same particle impinging on the MCP.

6.2.2 Cycles

The start of a WITCH measurement cycle is defined by the master trigger from REXTRAP, signaling that the ^{35}Ar ion cloud is prepared and going to be sent to the WITCH beam line. REXTRAP itself is synchronized with the PS Booster accelerator, which is able to provide proton pulses separated by a minimum of 1.2 s. That constrains the WITCH cycle length to multiples of 1.2 s, the total typically being 6 s. After being initially triggered, a National Instruments PCI-7811R FPGA card creates an array of triggers that can be roughly divided into:

1. The fast part of the cycle,
2. Preparation of the ion cloud,
3. Retardation part of the cycle.

The detailed time structure of the cycle is shown in Figure 6.1. The first part lasts only a few tens of microseconds and consists of guiding the ions through the beam line and reducing their energy to ∼100 eV, enabling their containment in the cooler trap (details in Chapter 2).

In the second part of the cycle, the ions are captured into the cooler trap and cooled with He_2 buffer gas without excitation for 300 ms. This procedure is performed 3 times consecutively, at 0 ms, 300 ms and 600 ms within a cycle, in order to maximize the number of ions in the trap. During the cooling and all later measurements, a beam gate was configured on the VBSTEE03R steering electrodes with the purpose of reducing ionized rest gas that appeared to be coming from the high voltage electrodes of the Pulsed Drift Tube.

After the preparation phase, at 800 ms from the cycle start, the ion cloud is transferred into the decay trap where the ions are left to decay and the retardation spectrometer power supply (Keithley SourceMeter 2400) is triggered to start the retardation voltage pattern (Figure 6.2). After the first trigger, the power supply repeats the retardation pattern autonomously with bins of constant voltage and 0.2 s in duration. Two retardation voltages are probed in each run, along with a number of 50 V and 600 V bins included for normalization and background characterization purposes, respectively. This phase lasts until 3.2 s from the start of the cycle.

At 3.2 s the decay measurement is completed and the remaining ions ejected by a simultaneous application of dipolar excitation for 10 ms at the magnetron frequency, and electrostatic ejection downstream onto the diaphragm between the cooler and decay traps. After colliding with the diaphragm, the ^{35}Ar ions are neutralized and quickly desorbed. It was later found that this lingering radiation can cause a measurable background on the MCP through β^+ particles created in the decay (see section 6.3).

Following the completion of the radioactive measurement at 3.2 s, data-taking is continued until the end of the full cycle of 6 s with the retardation pattern applied as in the first part. This was done in order to characterize the dependence of background on the retardation voltage without the presence of radioactive ions in the decay trap. Furthermore, after each full 6 s cycle, another identical cycle was performed without any ^{35}Ar present in the system. This additional measurement enabled a more thorough background characterization without

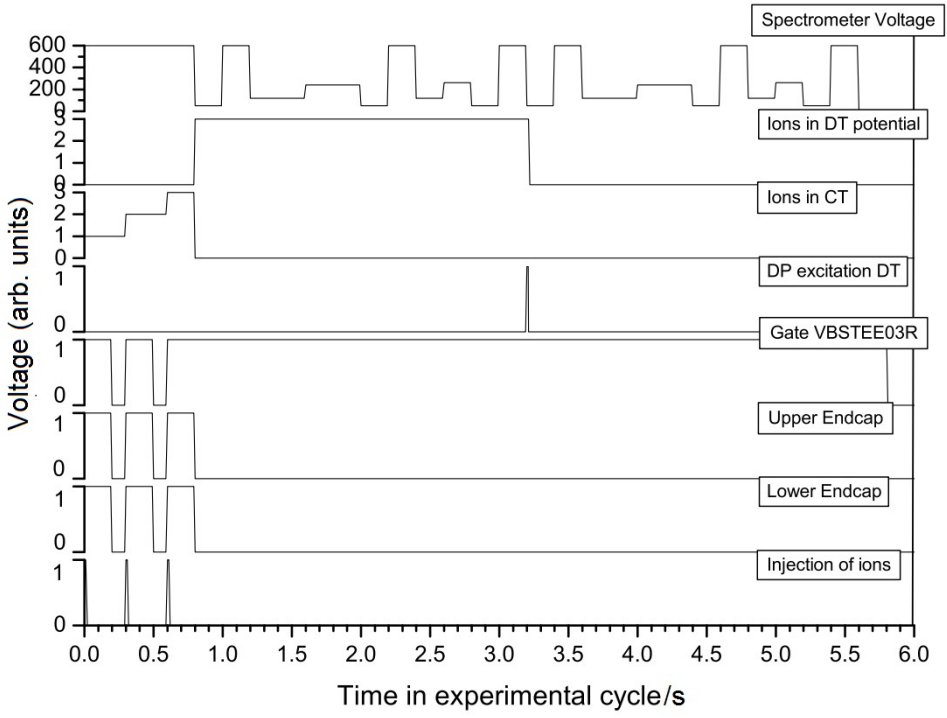


Figure 6.1: Schematic overview of the various triggers created by the FPGA card used in all runs and an example retardation voltage. Zero represents the low voltage, and one the high voltage case. ***Spectrometer voltage*** represents a particular retardation potential pattern in a cycle. ***Ions in DT potential*** shows the period in which the end cap voltages were "high" and thus the ions are confined in the decay trap. ***Ions in CT*** represents the 3 consecutive fillings of the cooler trap and the subsequent buffer-gas cooling periods. ***DP excitation DT*** shows the ejection of the ion cloud from the DT with dipolar excitation at the magnetron frequency. ***Gate VBSTEE03R*** shows the periods when a beam gate was applied on a steerer between the pulsed drift tube and the traps to reduce background ionization. ***Upper endcap*** and ***Lower endcap*** show the periods with the upper and lower end caps on, respectively. Injection of ions shows the REXTRAP trigger signaling the arrival of an ion bunch.

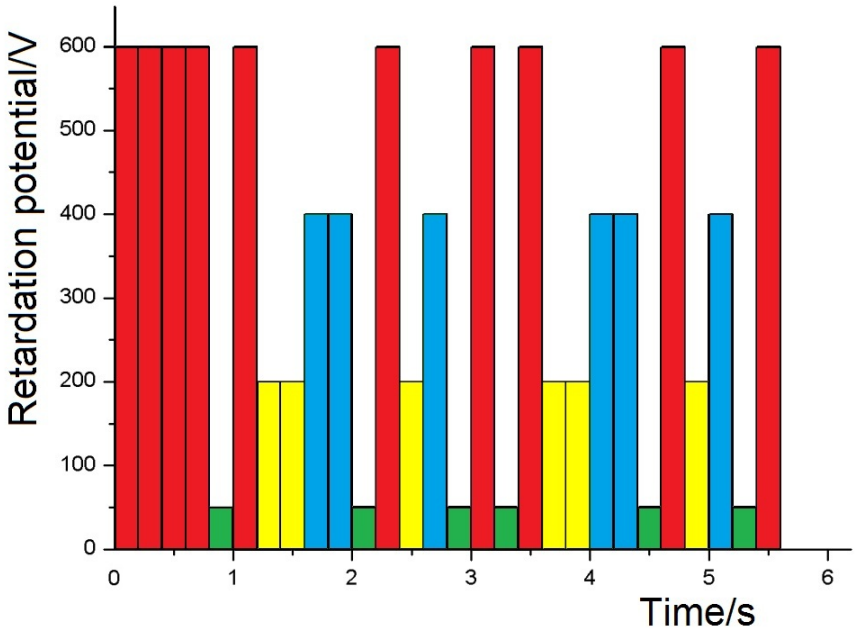


Figure 6.2: Schematic overview of a retardation cycle. Red and green denote the 600 V that blocks all recoil ions and the 50 V retardation potentials used for normalization, respectively. Blue and yellow denote the two retardation potentials that vary from run to run (see Table 6.1).

lingering radiation that could cause background, either through ionization of the rest gas or otherwise.

6.2.3 Runs

Each run consists of data taken during a period of 30 minutes under unchanged experimental parameters, i.e. ∼300 cycles with identical settings of the apparatus. Because of the large variation over the course of the experiment in injection/trapping efficiency, yield from the target, and the long-term and short-term background levels, only the runs with the highest quality of data were considered in this analysis (see Table 6.1) and used to extract the recoil ion spectrum. This resulted in a dataset of 14 runs with recoil ions and 4 runs

Run number	RV1/V	RV2/V
96	120	260
97	20	200
98	100	420
99	80	300
100	160	360
101	300	220
102	500	20
103	340	120
104	260	60
105	600	50
106	40	340
107	140	280
108	460	320
109	540	700

Table 6.1: List of runs used for extracting the ion decay intensities. The first column shows the designated run number in the experimental sequence, while the second and third columns show the two retardation voltages applied in the run.

dedicated to constrain the implantation and decay trap half-lives (see next section) with $\sim 3 \times 10^7$ events in total.

6.3 Background reduction

In view of WITCH's goal to determine $a_{\beta-\nu}$ to a high degree of precision, a comprehensive approach to background reduction and characterization was taken. As already noted, half of each cycle with radioactive ions was designated for background characterization. In addition, every other cycle was recorded without radioactive ions to monitor and characterize the background caused by ionization of rest gas and of cooler trap buffer gas ions caused by the electrodes, particularly the high-voltage switching electrodes of the PDT and the retardation section, as well as the static high-voltage electrodes of the reacceleration section.

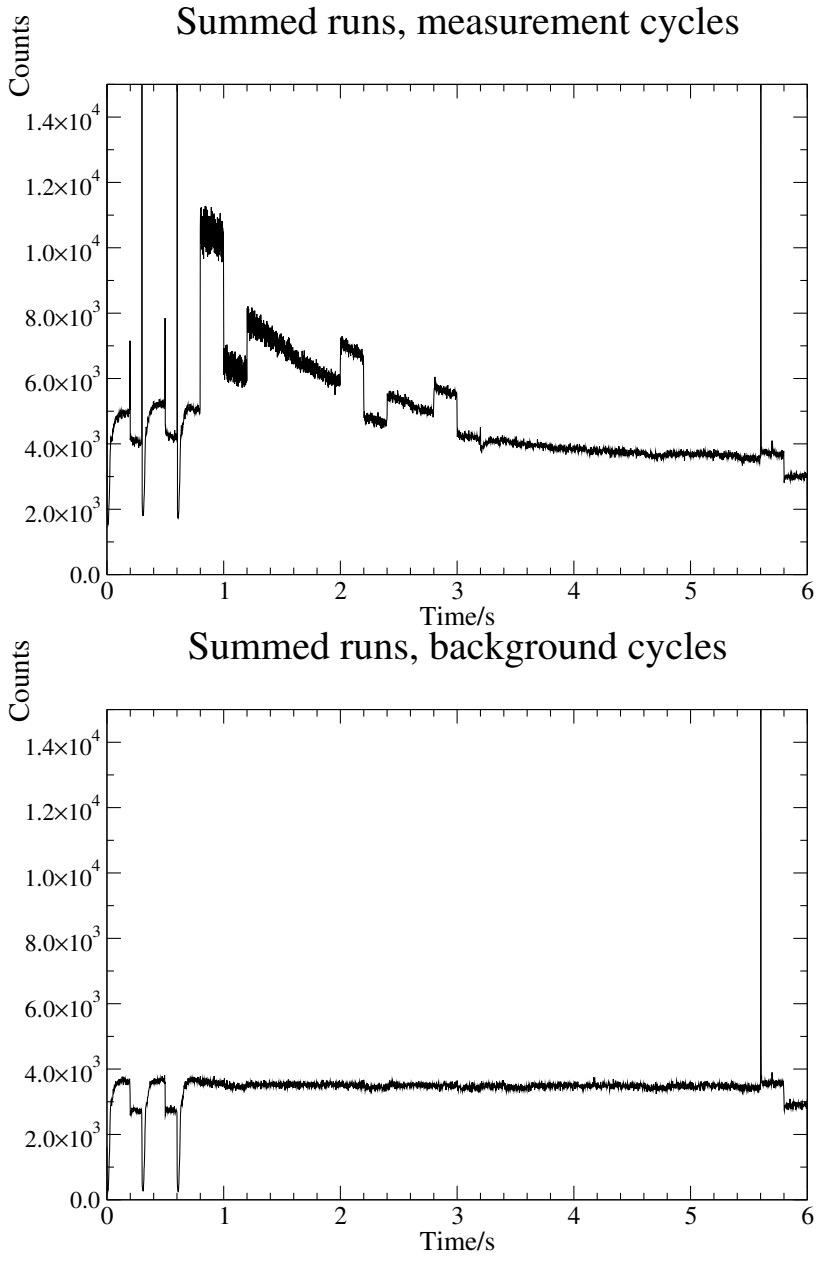


Figure 6.3: Summed (**top**) measurement cycles and (**bottom**) background cycles spectrum of all runs used in this analysis (96 – 109), including preparation of the ion cloud (0 s – 0.8s), decay and retardation (0.8 s – 3.2 s), background measurement after ejection (3.2 s – 6 s).

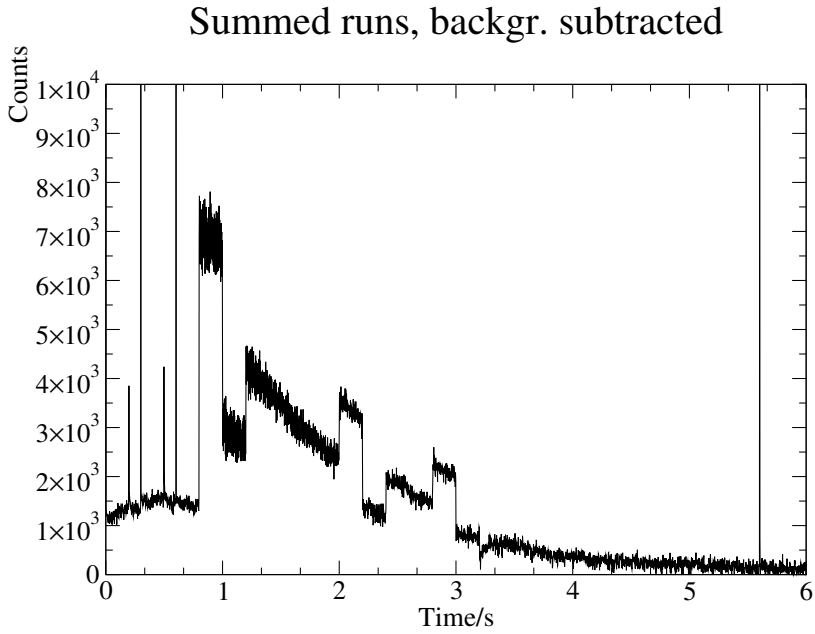


Figure 6.4: Summed spectrum of all runs used in this analysis (96 – 109), including preparation of the ion cloud (0 s – 0.8s), decay and retardation (0.8 s – 3.2 s), background measurement after ejection (3.2 s – 6 s). Background cycles (Figure 6.3) were subtracted from the measurement cycles.

6.3.1 Sources of background

6.3.1.1 Implantation

Before the injection into the cooler trap, the ion bunch is pulsed down from 30 keV to ∼100 eV by the PDT. If the ion bunch is too long or not adequately synchronized with the switching of the PDT, a significant number of ions can remain on high energies and overshoot the cooler trap end cap potential as well as the retardation potential of 600 V set at that moment in the cycle. These occurrences can be seen on Figure 6.3 and Figure 6.4 as the 3 large spikes at 0 ms, 300 ms and 600 ms. Afterwards, these high-energy radioactive ions can become implanted in the surface layer of the MCP and decay there.

Based on SRIM [3] simulation results, 30 keV ions impinging on a material similar to the MCP coating are expected to implant to a depth of ∼10 nm. Due to low-energetic recoil after the decay, ^{35}Cl daughter ions are expected to move

within the material by ∼1 nm at most, thus not being capable of triggering an avalanche in the micro-channels. On the other hand, the β^+ particle can produce enough energy to trigger one or more channels. However, in a more realistic case, not all of the ions in the bunch will traverse the PDT unhindered and impinge onto the MCP with 30 keV of kinetic energy, since a fraction of the late or early ions (with respect to the time window of the PDT) will be at least partially pulsed down [29], resulting in a distribution of implantation depths up to ∼10 nm. Since Argon is a noble gas, a fraction of the implanted ions is likely to diffuse out of the MCP. As this is a loss mechanism in addition to the radioactive decay, the measured half-life of the implanted radioactivity is expected to be less than the pure ^{35}Ar decay half-life T_{Ar}. For the purpose of quantifying this component of the background, dedicated implantation runs have been performed in which the ions were injected directly onto the MCP without being captured in the Penning traps (see Section 6.4).

6.3.1.2 Background ions

Ionization of the rest gas or the He_2 buffer gas from the cooler trap has been identified as a recurring issue in the WITCH spectrometer (see an in-depth analysis in [103]). It is challenging to avoid, since various configurations of electric and magnetic fields, such as the one in the spectrometer, can act as unwanted Penning traps, confining ionized rest gas and amplifying it via collisions with the rest gas. Primary ions that ignite these discharge processes typically originate on the high voltage electrodes in the spectrometer or the PDT, especially if the vacuum conditions are not optimal (that is, $\sim 10^{-9}$ mbar or lower). During the 2012 experiment, the vacuum was $\sim 10^{-8}$ mbar. When present, the background ions are influenced by the retardation potential, resulting in retardation-dependent background levels. This effect is clearly visible in the summed background cycles (Figure 6.3). Background levels are correlated with the retardation potential, with the lowest level corresponding to the highest retardation potential, although this dependence is not greater than $\sim 10\%$ over the whole range. This is seen more clearly on Figure 6.5 showing the dependence of normalized background intensity on the retardation potential. Also, at 5.6 s in the cycle a large peak appears in both the measurement and background cycle data. This coincides with the retardation potential being set to 0 V, indicating that background ions from an unwanted Penning trap situated between the decay trap and the analysis plane are being released.

Furthermore, the gradually increasing background seen at 0 s, 0.3 s and 0.6 s (Figure 6.3) coincides with the charging of the PDT, indicating that it contributes significantly to the overall background ionization. At 0.2 s, 0.5 s and 5.8 s a drop in both the measurement and the background cycles is visible, coinciding

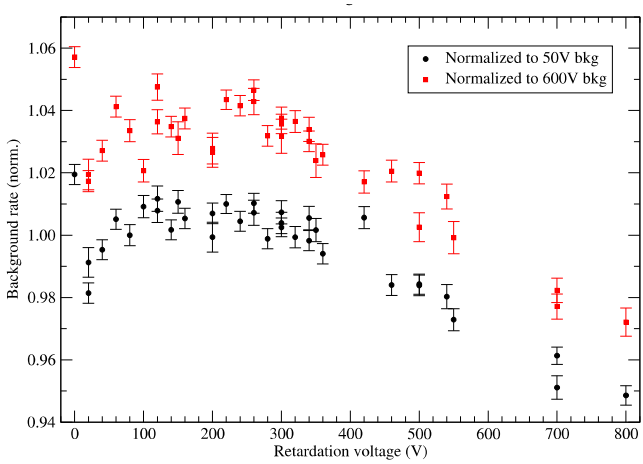


Figure 6.5: Constant background versus the retardation potential in runs with radioactive ions. Values normalized to 50 V and 600 V background levels are shown.

with the switching of the VBSTEE0R3 steerer electrode from 0 V to working potential. The steerer was kept on 0 V, during periods when the ion bunch was not traversing the beam line, to steer away any possible background ions incoming from below the Penning traps. Moreover, in the measurement cycles a narrow peak is seen coinciding with the steerer switch. The causality of these effects is unclear, but based on the coincidence it seems likely that the steerer electrode in fact increased the background ionization level when it was supposed to decrease it.

6.3.1.3 β particles and magnetron motion

The magnetron motion of the entire ion cloud around the decay trap center manifests itself as a minute sinusoidal component superimposed on the retardation spectrum (Figure 6.6). The observed sinusoidal frequency of ~ 172 Hz is in agreement with the theoretical magnetron frequency of Ar ions in a 15 V Penning trap. This effect was first observed during the October/November 2011 experiments. Although the cause for the eccentric motion of the ion cloud around the trap center has not been identified with certainty, it is likely an imperfection of the Penning trap; a misalignment of the electric and the magnetic field, or an asymmetry in the contact potential of the electrodes. The properties of the cloud's magnetron motion and the influence of space-charge,

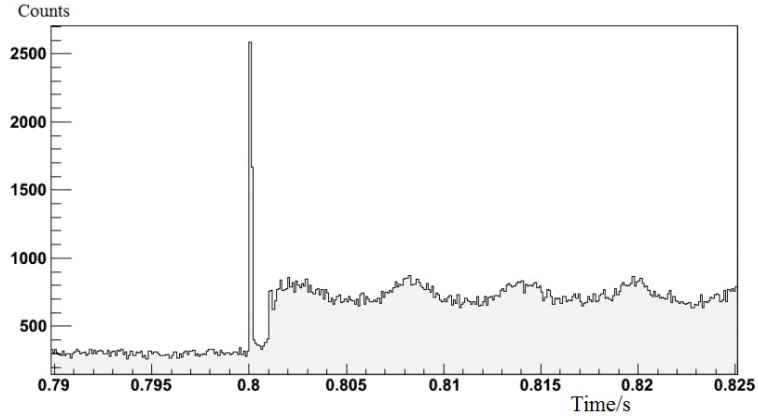


Figure 6.6: A part of the spectrum showing the influence of an eccentric magnetron motion of the entire ion cloud in the decay trap (sinusoidal pattern) as well as the effect of a finite spectrometer charging time at 0.8 s. Graph from [117].

i.e. the number of ions, on the magnetron frequency have been characterized in detail (see Chapter 4).

The effect is not caused by ^{35}Cl recoiled daughter ions on the phase of the magnetron motion. Rather, it is caused by the β^+ particles. Since the β^+ particles have energies in the MeV range, they are not affected by the electric fields. However, they are guided by the magnetic field to the MCP. This is supported by the observation of the sinusoidal pattern in the 600 V parts of the spectrum (1.0 – 1.2 s, 2.2 – 2.4 s, 3.0 – 3.2 s) where no recoil ions are present, and by the independence of the sine amplitude on the retardation potential [117]. In order to quantify the β-particle component of the spectrum, dedicated runs with ^{35}Ar in the decay trap and with the retardation potential constantly at 600 V have been performed (see Section 6.4). However, the mechanism of loss causing such a reduced half-life is presently unknown.

6.3.1.4 Ejected ions

After the retardation measurement, at 3.2 s in the cycle, the ions are ejected radially from the center of the decay trap by a dipolar excitation at the magnetron frequency (with 10 V amplitude and 10 ms duration) and at the same time axially upstream. This results in them hitting the electrode walls and

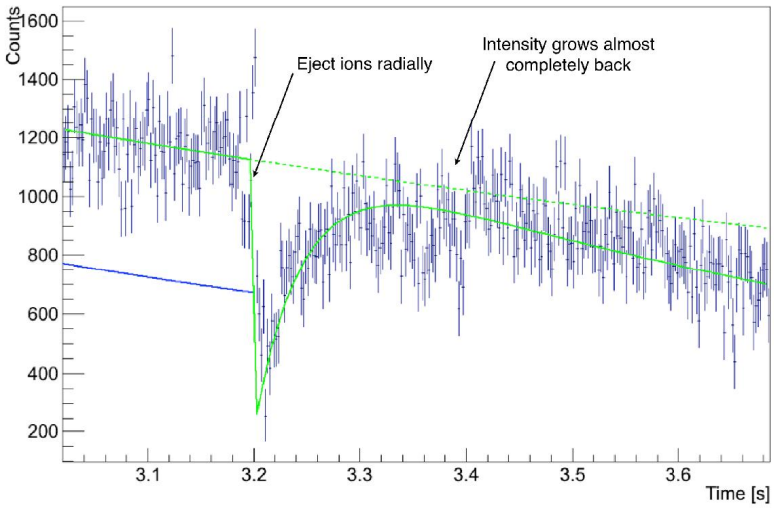


Figure 6.7: At 3.2 s in the measurement cycle, the ions are ejected radially as well as axially; the activity drops but then reappears due to neutralization and desorption of ions from the electrode walls and the diaphragm.

the diaphragm between the two traps and neutralizing. The low-energy ions can then desorb from the walls and decay in the trap volume. Although neutral Ar atoms are unlikely to ionize during decay and to end up on a trajectory towards the MCP, activity is seen to partially reappear in the retardation spectrum (Figure 6.7) after ejection. This component also appears unaffected by the retardation potential, supporting the hypothesis that it is caused by the β^+ particles from the neutral Ar atoms decaying in the trap volume. It is important to note that this background component does not appear in the ion retardation spectrum, since it occurs only at 3.2 s and later times. However, it has to be taken into account when extracting other background components present during the entire cycle, i.e. from the implanted ions and the background ionization.

6.3.1.5 Spectrometer charging time

Due to its relatively large capacity and the high voltages involved, the main retardation electrode SPRETA06 (see Figure 2.6) can require significant time to charge, i.e. achieve the desired voltage. This renders unreliable a certain amount

of data taken immediately after a nominal retardation potential change due to the transience of the actual potential. The time needed for the spectrometer to reach the nominal retardation potential was measured with an oscilloscope and it was found that it takes under 10 ms to reach a voltage $\geq$99% of the nominal value. For this reason, data taken in the first 10 ms after a change of retardation potential was discarded.

6.3.2 Data filtering

6.3.2.1 Cycle selection

As previously mentioned, an assembly of electric and magnetic fields such as the spectrometer can create a number of unwanted Penning traps that act as storage for background ions and can energize them, causing secondary or even runaway ionization. When the configuration of the potential in the spectrometer is altered, these unwanted traps release ions that can reach the MCP [103]. This is observed as a sudden large shift in the background level as seen on Figure 6.8. To additionally improve the reliability of the data, every other cycle was recorded as a *background cycle*, with all the parameters the same as a *measurement cycle*, except for the presence of radioactive ions.

Both measurement and background cycles were inspected visually for sudden, nonstatistical features that are a sign of a background discharge. Such *bad cycles* (see Figure 6.9) were then excluded from the analysis.

6.3.2.2 Position distribution

The position distribution of a typical background subtracted recoil ion beam spot is shown on Figure 6.10. Most importantly, it can be seen that the recoil ions that form the largest part of the background subtracted data are spread accross most of the surface of the MCP. Therefore, it is not possible to filter the data based on position. Furthermore, it was noted [117] that the background cycle positional data has a dependence on the retardation potential, i.e. that the potential changes the focusing of the background ions on the MCP. However, this dependence disappears in the background-subtracted data.

6.3.2.3 Pulse-height distribution

Ideally, the pulse-height data can be used to distinguish between the recoil ions and β particle background [108]. However, this approach was precluded in

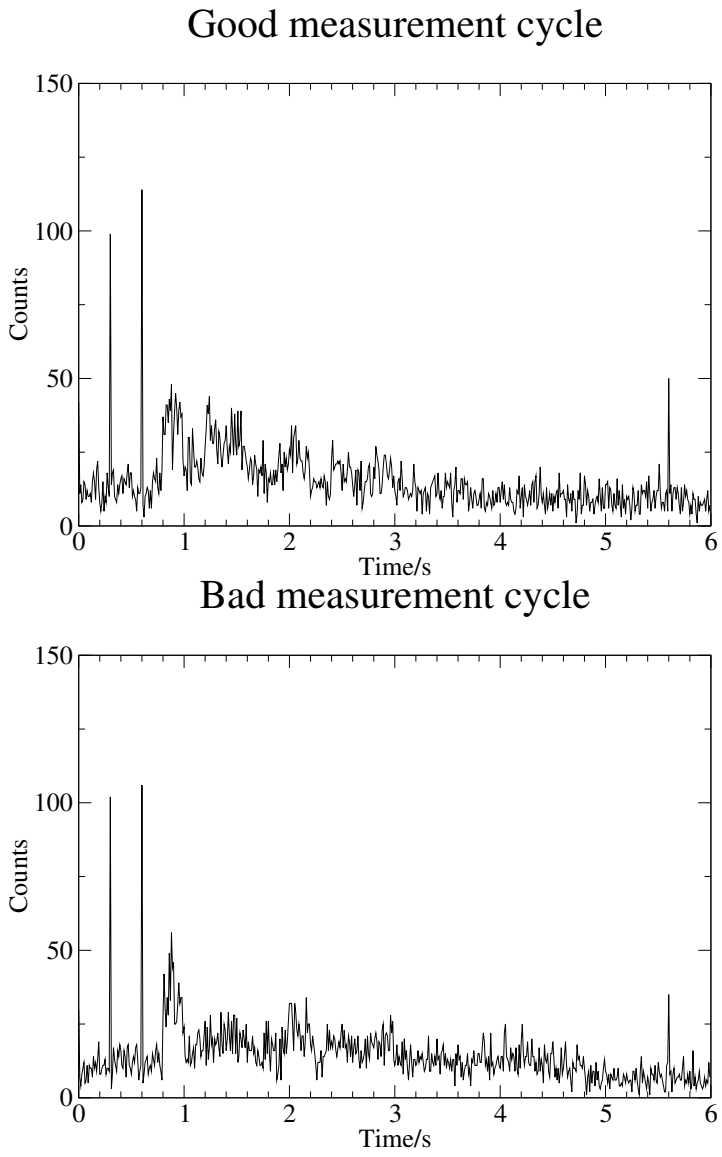


Figure 6.8: Examples of a good measurement cycle (**top**) and a bad measurement cycle (**bottom**). After the ejection of the ions at t=3.2 s, the good cycle exhibits a flat background, while in the bad one a variation in the background is seen.

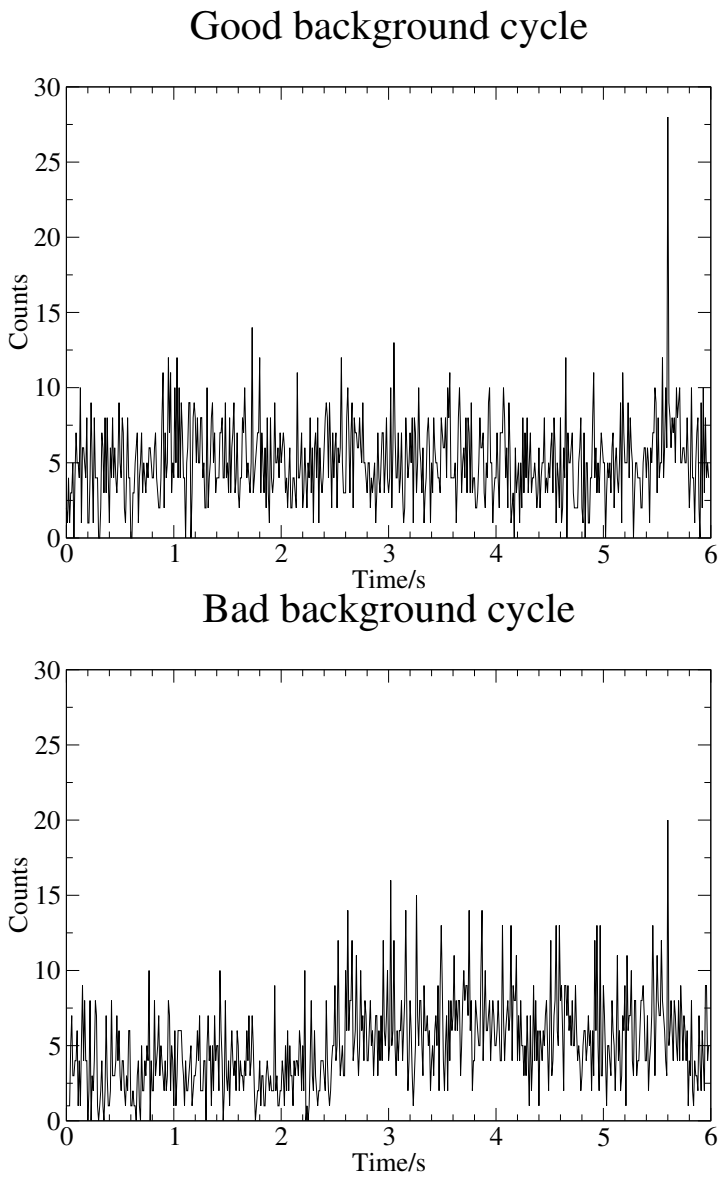


Figure 6.9: Examples of a good background cycle (**top**) and a bad background cycle (**bottom**). The good cycle exhibits a flat background over the entire duration, while in the bad one a shift of the background is seen.

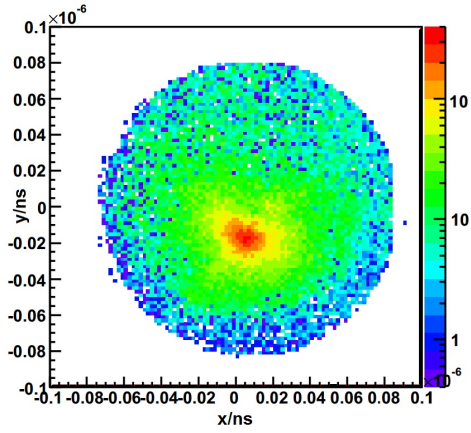


Figure 6.10: The position distribution of recoil ions.

the case of the November 2012 dataset due to the damage caused to the MCP surface, most likely by an α-source calibration procedure (see Chapter 5). The only data filtering based on pulse-height was then in cases of saturation, i.e. the data with a pulse height greater than the FASTER DAQ limit was observed to be constant throughout the cycle and was therefore discarded.

6.4 Data fitting

This section describes the extraction of experimental intensities and half-lives of the components of the retardation spectrum related to the ^{35}Cl recoil ions as well as to the background. This was accomplished by fitting a function to the data, tailored to incorporate all known background effects, as well as the contribution of the recoil ions. The retardation spectrum of recoil ions was extracted from runs 96 – 109 (see Table 6.1). The time in the cycle was limited to the 0.7 – 3.2 s interval, i.e. from 100 ms before the ions are transferred to the decay trap, to the moment they are ejected. Since the part of the cycle after 3.2 s was not used, the neutralization and desorption (see Section 6.3.1.4) could be ignored. An alternative analysis in which the whole cycle was fitted is presented in [117].

Year	Trapped Ions/s	Implanted ions/s	β/s
2007	-	1.38(8)	-
2009	1.10(17)	1.31(6)	1.12(3)
2011	1.32(6)	-	0.67(1)
2012	1.194(15)	1.311(31)	0.607(30)

Table 6.2: Various effective half-lives measured at WITCH.

6.4.1 Structure of the fit function

6.4.1.1 Implantation

The background caused by the decay of radioactive ions implanted into the surface of the MCP detector (see Section 6.3) is expected to follow an exponential decay curve, although (due to desorption or other loss mechanisms) not necessarily with the same half-life as the true ^{35}Ar half-life (T_{Ar}) or the observed half-life of ^{35}Ar ions in the decay trap (T_{ion}). Therefore, a component with the form

$$A_{imp}e^{-t/T_{imp}} \tag{6.1}$$

is added to the fit function. This is the only spectrum component connected to radioactive decay that can be measured independently, without other decay components coming from the trap. Conversely, since it is not possible to fill the trap without overshooting a fraction of the ions, the implanted decay is present in all other measurements. A run dedicated to characterize the implantation half-life, without trapping any ions, is used to constrain the T_{imp} half-life with greater precision.

Under the assumption that the implanted component does not change except in intensity (the number of ions implanted), T_{imp} can be fitted simultaneously (i.e., as a common parameter) in both the dedicated implantation run and the runs with recoil data listed in Table 6.1. However, the intensity parameter A_{imp} is expected to change from run to run, and is therefore constrained for each run independently in the beginning of the cycle when the ions are still in the cooler trap and the additional components from the β-particles and recoil ions are not present in the spectrum. The implantation component is fitted in the 0.7 – 3.2 s range. The fit of the dedicated runs yields T_{imp}=1.311(31) s, in good agreement with the experiments from 2009 and 2007 (see Table 6.2).

$A_{BG,50V}$	$A_{BG,600V}$	$A_{BG,R1}$	$A_{BG,R2}$
0.81 s – 1.00 s	1.01 s – 1.20 s	1.21 s – 1.60 s	1.61 s – 2.00 s
2.01 s – 2.20 s	2.21 s – 2.40 s	2.41 s – 2.60 s	2.61 s – 2.80 s
2.81 s – 3.00 s	3.01 s – 3.20 s	3.61 s – 4.00 s	4.01 s – 4.40 s
3.21 s – 3.40 s	3.41 s – 3.60 s	4.81 s – 5.00 s	5.01 s – 5.20 s
4.41 s – 4.60 s	4.61 s – 4.80 s		
5.21 s – 5.40 s	5.41 s – 5.60 s		

Table 6.3: Intervals within a cycle at which specific constant background components are present (see Section 6.4.1.3).

6.4.1.2 β-particles

The spectrum component caused by the β-particles coming from the decay trap was expected to have the same half-life (T_β) as the ions in the trap (T_{ion}) and as the nominal ^{35}Ar half-life ($T_{1/2}$=1.775(4) s [77]). However, this was found not to be the case, likely due to other loss mechanisms specific to β-particles that are presently unknown. A damping of the magnetron oscillation is also seen in the spectrum and is consistent with $T_\beta \approx 0.6$ s. To incorporate the β background, a function of the form

$$A_\beta e^{-t/T_\beta} \tag{6.2}$$

was employed. This component was fitted in the region from 0.81 s to 3.2 s, i.e. while the radioactive ions were in the decay trap. The magnetron effect was averaged out by increasing the bin size to around 2 periods of 5.8 ms, the period corresponding to a sinusoidal frequency of $\sim$ 172 Hz. This approach did not reduce precision in comparison with fitting an under-damped sinusoidal component to the spectrum, as was performed in [117].

6.4.1.3 Constant background

A separate constant background level is assumed for each retardation potential applied in the experiment. Therefore, additive constants $A_{BG,50V}$, $A_{BG,600V}$, $A_{BG,R1}$ and $A_{BG,R2}$, where R1 and R2 denote the retardation potential used in the run (as listed in Table 6.3), are added to the fit function in both measurement cycles and respective background cycles.

A_{50V}	A_{R1}	A_{R2}
0.81 s – 1.00 s	1.21 s – 1.60 s	1.61 s – 2.00 s
2.01 s – 2.20 s	2.41 s – 2.60 s	2.61 s – 2.80 s
2.81 s – 3.00 s		

Table 6.4: Amplitudes of the recoil ion components that are present in different intervals within a cycle.

6.4.1.4 Recoil ions

The recoil ion spectral component is expected to have an independent amplitude A_R for each retardation voltage. However, since the recoil ions for different retardation voltages originate from the same source, the half-life T_{ion} is expected to be common to all retardation potentials and all runs. Since two retardation voltages along with the 50 V intervals are present in each run, the recoil spectral component is fit to a function of the form:

$$A_i e^{-t/T_{ion}}, \tag{6.3}$$

where $i = 50V, R_1, R_2$, depending on the time in the cycle (see Table 6.1) This component is fitted in cycle intervals in which recoil ions are expected to be present (Table 6.4), i.e. after the transfer to the decay trap at 0.8 s and before the ejection of the cloud. Excluded are the parts with the retardation voltage higher than the maximal ^{35}Cl energy of recoil of 452 eV and the very first bin at 0.8 s, due to a small amount of overshoot during the transfer of ions from the cooler trap to the decay trap.

6.5 Fit results

The optimal parameters of the fit function were obtained by a fitting routine that employs the χ^2 minimization technique. Since the individual cycles typically contain a low number of events, they were summed for each run before fitting. The cycles, deemed bad according to the criteria from subsection 6.3.2 were excluded. In order to avoid subtraction, which alters the statistical distribution of the events in each bin, the background and the measurement cycles were fitted simultaneously. Furthermore, three dedicated runs were used to improve the constraints on the implantation, β-particles and ion half-lives:

- a dedicated implantation run (with implanted ions only, run 76),
- a dedicated β run (with implanted ions and β-particles, run 95),
- a dedicated ion half-life run (with implanted ions, β-particles and recoil ions, run 94).

Individual fits of these three dedicated runs are shown on Figure 6.11. In order to extract the recoil ion spectrum, they were then fitted simultaneously with the recoil ion and background runs (96 – 109), with the half-lives as common parameters so that the uncertainties in the fitted half-lives were properly accounted for in the determination of the recoil ion intensities. This procedure was employed also because simple background subtraction would cause the event distribution to change from Poisson's to Skellam's.

An example of a retardation spectrum with a function fitted is shown on Figure 6.12. The fit function employed in a run such as this one contains all the components described in section 6.4, while the simultaneously fitted dedicated half-life runs contain only the components applicable (i.e. the implantation curve only in run 76, implantation and β-particle curves in run 95, and implantation, β-particle and ion curves in run 94). Furthermore, not all cycle sub-intervals in the run in Figure 6.12 contain all three decay components. The effect of this on the quality of the fit is considered in the next section.

6.5.1 Quality of the fit

Figure 6.13 shows a semi-logarithmic version of the plot of all runs with recoil ions (runs 96 – 109) summed. One unexpected feature of the decay is revealed by the logarithmic scale of the y-axis: the slope of the first 50 V sub-intervals (0.8 s – 1.0 s) is significantly different than the slopes of other sub-intervals in the interval with recoil ions (0.8 s – 3.2 s). Furthermore, each individual run exhibits this same behavior. However, it is not consistent with a spectrum that would result from a sum of three exponential decays with T_{imp}, T_{β} and T_{ion} half-lives.

This inconsistency indicates that other sources of background that build up exponentially could be present in this time interval of the spectrum, e.g. background ions correlated with the radioactive ions.

To systematically test the fitting model for inconsistencies such as this one, it is useful to perform multiple fits, each with a number of leading channels removed. In that way, the evolution of the fit parameters across the cycle can be quantified.

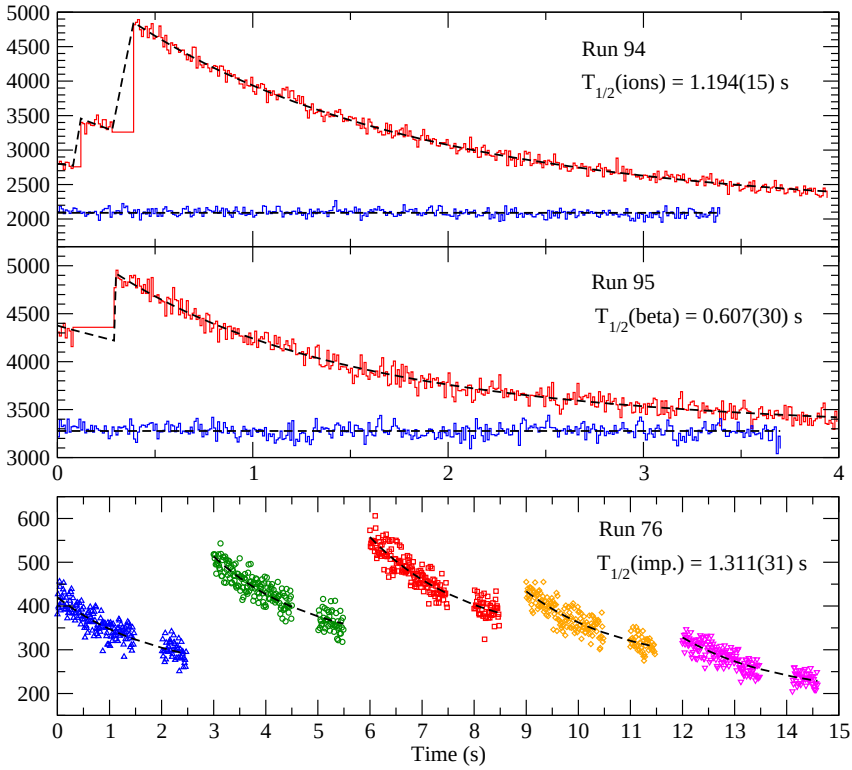


Figure 6.11: Dedicated ion run No. 94 (**top**), β particles run No. 95 (**middle**) and implantation run No. 76 (**bottom**). Background cycles are shown in blue in the top and middle plots. The implantation run shows only the 5 good cycles that were used for analysis. The χ^2/ν of the fit is 1.14, with $\nu = 257$.

6.5.1.1 Amplitudes

Figure 6.14 shows such a plot of the intensities A_β, A_{50V}, A_{120V} and A_{260} for a representative run. It can be seen that the error bars increase as more leading channels are removed, due to reduced statistics. Furthermore, all of the amplitudes vary in the first 50 V and the first 600 V cycle intervals (0.8 s – 1.0 s and 1.0 s – 1.2 s).

This behavior indicates the existence of processes not accounted for by the fit function model. In the two retardation intervals shown ($V_{ret.}(1)$=120 V and

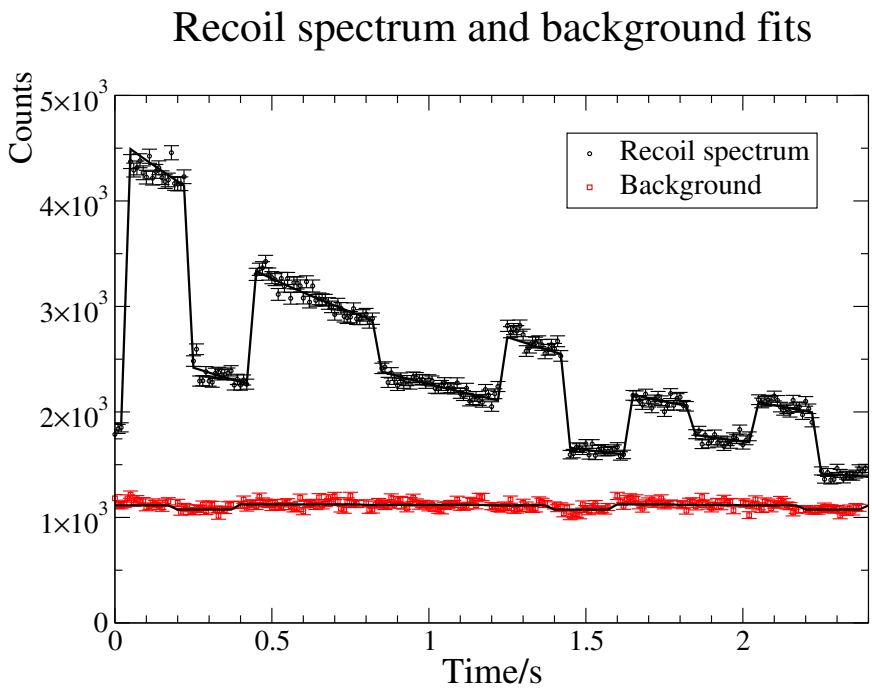


Figure 6.12: A recoil ion run with a fit function. The spectrum is fitted until the ejection of the ion from the decay trap.

$V_{ret.}(2)$=260 V) the amplitudes are significantly more stable, although still exhibiting a sudden shift close to the end of the first interval. This behavior is not unexpected. Both $V_{ret.}(1)$ and $V_{ret.}(2)$ intervals contain all three decay processes, i.e. ions, β-particles and implanted ions. However, the A_β amplitude would be constrained mostly by the first 600 V interval, which is excluded in the retardation intervals. It is then constrained by the remaining two 600 V intervals (2.2 s – 2.4 s and 3.0 s – 3.2 s, see Figure 6.2), which have much less statistics, causing the A_β to drift across a large part of the cycle with increasing error bars. This lack of constraint of the A_β amplitude also causes an increased correlation with the ion amplitudes A_{120V} and A_{260} and their shifting, since the β-particle component is also present and fitted in the retardation intervals $V_{ret.}(1)$ and $V_{ret.}(2)$. Furthermore, the implanted activity A_{imp} is constrained only by the short 0.7 s – 0.8 s period with modest statistics and is present underneath the ion and the βs' signal throughout the cycle. Having a similar $T_{1/2}$ as the ions, a correlation between their amplitudes can result.

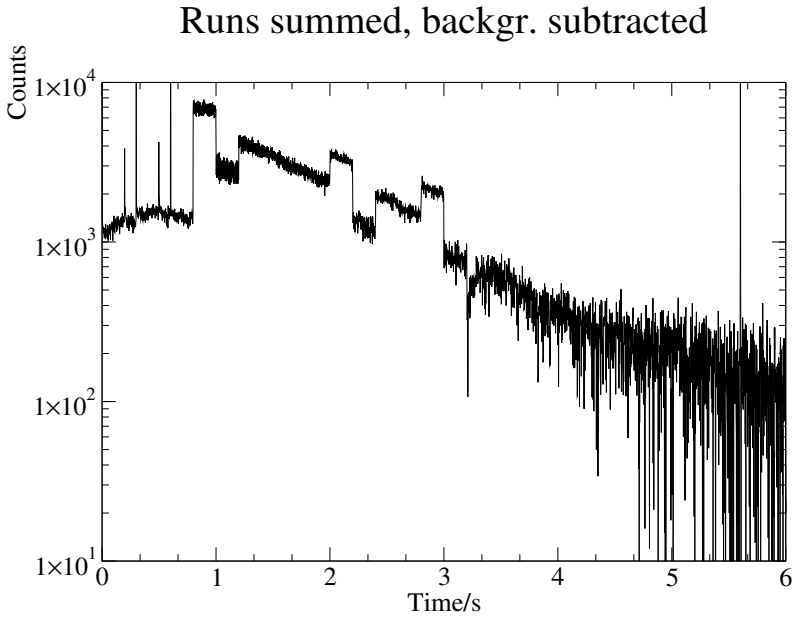


Figure 6.13: A semi-logarithmic plot of all recoil ion runs (96 – 109) summed with the background cycles subtracted. See text for details.

Considering Figure 6.14 it seems prudent to exclude at least the first 50 V interval from the fitted data due to processes not yet understood or properly modeled by the fit function. It is also clear that even with the first 50 V interval excluded, the ionic amplitudes exhibit some drift, typically up to $\sim$3 – 4%.

6.5.1.2 Half-lives

Figure 6.15 shows the T_{imp}, T_{β} and T_{ion} half-lives fit with the leading channels removed in the same way. The half-lives also exhibit significant drift in the first 50 V interval. However, unlike the amplitudes, they are stable in the first 600 V interval. Furthermore, both the T_{imp} and T_{ion} are very stable in both retardation voltage sequences, in contrast with the amplitudes. This is because the half-lives are fitted simultaneously with the three dedicated runs and are therefore much better constrained as a consequence of considerably more statistics. However, T_{β} exhibits a very small drift that is strongly anti-correlated with T_{imp}. A full overview of the correlations between fit parameters of the decays is shown in Figure 6.16.

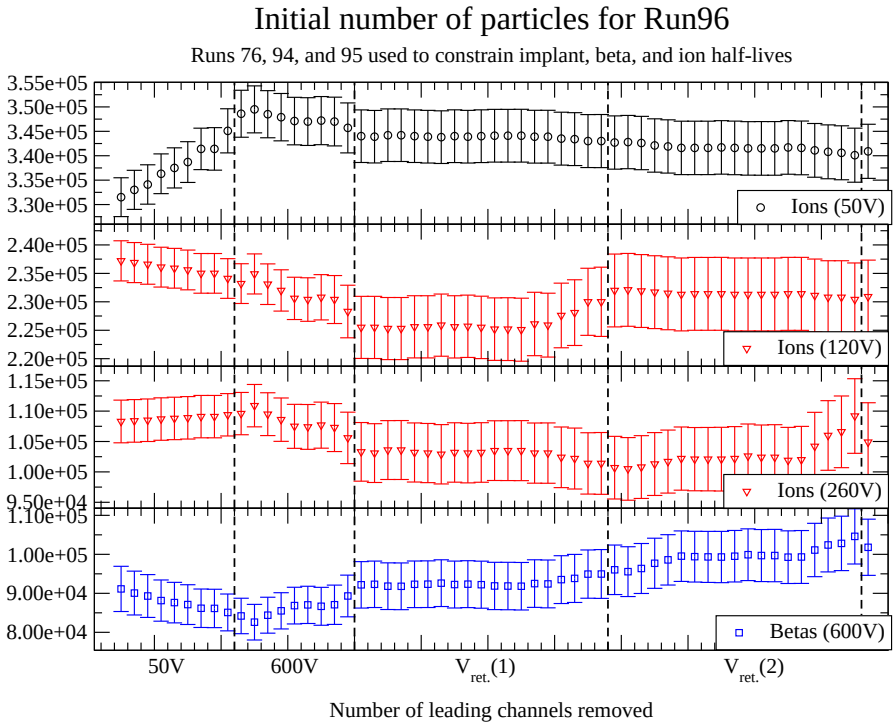


Figure 6.14: A plot of the dependence of the intensities A_β, A_{50V}, A_{120V} and A_{260V} on the number of leading channels removed. The parts of the cycle corresponding to the first 50 V, the first 600 V cycle intervals (0.8 s – 1.0 s and 1.0 s – 1.2 s) and the intervals with both retardation potentials used for the given run are shown on x-axis. Amplitudes are extracted from the data of run 96.

The half-lives dependence on the number of leading channels excluded is also stable and reproducible in other runs; Figure 6.17 shows the T_{imp}, T_β and T_{ion} for runs 96 – 109. The half-life of the ions is constrained exceedingly well and does not change significantly from run to run. On the other hand, T_{imp} is constrained less well and the mean value fluctuates from run to run, although within error bars. T_β exhibits even more fluctuation, in some cases the mean exceeding the error bars. Furthermore, the T_{imp} and T_β half-lives are anti-correlated. The reason that the ionic half-life T_{ion} is much more stable and consistent with respect to T_{imp} and T_β is most likely due to more statistics available in the former case. The lack of statistics to consistently constrain T_{imp}

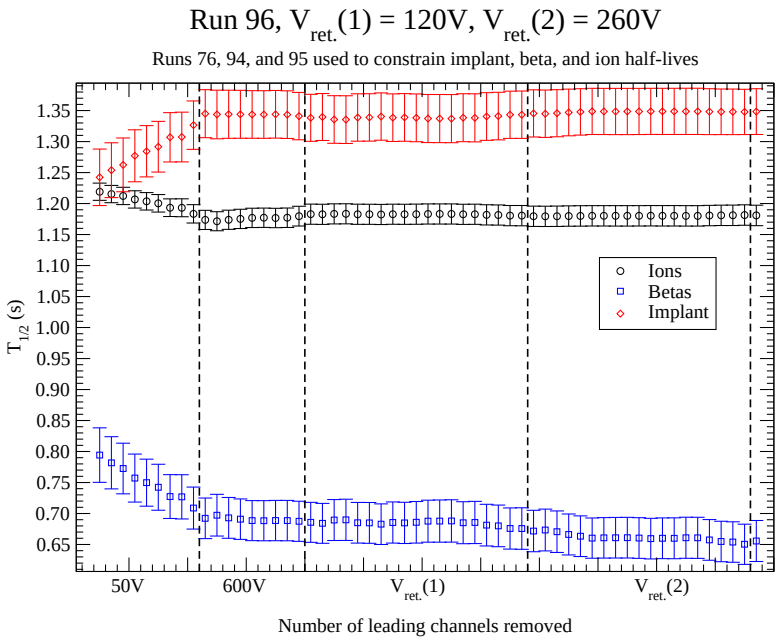


Figure 6.15: A plot of the dependence of the half-lives T_β, T_{ions} and T_{imp} on the number of leading channels removed for the run 96. Parts of the cycle corresponding to the first 50 V, the first 600 V cycle intervals (0.8 s – 1.0 s and 1.0 s – 1.2 s) and the intervals with both retardation potentials for the given run are shown. Amplitudes are extracted from the data of run 96.

and T_β, although not as visible within a single run on Figure 6.15, becomes apparent in their fluctuation from run to run. Analogous behavior is observed in the amplitudes A_{imp} and A_β relative to A_{ion}.

Another striking feature of the data is the discrepancy between the half-lives T_{imp}, T_β, T_{ion} and T_{Ar} themselves. Considering that all three processes are ultimately driven by the decay of ^{35}Ar, the reason for appearance of three distinct half-lives, all significantly shorter than the nominal T_{Ar}=1.773 s, is not obvious. The lower half-life of the implanted component T_{imp} can be readily explained by another loss mechanism in addition to radioactive decay, i.e. the desorption and escape of implanted ions (see Section 6.3 for a more detailed discussion).

However, a loss mechanism affecting the βs is less certain. Its existence is obvious not only from the very short T_β with respect to both T_{ion} and nominal half-life T_{Ar}, but also from the effect of the magnetron motion that is observed only in the β signal (see Section 6.3). A sinusoidal dependence of the magnetron pattern in the spectrum implies that the transmission efficiency of the βs depends on the phase of the ion cloud's magnetron motion in the trap. Since the motion is eccentric, larger radii can lead to higher losses, especially considering that the βs, depending on their energy, can have a larger cyclotron radius through the spectrometer than recoil ions. Furthermore, the spectrometer contains symmetry-breaking elements, e.g. an anti-ionization wire placed radially that could result in the loss β-particles. However, such a mechanism would account only for the observed modulation of the spectrum, and not for the low βs half-life.

The ion half-life T_{ion} is also found to be significantly shorter than the nuclear half-life of ^{35}Ar. This is caused most likely by losses of ions in the decay trap. It

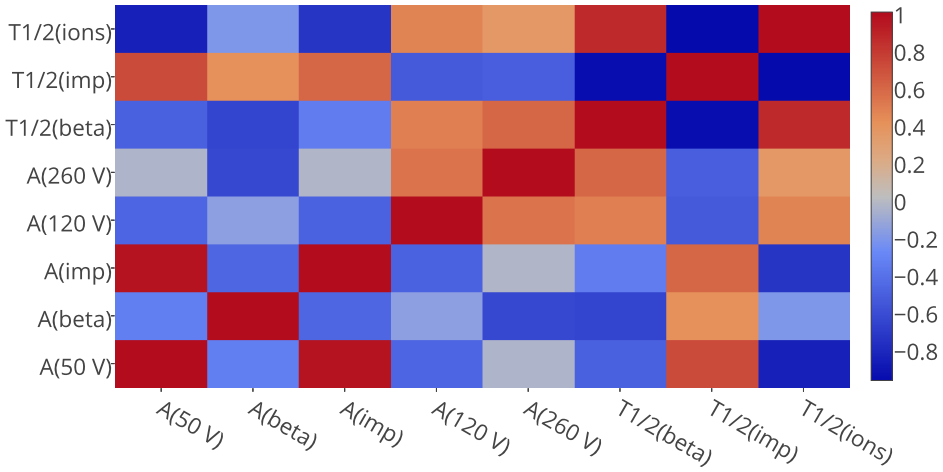


Figure 6.16: Correlations between the parameters of the 3 decay components of the fit function. The correlation is calculated from the evolution of the parameters when leading channels are removed (Figure 6.14) and Figure 6.15) for run 96. The three half-lives are correlated (T_β and T_{ions} positively, and T_β and T_{imp} negatively). The amplitudes of the respective processes appear to be correlated in the same way.

is not clear where the lost ions end up. However, it is possible for them to cause another source of background not yet accounted for. It is notable that stable ^{39}K ions, usually used for testing and optimization of the apparatus do not exhibit such significant losses. However, the losses of radioactive ions from the trap influence the value of $a_{\beta-\nu}$ only if the effective T_{ion} is not well-known [103], i.e. trap losses do not cause systematic error in $a_{\beta-\nu}$ if the loss time is known with good precision.

Finally, it can be concluded that the simultaneous fitting of each recoil ion run with three dedicated half-life runs determines both the amplitudes and the half-lives of the underlying decay processes reasonably well. However, features not accounted for by the fit functions are still observed. The exponential build-up process seen in the first 50 V interval seems most severe, although it can be mitigated simply by excluding the data in question. Unfortunately, that does not account for any consequent relaxation process that is likely to follow the build-up. Furthermore, a correlation between the implanted and βs signal is seen as a result of insufficient statistics and the difficulty of separating the two components.

6.5.2 Amplitudes

The correlation coefficient $a_{\beta-\nu}$ is extracted from the integral energy spectrum of the recoil ions, i.e. from the ionic amplitudes A_{20V} ... A_{600V} of the fitted function. Recoil ion amplitudes are then simulated by a Monte Carlo based simulation, for different values of $a_{\beta-\nu}$ and a best fit of $a_{\beta-\nu}$ to the experimental amplitudes is extracted. The simulations encompass all relevant parts of the apparatus. Preparation of the ion cloud in the cooler trap and its subsequent transfer to the decay trap is simulated by the Simbuca [107] software package with realistic electric and magnetic fields. The coordinates and velocities of the ions in the cloud are then used as input for SimWITCH [41], a software package that simulates the decay of ions in the trap as well as the trajectory of recoil daughter ions through the spectrometer until the main MCP detector.

The normalized amplitudes obtained from the fit of the experimental data are shown in Figure 6.18, along with simulated spectra for $a_{\beta-\nu} = 1$, $a_{\beta-\nu} = 0$ and $a_{\beta-\nu} = -1$. Table 6.5 shows the corresponding amplitudes without normalization. The value of $a_{\beta-\nu}$ for ^{35}Ar expected from the Standard Model is 0.9004(16) [99]. However, the spectrum extracted from the experimental data appears to be significantly discrepant with respect to the boundaries imposed by the Standard Model. The low energy part of the spectrum is very pronounced, although the decay of ^{35}Ar is expected to have a much larger high-energy component, since $a_{\beta-\nu} \sim 0.9$ implies a highly correlated momentum

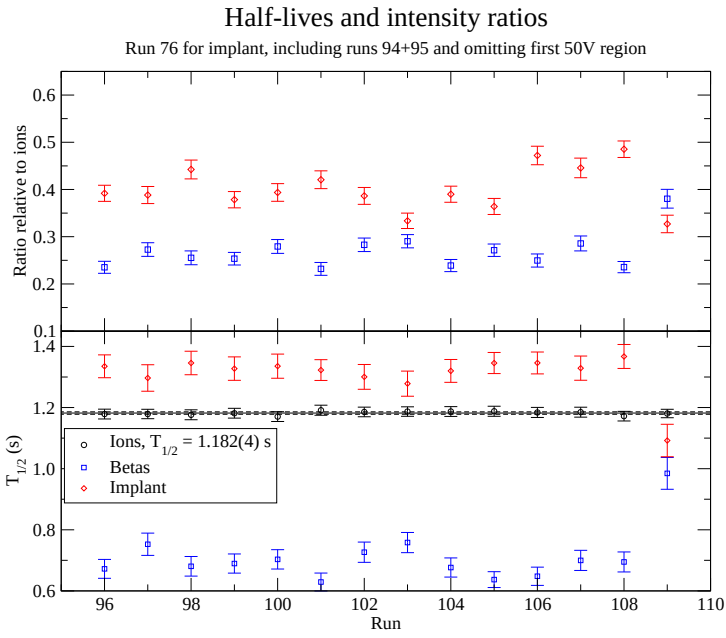


Figure 6.17: (**bottom**) T_{imp}, T_β and T_{ion} for runs 96 – 109. (**top**) Amplitudes of the implanted ions and the βs relative to amplitudes of the ions in the decay trap. The ionic half-life T_{ion} is remarkably stable and well-constrained, whereas the two background components (βs and implanted) fluctuate from run to run and are correlated (see text for details).

between the emitted electron and the neutrino, leading to a high recoil energy. Furthermore, Figure 6.19 shows the goodness of fit for all runs used to extract the amplitudes shown in Figure 6.18 as characterized by their χ^2/ν. The average reduced χ^2 is significantly greater than 1, indicating that the model employed in the fit function does not fully describe the relevant physical processes of the experiment.

The most important known systematic effects not included in the experimental spectrum of Figure 6.18 are the ones concerning the MCP detector, i.e. the position dependent efficiency and the energy dependent efficiency. The former was investigated [60] and found to vary $\sim 3\%$ across the surface of the MCP, insufficient to cause such an effect in the retardation spectrum, if any. An energy dependence in the efficiency of the MCP is more likely to result in a distorted

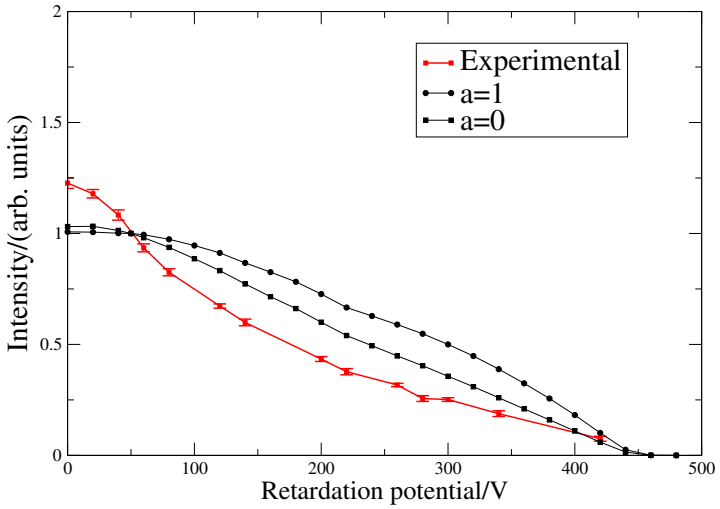


Figure 6.18: Experimental amplitudes of the recoil ions versus retardation voltage. Simulated spectra for various values of $a_{\beta-\nu}$ are shown for comparison.

spectrum. Indeed, it was found that the MCP plates suffered radiation damage from previous use and were not functioning properly, exhibiting a significant reduction in efficiency for low energy ions (see Chapter 5). A significant fraction of ^{35}Ar daughter nuclei ends up in the 2^+ charge state (17.3(4)%) in addition to the 1^+ (74.6(1.0)%). These charge states arrive at the MCP with ∼6 keV and ∼3 keV, respectively, resulting in a greater proportion of 2^+ ions detected. Since the 2^+ charge state is contained in the first 226 eV of the retardation spectrum, a pronounced low energy part of the spectrum can result. However, the reduction of efficiency for the 1^+ charge state that was found in the offline measurements amounts to only ∼5 – 10% in the case of recoil $^{35}Cl^{1+}$ charge state, insufficient to account for the behavior seen in the experimental spectrum. Therefore, it is likely that the high reduced χ^2 of the fits and the discrepancies in the integral retardation spectrum are a manifestation of a still unknown component of the background. This hypothesis is explored in the next section.

6.6 Monte Carlo background simulations

Motivated by the unexpected properties of the experimental retardation spectrum (Figure 6.18) and the rather poor goodness of fit (Figure 6.19), the properties of possible backgrounds that would account for the observed

Ret. potental/V	A_R//ions	error/ions
0	4.486×10^5	8.772×10^3
20	4.282×10^5	4.001×10^3
40	3.698×10^5	4.457×10^3
60	3.886×10^5	4.661×10^3
80	3.244×10^5	4.198×10^3
100	2.522×10^5	3.811×10^3
120	2.332×10^5	3.491×10^3
140	2.067×10^5	3.910×10^3
200	1.592×10^5	3.350×10^3
220	1.258×10^5	4.227×10^3
260	1.096×10^5	3.477×10^3
280	9.249×10^4	4.100×10^3
300	8.383×10^4	3.662×10^3
340	8.310×10^4	3.320×10^3
420	2.956×10^4	3.636×10^3

Table 6.5: Experimental amplitudes of the recoil ions for different retardation potentials. See Figure 6.18 for a comparison of the normalized experimental amplitudes to simulated for a=1, 0 and -1.

inconsistencies were investigated. To this end, a Monte Carlo simulation was used to model a background process that would fit the observed spectrum and shed some light on its physical properties and likely origins.

The data was generated with a C++ program that produced the times between subsequent decay events according to a random distribution $-log(r)/\lambda$, where r is a random 48 bit floating point number between 0 and 1 generated by the drand48() routine. Decay times were calculated for N nuclei and decay curves constructed by sorting them from smallest to largest. In this way, decay data for the relevant part of the cycle (0.8 s to 3.2 s) was generated for implantation, βs and ion activity components. The experimental half lives T_{imp}, T_β and T_{ion} from the dedicated runs (Table 6.2) were used. The intensities A_{imp}, A_β and A_{ion} of the generated data were based on SimWITCH simulations for the Standard Model value of $a_{\beta-\nu}$ (see Table 6.6). A constant overall background was also added. Finally, various background models were incorporated to study their impact on the retardation spectrum if they were present but not accounted

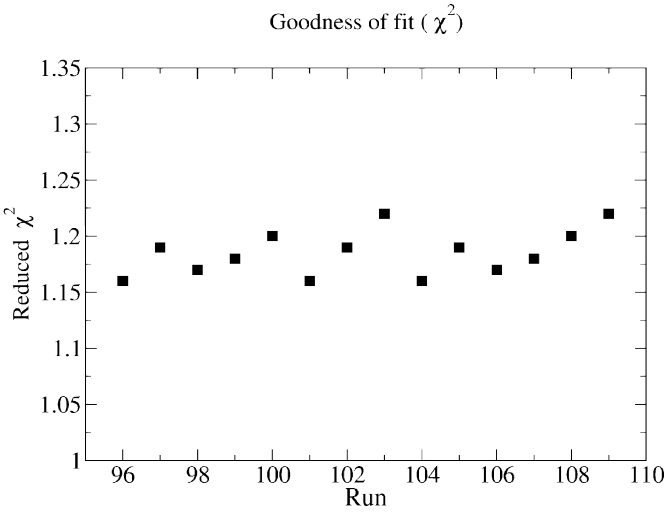


Figure 6.19: Reduced χ^2s ($\chi^2/257$) of the fits for runs 96 – 109.

for in the fit function.

An example of such randomly generated retardation spectrum is shown on Figure 6.20. A function with identical structure as the one used for fitting the experimental spectrum is then fitted to this generated spectrum and the amplitudes are extracted. In this way, it is possible to estimate the influence of different backgrounds on the spectral amplitudes. Furthermore, it is possible to identify a background that reproduces them by scanning the parameter space of the background model. In view of the low-energetic tail present in the experimental spectrum and the radioactive properties of the source, two main types of background ions were considered:

1. Constant in time throughout the ion cycle, with Gaussian energy distribution (both mean and σ in the 0 eV – 200 eV range), but absent in the background cycle,

2. Time-correlated to the decay of the ion cloud, Gaussian energy distribution (both mean and σ in the 0 eV – 200 eV range).

These energy distributions of ions are then integrated to include all ions with energies higher than the current retardation voltage. That is, the model

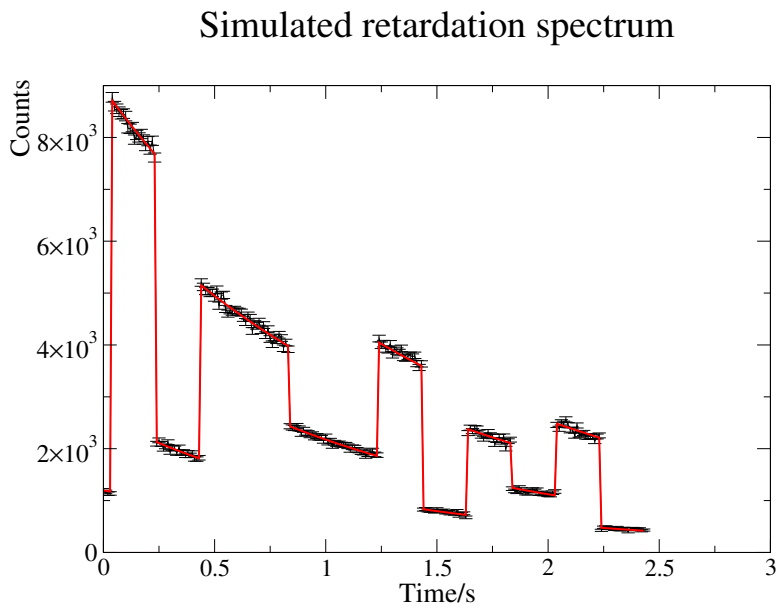


Figure 6.20: A Monte Carlo simulated retardation spectrum and fitted function. (See text for details.)

posits that only the fraction of the background ions with the energy above the retardation potential arrives to the main MCP, i.e. that they are being created between the decay trap and the analysis plane.

Fits of the generated spectra revealed that it is possible to find energy distributions of background ions that reproduce the experimental spectrum of Figure 6.18 fairly well. However, fits of the spectrum with the background constant in time (1.) exhibited unreasonably high reduced χ^2 (i.e. $\chi^2/\nu \approx 15$), while assuming a decaying background (2.) showed a much better goodness of fit, around $\chi^2/\nu \sim 1.1$ (see Figure 6.22). On Figure 6.23 the amplitudes of the simulated spectra with the experimental spectrum is shown, with the background ionization decaying with the same half-life as the radioactive ion source, T_{ion}. Furthermore, the background energy distribution that resulted in the best fit had a mean of 50 eV and a standard deviation of 100 eV (Figure 6.21). The low energy part of the retardation spectrum that contains the decaying background as well as the 2^+ charge states of the recoil ions is fairly well reproduced by the simulation. The high energy region, that for the most part does not contain the time-dependent background in the simulated spectrum, is also reasonably well reproduced. The goodness of fit is shown in Figure 6.22 and

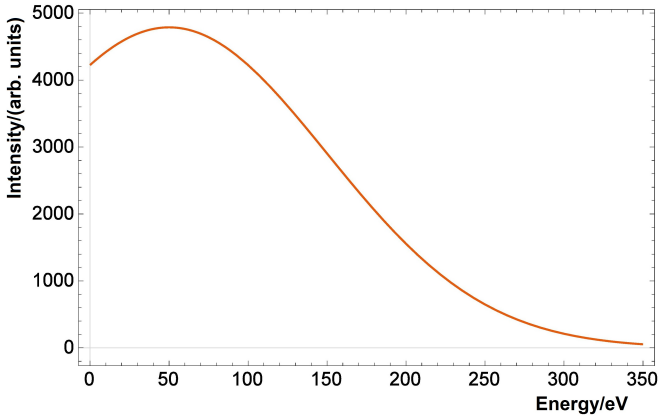


Figure 6.21: Energy distribution of the background correlated with radioactive ions in the trap that was found to reproduce the experimental recoil ion spectrum.

Intensity	ions	Half-life	time/s
A_{imp}	2.25×10^5	T_{imp}	1.31
A_{β}	1.25×10^5	T_{β}	0.61
$A_{ion,50V}$	5.00×10^5	T_{ion}	1.19
$A_{backgr.}$	6.00×10^5	$T_{backgr.}$	1.19

Table 6.6: Amplitudes and half-lives of the decay components used in Monte Carlo simulations of the background.

is typically $\chi^2/\nu \sim 1.1$. That gives an indication that the low energy part could be problematic, while the dynamics in the high energy part of the spectrum might be better captured by the fit function and $a_{\beta-\nu}$ could be closer to the Standard model expectation. However, fitting only a part of the experimental amplitudes (Figure 6.18) in the upper half of the spectrum, i.e. limiting to the 1^+ charge state, yields $a_{\beta-\nu} = (0.31 \pm 0.16)$, significantly different than the Standard model value. This is likely due to the tail of the background energy distribution (Figure 6.21) that is still significant in the 1^+ interval.

Based on the simulated retardation spectrum, it appears likely that low energy background ions correlated with the radioactive ion cloud in the decay trap are present in the spectrometer. This is in agreement with the observed flatness of

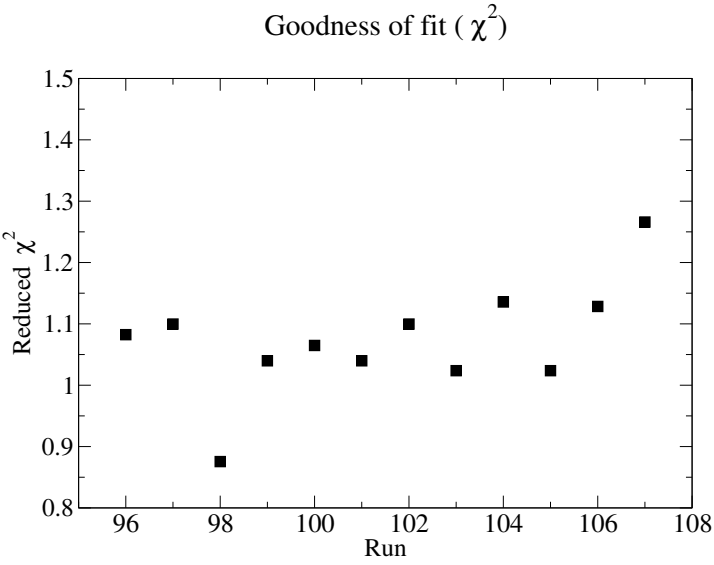


Figure 6.22: Reduced χ^2s ($\chi^2/257$) of the fits for runs 96 – 109 including an assumed background from rest gas ionization by the radioactivity in the system, i.e. time-correlated to the decay of the ion cloud.

the first 50 V interval that coincides with radioactive ions entering the decay trap and resembles a build-up process. If the rest gas is indeed ionized by the presence of radioactivity, the amount of background ions would suddenly increase with the ^{35}Ar entering the decay trap, and then decay in correlation with the radioactive ions in the trap. This background does not only depend on the number of ions in the ion cloud in the decay trap, but also on the position, size and shape of the ion cloud and requires additional monitoring to correct for it.

6.7 Conclusion and outlook

In this chapter, the most recent experimental results of WITCH have been presented and analyzed. The retardation spectrum has been fitted and the amplitudes of the recoil ions extracted from the fit parameters.

Furthermore, important systematic effects have been observed in the experimental data. Since the current data set is the first one with high statistics,

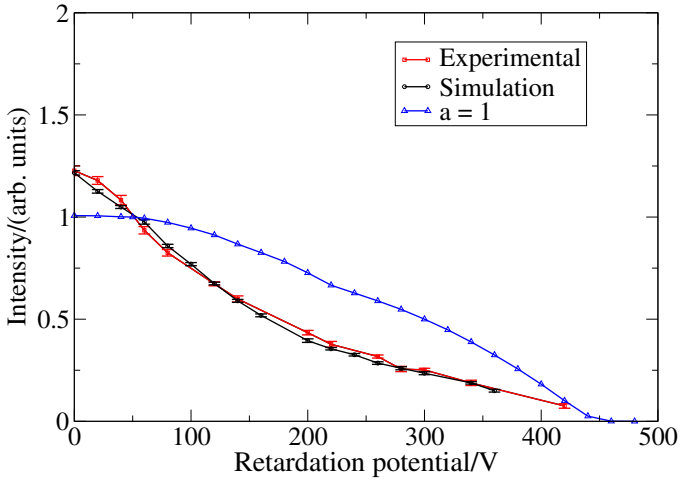


Figure 6.23: Monte Carlo simulated ion amplitudes compared with experimental data. The $a_{\beta-\nu} = 1$ spectrum is shown for reference.

several new components of the background have been identified, characterized experimentally and modeled within the fit function.

Retardation dependent background as well as background ions correlated with the charging of high-voltage sections of the pulsed drift tube were found.

Radioactive backgrounds caused by the fraction of high-energy ion bunches not fully pulsed down by the pulsed drift tube and subsequently implanted into the MCP was found.

Another radioactive background from the β-particles coming from the decay trap was found. The latter two components, together with the decay of the ion cloud, are driven by the radioactive decay of ^{35}Ar. However, all three half-lives T_{ions}, T_{β} and T_{imp} differ significantly from the nominal ^{35}Ar half-life, likely due to specific additional loss mechanisms presently not known.

A background component stemming from the neutralization of Ar^{+} ions on the walls of the decay trap and their subsequent desorption and decay in the trap volume was observed.

Evidence of a magnetron motion of the entire ion cloud around the trap center was found in the retardation spectrum.

These background effects have been successfully incorporated into the fit function.

However, even with these known sources of background taken into account, the ionic amplitudes and consequently the $a_{\beta-\nu}$ turned out to be well outside the limits imposed by previous experiments. The reason is hypothesized to be an unknown background component correlated to the amount of radioactive ions in the decay trap. Background of a similar origin, caused by β-particles, was already observed in the KATRIN experiment [73]. This hypothesis was tested with a Monte Carlo simulation of the retardation spectrum including the background component in question. It was found that the introduction of a low energy background ion component correlated with the radioactive decay intensity (see Table 6.6) indeed results in a reproduction of the experimental spectrum. However, in order to conclusively prove this hypothesis and mitigate the effects of the additional background, further online measurements and improvements of the apparatus would be required.

The former is constrained by the extremely limited beam availability at the ISOLDE facility, while the latter would entail significant modifications of the Penning traps and the spectrometer. An iris shutter mounted on the diaphragm between the two traps would significantly reduce leakage of the buffer gas to the decay trap and would prevent high energy ions from reaching the MCP during the loading of the cooler trap (implanted ions). Furthermore, the buffer gas flows into the cooler trap continuously, although it is typically required only in the first 0.7 s of the cycle. Piezo valves can produce short pulses of gas (with a repetition rate up to a few kHz). Such a valve on the buffer gas inlet would allow the presence of buffer gas to be limited to the early part of the cycle only, when cooling takes place. It could also reduce cooling time by allowing a higher buffer gas pressure. Limited to a short duration, it would not significantly increase the background He_2 pressure in other parts of the system. A similar buffer gas system is already employed at ClusterTrap [93]. These upgrades would significantly decrease the leakage of He_2 to the decay trap and other parts of the system where they can be ionized by the electrodes or radiation and thereby become a source of background in the retardation spectrum.

Furthermore, in order to characterize the radiation correlated background, the position, size and shape of the ion cloud would have to be monitored with detectors mounted in the decay trap and in the spectrometer. This would require an extensive redesign of the decay trap and the spectrometer, in addition to a dedicated online campaign.

Chapter 7

Conclusion

The primary physics goal of WITCH is to determine the $a_{\beta-\nu}$ correlation coefficient in ^{35}Ar with a precision of $\leq 0.5\%$, thereby constraining a possible exotic scalar admixture to the currently prevailing V-A (vector - axial vector) model of the weak interaction. This would result in a more stringent limit to the physics beyond the Standard Model in the electroweak sector. Considering the availability and production rates of isotopes at ISOLDE and the physics constraints, ^{35}Ar was found to be the optimal choice for reaching this goal.

Within the scope of this thesis the WITCH experimental setup, several of its systematic effects and the analysis of its first high-statistics high-resolution online experiment have been presented.

A main focus was on the systematic effects related to space-charge in the Penning traps. First the paper *Space-charge effects in Penning ion traps* was presented, containing experimental and computational studies of space-charge related systematic effects that present challenges to WITCH as well as other high capacity ion traps. The influence of space-charge and buffer gas pressure on the cooling resonance frequency ν_{cool} used in buffer gas cooling was investigated with stable $^{39}K^{+}$ ions. It was found that both space-charge and buffer gas increase the center frequencies and FWHMs of the resonances, confirming previous results from REXTRAP, another high capacity gas-filled Penning trap. Further, the Simbuca software package for *ab initio* simulations of ion dynamics in ion traps was used to simulate these effects. Simbuca employs GPU parallelism to improve computational speed by orders of magnitude in comparison with a CPU, enabling exact Coulomb simulations for $\sim 10^3$ ions or $\sim 10^6$ with a scaled Coulomb approach. Realistic electric and magnetic field maps were used and the experimental data was accurately reproduced for the space-charge induced

shift of ν_{cool} frequency. The influence of space-charge and the buffer gas on the FWHM of the resonance was reproduced qualitatively. The properties of the ν_{cool} in specific experimental conditions and their reproducibility in simulations are of special interest for improving the understanding of existing high-capacity Penning traps as well as the design of new ones.

In addition, the effect of space-charge on the magnetron frequency of the entire ion cloud around the trap center has been studied. This can provide an important correction to the systematic effect observed in the online retardation spectrum that was caused by the magnetron motion. Furthermore, the buffer gas pressure in the cooler trap, otherwise experimentally unavailable, was determined by comparing experimental cooling rates with simulations.

The second part of Chapter 4 further expanded on the topic of space-charge effects, specifically on the energy of the ion cloud and the validity of the Coulomb scaling approximation, confirming its accuracy up to a value of $\sim$100 for the scaling factor.

Chapters 5 and 6 dealt with the analysis of the WITCH data. First, an offline investigation of the energy dependent efficiency of WITCH's main MCP detector was presented. Various stable ion species were used with a setup at LPC Caen to determine this efficiency in the energy range relevant for ^{35}Ar recoil ions. A reduction of efficiency of up to 10% at low energies was found.

Finally, the analysis of the most recent online experiment at WITCH was presented. Most importantly, several new background components have been observed in the retardation spectrum and mostly incorporated in the model describing the dynamics of various processes in the system, that serves as the basis for the retardation spectrum fit function. However, one of the components of the background, correlated with the presence of radioactive ions in the decay trap, is impossible to constrain with the experimental data available. It was modeled with Monte Carlo simulation under the assumption of the Standard Model value of $a_{\beta-\nu}$ and found to correspond to a broad, low energetic Gaussian ion distribution correlated with the amount of radioactive ions in the trap. However, its experimental characterization would require extensive modification of the apparatus (see Section 6.7 for details) and dedicated online measurements.

Finally, in order to reach the goal of WITCH - i.e. the determination of $a_{\beta-\nu}$ with precision of $\leq 0.5\%$ - a precise and accurate knowledge of all systematic effects is essential. This would entail, among other things, extensive characterization of the background with a radioactive beam, which is extremely difficult at the ISOLDE facility due to the very large demand for beam time. Combined, these circumstances make it exceedingly difficult for WITCH to remain competitive with other $a_{\beta-\nu}$ experiments, e.g. LPCTrap [12]. With these constraints

in mind, it was decided to discontinue the use of WITCH as a retardation spectrometer.

Bibliography

[1] COMSOL Multiphysics Software. *http://www.comsol.com.*

[2] FASTER Data Acquisition System. *LPC Caen, http://faster.in2p3.fr.*

[3] SRIM software package. *http://www.srim.org.*

[4] MCP delay line detector manual. *RoentDek Handels GmbH, http://www.roentdek.com/manuals/ MCP Delay Line manual(9.22.1003.1).pdf*, 2011.

[5] Root Histogram Builder. *LPC Caen, http://faster.in2p3.fr/index.php /documentation-rhb?download=9:rhbshortuserguide-pdf*, 2012.

[6] E. G. Adelberger, C. Ortiz, A. Garcia, H. E. Swanson, M. Beck, O. Tengblad, M. J. G. Borge, I. Martel, H. Bichsel, and the ISOLDE Collaboration. Positron-neutrino correlation in the $0^+ \rightarrow 0^+$ decay of ^{32}Ar. *Physical Review Letters*, 83:3101, 1999.

[7] F. Ames, G. Bollen, P. Delahaye, O. Forstner, G. Huber, O. Kester, K. Reisinger, and P. Schmidt. Cooling of radioactive ions with the Penning trap REXTRAP. *Nuclear Instruments and Methods in Physics Research Section A: Accelerators, Spectrometers, Detectors and Associated Equipment*, 538(1–3):17 – 32, 2005.

[8] C. Amole, G.B. Andresen, M.D. Ashkezari, M. Baquero-Ruiz, W. Bertsche, P.D. Bowe, E. Butler, A. Capra, P.T. Carpenter, C.L. Cesar, S. Chapman, M. Charlton, A. Deller, S. Eriksson, J. Escallier, J. Fajans, T. Friesen, M.C. Fujiwara, D.R. Gill, A. Gutierrez, J.S. Hangst, W.N. Hardy, R.S. Hayano, M.E. Hayden, A.J. Humphries, J.L. Hurt, R. Hydomako, C.A. Isaac, M.J. Jenkins, S. Jonsell, L.V. Jørgensen, S.J. Kerrigan, L. Kurchaninov, N. Madsen, A. Marone, J.T.K. McKenna, S. Menary, P. Nolan, K. Olchanski, A. Olin, B. Parker, A. Povilus, P. Pusa, F. Robicheaux, E. Sarid, D. Seddon, S. Seif El Nasr, D.M. Silveira,

C. So, J.W. Storey, R.I. Thompson, J. Thornhill, D. Wells, D.P. van der Werf, J.S. Wurtele, and Y. Yamazaki. The ALPHA antihydrogen trapping apparatus. *Nuclear Instruments and Methods in Physics Research Section A: Accelerators, Spectrometers, Detectors and Associated Equipment*, 735(0):319 – 340, 2014.

[9] P. W. Anderson. Theory of flux creep in hard superconductors. *Physical Review Letters*, 9:309–311, 1962.

[10] P. Ascher, B. Blank, K. Blaum, P. Dupré, M. Gerbaux, S. Grévy, H. Guérin, M. Heck, D. Lunney, S. Naimi, and A. de Roubin. PIPERADE: a Penning trap isobar separator for the DESIR low-energy facility of SPIRAL2. *EPJ Web of Conferences*, 66:11002, 2014.

[11] O. Aviv, S. Vaintraub, T. Hirsh, A. Dhal, M.L. Rappaport, D. Melnik, O. Heber, D. Schwalm, D. Zajfman, K. Blaum, and M. Hass. Beta decay measurements from ^{6}He using an electrostatic ion beam trap. *Journal of Physics: Conference Series*, 337(1):012020, 2012.

[12] G. Ban, D. Durand, X. Fléchard, E. Liénard, and O. Naviliat-Cuncic. Precision measurements in nuclear β-decay with LPCTrap. *Annalen der Physik*, 525(8-9):576–587, 2013.

[13] J. Barnes and P. Hut. A hierarchical O(N log N) force-calculation algorithm. *Nature*, 324:446–449, 1986.

[14] J. Barnstedt. Versuch MCP-Detektoren. *http://astro.uni-tuebingen.de/seminars/praktikum/VersuchsAnleitungMCP.pdf*, 2012.

[15] D. Beck, F. Ames, M. Beck, G. Bollen, B. Delauré, P. Schuurmans, S. Schwarz, P. Schmidt, N. Severijns, and O. Forstner. Space charge effects in a gas filled Penning trap. *Atomic Physics at Accelerators: Mass Spectrometry Proceedings of the APAC 2000*, pages 473–478, 2001.

[16] M. Beck, F. Ames, D. Beck, G. Bollen, B. Delauré, V.V. Golovko, V.Yu. Kozlov, I.S. Kraev, A. Lindroth, T. Phalet, W. Quint, P. Schuurmans, N. Severijns, B. Vereecke, and S. Versyck. WITCH: a recoil spectrometer for weak interaction and nuclear physics studies. *Nuclear Instruments and Methods in Physics Research Section A: Accelerators, Spectrometers, Detectors and Associated Equipment*, 503(3):567 – 579, 2003.

[17] M. Beck, S. Coeck, V.Yu. Kozlov, M. Breitenfeldt, P. Delahaye, P. Friedag, F. Glück, M. Herbane, A. Herlert, I.S. Kraev, J. Mader, M. Tandecki, S. Van Gorp, F. Wauters, Ch. Weinheimer, F. Wenander, and N. Severijns. First detection and energy measurement of recoil ions following beta decay in a Penning trap with the WITCH experiment. *The European Physical Journal A - Hadrons and Nuclei*, 47(3):45, 2011.

[18] K. Blaum. High-accuracy mass spectrometry with stored ions. *Physics Reports*, 425(1):1 – 78, 2006.

[19] K. Blaum, G. Audi, D. Beck, G. Bollen, F. Herfurth, A. Kellerbauer, H.-J. Kluge, E. Sauvan, and S. Schwarz. Masses of ^{32}Ar and ^{33}Ar for fundamental tests. *Physical Review Letters*, 91:260801, 2003.

[20] M. Block, D. Ackermann, D. Beck, K. Blaum, M. Breitenfeldt, A. Chauduri, A. Doemer, S. Eliseev, D. Habs, S. Heinz, F. Herfurth, F.P. Heßberger, S. Hofmann, H. Geissel, H.-J. Kluge, V. Kolhinen, G. Marx, J.B. Neumayr, M. Mukherjee, M. Petrick, W. Plass, W. Quint, S. Rahaman, C. Rauth, D. Rodrıguez, C. Scheidenberger, L. Schweikhard, M. Suhonen, P.G. Thirolf, Z. Wang, and C. Weber. The ion-trap facility SHIPTRAP. *The European Physical Journal A - Hadrons and Nuclei*, 25(1):49–50, 2005.

[21] G. Bollen, R.B. Moore, G. Savard, and H. Stolzenberg. The accuracy of heavy ion mass measurements using Time-of-Flight ion cyclotron resonance in a Penning trap. *Journal of Applied Physics*, 68(9):4355–4374, 1990.

[22] J. J. Bollinger, T. B. Mitchell, X.-P. Huang, W. M. Itano, J. N. Tan, B. M. Jelenković, and D. J. Wineland. Crystalline order in laser-cooled, non-neutral ion plasmas. *Physics of Plasmas*, 7(1):7–13, 2000.

[23] L. Bornschein. The {KATRIN} experiment - a direct measurement of the electron antineutrino mass in the sub-ev region. *Nuclear Physics A*, 752(0):14 – 23, 2005.

[24] L. Brillouin. A theorem of Larmor and its importance for electrons in magnetic fields. *Physical Review*, 67:260–266, 1945.

[25] L.S. Brown and G. Gabrielse. Geonium theory: Physics of a single electron or ion in a Penning trap. *Reviews of Modern Physics*, 58:233–311, 1986.

[26] N. Cabibbo. Unitary symmetry and leptonic decays. *Physical Review Letters*, 10:531–533, 1963.

[27] S. Coeck. Search for non-Standard Model physics. *PhD thesis, KU Leuven*, 2007.

[28] S. Coeck, M. Beck, B. Delaure, V.V. Golovko, M. Herbane, A. Lindroth, S. Kopecky, V.Y. Kozlov, I.S. Kraev, T. Phalet, and N. Severijns. Microchannel plate response to high-intensity ion bunches. *Nuclear Instruments and Methods in Physics Research Section A: Accelerators, Spectrometers, Detectors and Associated Equipment* , 557(2):516–522, 2006.

[29] S. Coeck, B. Delaure, M. Herbane, M. Beck, V. V. Golovko, S. Kopecky, V. Yu. Kozlov, I. S. Kraev, A. Lindroth, T. Phalet, D. Beck, P. Delahaye, A. Herlert, F. Wenander, and N. Severijns. A pulsed drift cavity to capture 30 keV ion bunches at ground potential. *Nuclear Instruments and Methods in Physics Research Section A: Accelerators, Spectrometers, Detectors and Associated Equipment*, 572(2):585–595, 2007.

[30] S. Coeck, B. Delauré, M. Herbane, V.Yu. Kozlov, I.S. Kraev, M. Tandecki, F. Wauters, M. Beck, P. Delahaye, A. Herlert, S. Sturm, and N. Severijns. Ab initio simulations on the behavior of small ion clouds in the WITCH Penning trap system. *Nuclear Instruments and Methods in Physics Research Section A: Accelerators, Spectrometers, Detectors and Associated Equipment*, 574(2):370 – 384, 2007.

[31] C. Couratin, X. Fabian, B. Fabre, B. Pons, X. Fléchard, E. Liénard, G. Ban, M. Breitenfeldt, P. Delahaye, D. Durand, A. Méry, O. Naviliat-Cuncic, T. Porobic, G. Quéméner, D. Rodríguez, N. Severijns, J.-C. Thomas, and S. Van Gorp. Electron shakeoff following the β^+ decay of trapped $^{35}Ar^+$ ions. *Physical Review A*, 88:041403, 2013.

[32] M. Dahan, R. Fishman, O. Heber, M. Rappaport, N. Altstein, D. Zajfman, and W. J. van der Zande. A new type of electrostatic ion trap for storage of fast ion beams. *Review of Scientific Instruments*, 69(1):76–83, 1998.

[33] J.R. Dormand and P.J. Prince. A family of embedded Runge-Kutta formulae. *Journal of Computational and Applied Mathematics*, 6(1):19 – 26, 1980.

[34] V. Egorov, Ch. Briancon, V. Brudanin, J. Dionisio, J. Deutsch, V. Gorozhankin, Yu. Gurov, R. Prieels, V. Sandukovsky, N. Severijns, M. Simoes, Yu. Shitov, Ch. Vieu, V. Vorobel, Ts. Vylov, I. Yutlandov, and Sh. Zaparov. Beta-neutrino angular correlation in the decay of ^{18}Ne. *Nuclear Physics A*, 621(3):745 – 753, 1997.

[35] V.N. Fedosseev, D.V. Fedorov, R. Horn, G. Huber, U. Köster, J. Lassen, V.I. Mishin, M.D. Seliverstov, L. Weissman, and K. Wendt. Atomic spectroscopy studies of short-lived isotopes and nuclear isomer separation with the ISOLDE RILIS. *Nuclear Instruments and Methods in Physics Research Section B: Beam Interactions with Materials and Atoms*, 204(0):353 – 358, 2003.

[36] R. P. Feynman and M. Gell-Mann. Theory of the Fermi interaction. *Physical Review*, 109:193–198, 1958.

[37] X Fléchard, Ph Velten, E Liénard, A Méry, D Rodríguez, G Ban, D Durand, F Mauger, O Naviliat-Cuncic, and J C Thomas. Measurement

of the β-ν correlation coefficient $a_{\beta\nu}$ in the β decay of trapped $^6He^+$ ions. *Journal of Physics G: Nuclear and Particle Physics*, 38(5):055101, 2011.

[38] C. Fontbonne. FASTER manual. *http://faster.in2p3.fr/index.php/documentation?download=16:faster-qdc-tdc-module-user-manual*, 2012.

[39] G.W. Fraser. The ion detection efficiency of microchannel plates (MCPs). *International Journal of Mass Spectrometry and Ion Processes*, 215(1–3):13 – 30, 2002.

[40] P. Friedag. Bahnverfolgungssimulationen für das WITCH-Experiment. *Diploma thesis, Westfälischen Wilhelms-Universität Munster*, 2008.

[41] P. Friedag. Setup and calibration of a position sensitive microchannel plate detector and analysis of a test run optimizing the WITCH experiment. *PhD thesis, Westfälischen Wilhelms-Universität Munster*, 2013.

[42] G. Gabrielse. Open-endcap Penning traps for high precision experiments. *International Journal of Mass Spectrometry and Ion Processes*, 88(2–3):319 – 332, 1989.

[43] G. Gamow and E. Teller. Selection rules for the β-disintegration. *Physical Review*, 49:895–899, 1936.

[44] Sheldon L. Glashow. Partial-symmetries of weak interactions. *Nuclear Physics*, 22(4):579 – 588, 1961.

[45] F. Gluck, S. Baeßler, J. Byrne, M.G.D. van der Grinten, F.J. Hartmann, W. Heil, I. Konorov, G. Petzoldt, Yu. Sobolev, and O. Zimmer. The neutron decay retardation spectrometer aspect: Electromagnetic design and systematic effects. *The European Physical Journal A - Hadrons and Nuclei*, 23(1):135–146, 2005.

[46] Glück, F., Baeßler, S., Byrne, J., van der Grinten, M. G. D., Hartmann, F. J., Heil, W., Konorov, I., Petzoldt, G., Sobolev, Yu., and Zimmer, O. The neutron decay retardation spectrometer aSPECT: Electromagnetic design and systematic effects. *The European Physical Journal A - Hadrons and Nuclei*, 23(1):135–146, 2005.

[47] A. Gorelov, D. Melconian, W. P. Alford, D. Ashery, G. Ball, J. A. Behr, P. G. Bricault, J. M. D'Auria, J. Deutsch, J. Dilling, M. Dombsky, P. Dubé, J. Fingler, U. Giesen, F. Glück, S. Gu, O. Häusser, K. P. Jackson, B. K. Jennings, M. R. Pearson, T. J. Stocki, T. B. Swanson, and M. Trinczek. Scalar interaction limits from the beta-neutrino correlation of trapped radioactive atoms. *Physical Review Letters*, 94:142501, 2005.

[48] A. Gustafsson, A. Herlert, and F. Wenander. Mass-selective operation with REXTRAP. *Nuclear Instruments and Methods in Physics Research Section A: Accelerators, Spectrometers, Detectors and Associated Equipment*, 626–627(0):8 – 15, 2011.

[49] D. Habs, O. Kester, T. Sieber, H. Bongers, and S. Emhofer. The REX-ISOLDE project. *Hyperfine Interactions*, 192(1):43 – 66, 2000.

[50] Tsuyoshi Hamada and Toshiaki Iitaka. The Chamomile scheme: An optimized algorithm for N-body simulations on programmable graphics processing units. *http://arxiv.org/abs/astro-ph/0703100*, 2007.

[51] J. C. Hardy and I. S. Towner. Superallowed $0^+ \rightarrow 0^+$ nuclear β decays: 2014 critical survey, with precise results for V_{ud} and CKM unitarity. *Physical Review C*, 91:025501, 2015.

[52] A. Herlert, C. Borgmann, D. Fink, C.H. Christensen, M. Kowalska, and S. Naimi. Effects of space charge on the mass purification in Penning traps. *Hyperfine Interactions*, 199(1-3):211–220, 2011.

[53] G. Zs. K. Horvath, J.-L. Hernandez-Pozos, K. Dholakia, J. Rink, D. M. Segal, and R. C. Thompson. Ion dynamics in perturbed quadrupole ion traps. *Physical Review A*, 57:1944–1956, 1998.

[54] J. D. Jackson. Classical electrodynamics. *Wiley*, 1998.

[55] J. D. Jackson, S. B. Treiman, and H. W. Wyld. Possible tests of time reversal invariance in beta decay. *Physical Review*, 106:517–521, 1957.

[56] J.B. Jeffries, S.E. Barlow, and G.H. Dunn. Theory of space-charge shift of ion cyclotron resonance frequencies. *International Journal of Mass Spectrometry and Ion Processes*, 54(1–2):169 – 187, 1983.

[57] C. H. Johnson, Frances Pleasonton, and T. A. Carlson. Precision measurement of the recoil energy spectrum from the decay of He^6. *Physical Review*, 132:1149–1165, 1963.

[58] A. Kellerbauer. A study of the accuracy of the Penning trap mass spectrometer isoltrap and standard-model tests with superallowed beta decays. *PhD thesis, University of Heidelberg*, 2002.

[59] V. Khachatryan et al. Search for physics beyond the standard model in final states with a lepton and missing transverse energy in proton-proton collisions at $\sqrt{s} = 8$ TeV. *Physical Review D*, 91:092005, 2015.

[60] A. Knecht. internal communication. 2013.

[61] A. Knecht, Z. T. Alexander, Y. Bagdasarova, T. M. Cope, B. G. Delbridge, X. Fléchard, A. García, R. Hong, E. Liénard, P. Mueller, O. Naviliat-Cuncic, A. S. C. Palmer, R. G. H. Robertson, D. W. Storm, H. E. Swanson, S. Utsuno, F. Wauters, W. Williams, C. Wrede, and D. W. Zumwalt. Weak interaction studies with ^{6}He. *AIP Conference Proceedings*, 1560(1):636–640, 2013.

[62] M. Kobayashi and T. Maskawa. CP-violation in the renormalizable theory of weak interaction. *Progress of Theoretical Physics*, 49(2):652–657, 1973.

[63] M. Kowalska, S. Naimi, J. Agramunt, A. Algora, G. Audi, D. Beck, B. Blank, K. Blaum, Ch. Böhm, M. Breitenfeldt, E. Estevez, L.M. Fraile, S. George, F. Herfurth, A. Herlert, A. Kellerbauer, D. Lunney, E. Minaya-Ramirez, D. Neidherr, B. Olaizola, K. Riisager, M. Rosenbusch, B. Rubio, S. Schwarz, L. Schweikhard, and U. Warring. Preparing a journey to the east of ^{208}Pb with ISOLTRAP: Isobaric purification at A = 209 and new masses for $^{211-213}$Fr and ^{211}Ra. *The European Physical Journal A - Hadrons and Nuclei*, 42(3):351–359, 2009.

[64] V.Yu. Kozlov, M. Beck, S. Coeck, P. Delahaye, P. Friedag, M. Herbane, A. Herlert, I.S. Kraev, M. Tandecki, S. Van Gorp, F. Wauters, Ch. Weinheimer, F. Wenander, D. Zákoucký, and N. Severijns. The WITCH experiment: Acquiring the first recoil ion spectrum. *Nuclear Instruments and Methods in Physics Research Section B: Beam Interactions with Materials and Atoms*, 266(19–20):4515 – 4520, 2008.

[65] V.Yu. Kozlov, N. Severijns, D. Beck, M. Beck, S. Coeck, B. Delauré, A. Lindroth, S. Kopecky, P. Delahaye, F. Wenander, V.V. Golovko, I.S. Kraev, and T. Phalet. The WITCH experiment: Completion of a set-up to investigate the structure of weak interactions with a Penning trap. *International Journal of Mass Spectrometry and Ion Processes*, 251(2–3):159 – 172, 2006.

[66] E. Kugler. The ISOLDE facility. *Hyperfine Interactions*, 129(1):23–42, 2003.

[67] T. D. Lee and C. N. Yang. Question of parity conservation in weak interactions. *Physical Review*, 104:254–258, 1956.

[68] G. Li, R. Segel, N. D. Scielzo, P. F. Bertone, F. Buchinger, S. Caldwell, A. Chaudhuri, J. A. Clark, J. E. Crawford, C. M. Deibel, J. Fallis, S. Gulick, G. Gwinner, D. Lascar, A. F. Levand, M. Pedretti, G. Savard, K. S. Sharma, M. G. Sternberg, T. Sun, J. Van Schelt, R. M. Yee, and B. J. Zabransky. Tensor interaction limit derived from the α-β-$\overline{\nu}$ correlation in trapped ^{8}Li ions. *Physical Review Letters*, 110:092502, 2013.

[69] E. Liénard, M. Herbane, G. Ban, G. Darius, P. Delahaye, D. Durand, X. Fléchard, M. Labalme, F. Mauger, A. Mery, O. Naviliat-Cuncic, and D. Rodríguez. Performance of a micro-channel plates position sensitive detector. *Nuclear Instruments and Methods in Physics Research Section A: Accelerators, Spectrometers, Detectors and Associated Equipment*, 551(2–3):375 – 386, 2005.

[70] E.A. Mason and E.W. McDaniel. Transport properties of ions in gases. 1988.

[71] M. Mehlman, D. Melconian, and P.D. Shidling. Texas A&M Penning trap facility - design of the measurement trap. *http://arxiv.org/abs/1208.4078*, 2012.

[72] M. Mehlman, P.D. Shidling, S. Behling, L.G. Clark, B. Fenker, and D. Melconian. Design of a unique open-geometry cylindrical Penning trap. *Nuclear Instruments and Methods in Physics Research Section A: Accelerators, Spectrometers, Detectors and Associated Equipment*, 712(0):9 – 14, 2013.

[73] S. Mertens. Study of Background Processes in the Electrostatic Spectrometers of the KATRIN Experiment. *PhD thesis, Karlsruhe Institute of Technology*, 2012.

[74] M. Mukherjee, D. Beck, K. Blaum, G. Bollen, P. Delahaye, J. Dilling, S. George, C. Guénaut, F. Herfurth, A. Herlert, A. Kellerbauer, H.-J. Kluge, U. Köster, D. Lunney, S. Schwarz, L. Schweikhard, and C. Yazidjian. Mass measurements and evaluation around A = 22. *The European Physical Journal A - Hadrons and Nuclei*, 35(1):31–37, 2008.

[75] M. Mukherjee, D. Beck, K. Blaum, G. Bollen, J. Dilling, S. George, F. Herfurth, A. Herlert, A. Kellerbauer, H.-J. Kluge, S. Schwarz, L. Schweikhard, and C. Yazidjian. ISOLTRAP: An on-line Penning trap for mass spectrometry on short-lived nuclides. *The European Physical Journal A - Hadrons and Nuclei*, 35(1):1–29, 2008.

[76] O. Naviliat-Cuncic and M. González-Alonso. Prospects for precision measurements in nuclear β decay in the LHC era. *Annalen der Physik*, 525(8-9):600–619, 2013.

[77] NUDAT 2.5. National nuclear data center, Brookhaven National Laboratory. *http://www.nndc.bnl.gov/nudat2/index.jsp*, 109:193–198, 1958.

[78] J. Oberheide, P. Wilhelms, and M. Zimmer. New results on the absolute ion detection efficiencies of a microchannel plate. *Measurement Science and Technology*, 8(4):351, 1997.

[79] E.S. Parilis and L.M. Kishinevskii. *Soviet Physics - Solid State*, 215(1–3):885, 1960.

[80] L. Penescu, R. Catherall, J. Lettry, and T. Stora. Development of high efficiency versatile arc discharge ion source at CERN ISOLDE. *Review of Scientific Instruments*, 81(2):02A906, 2010.

[81] M. Peterson. A Monte Carlo method for the simulation of buffer–gas cooling inside a radio frequency quadrupole. *PhD thesis, Linkoping University*, 2002.

[82] A. J. Peurrung, R. T. Kouzes, and S. E. Barlow. The non-neutral plasma: an introduction to physics with relevance to cyclotron resonance mass spectrometry. *International Journal of Mass Spectrometry and Ion Processes*, 157:80, 1996.

[83] A. Picard, H. Backe, H. Barth, J. Bonn, B. Degen, T. Edling, R. Haid, A. Hermanni, P. Leiderer, T. Loeken, A. Molz, R.B. Moore, A. Osipowicz, E.W. Otten, M. Przyrembel, M. Schrader, M. Steininger, and C. Weinheimer. A solenoid retarding spectrometer with high resolution and transmission for keV electrons. *Nuclear Instruments and Methods in Physics Research Section B: Beam Interactions with Materials and Atoms* , 63(3):345–358, 1992.

[84] T. Porobić. *PhD thesis, KU Leuven*, 2015.

[85] D. Počanić, R. Alarcon, L.P. Alonzi, S. Baeßler, S. Balascuta, J.D. Bowman, M.A. Bychkov, J. Byrne, J.R. Calarco, V. Cianciolo, C. Crawford, E. Frlež, M.T. Gericke, G.L. Greene, R.K. Grzywacz, V. Gudkov, F.W. Hersman, A. Klein, J. Martin, S.A. Page, A. Palladino, S.I. Penttila, K.P. Rykaczewski, W.S. Wilburn, A.R. Young, and G.R. Young. Nab: Measurement principles, apparatus and uncertainties. *Nuclear Instruments and Methods in Physics Research Section A: Accelerators, Spectrometers, Detectors and Associated Equipment*, 611(2–3):211 – 215, 2009.

[86] H. Raimbault-Hartmann, D. Beck, G. Bollen, M. König, H-J. Kluge, E. Schark, J. Stein, S. Schwarz, and J. Szerypo. A cylindrical Penning trap for capture, mass selective cooling, and bunching of radioactive ion beams. *Nuclear Instruments and Methods in Physics Research Section B: Beam Interactions with Materials and Atoms*, 126(1):378–382, 1997.

[87] J.P. Ramos. Effect of calcium oxide microstructure on the diffusion of isotopes. *Master thesis, University of Aveiro*, 2012.

[88] J.P. Ramos, A. Gottberg, T.M. Mendonça, C. Seiffert, A.M.R. Senos, Hans Otto Uldall Fynbo, O. Tengblad, J.A. Briz, M.V. Lund, G. T. Koldste, et al. Intense $^{31-35}$Ar beams produced with a nanostructured CaO target at ISOLDE. *Nuclear Instruments and Methods in Physics Research Section B: Beam Interactions with Materials and Atoms*, 320:83–88, 2014.

[89] D. Rodríguez, A. Méry, G. Ban, J. Brégeault, G. Darius, D. Durand, X. Fléchard, M. Herbane, M. Labalme, E. Liénard, F. Mauger, Y. Merrer, O. Naviliat-Cuncic, J.C. Thomas, and C. Vandamme. The LPCTrap facility: A novel transparent Paul trap for high-precision experiments. *Nuclear Instruments and Methods in Physics Research Section A: Accelerators, Spectrometers, Detectors and Associated Equipment*, 565(2):876 – 889, 2006.

[90] V. Rokhlin. Rapid solution of integral equations of classical potential theory. *Journal of Computational Physics*, 60(2):187 – 207, 1985.

[91] S. Van Gorp. Search for physics beyond the standard electroweak model with the WITCH experiment. *PhD thesis, Katholieke Universiteit Leuven*, 2012.

[92] G. Savard, St. Becker, G. Bollen, H.-J. Kluge, R.B. Moore, Th. Otto, L. Schweikhard, H. Stolzenberg, and U. Wiess. A new cooling technique for heavy ions in a Penning trap. *Physics Letters A*, 158(5):247 – 252, 1991.

[93] L. Schweikhard, K. Hansen, A. Herlert, G. Marx, and M. Vogel. New approaches to stored cluster ions. *The European Physical Journal D - Atomic, Molecular, Optical and Plasma Physics*, 24(1):137–143, 2003.

[94] N.D. Scielzo, S.J. Freedman, B.K. Fujikawa, and P.A. Vetter. Measurement of the β-ν correlation using magneto-optically trapped ^{21}Na. *Physical Review Letters*, 93:102501, 2004.

[95] N.D. Scielzo, G. Li, M.G. Sternberg, G. Savard, P.F. Bertone, F. Buchinger, S. Caldwell, J.A. Clark, J. Crawford, C.M. Deibel, J. Fallis, J.P. Greene, S. Gulick, A.A. Hecht, D. Lascar, J.K.P. Lee, A.F. Levand, M. Pedretti, R.E. Segel, H. Sharma, K.S. Sharma, I. Tanihata, J. Van Schelt, R.M. Yee, and B.J. Zabransky. The Paul trap: A radiofrequency-quadrupole ion trap for precision studies. *Nuclear Instruments and Methods in Physics Research Section A: Accelerators, Spectrometers, Detectors and Associated Equipment*, 681(0):94 – 100, 2012.

[96] N. Severijns. Correlation and spectrum shape measurements in β-decay probing the standard model. *Journal of Physics G: Nuclear and Particle Physics*, 41(11):114006, 2014.

[97] N. Severijns and O. Naviliat-Cuncic. Symmetry tests in nuclear beta decay. *Annual Review of Nuclear and Particle Science*, 61:23–46, 2011.

[98] N. Severijns and O. Naviliat-Cuncic. Structure and symmetries of the weak interaction in nuclear beta decay. *Physica Scripta*, (T152):014018, 2013.

[99] N. Severijns, M. Tandecki, Phalet T., and I. Towner. Ft values of the T = 1/2 mirror β transitions. *Physical Review C*, 78(2):55501, 2008.

[100] S. Sturm. Implementation of a mass separation method in the Penning trap REXTRAP and investigation of space-charge related phenomena. *PhD thesis, University of Heidelberg*, page 36, 2007.

[101] E. C. G. Sudarshan and R. E. Marshak. Chirality invariance and the universal Fermi interaction. *Physical Review*, 109:1860–1862, 1958.

[102] J.N. Tan, J.J. Bollinger, B. Jelenkovic, and D.J. Wineland. Long-range order in laser-cooled, atomic-ion Wigner crystals observed by Bragg scattering. *Physical Review Letters*, 75:4198–4201, 1995.

[103] M. Tandecki. Progress at the WITCH experiment towards Weak Interaction Studies. *PhD thesis, Katholieke Universiteit Leuven*, 2011.

[104] M. Tandecki, D. Beck, M. Beck, H. Brand, M. Breitenfeldt, V. De Leebeeck, P. Friedag, A. Herlert, V. Kozlov, J. Mader, S. Roccia, G. Soti, E. Traykov, S. Van Gorp, F. Wauters, Ch. Weinheimer, D. Zakoucky, and N. Severijns. Computer controls for the WITCH experiment. *Nuclear Instruments and Methods in Physics Research Section A: Accelerators, Spectrometers, Detectors and Associated Equipment* , 629(1):396–405, 2011.

[105] E. Traykov, M. Beck, M. Breitenfeldt, P. Delahaye, V. De Leebeeck, P. Friedag, A. Herlert, N. Geeraert, W. Heirman, P. I. Lonne, J. Mader, S. Roccia, G. Soti, M. Tandecki, M. Timmermans, J. Thiboud, S. Van Gorp, F. Wauters, C. Weinheimer, D. Zakoucky, and N. Severijns. A compact radio frequency quadrupole for ion bunching in the WITCH experiment. *Nuclear Instruments and Methods in Physics Research Section A: Accelerators, Spectrometers, Detectors and Associated Equipment*, 648(1):1–14, 2011.

[106] K. Valerius. Spectrometer-related background processes and their suppression in the KATRIN experiment. *PhD thesis, Westfälischen Wilhelms-Universität Münster*, page 218, 2009.

[107] S. Van Gorp, M. Beck, M. Breitenfeldt, V. De Leebeeck, P. Friedag, A. Herlert, T. Iitaka, J. Mader, V. Kozlov, S. Roccia, G. Soti,

M. Tandecki, E. Traykov, F. Wauters, Ch Weinheimer, D. Zakoucky, and N. Severijns. Simbuca, using a graphics card to simulate Coulomb interactions in a Penning trap. *Nuclear Instruments and Methods in Physics Research Section A: Accelerators, Spectrometers, Detectors and Associated Equipment*, 638(1):192–200, 2011.

[108] S. Van Gorp, M. Breitenfeldt, M. Tandecki, M. Beck, P. Finlay, P. Friedag, F. Glück, A. Herlert, V. Kozlov, T. Porobic, G. Soti, E. Traykov, F. Wauters, Ch. Weinheimer, D. Zákoucký, and N. Severijns. First β-ν correlation measurement from the recoil-energy spectrum of Penning trapped ^{35}Ar ions. *Physical Review C*, 90:025502, 2014.

[109] P. A. Vetter, J. R. Abo-Shaeer, S. J. Freedman, and R. Maruyama. Measurement of the β-ν correlation of ^{21}Na using shakeoff electrons. *Physical Review C*, 77:035502, 2008.

[110] D. Voulot, F. Wenander, E. Piselli, R. Scrivens, M. Lindroos, H.B. Jeppesen, L.M. Fraile, S. Sturm, and P. Delahaye. Radioactive beams at REX–ISOLDE: Present status and latest developments. *Nuclear Instruments and Methods in Physics Research Section B: Beam Interactions with Materials and Atoms*, 266(19–20):4103 – 4107, 2008.

[111] S. Weinberg. A model of leptons. *Physical Review Letters*, 19:1264–1266, 1967.

[112] W. C. Wiley and I. H. McLaren. Time-of-Flight mass spectrometer with improved resolution. *Review of Scientific Instruments*, 26(12):1150–1157, 1955.

[113] D.F.A. Winters, M. Vogel, D.M. Segal, and R.C. Thompson. Electronic detection of charged particle effects in a Penning trap. *Journal of Physics B: Atomic, Molecular and Optical Physics*, 39(14):3131, 2006.

[114] J.L. Wiza. Microchannel plate detectors. *Nuclear Instruments and Methods*, 162(1):587–601, 1979.

[115] R.N. Wolf, F. Wienholtz, D. Atanasov, D. Beck, K. Blaum, Ch. Borgmann, F. Herfurth, M. Kowalska, S. Kreim, Yu. A. Litvinov, D. Lunney, V. Manea, D. Neidherr, M. Rosenbusch, L. Schweikhard, J. Stanja, and K. Zuber. ISOLTRAP's multi-reflection time-of-flight mass separator/spectrometer. *International Journal of Mass Spectrometry and Ion Processes*, 349–350(0):123 – 133, 2013.

[116] C. S. Wu, E. Ambler, R. W. Hayward, D. D. Hoppes, and R. P. Hudson. Experimental test of parity conservation in beta decay. *Physical Review*, 105:1413–1415, 1957.

[117] E. Wursten. Searching for Exotic Weak Currents with the WITCH Experiment. *MSc thesis, Katholieke Universiteit Leuven*, page 58, 2013.



FACULTY OF SCIENCE
DEPARTMENT OF PHYSICS AND ASTRONOMY
NUCLEAR AND RADIATION PHYSICS
Celestijnenlaan 200D box 2418
B-3001 Leuven
tomica.porobic@fys.kuleuven.be
http://fys.kuleuven.be